Modeling and numerical simulation of implantable cardiovascular devices

Ludovic Boilevin-Kayl

▶ **To cite this version:**

Ludovic Boilevin-Kayl. Modeling and numerical simulation of implantable cardiovascular devices. Numerical Analysis [math.NA]. Sorbonne Université, 2019. English. NNT : . tel-02217259v1

HAL Id: tel-02217259

https://inria.hal.science/tel-02217259v1

Submitted on 31 Jul 2019 (v1), last revised 10 Sep 2020 (v2)

HAL is a multi-disciplinary open access archive for the deposit and dissemination of scientific research documents, whether they are published or not. The documents may come from teaching and research institutions in France or abroad, or from public or private research centers.

L'archive ouverte pluridisciplinaire **HAL**, est destinée au dépôt et à la diffusion de documents scientifiques de niveau recherche, publiés ou non, émanant des établissements d'enseignement et de recherche français ou étrangers, des laboratoires publics ou privés.

Modeling and numerical simulation of implantable cardiovascular devices

THÈSE DE DOCTORAT

présentée par

Ludovic Boilevin-Kayl

pour obtenir le grade de

DOCTEUR DE
L'UNIVERSITÉ PIERRE ET MARIE CURIE - Paris VI

Spécialité : Mathématiques Appliquées

Soutenue publiquement le 10 Juillet 2019 devant le jury composé de :

Miguel Ángel Fernández	Codirecteur de thèse
Pascal Frey	Examinateur
Jean-Frédéric Gerbeau	Directeur de thèse
Emmanuel Maitre	Examinateur
Simon Mendez	Rapporteur
Anne-Virginie Salsac	Examinatrice
Daniele Zanotti	Examinateur

Après avis favorables des rapporteurs : Simon Mendez et Djordje Peric

Thèse préparée au sein de l'équipe-projet REO
Laboratoire Jacques-Louis Lions
Université Pierre et Marie Curie - Paris 6
et **Centre de Recherche Inria de Paris**
2 rue Simone Iff
75589 Paris Cedex 12

À Monique et Rodolphe,

"Mistakes are the portals of discovery."
- James Joyce, *Ulysses*, 1922

Remerciements

Je pense que tous ceux qui m'ont précédés seront d'accord pour dire qu'un doctorat, en plus d'être indéniablement une incroyable entreprise scientifique, est également une aventure humaine parsemée de rencontres. C'est donc à vous – connaissances, collègues, amis et famille – qui m'avez côtoyé plus ou moins assidûment pendant ces trois (et un peu plus) dernières années, que je dédie ce qui suit. J'ai toujours considéré que les remerciements étaient les lignes les plus exigeantes à écrire d'un manuscrit de thèse, d'une part parce qu'ils en constitueront sans nul doute les pages les plus lues mais aussi parce qu'ils risquent de souffrir d'un manque de concision ou encore de pudeur aux yeux de certains. Mais l'occasion de remercier ses proches, quand bien même maladroitement, est trop précieuse alors laissez-moi quand même essayer !

Pour commencer, j'aimerais naturellement remercier Simon Mendez et Djordje Peric qui ont accepté de rapporter cette thèse. Merci pour votre lecture détaillée de mon manuscrit ainsi que pour vos remarques constructives sur mon travail, aussi bien sur la forme que sur le fond. Merci également à Pascal Frey, à Emmanuel Maitre, à Anne-Virginie Salsac et à Daniele Zanotti d'avoir accepté de faire partie de mon jury de thèse.

Je n'ai pas de mots assez forts pour exprimer l'étendue de ma gratitude envers mes deux directeurs de thèse, Jean-Frédéric Gerbeau et Miguel Fernández. Merci de m'avoir proposé ce sujet de thèse et de m'avoir accompagné tout au long de ce travail. J'ai énormément appris. Merci à toi, Jean-Frédéric, pour ton calme et ta sérénité en toute circonstance. Ta grande pédagogie et ton aisance à expliquer si simplement des concepts pointus m'ont toujours bluffé. Je te souhaite bonne chance dans tes nouvelles fonctions. Merci à toi, Miguel, pour ton soutien scientifique et surtout humain. Ta passion et ton dévouement pour la science n'auront pas manqué de m'impressionner à plusieurs reprises et je suis honoré d'avoir fait mes premiers pas dans le monde de la recherche à tes côtés. Ta grande disponibilité et ta patience face à mes incompréhensions (et parfois ma mauvaise foi :)) quant aux méandres de l'interaction fluide-structure m'ont été d'une aide précieuse. Je me rappelle qu'un de mes professeurs avait l'habitude de dire, en parlant de la thèse, que "le choix" des encadrants était aussi important, si ce n'est même plus, que le choix du sujet lui-même. En ce qui me concerne, je pense que je n'aurais pas pu espérer mieux.

Ensuite, je souhaite remercier tous les autres permanents du troisième étage du bâtiment A et en particulier ceux de l'ex-équipe REO : Marina, Damiano, Irène, Céline et, moins souvent croisés, Muriel, Laurent et Marc. Merci pour votre accueil et pour votre bienveillance. Merci en particulier à Marina et à Damiano pour toutes les sympathiques discussions partagées autour d'un repas ou d'un café. Mention particulière à Irène et à Céline pour notre rencontre à Air Liquide lorsque je n'étais encore qu'un simple stagiaire et qui m'ont introduit auprès de REO. J'ai également une pensée particulière pour Maryse

: merci de m'avoir accompagné et d'avoir rendu mes tâches administratives beaucoup plus faciles à appréhender. Force et courage à Julien pour prendre le relais. Longue vie à la future équipe COMMEDIA !

Merci à tous les doctorants, post-docs et stagiaires qui, au gré du temps, sont devenus pour certains des amis. Merci d'avoir partagé avec moi des repas, des pintes, des conférences voire même des vacances. Merci à Nicolas (pour ta positivité à toute épreuve (ou presque) depuis Air Liquide, je tâcherai de m'en inspirer dans le futur), à Axel (pour m'avoir prouvé qu'il y avait toujours plus cynique que soi), à Matteo (pour m'avoir transmis ton amour de l'intégration continue et du C++ bien écrit), à Chloé et à Noémie (pour notre aventure à Pittsburgh), à Fabien (pour m'avoir fait découvrir Nantes), à Florian (pour ton abnégation et ton amour de FELiScE (ou pas)), à Gautier (pour ton aide précieuse sur HeartLab et autre MoReFEM), à Gaëtan (pour nos pauses musicales), à Sanjay (*for having been my first co-worker when I arrived at Inria and for your wonder about the pronunciation of "vraisemblablement"*), à Felipe (*Feliz cumpleaños!*) et à Daniele (*il ragazzo che ha guardato l'intero Game of Thrones in meno di 3 settimane*). Merci aussi aux autres (Mikel, Mikele, Eliott, Faisal, Justine, Léa, Fabien W., Mathieu, Lara, Alberto, Yi, ...) et à ceux que j'ai (involontairement bien sûr :)) oubliés de citer. Je terminerai par les deux plus importants à mes yeux, mes compagnons d'infortune, mes frère et sœur académiques (comme dirait l'autre...), mes co-bureaux préférés : Fannie et Alexandre. Merci à toi, Fannie (*o mangiatore di spaghetti italiani*) pour ta bonne humeur quotidienne qui a embelli le bureau A312. Je n'oublierai ni ton accent bizarre quand tu essayes de dire "bonjour" ni ton amour du mode de vie bobo parisien (à grand renfort de Ground Control, de trajets en trottinette électrique et autres barbecues sur balcon d'appartement). Merci à toi, Alexandre, pour nos querelles Alsace-Lorraine, pour notre amour commun de la gastronomie française, pour avoir été si friand de mes provocations et mes invectives diverses et pour nos multiples échanges sur Hangouts. N'oublie pas que "le benzaldéhyde, c'est sublime" !

Sortons enfin du monde académique ! J'ai l'habitude de dire que les amitiés se font et se défont au gré du temps mais force est de constater qu'il y en a qui résistent. Frédéric, Jean-Claude, Nabil, Mathieu, Louis, Timothée, Paul, Élise, Victor, Sophie, Sandy, Karine, Nicolas, Adrien, Maxime, Marc-Arthur, Julien, Johan, Émilie, Charlotte, Florent, Laëtitia, Olivier, Marie-Élise, Anne et compagnie : merci d'avoir su me faire oublier (un peu mais pas trop) mes soucis de modélisation et de simulation de valves cardiaques le temps de soirées, de sorties, de vacances ou même de simples discussions. Vous avez été mes harnais de sécurité. Pour terminer, je souhaiterais évidemment remercier mes parents, ma tante, Hugo, Julie et également la "belle-famille" pour leur présence, leur soutien et leurs encouragements. J'ai gardé la meilleure pour la fin : merci à toi, Camille, pour l'amour infini et le soutien perpétuel dont tu m'as fait grâce pendant ces dernières années. J'espère que nous aurons à en partager encore beaucoup d'autres ensemble.

Paris, Mai 2019 *Ludovic Boilevin-Kayl*

Modélisation et simulation numérique de dispositifs cardiovasculaires implantables

Résumé : Cette thèse, réalisée dans le cadre du projet Mivana, est consacrée à la modélisation et à la simulation numérique de dispositifs cardiaques implantables. Ce projet est mené par les start-up Kephalios et Epygon, concepteurs de solutions chirurgicales non invasives pour le traitement de la régurgitation mitrale. La conception et la simulation de tels dispositifs nécessitent des méthodes numériques efficaces et précises capables de calculer correctement l'hémodynamique cardiaque. C'est le but principal de cette thèse.

Dans la première partie, nous décrivons le système cardiovasculaire et les valves cardiaques avant de présenter quelques éléments de théorie concernant la modélisation mathématique de l'hémodynamique cardiaque. En fonction du degré de complexité adopté pour la modélisation des feuillets de la valve, deux approches sont identifiées : le modèle de surfaces résistives immergées et le modèle complet d'interaction fluide-structure.

Dans la deuxième partie, nous étudions la première approche qui consiste à combiner une modélisation réduite de la dynamique des valves avec un découplage cinématique de l'hémodynamique cardiaque et de l'électromécanique. Nous l'enrichissons de données physiologiques externes pour la simulation correcte des phases isovolumétriques, pierres angulaires du battement cardiaque, permettant d'obtenir un modèle relativement précis qui évite la complexité des problèmes entièrement couplés. Ensuite, une série d'essais numériques sur des géométries 3D physiologiques, impliquant la régurgitation mitrale et plusieurs configurations de valves immergées, illustre la performance du modèle proposé.

Dans la troisième et dernière partie, des modèles complets d'interaction fluide-structure sont considérés. Ce type de modélisation est nécessaire pour étudier des problèmes plus complexes où la précédente approche n'est plus satisfaisante, comme par exemple le prolapsus de la valve mitrale ou la fermeture d'une valve mécanique. D'un point de vue numérique, le développement de méthodes précises et efficaces est indispensable pour pouvoir simuler de tels cas physiologiques. Nous considérons alors une étude numérique complète dans laquelle plusieurs méthodes de maillages non compatibles sont comparées. Puis, nous présentons un nouveau schéma de couplage explicite dans le cadre d'une méthode de type domaine fictif pour lequel la stabilité inconditionnelle au sens de la norme en énergie est démontrée. Plusieurs exemples numériques en 2D sont proposés afin d'illustrer les propriétés et les performances de ce schéma. Enfin, cette méthode est finalement utilisée pour la simulation numérique 2D et 3D de dispositifs cardiovasculaires implantables dans un modèle complet d'interaction fluide-structure.

Mots-clés : Dispositifs cardiovasculaires, Modélisation, Hémodynamique cardiaque, Surfaces résistives immergées, Interaction fluide-structure, Structures minces immergées, Schémas de couplage explicite, Méthodes de maillages non compatibles.

Modeling and numerical simulation of implantable cardiovascular devices

Abstract: This thesis, taking place in the context of the Mivana project, is devoted to the modeling and to the numerical simulation of implantable cardiovascular devices. This project is led by the start-up companies Kephalios and Epygon, conceptors of minimally invasive surgical solutions for the treatment of mitral regurgitation. The design and the simulation of such devices call for efficient and accurate numerical methods able to correctly compute cardiac hemodynamics. This is the main purpose of this thesis.

In the first part, we describe the cardiovascular system and the cardiac valves before presenting some standard material for the mathematical modeling of cardiac hemodynamics. Based on the degree of complexity adopted for the modeling of the valve leaflets, two approaches are identified: the resistive immersed surfaces model and the complete fluid-structure interaction model.

In the second part, we investigate the first approach which consists in combining a reduced modeling of the valves dynamics with a kinematic uncoupling of cardiac hemodynamics and electromechanics. We enhance it with external physiological data for the correct simulation of isovolumetric phases, cornerstones of the heartbeat, resulting in a relatively accurate model which avoids the complexity of fully coupled problems. Then, a series of numerical tests on 3D physiological geometries, involving mitral regurgitation and several configurations of immersed valves, illustrates the performance of the proposed model.

In the third and final part, complete fluid-structure interaction models are considered. This type of modeling is necessary when investigating more complex problems where the previous approach is no longer satisfactory, such as mitral valve prolapse or the closing of a mechanical valve. From the numerical point of view, the development of accurate and efficient methods is mandatory to be able to compute such physiological cases. We then consider a complete numerical study in which several unfitted meshes methods are compared. Next, we present a new explicit coupling scheme in the context of the fictitious domain method for which the unconditional stability in the energy norm is proved. Several 2D numerical examples are provided to illustrate the properties and the performance of this scheme. Last, this method is finally used for 2D and 3D numerical simulation of implantable cardiovascular devices in a complete fluid-structure interaction framework.

Keywords: Cardiovascular devices, Modeling, Cardiac hemodynamics, Resistive immersed surfaces, Fluid-structure interaction, Immersed thin-walled structures, Loosely coupled schemes, Unfitted mesh methods.

Contents

Nomenclature

Notation	Meaning
ALE	**A**rbitrary **L**agrangian-**E**ulerian
ARIS	**A**ugmented **R**esistive **I**mmersed **S**urface
AV	**A**trio**V**entricular
CC	**C**ardiac **C**ycle
CD	**C**ardiovascular **D**isease
CT	**C**omputerized **T**omography
ECG	**E**lectro**C**ardio**G**raphy
FD	**F**ictitious **D**omain
FSI	**F**luid-**S**tructure **I**nteraction
GMRES	**G**eneralized **M**inimal **RES**idual
IB	**I**mmersed **B**oundary
LA	**L**eft **A**trium
LH	**L**eft **H**eart
LV	**L**eft **V**entricle
LVOT	**L**eft **V**entricular **O**utflow **T**ract
MIMVS	**M**inimally **I**nvasive **M**itral **V**alve **S**urgery
MIT	**M**inimally **I**nvasive **T**echniques
MITC	**M**ixed **I**nterpolation of **T**ensorial **C**omponents
MMA	**M**ethod of **M**oving **A**symptotes
MR	**M**itral **R**egurgitation
MVR	**M**itral **V**alve **R**eplacement
NXFEM	**N**itsche-e**X**tended **F**inite **E**lement **M**ethod
PSPG	**P**ressure-**S**tabilized **P**etrov-**G**alerkin
RA	**R**ight **A**trium
RH	**R**ight **H**eart
RIS	**R**esistive **I**mmersed **S**urface
RMS	**R**oot **M**ean **S**quare
RV	**R**ight **V**entricle
SAM	**S**ystolic **A**nterior **M**otion
SL	**S**emi**L**unar
SUPG	**S**treamline **U**pwind **P**etrov-**G**alerkin
TMVR	**T**ranscatheter **M**itral **V**alve **R**eplacement
VHD	**V**alvular **H**eart **D**isease
XFEM	e**X**tended **F**inite **E**lement **M**ethod

Introduction

Thesis general context

Many mechanical systems are based on the coupling of a deformable thin-walled structure with an incompressible fluid flow. These systems appear in a large range of engineering, scientific and industrial fields. Among them, we can mention, for instance, ship hydrodynamics (see, e.g., [WDHY06]), the dynamics of parachutes (see, e.g., [TT12]), the flight ability of insects (see, e.g., [NL12]), and aerodynamics (see, e.g., [LLX08, FAYA13]). In the field of biomechanics, these coupled problems have seen a surge of interest in areas such as: cell aggregation and deformation (see, e.g., [LL06]), blood-heart interaction (see, e.g., [VABV05]), cilliary beating (see, e.g., [HP18]), sperm motility (see, e.g., [ZD11]). This thesis is devoted to the numerical simulation of blood flow into the left heart. This includes, for instance, the interaction between blood and the myocardium (see, e.g., [Smi04]) or the opening and closing dynamics of heart valves interacting with blood flow (see, e.g., [LDSB10]).

With recent major advances in mathematical modeling and computer technology, simulations of such systems can provide useful insights about diseases or malfunction through the computation of physical values (e.g., wall shear stress [SFGL06] or pressure jumps [VRDV00]) that are not always easily accessible by measurements (i.e., imaging or *in vitro* experiments). Therefore, new experimental devices can be designed by using these additional data provided by the numerical simulations (see, e.g., [SGN+11, KBT+16, SHN13]). Moreover, physicians can potentially enhance their diagnosis and their therapy planing by using simulations in patient-specific geometries (see, e.g., [TDK+99, FQV09]). This explains the increasing clinical interest for efficient predictive numerical simulations able to correctly compute cardiac hemodynamics. This is the main purpose of this thesis.

Position and content of the thesis

This thesis has been carried out in the framework of the Mivana project, led by the start-up companies Kephalios, conceptor of a mitral annulus ring, and Epygon, conceptor of a transcatheter cardiac valve. The work plan involves two fundamental problems, which are detailed below, in terms of industrial interest and of scientific computing challenges.

Problem 1 – Influence of the valves on intraventricular hemodynamics
In a realistic geometry of the ventricle of the left heart, intraventricular hemodynamics is simulated for three different configurations of valves: native mitral valves, artificial tricuspid valves and artificial valves with an unique leaflet. First, the valves will be approached with a Resistive Immersed Surfaces (RIS) model. Then, a full Fluid-Structure Interaction (FSI) model will be proposed for the monoleaflet valve, in order to simulate its opening dynamics and its influence on intraventricular hemodynamics.

Problem 2 – Influence of the annulus ring on the regurgitation
We will propose a model taking into account the contact between the leaflets, allowing to evaluate the influence of the annulus ring on the prolapse of the valves and on mitral regurgitation.

From the numerical point of view, the development of efficient and accurate methods will be fundamental to be able to handle complex and physiological 3D cases. In order to reduce the computational complexity of the simulations, the basic idea is that the numerical methods must avoid strong coupling between the fluid and solid solvers.

In order to avoid the use of complex coupled problems, another alternative is (i) to neglect the mechanical behavior of the valve by considering simplified models of valve dynamics (such as the RIS model) and (ii) to consider an *one-way* uncoupling of cardiac hemodynamics with myocardium mechanics. In Part II of this thesis, this simplified approach is investigated and enhanced with physiological data for the simulation of cardiac hemodynamics in presence of isovolumetric phases (see Chapter 3) before being applied to realistic cases, including different configurations of immersed valves and the computation of cardiac hemodynamic quantities (see Chapter 4).

On the opposite, for problems involving the study of valve prolapses, with the leaflets entering into contact, the situation is much more delicate. In particular, the previous RIS approach is too simple for these problems. A preferred alternative is to work with a complete FSI model with unfitted meshes for the fluid and the structures. This allows to manage topological changes without inducing ill-conditioning problems due to skewed elements or numerical diffusion due to remeshing. Moreover, it must be noted that in incompressible FSI, most of the loosely coupled schemes are known to present problems of stability and accuracy, requiring severe time-step restrictions, or to be limited by the amount of added-mass effect (see Section 2.5.3.3 and Section 6.1). These difficulties related to the FSI approach are addressed and studied in Part III of the thesis: several implicit methods with immersed thin-walled structures are introduced and compared (see Chapter 5) before proposing a new loosely coupled scheme for one of them (see Chapter 6) which overcomes the above-mentioned difficulties. Finally, this method is applied to the simulation of implantable cardiovascular devices (see Chapter 7).

Thesis outline and main contributions

In the following, we review the contributions of this work chapter by chapter. For the sake of completeness, they are recalled and detailed at the beginning of each chapter.

Part I: Physiological and mathematical contexts

Chapter 1. This in an introductory chapter where the physiological context of this thesis is presented. We describe the cardiovascular system, from both biological and clinical points of view, highlighting the crucial role of the cardiac valves and their most common

pathologies. Clinical devices to correct these pathologies, main motivation of this thesis, are then introduced. A particular attention is given to the transcatheter mitral valve and to the adjustable mitral ring which are the implantable intracardiac devices realized, respectively, by the start-up companies Epygon and Kephalios.

Chapter 2. In this chapter, some models commonly considered in the context of the mathematical modeling and simulation of cardiac hemodynamics are presented as well as the associated coupling strategies. Two main approaches, based on the degree of complexity adopted for the description of the cardiac valves, will be investigated to describe the problems considered in this thesis: the RIS model and the FSI model. Each model is then carefully described and does have a dedicated part in the rest of this thesis, as detailed below. This chapter ends with a review of the existing numerical techniques for the FSI approach based on the following classification criteria: the spatial discretization of the problem and the nature of the splitting between the fluid and the structure solvers. Finally, some elements about contact modeling are provided.

Part II: Simulation of intracardiac blood flow with a simplified model of valves

Chapter 3. This chapter introduces the RIS model as an alternative to the FSI model for the simulation of cardiac hemodynamics. Because of its simplicity, this *one-way* uncoupling struggles to capture the correct intraventricular pressure when both valves are closed, thus compromising their correct opening during a heartbeat. We propose an augmented formulation of this model, named Augmented Resistive Immersed Surface (ARIS) model, which overcomes this issue and enhances the simulation with data coming from external physiological electromechanical simulations. A numerical study, including the simulation of intraventricular blood flow within a realistic 3D geometry of the left heart, is presented and the benefits of this new approach are highlighted.

Chapter 4. In this chapter, we illustrate the capabilities of the RIS and ARIS models when applied to realistic cases. First, a simplified case of mitral regurgitation is computed with the RIS model and is compared to its corresponding healthy configuration to evaluate the main differences. Then, intraventricular hemodynamics induced by three different configurations of the mitral valve (namely, (i) the native valve, (ii) the bioprosthetic tricuspid valve and (iii) the artificial valve from Epygon) is computed with the ARIS model. In addition of the velocity and pressure fields, several physical values of interest (e.g., kinetic energy, vorticity, residence time of Lagrangian particles, ...) are evaluated and compared between these three configurations.

Part III: Simulation of intracardiac blood flow with a complete fluid-structure interaction model

Chapter 5. We present in detail a representative sample of state-of-the-art numerical methods (with fitted and unfitted meshes) for FSI in the context of immersed thin-walled solids. For the first time, different unfitted mesh methods are compared and validated against a benchmark of 2D academic cases which address common topological difficulties. The pros and cons of each method are highlighted. Moreover, we show that the method of choice for the problems addressed in this thesis – the Fictitious Domain (FD) method – usually known for its lower accuracy compared to other approaches, is able to show very good adequacy with reference solutions.

Chapter 6. The design of loosely coupled schemes is of crucial interest, especially for three-dimensional simulations, but the existing approaches are known to suffer from severe stability and/or time accuracy issues. In this chapter, we introduce for the first time an explicit coupling scheme for the numerical approximations of incompressible FSI problems involving immersed thin-walled structures, in the context of the FD method, which overcomes these difficulties. Then, several 2D academic cases illustrate the benefits of this new loosely coupled scheme. In particular, it is showed that this scheme delivers very good performance in terms of accuracy and robustness with respect to strongly coupled unfitted mesh approaches.

Chapter 7. The main motivation of this chapter is to illustrate the capabilities and benefits of this explicit coupling scheme for the FD method when applied to realistic problems. For this purpose, several 2D and 3D numerical examples motivated by the simulation of implantable cardiovascular devices are considered in a complete FSI framework. In particular, the adjustable mitral ring developed by Kephalios is applied to a 2D case of native mitral valve taking into account the contact between its leaflets. Then, the artificial valve from Epygon, previously investigated with the ARIS model, is now considered in a full FSI framework and is immersed into a realistic 3D geometry of the left heart.

Author's bibliography

- Papers in peer reviewed journals:

  1. L. Boilevin-Kayl, M.A. Fernández and J.F. Gerbeau, **Numerical methods for immersed FSI with thin-walled structures.** *Computers & Fluids*, DOI: 10.1016/j.compfluid.2018.05.024, *2019*. Available online: https://hal.inria.fr/hal-01704575.

  2. L. Boilevin-Kayl, M.A. Fernández and J.F. Gerbeau, **A loosely coupled scheme for fictitious domain approximations of fluid-structure interaction problems with immersed thin-walled structures.** *SIAM Journal*

on Scientific Computing, DOI: 10.1137/18M1192779, *2019*. Available online: https://hal.inria.fr/hal-01811290.

3. L. Boilevin-Kayl, A. This, M.A. Fernández and J.F. Gerbeau, **Augmented Resistive Immersed Surfaces valve model for the simulation of cardiac hemodynamics with isovolumetric phases.** *International Journal for Numerical Methods in Biomedical Engineering*, in press, *2019*. Available online: https://hal.inria.fr/hal-01944798.

- Papers in conference proceedings:

4. L. Boilevin-Kayl, A. This, M.A. Fernández and J.F. Gerbeau, **An efficient valve model based on resistive immersed surfaces enhanced with physiological data.** *CMBE 2017 – 5th International Conference on Computational and Mathematical Biomedical Engineering, April 2017, Pittsburgh, United States.* Available online: https://hal.inria.fr/hal-01519602.
5. A. This, L. Boilevin-Kayl, H. Morales, O. Bonnefous, P. Allain, M.A. Fernández and J.F. Gerbeau, **One Mesh To Rule Them All: Registration-Based Personalized Cardiac Flow Simulations.** *FIMH 2017 – 9th International Conference on Functional Imaging and Modeling of the Heart, June 2017, Toronto, Canada.* Available online: https://hal.inria.fr/hal-01512309.

Funding

This work has been partially supported by the Mivana consortium. Mivana is a collaborative project for the development of new technologies for mitral valve repair. It is led by the start-up company Kephalios, with the participation of the start-up company Epygon, and it has received funds from the French government, in the context of the program "Investissement d'Avenir". The purpose of this project[1] is the improvement of the french cardiovascular sector thanks to the new fabric technologies and to the groundbreaking medical devices dedicated to the treatment of mitral valve disease. These two companies belong to the Affluent Medical group[2] which develops new generations of minimally invasive prostheses.

[1] See https://www.gazettelabo.fr/breves/breves.php?id=6370/ (in French).
[2] See https://www.affluentmedical.com/.

Part I

Physiological and mathematical contexts

Chapter 1

The cardiovascular system

In this chapter, we describe the cardiovascular system, from both biological and clinical points of view. The purpose here is to highlight its structure and to provide useful insights about its functioning. A particular focus is given to the valves of the left heart, their pathologies and the existing solutions to treat them, cornerstones of this thesis. This opening chapter will motivate and justify our choices of modeling further detailed in Chapter 2.

Contents

1.1 Introduction

The Cardiovascular System (CS) is a complex living organ made of several layers and composed of the heart, which pumps blood, and the network of blood vessels that convey blood to the body and drain it from the body tissues to the heart [MH18]. The whole structure of the CS is characterized by multiple components and physiological phenomena, both widely scaled in space and time. We can mention, for instance, the blood cell and the vessel, whose typical lengths are, respectively, in the orders of magnitude of several micrometers [SS99] and of several centimeters [Wie63]. In addition, we can also cite the

quick chemical process in the capillaries and remodeling phenomena, whose typical duration are in the orders of magnitude of the millisecond [EH87] and of several days [BLS03].

All parts of the CS work in concert, but describing all the couplings occurring between its components and the induced physiological phenomena would clearly be out of the scope of this thesis. For the sake of simplicity in this preliminary chapter, all these parts will briefly and individually be described and only the interactions of interest for the problems considered in this thesis will be addressed. We refer the reader to specialized literature for further details about the physiology of the human heart (see, e.g., [AN04, BBBB10, MH18]).

The aim of this work is the modeling and numerical simulation of implantable cardiovascular devices dedicated to the treatment of valvular heart diseases. In this chapter, we introduce the physiological framework of the thesis. A general overview of the cardiovascular system, more particularly its function and its components, is given in Section 1.2, with a particular focus on the left heart. In Section 1.3, the main steps of a typical cardiac cycle are highlighted and correlated with the associated heart valves. Their common pathologies are described in Section 1.4 and the intracardiac devices developed to treat them are addressed in Section 1.5. A particular attention is then given to the devices developed by the start-up companies Epygon and Kephalios. This chapter ends with the conclusions in Section 1.6.

1.2 Organizational structure

The basic and primary function of the CS is the transport of oxygen and nutrients to the organs [Ste99]. This complex vital system is composed of blood vessels (the routes taken by blood), blood (the fluid transporting oxygen and nutrients) and the heart (a muscular pumping organ) [AN04, MH18]. Its function and structure are detailed in what follows.

1.2.1 Function

The whole circulation system is generally subdivided into 2 parts, namely the pulmonary circuit and the systemic circuit, as depicted in Figure 1.1. These two circuits are working thanks to the pumping chambers of the heart (see Section 1.2.2.3 below): the pulmonary circuit is pumped by the Right Atrium (RA) and by the Right Ventricle (RV) and the systemic circuit is pumped by the Left Atrium (LA) and by the Left Ventricle (LV) [AN04]. Without these pumping chambers, blood could not counteract gravity and flow inside the body.

The pulmonary circuit is responsible for the transport of the deoxygenated blood from the right side of the heart to the lungs, by pumping it through the pulmonary arteries (see Figure 1.1). In the lungs, blood flows in the capillary beds, where gas exchange occurs between blood capillaries and alveoli thanks to diffusion through the alveolar-capillary barrier [Sch78], and becomes oxygenated [AN04, MH18]. The recently enriched blood is then flowing towards the left side of the heart by being pumped into the pulmonary veins (see Figure 1.1).

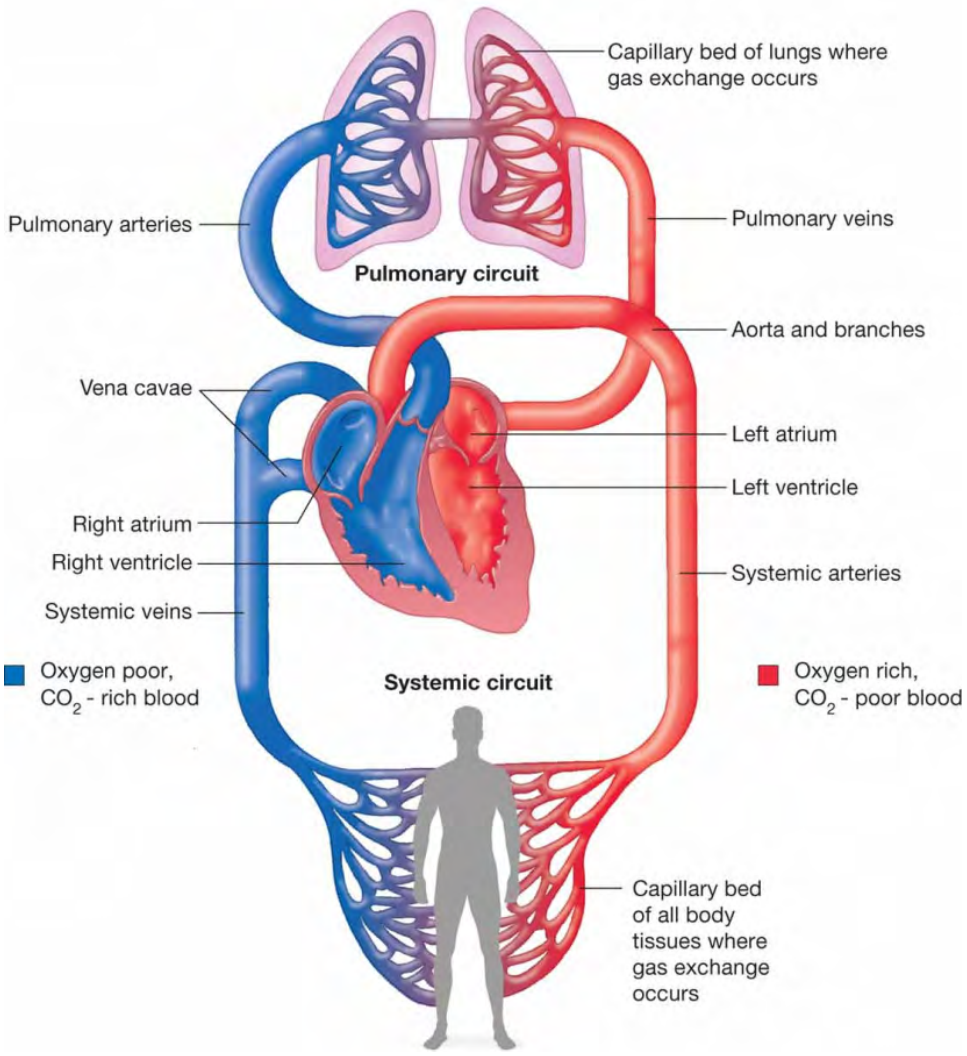

Figure 1.1 – Schematic representation of the human CS. The pulmonary circuit and the systemic circuit are represented, respectively, at the top and at the bottom. The deoxygenated blood is colored in blue and the oxygenated blood is colored in red. Image from [Sch].

The systemic circuit is responsible for the transport of the oxygenated blood from the left side of the heart to the rest of the body, by pumping it through the systemic arteries (see Figure 1.1). In the capillary beds, the same phenomenon of gas exchange, previously described for the lungs, occurs between blood capillaries and the body tissues [Pit11], and blood becomes deoxygenated [AN04, MH18]. The recently depleted blood is then flowing towards the right side of the heart by being pumped into the systemic veins (see Figure 1.1).

Note that, not only blood is carrying oxygen, but also nutrients, required by the body and by the heart to function properly. This is ensured by the coupling between the digestive system and the circulatory system [BBBB10].

1.2.2 Structure

We here describe the nature of each component of the CS with a particular focus on the heart valves, given that their crucial importance in its correct function.

1.2.2.1 Blood vessels

In terms of function, blood vessels are living tubes which carry blood. Both the systemic and pulmonary circuits are composed of three types of blood vessels: the veins, the arteries and the capillaries [BBBB10]. The veins and the arteries are responsible for the macro-circulation of blood (e.g., transport by pressure differentials) whereas the capillaries are responsible for its micro-circulation (e.g., gas exchange by diffusion with various capillary beds) [AN04, MH18]. The veins carry blood from the body and from the lungs back to the heart whereas arteries carry blood from the heart to the body and to the lungs. Inside each circuit, the capillaries are the microscopic blood vessels which connect the arteries and veins together [AN04, MH18].

In terms of structure, the walls of the arteries are thicker, more elastic and more muscular than those of veins or capillaries. This is explained by the fact that arteries face high levels of blood pressure: blood inside the arteries is strongly pushed away from the pumping heart with great force and the walls need to be more robust to withstand this pressure [FQV09]. Moreover, the largest arteries (such as the aorta and the pulmonary artery) also possess elastic properties (coming from the tissue they are made of) which allow them to distort and to adapt to the pressure imposed by the heart [FQV09]. The veins are similar to the arteries, except for their reduced thickness and their less developed elastic properties as the inner blood pressure is much smaller [TM]. Moreover, the typical compliance of a vein is around 24 times larger than an artery's one. Capillaries are very different in their size and in their connectivity. The size of a capillary decreases when going deeper in the capillary beds network. The smallest capillaries have a typical size of 5 μm [FQV09], smaller than the diameter of a red blood cell, whose typical value is around 6 and 8 μm [Tur12]. Whereas the arterial and venous systems are primarily bifurcating trees, the capillary beds are much more complex with many interconnections between them [Her07]. There is an average of twenty generations of bifurcations (possibly slightly more or less due to morphological variability) between the heart to the most distant capillary beds [Her07].

1.2.2.2 Blood

Blood is a complex non-Newtonian fluid, characterized by a suspension of living cells in a liquid, named plasma, made by water approximately for the 90% of its volume [AN04, BBBB10, MH18]. The particulate phase of blood consists mainly of erythrocytes (red blood cells), leukocytes (white blood cells) and platelets. The aggregatable and deformable nature of red blood cells, that occupy almost half of the total blood volume, is the main responsible for its non-Newtonian effects [Thi08a]. The amplitude of these effects is not the same in the whole CS and depends on the nature and size of each blood vessel. The way blood is mathematically modeled will be further addressed in Section 2.2.2.

The chemical composition of blood is evolving with time as it flows through the network of blood vessels of the CS [AN04], as depicted in Figure 1.1. In the systemic veins and in the pulmonary arteries, blood is low in oxygen and high in carbon dioxide. In the lungs, blood is enriched in oxygen (thanks to the inspiration) and depleted in carbon dioxide (thanks to the expiration) [AN04, MH18]. In the pulmonary veins and in the systemic arteries, blood is rich in oxygen and low in carbon dioxide.

As regards the total body weight, blood represents on average 7% of it. In an average adult, this represents a volume between 4.7 and 5.7 liters [FK07]. Its average density and dynamic viscosity are, respectively, around 1 050 kg/m^3 and 0.003 kg/m/s for a healthy human [FQV09].

1.2.2.3 The heart

The heart is a muscular pumping organ of the size of an adult's closed fist [AN04]. It is located medial to the lungs, along the body's midline in the thoracic region [BBBB10]. The bottom part of the heart, named the apex, is not perfectly pointing downwards, which makes about 2/3 of the heart being located on the left side of the body and the other 1/3 on the right side [AN04, MH18]. The top part of the heart, called the heart's base, is connected to the largest blood vessels of the body, namely the aorta, the pulmonary trunk, the superior vena cava and the inferior vena cava [AN04, MH18], as depicted in Figure 1.2 where its cross section is represented.

The external layer of the heart is composed of three sub-layers: the external pericardium, the inner thick muscular myocardium and the internal endocardium [FQV09]. The pericardium is mostly made of connective tissue and functions as a protective and lubricating sub-layer for the myocardium [Iai15]. The myocardium, which forms the bulk of the heart, is a muscular tissue which has a very high resistance to fatigue and stress [AN04, MH18]. It is made of several sheets of cardiac muscle cells, called the cardiomyocytes, able to contract in a coordinated manner to squeeze out blood during a heartbeat [SSBW16]. The endocardium, mainly made of endothelium [FQV09], controls the myocardial function. Its soft surface allows blood to flow without clotting. It also provides protection to the valves and heart chambers [New18]. The different sub-layers of the heart wall are pointed out in Figure 1.2.

The interior of the heart is made of four cavities, named chambers by physicians: the LA, the RA, the LV and the RV. The two atria, the left one and the right one, collect blood, respectively, from the lungs and from the body. The two ventricles, the left one and the right one, pump blood, respectively to the body and to the lungs [MH18]. Both ventricles receive blood from their corresponding atrium. The LA, the LV, the RA and the RV, are connected, respectively, to the pulmonary veins, to the aorta, to the venae cavae (made of the superior vena cava and of the inferior vena cava) and to the pulmonary trunk [BBBB10]. The ensemble made of the LA and the LV defines the Left Heart (LH). On the same basis, the RA and the RV constitute the Right Heart (RH). The four chambers and their surroundings are depicted in Figure 1.2.

Blood is ejected from the heart into the main arteries under high pressure and in discrete pulses [BBBB10]. The pressure of ejection in the pulmonary circuit is lower than

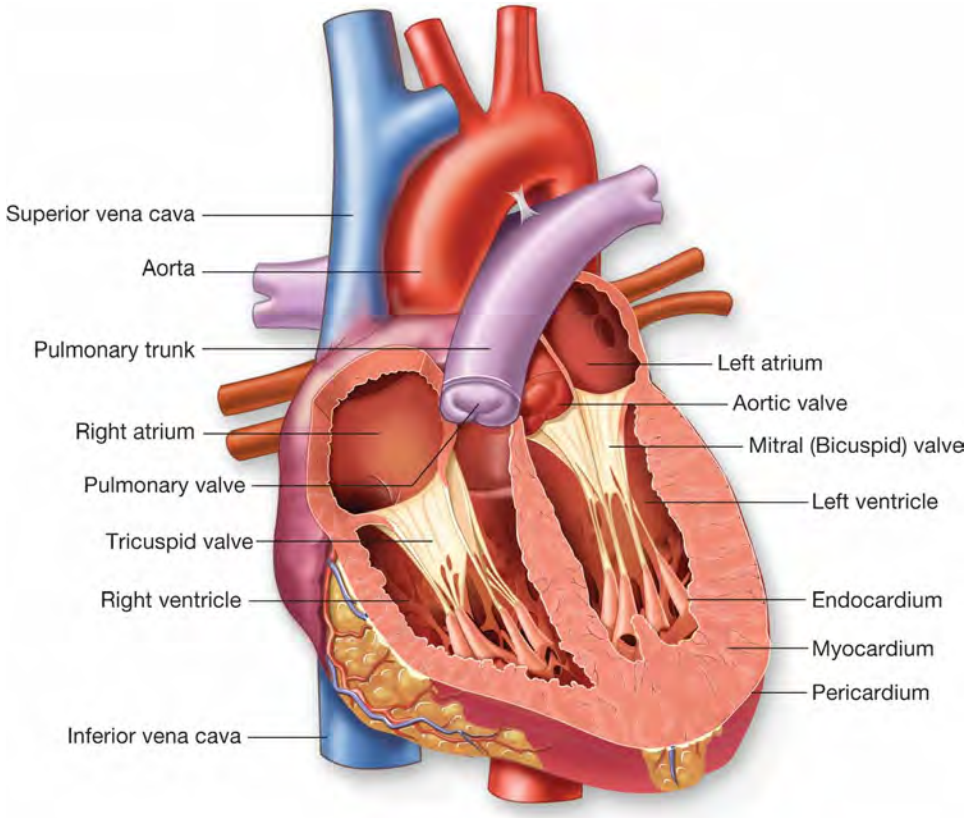

Figure 1.2 – Cross section of the human heart. The pulmonary veins, not pointed out by the text, are located behind the heart and colored in dark orange. Image from [Cro].

the one in the systemic circuit, as the resistance induced by the lungs is smaller than the one induced by the rest of the body [HSR67]. At rest, the heart pumps over 5 liters of blood through the body every minute [FQV09] and almost 6 times more during high-intensity physical efforts. The values of some physical quantities characterizing the human heart of a young healthy adult are given in Table 1.1.

The way blood is flowing inside the heart and ejected from it is controlled by the heart valves, as detailed in what follows.

1.2.2.4 The heart valves

Heart valves are anatomic sub-elements categorized as complex connective tissues whose structure evolves over a life-time [Sch08]. For the sake of simplicity, we will only consider them as not-evolving simple tissue structures. More information about their dynamic living composition can be found in the literature (see, e.g., [Sch08]). The basic function of a heart valve is the regulation of blood flow: it ensures that blood is circulating in one direction through the chambers of the heart by opening and closing at particular time instants during the CC [HY11]. As regards its working principle, a heart valve can be considered as a mechanical one: starting from the closed position, it opens to let blood enter the chamber

Property		Units	Typical	Range
Volume of the LV		mL		
	Before ejection		120	70–150
	After ejection		40	20–50
	Stroke volume		80	50–100
	Ejection fraction	%	67	60–80
Flow rate		mL/s	100	70–120
Heart rate		Hz	1.25	0.6–4.0

Table 1.1 – Values of some physical quantities characterizing the human heart of a young healthy adult. The stroke volume, usually related to the LV, is defined as the volume of blood ejected from the ventricle per heartbeat [Vin08]. Table adapted from [FQV09].

if there is a positive pressure gradient across it [SMS09]. On the opposite, starting from the open position, it closes to prevent any reflux if a backflow of blood is observed through the valve [SMS09].

The heart contains four valves (as depicted in Figure 1.3) which can be split in two categories, depending on their physiology and relative position into the heart:

- The aortic valve, belonging to the LH, and the pulmonary valve belonging to the RH. They are called the SemiLunar (SL) valves. As depicted in Figure 1.3, they are located between the ventricle and the upper arteries and their leaflets are located towards the upper arteries [HY11].
- The mitral valve (also known as the bicuspid valve), belonging to the LH, and the tricuspid valve, belonging to the RH. They are called the AtrioVentricular (AV) valves. As depicted in Figure 1.3, these valves are located between the atrium and the ventricle and their leaflets are located towards the ventricle [HY11].

A healthy and young human heart valve is typically less than 1 mm thick, even if it can slightly evolve with its nature and its considered sub-region [SENT88]. The AV valves are slightly thicker than the SL valves and the middle of a valve is less thick that its extremities. Generally, the thickness of the heart valves increases with the age of the patient [SENT88]. As depicted in Figure 1.3, the mitral valve is directly connected to the aortic valve, unlike the tricuspid valve, which is separated from the pulmonary valve by some length of muscular tissue [SENT88].

Among these four types of valves, the ones in the LH are more subject to diseases and pathologies than the others because of the existence of higher pressures compared to the ones in the RH, as stated above in the description of the heart. Therefore, in what follows, we will focus on the aortic and mitral valves.

The aortic valve: The anatomy of the aortic valve is rather simple: it is composed of three cusps (also known as flaps or leaflets), named for their relationship to the surroundings coronary arteries, as depicted in Figure 1.4b, namely the left coronary, the right coronary

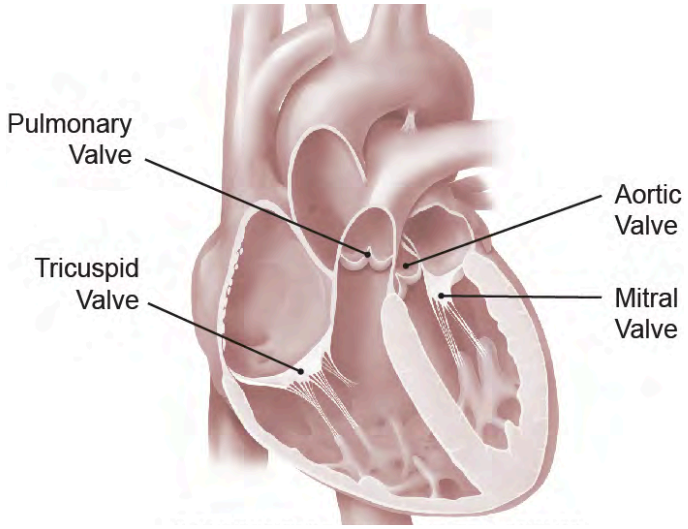

Figure 1.3 – Overview of the four valves of the heart. Image from [Ove].

and the non-coronary cusp. These three cusps are symmetric [Ho09], play the same role and coapt together in the middle of the aortic root, as depicted in Figure 1.4a.

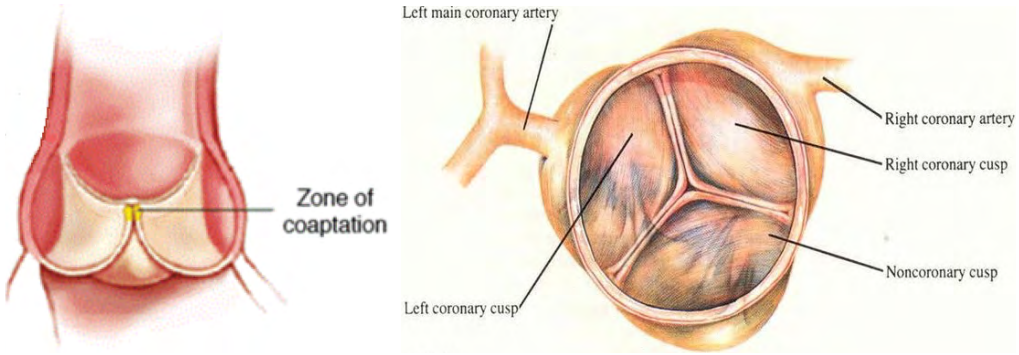

(a) Schematic profile view.

(b) Schematic top view.

Figure 1.4 – Schematic views of the physiology of the aortic valve and its surroundings. Images adapted from [Proa] and [Topa].

Note that due to morphological variability and aging, the area and weight of each cusp can increase [SR85]. This increasing may be cusp-dependent, thus inducing a lost of symmetry in the 3 cusps, where a particular one would become larger and heavier than the others [SR85], slightly disturbing the way blood is ejected from the LV to the aorta.

The mitral valve: The anatomy of the mitral valve is more complex than the aortic one, due to the presence of additional anatomic sub-elements. The whole apparatus is composed of the left atrial wall, the annulus, the leaflets, the chordae tendineae, the papillary muscles and the left ventricular wall (see Figure 1.5a) [Ho09].

The lower part of the mitral valve is anchored in the ventricle wall by numerous chordae

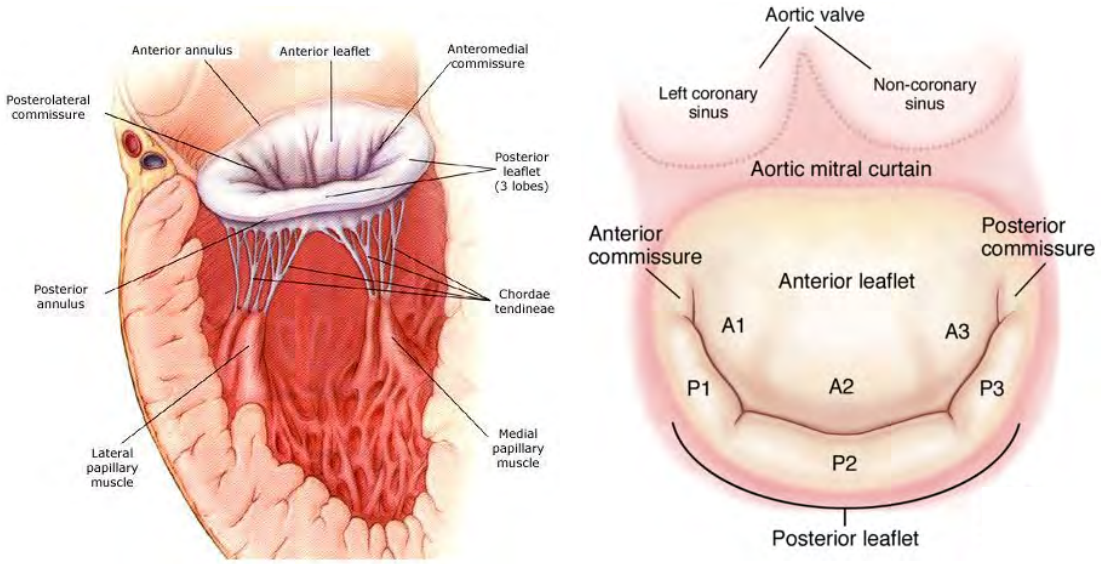

(a) Schematic profile view.

(b) Schematic top view.

Figure 1.5 – Schematic views of the physiology of the mitral valve and its surroundings. Images adapted from [Prob] and [Topb].

tendineae (depicted in Figure 1.5a). Their total number varies with the patient but an average human has 25 of them [RLWS70]. The choarde themselves are attached to one of the two existing papillary muscles – medial and lateral – arising from the area between the apex and the middle of the ventricle wall, as depicted in Figure 1.5a. The whole system made of chordae tendineae and papillary muscles is known as the subvalvular apparatus [NCS+00]. It is responsible for an additional stress on the leaflets, transmitted by the chordae, which prevents the valve from inverting into the atrium during the systole. In healthy configurations, this apparatus has no effect on the opening phases, which are still induced and decided by the pressure gradient across the valve [NCS+00].

The upper part of the mitral valve is, as the synonym bicuspid may suggest, made of two thin, pliable, and soft leaflets [Ho09]: the anterior and posterior ones (depicted in Figures 1.5a and 1.5b). These leaflets are named after their relative position in the heart against the aortic root. In particular, the anterior leaflet is anchored in the aortic valve [SH68].

In terms of geometric differences between the leaflets, the anterior one is the largest one and its length is higher than the one of the posterior leaflets [SH68]. Therefore, its shape and particularly its motion during the systole are the major factors responsible for the development of the intraventricular blood flow. Each leaflet can be divided into three scallops [SH68] separated by two commissures – anteromedial and posterolateral – as depicted in Figure 1.5a for the anterior leaflet and in Figure 1.5b for the posterior one. An alphanumeric nomenclature has been proposed by Carpentier [CLR+95] to distinguish these regions: the sub-regions A1, A2 and A3 are found in the anterior leaflet whereas the opposite sub-regions P1, P2 and P3 are found in the posterior leaflet (see Figure 1.5b).

1.3 The cardiac cycle

The Cardiac Cycle (CC) is defined as a sequence of events that occurs in one complete beat of the heart. The present section is focused on the role and behavior of the LH in the CC. As the RH follows the same patterns as the LH [FQV09], its role will not be detailed here, in spite of its equivalent importance. The choice of the starting point to describe the CC is arbitrary, due to its cyclic nature. Therefore, in the following, it is decided to start its description with the isovolumetric contraction phase.

1.3.1 Main phases

The heartbeat is basically a two stage pumping action, characterized by the diastole and systole phases, depicted in Figure 1.6 with their associated blood flow directions. Diastole is defined as the time period when the myocardium is relaxing and blood is filling the ventricle [BBBB10]. Systole is defined as the time period during which the myocardium contracts and blood is ejected from the ventricle [BBBB10].

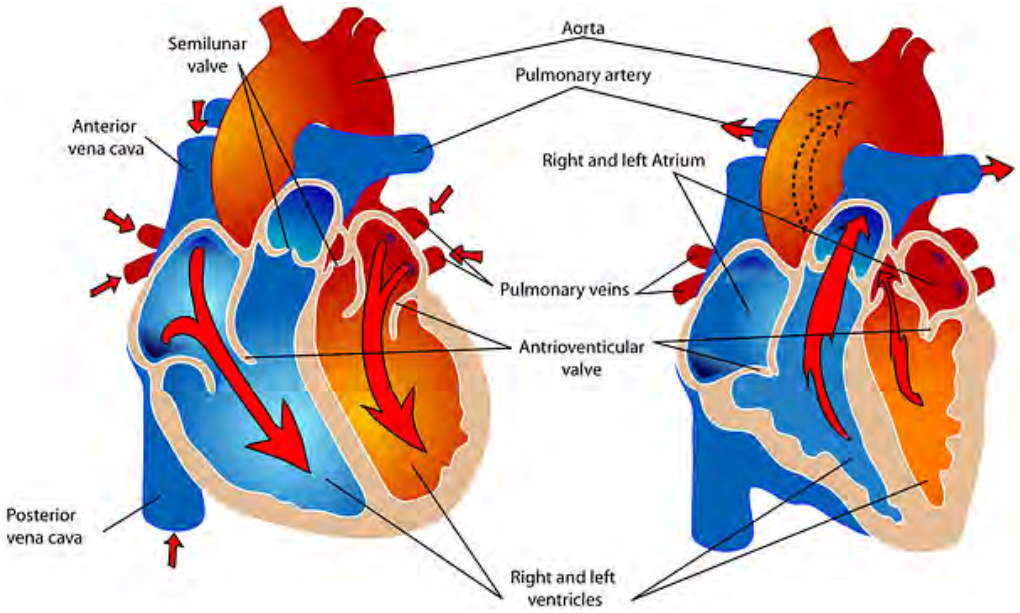

Figure 1.6 – Schematic representations of the heart during the diastole and systole phases of the CC. The red arrows indicate the direction of blood flow. On the left: the diastole (i.e., filling) phase. On the right: the systole (i.e., pumping) phase. Image from [The].

When looking at the ventricular activity, four main phases can be identified [AN04, BBBB10, MH18, FQV09]:

- The isovolumetric contraction phase: this phase takes place in early systole and starts with the closure of the mitral valve when the LV pressure increases above the LA pressure. It is characterized by the contraction of the myocardium (and thus the LV) even if both mitral and aortic valves stay closed, justifying the term "isovolumetric" as the volume of the LV does not change. Because blood is incompressible, the

contraction of the ventricle and its associated change of shape induce a great increasing of the pressure inside the LV.

- The ventricular ejection phase: this phase takes place in middle and late systole and starts with the opening of the aortic valve. It corresponds to the moment the pressure in the LV exceeds the pressure in the aorta. Because of the pressure differential in favor of the LV, blood in the LV is ejected in the aorta. As long as the myocardium keeps contracting quickly enough, the sign of the pressure difference remains the same and ejection of blood keeps going.
- The isovolumetric relaxation phase: this phase takes place in very early diastole and starts with the closure of the aortic valve when the LV pressure decreases below the pressure in the aorta. Acting on the same principle of the first phase, it is characterized by the relaxation of the myocardium (and thus the LV) even if both mitral and aortic valves stay closed. The relaxation of the ventricle, with the valves kept closed, induces a great decrease of its pressure.
- The ventricular filling phase: this phase takes place in a large portion of the diastole and starts with the opening of the mitral valve when the LV pressure decreases below the LA pressure. It can be subdivided in three sub-phases, namely, the rapid inflow, the diastasis and the atrial systole. The rapid inflow or rapid filling begins just after the opening of the mitral valve and allows blood to flow passively (i.e., without any muscular activity) into the LV due to the pressure differential. It contributes to around 80% of total diastolic volume. The diastatis or slow filling is an intermediate phase between the rapid filling and the atrial systole. It occurs when the LV pressure approaches the LA pressure, resulting into the progressive deceleration of the passive filling, and contributes to around 5% of total diastolic volume. Finally, the atrial systole corresponds to the moment when the LA contracts, inducing an additional active filling of blood inside the LV at the end of the diastole. It contributes to around 15% of total diastolic volume. After the end of the atrial systole, the part of the myocardium at the LV level begins to contract. This induces an increasing of the LV pressure which becomes higher than the LA one, and therefore a closing of the mitral valve [Khu08].

The typical duration of each of these four phases, for an average heart rate of 75 beats/mn in a young healthy adult, is given in Table 1.2. A normal heart rate is approximately 72 beats/minute, meaning the CC spreads over slightly more than 0.8 seconds [FQV09]. Note that the systole phase (lasting around 300 ms) is shorter than the diastole phase (lasting around 500ms).

Finally, a Wiggers diagram, representing blood pressure, the ventricular volume, the electrocardiogram and the phonocardiogram over time during a CC, is depicted in Figure 1.7. The different phases of the CC, previously described, are also pointed out.

This diagram, named after its creator Carl J. Wiggers, illustrates the correlation existing between the different physiological values and, more particularly, between the pressure of the different intra-cavity chambers of the LH over time [MW14]. Note that each time one of these pressures becomes higher or smaller than another one, a valve closes or opens,

Phase	Duration (ms)	Starting event
Isovolumetric relaxation	100	Aortic valve closure
Ventricular filling	400	Mitral valve opening
Isovolumetric contraction	50	Mitral valve closure
Ventricular ejection	250	Aortic valve opening

Table 1.2 – Typical duration of the phases of the cardiac cycle for an average heart rate of 75 beats/mn in a young healthy adult. Table from [FQV09].

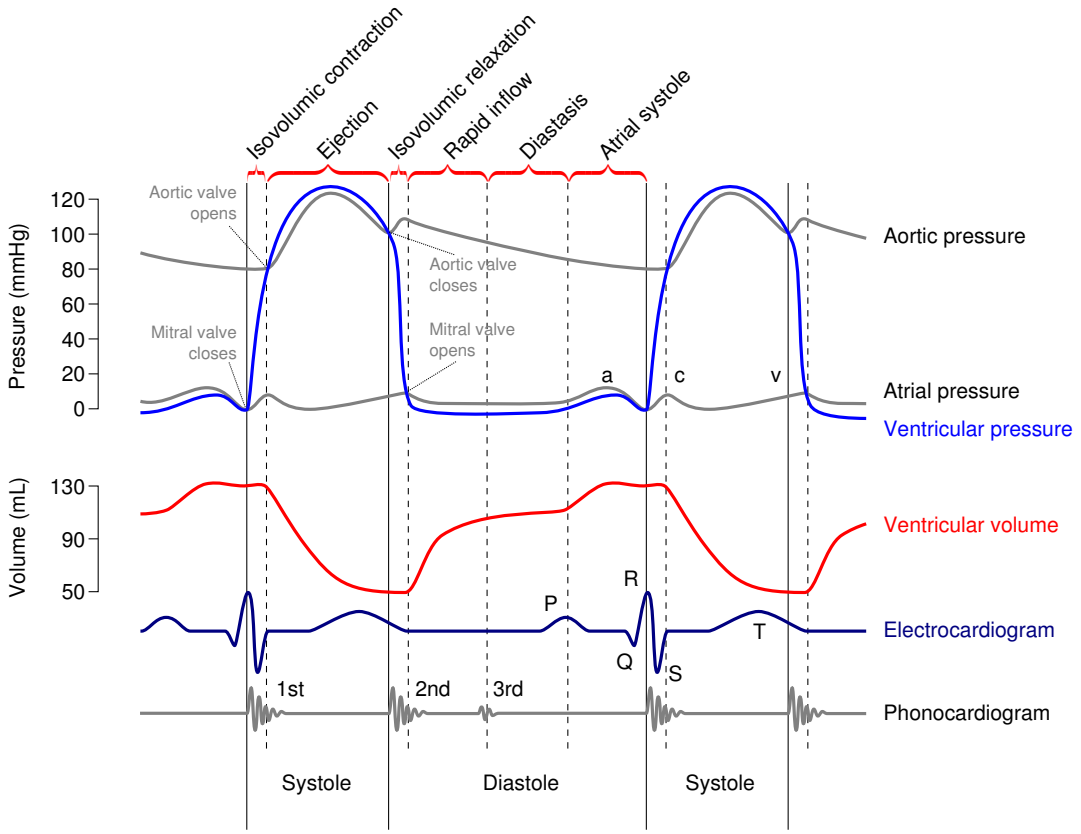

Figure 1.7 – Wiggers diagram. Image adapted from [Wig].

highlighting the importance of the aortic and mitral valves in the definition of the CC.

1.3.2 Role of the valves

Due to their significant localization inside the heart, valves play a crucial role into the regulation and definition of the systole and diastole phases, as depicted in Figure 1.6. Vascular surgeons even define these phases with respect to the status (open or closed) of each valve of the heart (and more particularly, the LH). Therefore, the diastole is defined as the period between the closing of the aortic valve and the successive closing of the mitral

valve [AN04, MH18]. Based on the same idea, the systole is defined as the period between the closing of the mitral valve and the subsequent closing of the aortic valve [AN04, MH18].

The aortic valve opens during the systole when the pressure inside the ventricle becomes higher than the one in the aorta. During the other phases of the cardiac cycle – where the ventricle pressure is lower than the one in the aorta – the aortic valve keeps being closed, thus preventing the ejected blood from going back into the LV [HY11].

The mitral valve opens during the diastole when the pressure inside the atrium becomes higher than the one in the ventricle. During the other phases of the cardiac cycle – where the ventricle pressure is higher than the one in the atrium – the mitral valve keeps being close, thus preventing the ejected blood from going back into the atrium [SH68]. The mitral valve is prevented from prolapsing into the LA thanks to the action of the chordae tendineae and papillary muscles.

1.4 Cardiovascular pathologies

A pathology affecting the cardiovascular system (either the heart or blood vessels) is called a Cardiovascular Disease (CD) [WWW11]. Some key facts about CDs are listed below in order to highlight their importance in the field of medical research:

- CDs are the first cause of death globally: each year, more people die from CDs than from any other cause [WWW11]. Nowadays, more and more people are affected by CDs. For instance, in 2015, among the annual 55.8 million deaths, 17.9 millions were due to CDs, hence representing 32% of the cases. For comparison purposes, in 1990, among the annual 47.7 millions of deaths, 12.3 millions were due to CDs, hence representing 26% of the cases [W+16]. By 2023, it is estimated that at least 23 million people will die from CDs each year [WWW11].
- About 80% of the deaths caused by CDs occured in poorer countries [WWW11]. Indeed while deaths rates due to CDs have declined in most of the developed world since the 1970s, deaths from CDs in the developing world are more common and have recently increased a lot [MFF+10].
- Aging is the major risk factor for the development of a CD: in 2013, CDs concerned 11% of Americans aged 20 to 40, 37% of those aged 40 to 60, 71% of those aged 60 to 80, and 85% of those over 80 years old [G+13]. The risk of developing a CD is tripled each decade of life [F+13].
- 90% of CDs are estimated to be preventable thanks to early diagnosis, cardiac stress and a healthy lifestyle avoiding the most important risk factors (such as tobacco, physical inactivity, excessive alcohol consumption, unhealthy diet and air pollution) [MMG08, KF+10, WWW11].

1.4.1 Classification

When considering cardiovascular diseases, two main categories can be distinguished: the ones involving blood vessels (the coronary artery diseases being the most common

ones) and the ones directly involving the heart. In the context of this thesis, we will focus on the Valvular Heart Disease (VHD) belonging to the latter category. VHDs concern more than 10% of patients aged 75 and over. [BBS+16].

The term VHD is used for any disease involving one or several valves of the heart [WWW11]. Three different types of anomalies are possible [MRSB10]. The first one, named stenosis, is characterized by a narrowing of the valvular orifice that prevents adequate outflow of blood [MRSB10]. The second one, called regurgitation or insufficiency, is the inability of the valve to prevent backflow of blood as its leaflets fail to join themselves correctly during the closure – we say that they do not coapt properly anymore [MRSB10]. Note that stenosis can also result in insufficiency if the resulting over-thick annulus or leaflets, responsible for the narrowing, do not ensure the leaf closure anymore. The last one, known as prolapse, occurs when the one of the valve leaflets prolapses back into the upper chamber. In the case of the mitral valve, this situation can occur for instance when some chordae tendineae broke [MRSB10]. Among all these anomalies, mitral regurgitation represents the most common form of VHDs [RZB+17].

1.4.2 The mitral regurgitation

The concept of Mitral Regurgitation (MR) is simply illustrated during the systole in Figures 1.8a and 1.8b, respectively, for the healthy and anomalous situations. In Figure 1.8a, the leaflets coapt properly during the systole and no anomaly is observed. On the opposite, in Figure 1.8b, the previous coaptation of the leaflets is lost and a backflow of blood towards the atrium is observed, characteristic of the regurgitation.

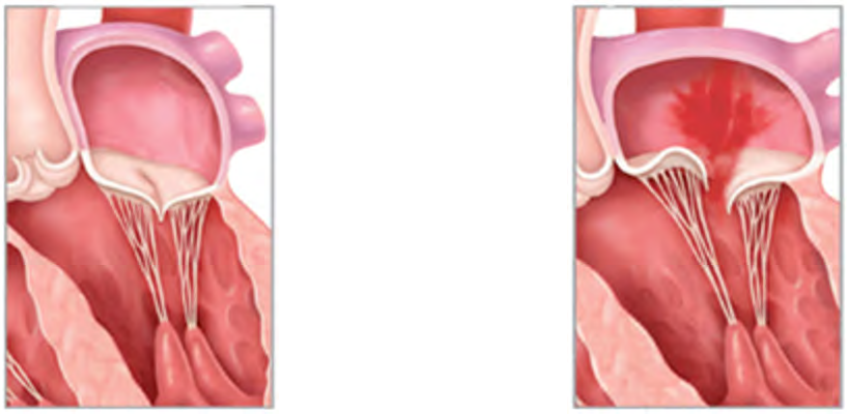

(a) Healthy situation.

(b) Anomalous situation.

Figure 1.8 – Illustration of MR during the systole. Images from [Ill].

MR can be induced by different phenomena. Usually, physicians and clinicians do consider two types of MR: primary MR and secondary MR. In the first case, MR is induced by either (i) a primary defect in the leaflets, (ii) an excess tissue or (iii) a ruptured chordae [Dif]. In the second case, MR is induced by a distortion and/or a stretching in the subvalvular apparatus inducing a malfunction in the mitral valve [Dif]. Another common classification of MRs is the one coming from Carpentier [Car83] (see Figure 1.9).

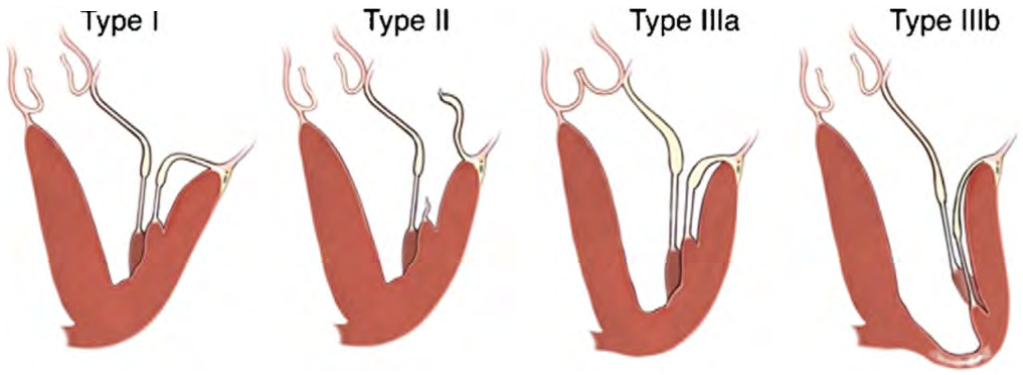

Figure 1.9 – Carpentier's functional classification. Type I: normal leaflet motion; Type II: increased leaflet motion; Type III: restricted leaflet motion. Image from [Car].

Based on the amplitude of the motion of the defecting valve, three functional types are distinguished:

- Type I: the motion of the leaflets is normal. In this case, MR is induced by dilatation of the mitral annulus [CAF11] (secondary MR).
- Type II: the motion of the leaflets is unusually increased. This might be induced by the elongation and/or the rupture of some chordae and/or papillary muscles [CAF11] (primary MR).
- Type III: the motion of the leaflets is unusually decreased. Type IIIa represents situations where the leaflet motion is restricted during both diastole and systole whereas the motion is restricted only during systole in type IIIb. The former are most of the time due to leaflets/chordae thickening (primary MR). The latter are caused by displacement of the apex and/or deformation of the papillary muscles [CAF11] (secondary MR).

MR affects about 2% of the whole population, regardless of gender [NGS+06]. It is significantly associated with normal aging: it is estimated to be present in over 9% of people over 75 [NGS+06]. MR is also a life-threatening condition: as the volume of blood flowing to the rest of the body decreases, due to the existence of the backflow, the heart needs to pump harder, an action that may result in the long run in heart failure [PKO+17]. Therefore, MR represents the second most frequent indication for valve surgery [Mita]. Out of 4 000 000 patients (in North America, the widest Europe and the Far East) suffering from severe MR and who could benefit from cardiac surgery, only 150 000 (3.8% of them) undergo a surgical intervention every year [Kep]. As detailed next in Section 1.5, the surgery of MR with use of implantable intracardiac devices shows many benefits and is curative.

1.5 Implantable intracardiac devices

The treatment of CDs is a major public health issue because it is the leading cause of death in developed countries [FQV09]. In spite of the progress made during the last years, current technologies of cardiovascular prostheses can still be further refined as they do not yet bring complete satisfaction (we can cite, e.g., post-surgery medication and complications), even if they already improve the quality of life of many patients [GLKP99, RKL+05]. Therefore, within this framework, the Mivana consortium, supported by Bpifrance since 2015, is responsible for the production of implantable cardiac devices with a particular focus on the mitral valve repair, as detailed in the introduction of this thesis.

When considering the implantable cardiovascular devices designed to correct MR, several types of solution exist. They can be split into two main categories [A+14]:

- The mitral valve replacement: this surgical procedure consists in completely replacing a patient's diseased mitral valve by either a new mechanical one or a new bioprosthetic one. The native leaflets are then either pushed towards the ventricle wall or cut off and do not intervene anymore in the regulation of blood flow [Glo12].
- The mitral valve repair where annuloplasty is the most common technique: this surgical procedure consists in reinforcing or tightening the annulus ring around the mitral valve with a prosthetic ring. The native leaflets are then not replaced but now supported by this new ring, allowing to restore their previously lost coaptation [CAF11]. When other parts of the defecting valve are subject to surgery (e.g., the leaflets themselves, the chordae tendineae, the papillary muscles, ...), alternative types of mitral valve repairs exist (e.g., the Alfieri stitch [SMBM11] or MitraClip [F+09]) but will not be considered in this thesis.

Until the beginning of this century, the most common surgical approaches to the mitral valve regurgitation was the open heart surgery [FCNH01], meaning the opening of the breastbone of the patient to gain direct access to the heart. Despite the fact that this technique provides an excellent access to the heart and to the pathology, the resulting wound requires several months of recovery with many activity restrictions. It can also induce numerous and severe complications (e.g., infection or nervous breakdown) possibly leading to death [FCNH01].

To counteract these major drawbacks, a new alternative called Minimally Invasive Mitral Valve Surgery (MIMVS), has been under development and clinical trial phase for the last fifteen years [BNAC13, CTR15]. To perform this type of minimally invasive operations, usually done by endoscopy, the patient is receiving full anesthesia and is connected to a heart-lung machine to deviate blood flow and prevent it from going through the heart. Robotic arms are then inserted in incisions (whose typical size is around 1/2 inches) made in the chest [LA16]. These arms are controlled by the surgeons who perform the surgery via cameras [CWL+15]. For this type of surgeries, the operation lasts about 3 hours and the patient is usually free to go home after only a few days of rest at the hospital. Some alternatives, called percutaneous [SKP+11], exist and do not even require cuts on the chest. Instead, a catheter is inserted though a groin artery.

These new Minimally Invasive Techniques (MIT), which do not require an open-heart

surgery, are a major improvement for patients who could not go under classical surgery due to other factors. Therefore, they represent a major revolution and are expected to replace the traditional mitral valve replacement surgery techniques in the future [M+15]. In the rest of this section, we will only focus on these MIT.

1.5.1 The mitral valve replacement

This type of mitral valve procedure used to be very invasive and required an open-heart surgery, involving a long incision in the middle of the chest of the patient and thus a general anesthesia. A new generation of mitral valve replacement devices, called Transcatheter Mitral Valve Replacement (TMVR), have been developed since 2014 [RGDRC17]. This new kind of device does not require an open-heart surgery as the replacement valve is directly inserted in the beating heart via physiological pathways thanks to the use of a catheter, as depicted in Figure 1.10.

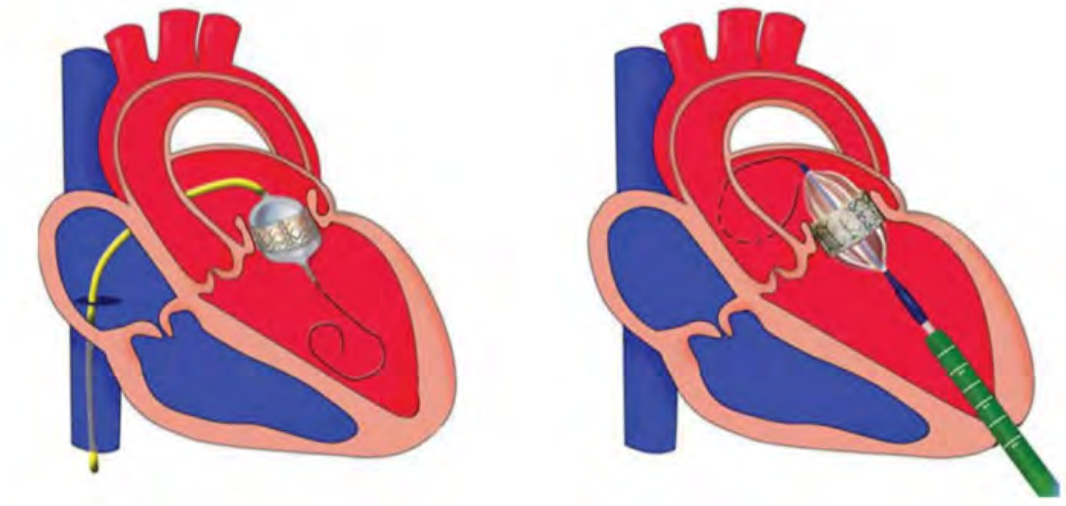

(a) Indirect access via the femoral vein. (b) Direct access via the ventricular apex.

Figure 1.10 – Schematic view of the routes transcatheter mitral valve replacement. Images from [S+16].

The main steps of the implantation of a transcatheter mitral valve, depicted in Figure 1.11, are listed below:

- The native leaflets of the defective mitral valve are either removed (see Figure 1.11a) or pushed towards the ventricle wall.
- The perimeter of the annulus ring is stiched (see Figure 1.11b). The other extremity of the threads is joining the bioprosthetic valve.
- The bioprosthetic valve, folded several times on itself, is introduced into the LH – either by going through the femoral vein or through the apex – thanks to a catheter (see Figure 1.11c).

- Once the catheter has reached the level of the mitral valve annulus, the valve is inflated (see Figure 1.11d) and some leakage tests are performed before finishing the stitches.

(a) Removal of the defecting leaflets.

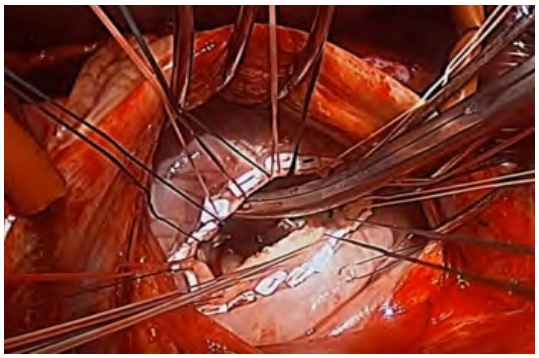

(b) Stiching of the annulus ring.

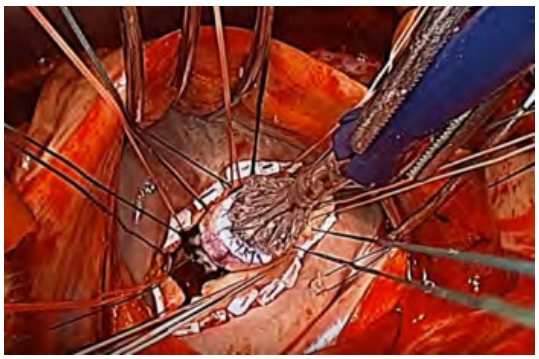

(c) Introduction of the catheter-prosthesis.

(d) Deployment of the bioprosthetic valve.

Figure 1.11 – Main steps of a surgical mitral valve replacement with a trileaflets bioprosthetic valve in the case of a mitral annular calcification. Images from [Vidb].

As regards the nature of the artificial mitral valve, two main families are identified: the mechanical and the biological ones. The first ones are usually made of metal and pyrolytic carbon and are designed to last the full lifetime of the patient [TM11]. Biological valves are made from natural materials or animal tissues, so anticoagulant drugs do not have to be prescribed to the patient, contrarily to the case of mechanical valves where blood clotting can happen [HCC15]. Nevertheless, their lifespan happens to be a major drawback: they only last from 10 to 15 years, so further surgery is then required to replace them after expiration [TM11, HCC15]. The choice of which valve type should be used for a given patient depends on many factors (e.g., age, medical condition, lifestyle, ...) [HCC15, KBL+06].

1.5.2 The mitral valve repair – annuloplasty

Similarly to what we have written so far about the mitral valve replacement, the mitral valve repair has historically been an invasive technique, requiring an open-heart surgery.

Major progress has recently been achieved on this subject and new minimally invasive techniques are under development [CLM+18, GCHR17] and may even surpass the classical ones [PKO+17]. As justified previously, only these (almost) non invasive techniques will be taken into consideration.

The most common observed dilatations of the mitral annulus are the ones impacting the posterior section of the valve (as depicted in Figure 1.12a), naturally slacker than the anterior one, due to the nature of its connective tissue. This dilatation can be reversed thanks to a bioprosthetic ring stitched along the perimeter of the annulus (as depicted in Figure 1.12b). Its purpose is to stabilize and strengthen the loosed annulus in order to restore a broad surface of coaptation of the leaflets, previously degraded and responsible for MR. An efficient coaptation is a critical factor to ensure a durable repair [Ant12].

(a) Initial mitral valve where the posterior section of the valve is defective.

(b) Corrected mitral valve whose annulus is strengthened by an annuloplasty band.

Figure 1.12 – Schematic view of the annuloplasty surgical technique. Images from [Ann].

The main steps of the implantation of an annuloplasty ring, depicted in Figure 1.13, are listed below:

- The mitral valve is inspected to confirm the origin of MR, previously observed with an transesophageal echocardiogram. In this case, the regurgitation is induced by an anterior leaflet prolapse, characterized by over-thick tendinous cords, as depicted in Figure 1.13a.
- The perimeter of the annulus ring is stiched (see Figure 1.13b). The other extremity of the threads connect the annuloplasty band.
- The annuloplasty band is introduced into the LH and the stitches are finished (see Figure 1.13c). If the case requires it, the height of the posterior leaflet can be diminished to ensure a better coaptation of the leaflets.
- Final leakage tests are performed (see Figure 1.13d). Depending of the outcome of these tests, the annuloplasty can be repositioned or tightened to restore the best possible coaptation.

The structure of the core of the annuloplasty is typically made of either silicone or metal, determining its elasticity (flexible, semirigid or rigid) [Ant12]. This core is "wrapped" in a cloth material, typically made of either dacron or polyester (see the white textile in Figures 1.13c–1.13d). The sutures are then placed through it. These annuloplasty devices are very versatile in their nature (i.e., in terms of size, rigidity, shape, composition, ...) and

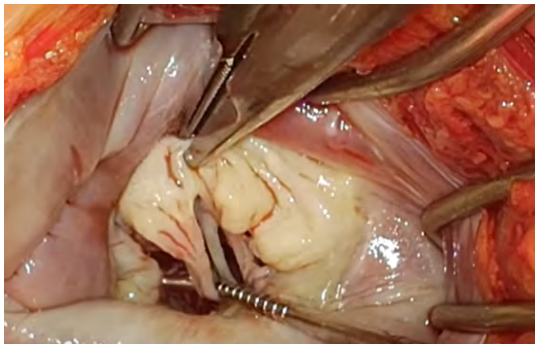

(a) Observation of over-thick tendinous cords.

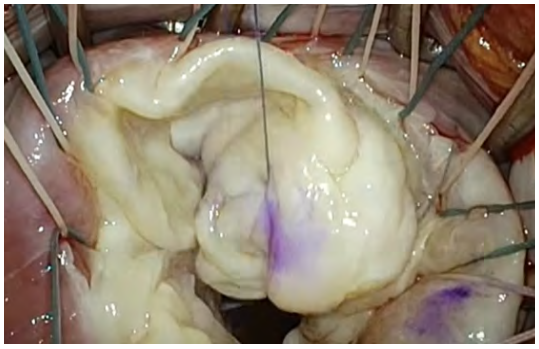

(b) Stitching of the annulus ring.

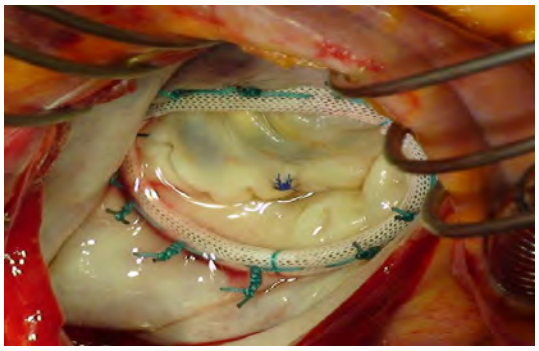

(c) Installation of the annuloplasty ring.

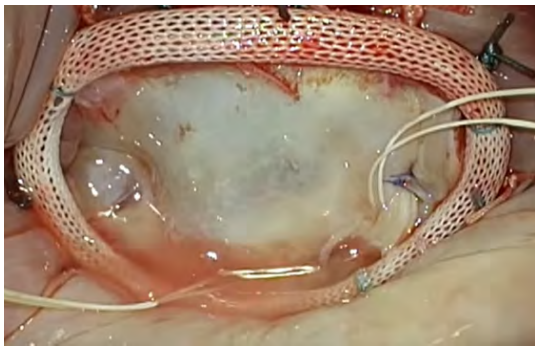

(d) Leakages tests.

Figure 1.13 – Main steps of a surgical mitral valve annuloplasty in the case of an anterior leaflet prolapse. Images from [Vida, Mitb].

are sometimes a complete ring (as depicted in Figures 1.13c–1.13d) or a partial band (as depicted in Figure 1.12b).

An interesting feature of these devices is their remodeling ability, enabling them to adapt themselves to whatever type of mitral annulus of the concerned patient. Therefore, two main families of devices are identified: the remodeling ones and the non-remodeling ones [Ant12]. The former aim to restore the size and the physiological shape (very close to a "D" as pictured on the left of Figure 1.12) of the loosed mitral annulus whereas the latter simply decrease the overall circumference of the annulus [Ant12].

Finally, after the implantation of any type of intracardiac device, an echocardiography of the LH is usually performed to assess if any residual leak is still observed [G+08]. Additional clinical values (e.g., the Left Ventricular Outflow Tract (LVOT) gradient or the regurgitant volume of blood) can also be measured and compared to reference values.

Being able to identify which solution should be preferred for a given patient is a difficult task and contributes to many debates between physicians and clinicians. Globally, the mitral valve repair, when it is possible, is usually preferred to mitral valve replacement [FDOA06]. This is explained by the fact that, when considering the mitral valve replacement, the mechanical prostheses may induce severe complications in a patient (e.g., formation of

blood clot to blood flow changes or mandatory prescription of anticoagulant drugs) and the bioprostheses naturally degrade with time, thus requiring a further surgery. Moreover, in case of severe MR, the tendency seems to be in favor of the mitral valve repair, appearing to be more efficient [L+17], even if this choice must be nuanced when other criteria are taken into account (e.g., the age which keeps being the principal significant risk factor [MEC+02] or the experience of the surgeons). Nevertheless, as there is no clear tendency of supremacy between the repair solution and the replacement solution for a standard case of MR [GBN+08], both of them are currently considered in-depth and are under ongoing clinical and industrial development.

In the sequel, we will particularly focus on the minimally invasive solutions provided by the two start-up companies, Kephalios and Epygon, members of the Mivana consortium and of the Affluent Medical group. Epygon elaborates a solution of transcatheter bioprosthetic mitral valve, thus belonging to the "mitral valve replacement" category, whereas Kephalios develops a solution of adjustable mitral valve annuloplasty ring belonging to the "mitral valve repair – annuloplasty" category.

1.5.3 Epygon – The transcatheter mitral valve

Epygon, founded in 2012 and now member of the Affluent Medical group, develops the first world-wide solution of "physiological" transapical transcatheter mitral prosthesis. This new bioprosthetic valve device claims to be less intrusive and more physiological than the current existing ones and able to restore the natural hemodynamics of blood flowing in the LV and through the aortic valve [Epy]. It was thought and designed to bring the best surgical results possible to the patients suffering from severe mitral insufficiency [Epy]. Indeed, the restoration of blood flow, similar to the native one, fosters the recovery of the ventricular function in the patients, especially for the fragile one presenting a seriously impaired cardiac function [Epy].

The particular features of this new device, as well as its induced benefits, are listed below:

- Contrary to the case of the native mitral valve, this device is made of a single leaflet (see Figure 1.14a). This ensures a physiological diastolic asymmetric flow towards the posterior wall to get an optimal LV filling and low pressure gradients [Epy]. Moreover, this asymmetric shape helps generating a vortex in the ventricle which minimizes the energy loss of blood flow. This ensures an optimal transport of blood towards the aorta as well as a minimization of the LVOT obstruction [Epy].
- The annular ring of the bioprosthesis has a D-shaped form (see Figure 1.14b). This prevents the possible LVOT obstruction encountered when using round trileaflet valves [Epy].
- The bioprosthesis is anchored in the native mitral valve with protected extension bodies (see Figure 1.14c), pushing the defecting leaflets towards the ventricle wall (see Figure 1.15c). This allows the device not to be disturbed by them. Moreover, the valve is enclosed in a surrounding stent (see Figure 1.14c), preventing it from flipping over towards the atrium due to any possible Systolic Anterior Motion (SAM) [Epy].

- The stent is self-expandable and is made of nitinol. The leaflet, usually made of polyester fabric in most of devices, is made of bovine pericardial monoleaflet. The absence of polyester fabric, classical component in most of devices, allows to reduce the risk of formation of blood clots [Epy].

(a) Lateral view. (b) Top view. (c) Side view.

Figure 1.14 – Synthetic images of the Epygon device. The stent and the leaflet are colored in camel and the anatomic anchoring system and the engagement arms are colored in light grey. Images from [Epy].

Process of implantation of the device: Preliminary to the beginning of the surgery, the Epygon device is prepared and folded on itself inside a catheter (see Figure 1.15a) in order to ease its motion inside the patient. This catheter is then inserted through the apex and the center of the Epygon device is optimally placed inside the native mitral valve (see Figure 1.15a), using echo guidance [Epy].

In the first stage of delivery, only the atrial portion of the device is released (see Figure 1.15b). Under 3D echo view, the atrial petals of the valve stent are gradually deployed immediately above the annular plane to obtain the desired D-shaped annulus [Epy].

In a second phase, the ventricular anchoring systems of the stent are then released below the annulus while two engagement arms capture the posterior and anterior leaflets to prevent LVOT obstruction (see Figure 1.15c). Deployed as such, the Epygon transcatheter mitral valve prosthesis is able to restore physiological blood flow within the ventricle while maintaining the native leaflets/tendinous chordae (depicted in Figure 1.15c) under traction to better preserve the LV function [Epy].

1.5.4 Kephalios – The adjustable mitral ring

Pioneer of the annuloplasty, the "Carpentier" rings implantation technique has been practiced routinely for several decades [DJR+90]. In spite of its numerous benefits [JDA+92], a major drawback is that any necessary post-operation adjustment due to residual regurgitation is simply impossible. Usually, after this kind of open-heart surgery, about 40% of patients suffering from MR are not completely healed [FHB03] and a new intervention is required in about 10% of cases [Kep]. The purpose of Kephalios is to correct that

(a) Early stage. (b) Intermediate stage. (c) Final stage.

Figure 1.15 – Typical steps of the implantation of the Epygon device. Images from [Epy].

by proposing an implantable device, inspired by the "Carpentier" rings, that still can be reached after surgery.

Founded in 2011, Kephalios, now member of the Affluent Medical group, develops minimally invasive and implantable intracardiac devices. Its first device consists in a mitral annuloplasty ring, made of metal and of dacron, that can be adjusted repeatedly and progressively, in a percateneous way thanks to minimally invasive interventions, even months after its implantation [Kep]. This device may improve both short (residual regurgitation) and long-term (recurrent regurgitation) patient outcome and, most of all, prevent the need for a second operation, a situation often met by patients with very low compliance [Kep]. This is a world premiere in the field of annuloplasty techniques.

The Kephalios device in its initial configuration and the catheter (and the associated mandrel) used for placing the device inside the patient are pictured in Figure 1.16a. Its adjusted configuration, where the posterior zones have been inflated thanks to the inner balloon catheter, is pictured in Figure 1.16b. Note the presence of the metal eyelets, used for the stitches and for the swelling of the textile, on both Figures.

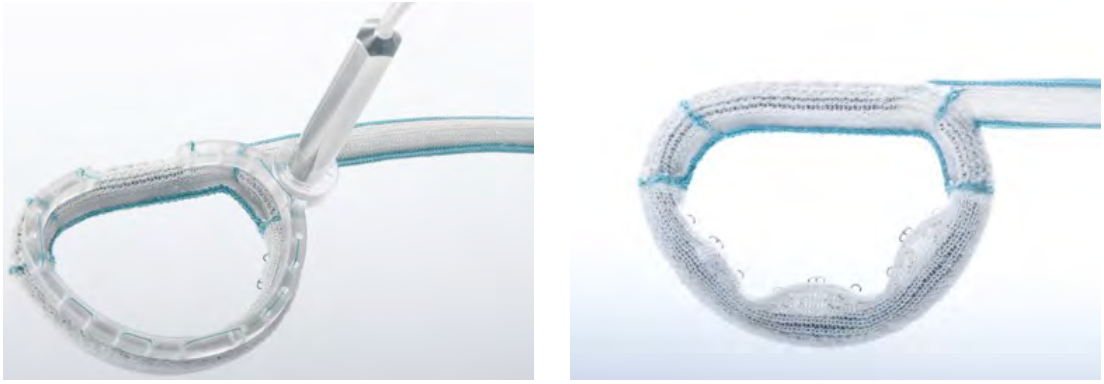

(a) Kephalios device, catheter and mandrel trio. (b) Ring adjusted with the inner balloon catheter.

Figure 1.16 – Pictures of the Kephalios device (with the catheter and the mandrel on the left) in two configurations. The metal core is wrapped by the white textile. The eyelets used for the stitches and for the adjustment of the device are visible. Images from [Kep].

Process of implantation of the device: The different typical steps of the implantation of this device, very similar to the ones of a "Carpentier" ring, are listed below:

- Preliminary to the beginning of the open-heart surgery, the device is stitched to the catheter which will be introduced via the femoral vein (as depicted in Figure 1.10a).
- Before introducing the device inside the patient, sutures on the left trigone, on the posterior annulus and on the right trigone are made. If the device is not a simple annuloplasty band but a full ring, additional sutures are then made on the anterior annulus.
- The device and the catheter are introduced and placed above the defecting mitral valve (see Figure 1.17a).
- Once correctly placed, the stitches connecting the device to the catheter are cut off and are passed through the eyelets and the sutures on the mitral valve (see Figure 1.17b).
- The thread passing through an eyelet are tied with the adjacent ones and the catheter is removed from the atrium (see Figure 1.17c).

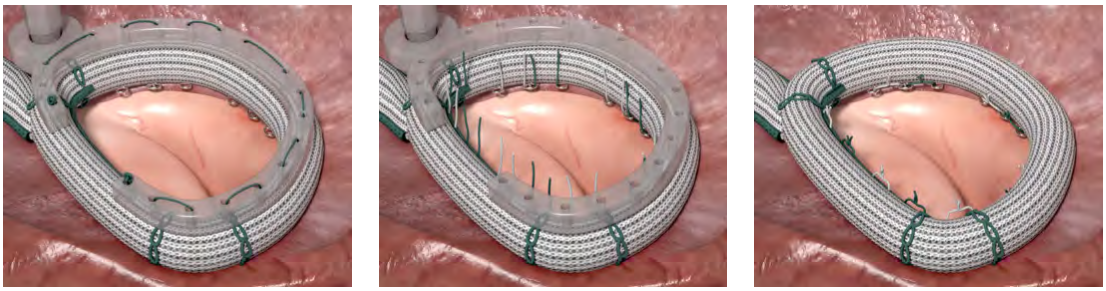

(a) Early stage. (b) Intermediate stage. (c) Final stage.

Figure 1.17 – Typical steps of the implantation of Kephalios device. The sutures on the trigones and on the annulus are not visible. Images from [Kep].

In terms of terminology, note that this ring is implanted by open-heart surgery [Kep], so it is more invasive than the Epygon device. Nevertheless, compared to other classical annuloplasty techniques which do require surgeries for the implantation and also for the post-surgery correction, the Kephalios device only requires one surgery for the implantation. Therefore, it is still considered as a minimally invasive device with regard to the other mitral valve repair devices.

Just after the surgery, the mitral ring remains accessible by replacing the previous mandrel (pictured in Figure 1.16a) with a balloon-catheter actuator, allowing to perform an adjustment of the ring shape [Kep]. Starting from the initial configuration (depicted in Figure 1.18a), and with ultrasound, the distance between the anterior and posterior parts of the annulus ring can be independently reduced along the P1, P2 and P3 axes (see Figure 1.18b). This ensures an increasing of the leaflets coaptation length only where required for the considered patient. Therefore, with proper adjustment, the previously

lost coaptation is restored again, without unnecessarily reducing the total valve orifice area [Kep].

(a) Initial configuration. (b) Adjusted configuration.

Figure 1.18 – The two typical configurations of the Kephalios device. The textile cover is colored in light grey, the posterior eyelets are colored in black and the anterior line used for the suturing is colored in green. Images from [Kep].

Finally, the same previous adjustment can be done again to correct recurrent MR, even months after the date of first surgery. The percutaneous solution made of the inner balloon catheter does not require any additional surgery [Kep].

1.6 Conclusions

In this chapter, the physiological context of this thesis has been addressed, highlighting the complexity and the crucial role of the CS. As we have seen, this living system, and more particularly the mitral valve, may be subject to many diseases, requiring open-heart and/or minimally invasive surgeries coupled with use of intracardiac devices to efficiently treat them. Due to the preponderance of MR among the population worldwide, many new experimental devices – such as the ones from Kephalios and Epygon – have been designed and tested in *in vivo* and *in vitro* conditions. As detailed in the introduction of this thesis, in the last decades, numerical simulation has appeared to be an efficient and reliable tool for the design of such devices, allowing to spare time and animal lives. This explains the strong clinical and industrial interests which have grown for predictive numerical simulations ever since, requiring an efficient and accurate mathematical modeling of cardiac hemodynamics to address these problems. This is what we further detail in Chapter 2.

Chapter 2

Modeling and simulation of cardiac hemodynamics

In this chapter, some models commonly considered in the context of the mathematical modeling and simulation of cardiac hemodynamics are presented as well as the associated coupling strategies. Then, based on the degree of complexity adopted for the description of the cardiac valves, two main approaches are considered: the RIS model and the FSI model. For the latter one, a consequent review of the existing numerical techniques are provided based on the following classification criteria: the spatial discretization of the problem and the nature of the splitting between the fluid and the structure solvers. The content of this chapter will be the fundamental mathematical background of the work presented later in Parts II and III.

Contents

2.1 Introduction

In this chapter, we address the modeling and the simulation of hemodynamics in the left heart, also termed cardiac hemodynamics in what follows. As detailed in Section 1.2, the left heart is recognized as a complex living system due to its inherent multi-physics nature. Therefore, its modeling calls for the consideration of several models, operating at different levels of complexity and inducing *two-way* effects between them. For instance, we can think of blood flowing inside the left heart and interacting with both the cardiac valves and the myocardium. This type of coupling gives birth to complex fluid-structure interactions which represent serious challenges of modeling (e.g., the large structural displacements and fast dynamics of the valves, the topological changes (when leaflets come into contact) and the induced high pressure-drops) and which require efficient numerical methods to address them. The coupling of such mathematical models, sometimes characterized by different temporal and spatial scales, is one of the most active aspects of research in hemodynamics (see, e.g., [VS06, dSGB08, JMS10, SASZA+18]).

In the sequel, it is assumed that the reader is familiar with continuum mechanics, and more particularly, with fluid and solid mechanics. The models and equations used in the context of this work will be introduced and described, but more in-depth references are available in the literature. Without being exhaustive, we cite [Mal69, Gur81, MPF92] for introductory general texts on continuum mechanics and [Cia88, MHC83] for more mathematical oriented ones. As regards fluid mechanics, we mention [MROH12, Fay94, Ari89] for the theory and [FFGQ09] for the derivation of the associated equations. Then, we refer to [Cia88, MHC83] for the mathematical aspect of solid mechanics and to [ATN04] for a particular focus on non-linear mechanics. Finally, for the shell theory, only briefly described in what follows, we refer to [Cia00] for the general mathematical theory. In addition, notions of linear shell theory can be found in [CB11, FFGQ09] and the treatment of the non-linear case is provided in [CB11, LS05].

The rest of this chapter is organized as follows. The key components of a simulation of cardiac hemodynamics (i.e., the geometrical description of the heart and blood modeling) are introduced in Section 2.2 before presenting the different coupling strategies considered in this work in Section 2.3. Based on the degree of complexity adopted for the description of the cardiac valves, two approaches are investigated: we start with the simple RIS model, presented in Section 2.4, before presenting the full FSI model in Section 2.5, more complex but allowing a more refined description of cardiac hemodynamics. Finally, the conclusions are given in Section 2.6.

2.2 Geometries and blood flow modeling

Realistic simulations of cardiac hemodynamics could not be carried out without using proper geometries of the left heart and accurate modeling of blood and its dynamics. These two concerns are addressed in Sections 2.2.1 and 2.2.2, respectively. The modeling of cardiac valves is postponed until Section 2.3.2.2.

2.2.1 Geometrical description of the left heart

In this thesis, the geometries used for the further 3D simulations of cardiac hemodynamics in the left heart come from Zygote Media Group[1], a company whose core business is the realization of anatomically accurate 3D human models thanks to Computerized Tomography (CT) scans [BH07]. The original Zygote CT scan of the human heart is shown in Figure 2.1.

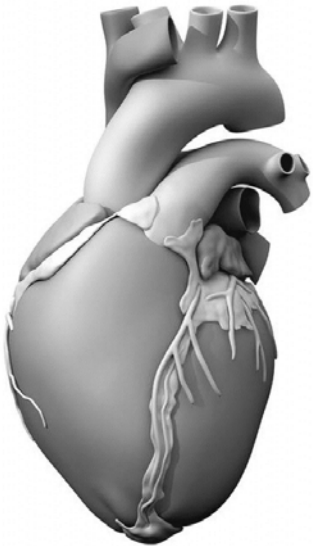

Figure 2.1 – Representation of the original Zygote CT scan of the human heart.

Inside this CT scan, the left heart and its adjacent vessel parts are of crucial interest for the numerical simulations investigated in this work. Therefore, their corresponding volumes, highlighted in Figure 2.2a, are extracted from the rest of the initial geometry. Values of some physical quantities relative to these volumes of interest for the simulations of cardiac hemodynamics are given in Table 2.1. Their typical dimensions are slightly smaller than the ones coming from physiological data (see, e.g., [RLWS70, RDKFO89, GSFA06]). This is explained by the fact that the CT scan has been realized on a dead body.

As already mentioned in Section 1.3.2, heart valves (and especially the mitral valve) are expected to play a crucial role in the development of the structure of the intraventricular flow. It is then mandatory to precisely model their geometry to be able to correctly compute this flow. The native mitral valve (in open configuration) and the native aortic valve (in closed configuration) are represented in the previous volume of interest (see Figure 2.2b). The native valves are not the only ones investigated in this work (see Chapters 4 and 7) and more information about the geometries of the different considered valves (either biological or artificial) are given in Appendix A.

The full workflow used to generate the computational meshes associated to these geometries is resumed below: starting from the Zygote[2] heart model, detailed above, and

[1] See https://www.zygote.com/.
[2] See http://www.3dscience.com/.

Physical quantity	Value
Ventricular volume	87 mL
Atrial volume	56 mL
Aortic root volume	10 mL
Ventricular long axis length	7.7 cm
Mitral valve orifice area	4.7 cm^2
Aortic cross sectional area	4.0 cm^2

Table 2.1 – Values of some physical quantities relative to the volume of interest for the simulations of cardiac hemodynamics.

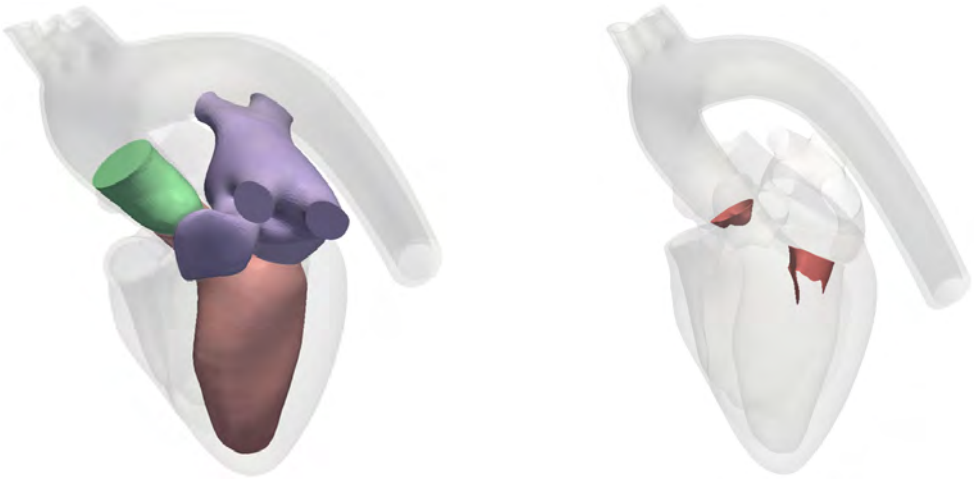

(a) Volume of interest for the simulations of cardiac hemodynamics.

(b) Native mitral and aortic valves in the extracted volume.

Figure 2.2 – Representation of the volume of interest for the simulations of cardiac hemodynamics and the corresponding native heart valves.

using the 3-matic[3] software, computationally-correct surface meshes are obtained. Then, the Mmg PLATFORM[4] based on the meshing software YAMS[5] [Fre01] is used to further process and refine them. Finally, using these refined surface meshes, the 3D meshing software GHS3D[6] [GHS90] generates the 3D computational meshes, where an example of such a final result is depicted in Figure 2.3.

[3]See https://www.materialise.com/.
[4]See https://www.mmgtools.org/.
[5]See https://www.ljll.math.upmc.fr/frey/publications/RT-0252.pdf.
[6]See https://team.inria.fr/gamma3/gamma-software/ghs3d/.

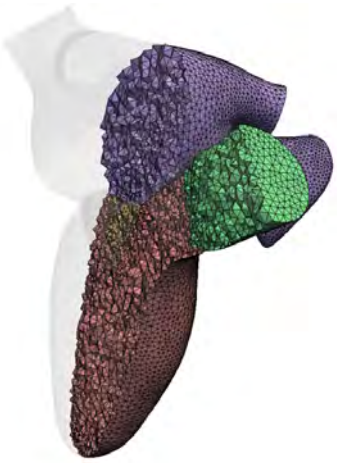

Figure 2.3 – 3D computational mesh corresponding to the volume of interest for the simulations of cardiac hemodynamics.

2.2.2 Blood flow modeling

The mathematical equations describing blood and its dynamics are the key components in the mathematical modeling of cardiac hemodynamics. Blood flow behavior is commonly assumed to be homogeneous, incompressible, Newtonian and governed by the Navier-Stokes equations. In Section 2.2.2.1, the physical validity of these hypotheses is justified before introducing these equations in different frameworks in Section 2.2.2.2.

2.2.2.1 Modeling choices

Two main criteria are commonly used when determining which fluid model should be used: the non-Newtonian effects and the laminar/turbulent nature of blood flow.

As detailed in Chapter 1, blood is not purely a fluid but a suspension of particles in the plasma, mostly made of water. Red cells represent the most important proportion of these particles and thus determine the mechanical properties of blood. In particular, they exhibit complex hemodynamic effects which induce a global non-Newtonian behavior. Such effects (e.g., shear thinning, thixotropy, viscoelasticity and yield stress [FQV09]) have been widely studied, from experimental and theoretical points of view, in the last century (see, e.g., [CLW06, YG08]). These studies have highlighted that these non-Newtonian effects are predominant in the small vasculature (meaning, capillaries and medium and small blood vessels) and negligible in the large one (meaning, large blood vessels and heart's chambers).

The Reynolds number (Re) is an important dimensionless quantity in fluid mechanics. Its value helps to predict the general flow pattern, either laminar or turbulent. At low values, the flow is dominated by laminar effects (meaning sheet-like or regular fluid motion), whereas at high values, the flow is dominated by turbulent effects (meaning eddy or unstable fluid motion). Laminar flow is characterized by smooth and steady fluid motion whereas turbulent flow is characterized by disruptive and chaotic changes in pressure and

velocity [Mal69]. The Reynolds number is defined as

$$Re = \frac{\rho^{\mathrm{f}} u D}{\mu},$$

where ρ^{f}, u, D and μ denote in the cardiac hemodynamics context, respectively, the density of blood, the typical velocity of blood in the considered vessel, the typical dimension of the considered vessel (e.g., its diameter or its length) and the dynamic viscosity of blood. Typical values of the Reynolds number and peaks of velocity in some blood vessels are given in Table 2.2.

Considered vessel	Peak velocity (cm/s)	Reynolds number
Ascending aorta	1.0	4000
Thoracic aorta	0.8	2500
Large vein	0.8	1700
Small vein	0.6	100
Small artery	0.2	100
Arteriole	0.01	0.5
Capillary	0.001	0.003

Table 2.2 – Values of peak velocity and Reynolds number in some blood vessels. Table adapted from [FQV09].

In healthy situations, no turbulence is observed in the whole CS, except at the exit of the aortic valve during peaks of velocity flow (i.e., limited to the systolic phase during short time intervals [FQV09]). This work focuses on the LH (large arteries, heart's chambers and cardiac valves), hence, it seems reasonable to not consider flow instabilities in our fluid model. Moreover, even if it must be kept in mind that local non-Newtonian effects can exist in the LH (due to, e.g., valve hinges and leakage jet during valve closure [SB09]), it is commonly assumed that blood is homogeneous, incompressible and Newtonian and thus governed by the Navier-Stokes equations.

2.2.2.2 The incompressible Navier-Stokes equations

When studying a continuous media like blood, two main approaches can be considered for the description of its motion: the Eulerian and the Lagrangian ones [Mal69, Gur81, FFGQ09]. In the Eulerian approach, the observer does not move and gazes at a fixed location in space through which the fluid flows as time passes. In the Lagrangian approach, the observer follows a small control volume as it evolves in time and space.

The Eulerian approach is the most commonly used when fixed geometries are considered. Nevertheless, as detailed in the description of the cardiac cycle in Section 1.3, the LV distorts drastically during a typical heartbeat. Thus, modeling the space occupied by blood with a fixed domain is not physiologically satisfying and a domain evolving with

time must be then considered. But, describing such a time-dependent domain with an Eulerian description is cumbersome and an alternative formulation, named Arbitrary Lagrangian-Eulerian (ALE), which combines the benefits of both Eulerian and Lagrangian approaches, has been developed to avoid such difficulties [DGH82].

In the sequel, we present the Navier-Stokes equations in the Eulerian and in the ALE frameworks. We also detail why the ALE formulation is preferred to the Eulerian one when handling moving domains.

Eulerian formulation: In what follows, Ω is assumed to be a bounded domain of $\mathbb{R}^d$, where $d = 2$ or 3. This domain possesses a Lipschitz continuous boundary, denoted $\partial\Omega$, and an exterior unit normal, denoted $\boldsymbol{n}$. The symbol t represents the physical time.

The Navier-Stokes equations in the Eulerian formalism read as follows: find the velocity $\boldsymbol{u} = \boldsymbol{u}(\boldsymbol{x},t) : \Omega \times \mathbb{R}^+ \to \mathbb{R}^d$ and pressure $p = p(\boldsymbol{x},t) : \Omega \times \mathbb{R}^+ \to \mathbb{R}$, such that

$$\begin{cases} \rho^{\mathrm{f}} \left(\dfrac{\partial \boldsymbol{u}}{\partial t} + \boldsymbol{u} \cdot \boldsymbol{\nabla} \boldsymbol{u} \right) - \boldsymbol{\nabla} \cdot \boldsymbol{\sigma}(\boldsymbol{u},p) = \boldsymbol{f}^{\mathrm{f}} & \text{in} \quad \Omega, \\ \boldsymbol{\nabla} \cdot \boldsymbol{u} = 0 & \text{in} \quad \Omega, \end{cases} \tag{2.1}$$

where the fluid Cauchy stress tensor is given by

$$\boldsymbol{\sigma}(\boldsymbol{u},p) \overset{\text{def}}{=} 2\mu\boldsymbol{\epsilon}(\boldsymbol{u}) - p\boldsymbol{I}, \quad \boldsymbol{\epsilon}(\boldsymbol{u}) \overset{\text{def}}{=} \frac{1}{2}\left(\boldsymbol{\nabla}\boldsymbol{u} + \boldsymbol{\nabla}\boldsymbol{u}^{\mathrm{T}}\right)$$

and where $\boldsymbol{I}$ denotes the identity tensor. $\boldsymbol{f}^{\mathrm{f}}$ is a body force, function of space and time, and is assumed to be equal to $\boldsymbol{0}$ when not specified. Due to the assumed nature of the fluid (homogeneous, incompressible and Newtonian), ρ^{f} and μ are constant in space and time.

The system (2.1) has to be completed with initial conditions:

$$\boldsymbol{u}(0) = \boldsymbol{u}_0 \quad \text{in} \quad \Omega$$

and with boundary conditions:

$$\begin{cases} \boldsymbol{u} = \boldsymbol{u}_{\mathrm{D}} & \text{on} \quad \Gamma_{\mathrm{D}}, \\ \boldsymbol{\sigma}(\boldsymbol{u},p)\boldsymbol{n} = \boldsymbol{g}_{\mathrm{N}} & \text{on} \quad \Gamma_{\mathrm{N}}, \end{cases} \tag{2.2}$$

where $\boldsymbol{u}_{\mathrm{D}}$ and $\boldsymbol{g}_{\mathrm{N}}$ are given vector functions and where Γ_{D} and Γ_{N} form a partition of $\partial\Omega$ such that $\partial\Omega = \Gamma_{\mathrm{D}} \cup \Gamma_{\mathrm{N}}$. $(2.2)_1$ is called the Dirichlet boundary condition on Γ_{D} and $(2.2)_2$ the Neumann boundary condition on Γ_{N}.

ALE formulation: In this paragraph, we reformulate the Navier-Stokes equations (2.1) in the ALE framework. Only the basic notions of the ALE formulation will be addressed here. For the interested reader, more information can be found in [Nob01, DHPRF04, FFGQ09].

When considering moving domains, the discretization of the time derivative $\dfrac{\partial \cdot}{\partial t}$ in $(2.1)_1$ is cumbersome as it cannot be naturally approximated on such domains [FFGQ09]. Then,

the motivation of the ALE formulation is to propose a framework that facilitates the time discretization of terms which involve quantities transported in space and time.

In what follows, the previous domain $\Omega \subset \mathbb{R}^d$ is now supposed to evolve with t and is denoted $\Omega(t)$. Similarly, its Lipschitz continuous boundary is now denoted $\partial\Omega(t)$. The time-dependent control volume $\Omega(t)$ is assumed to be parametrized as

$$\Omega(t) = \boldsymbol{\mathcal{A}}(\widehat{\Omega}, t), \quad \forall t \in \mathbb{R}^d, \tag{2.3}$$

where $\widehat{\Omega}$ is the reference configuration and $\boldsymbol{\mathcal{A}} : \widehat{\Omega} \times \mathbb{R}^+ \to \mathbb{R}^d$ is a one–to–one mapping given in terms of the fluid domain displacement $\boldsymbol{d}^{\mathrm{f}} : \widehat{\Omega} \times \mathbb{R}^+ \to \mathbb{R}^d$ with the expression: $\boldsymbol{\mathcal{A}} \overset{\text{def}}{=} \boldsymbol{I}_{\widehat{\Omega}\times\mathbb{R}^+} + \boldsymbol{d}^{\mathrm{f}}$. The fluid domain velocity $\boldsymbol{w} : \widehat{\Omega} \times \mathbb{R}^+ \to \mathbb{R}^d$ is then simply defined as $\boldsymbol{w} \overset{\text{def}}{=} \dfrac{\partial \boldsymbol{d}^{\mathrm{f}}}{\partial t}$. Note that by replacing t with 0 in (2.3), we get $\Omega(0) = \boldsymbol{\mathcal{A}}(\widehat{\Omega}, 0) = \widehat{\Omega}$, highlighting the fact that the current configuration Ω is initially identical to the reference configuration $\widehat{\Omega}$. We shall also use the notation $\boldsymbol{\mathcal{A}}_t$ for the deformation, defined by $\boldsymbol{\mathcal{A}}_t \overset{\text{def}}{=} \boldsymbol{\mathcal{A}}(\cdot,t)$, and $\dfrac{\partial \cdot}{\partial t}\Big|_{\boldsymbol{\mathcal{A}}}$ for the ALE time derivative, given by the following equality:

$$\frac{\partial q}{\partial t}\Big|_{\boldsymbol{\mathcal{A}}} = \boldsymbol{w} \cdot \boldsymbol{\nabla} q + \frac{\partial q}{\partial t}, \tag{2.4}$$

for any physical field q.

If any physical field q evaluated on the current configuration can also be defined on the reference configuration, we adopt the superscript $\widehat{\ }$ for the latter alternative to distinguish both fields q and $\widehat{q}$. We use $(\boldsymbol{x},t)$ and $(\widehat{\boldsymbol{x}},t)$ for the independent variables of q and $\widehat{q}$ for, respectively, the current and the reference configurations. The relations between q and $\widehat{q}$ are given by

$$\begin{aligned} \widehat{q}(\widehat{\boldsymbol{x}},t) &\overset{\text{def}}{=} q(\boldsymbol{\mathcal{A}}_t(\widehat{\boldsymbol{x}}),t), \quad && \forall (\widehat{\boldsymbol{x}},t) \in \widehat{\Omega} \times \mathbb{R}^+, \\ q(\boldsymbol{x},t) &\overset{\text{def}}{=} \widehat{q}(\boldsymbol{\mathcal{A}}_t^{-1}(\boldsymbol{x}),t), \quad && \forall (\boldsymbol{x},t) \in \Omega(t) \times \mathbb{R}^+ \end{aligned} \tag{2.5}$$

and are illustrated in Figure 2.4.

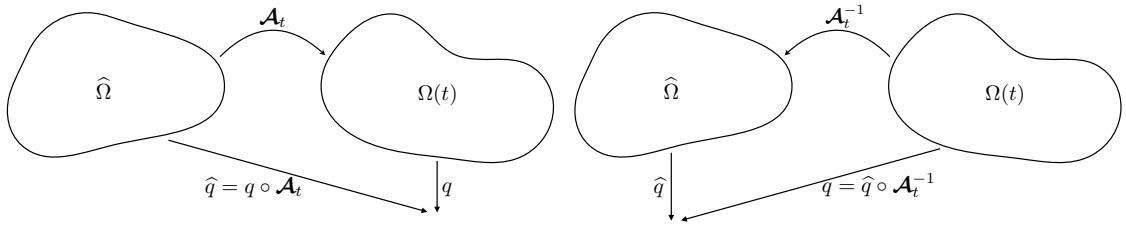

(a) From q to $\widehat{q}$. (b) From $\widehat{q}$ to q.

Figure 2.4 – Relations between q and $\widehat{q}$. Images adapted from [FFGQ09].

Remark 2.1

The choice of $\boldsymbol{\mathcal{A}}$ is not unique. Its only requirement is to satisfy the chosen domain boundary displacement. Therefore, a classical approach is to build $\boldsymbol{\mathcal{A}}$ from the evolution of the boundary $\partial\Omega(t)$ of the fluid domain $\Omega(t)$.

Finally, by applying (2.4) to $\boldsymbol{u}$, the following material derivative holds:

$$\frac{\partial \boldsymbol{u}}{\partial t} = \frac{\partial \boldsymbol{u}}{\partial t}\Big|_{\boldsymbol{\mathcal{A}}} - \boldsymbol{w} \cdot \boldsymbol{\nabla} \boldsymbol{u} \tag{2.6}$$

and the Navier-Stokes equations in the ALE formalism, obtained from (2.1), read as follows: find the velocity $\widehat{\boldsymbol{u}} = \widehat{\boldsymbol{u}}(\widehat{\boldsymbol{x}},t) : \widehat{\Omega} \times \mathbb{R}^+ \to \mathbb{R}^d$ and the pressure $\widehat{p} = \widehat{p}(\widehat{\boldsymbol{x}},t) : \widehat{\Omega} \times \mathbb{R}^+ \to \mathbb{R}$, such that

$$\begin{cases} \rho^{\mathrm{f}} \left(\dfrac{\partial \boldsymbol{u}}{\partial t}\Big|_{\boldsymbol{\mathcal{A}}} + (\boldsymbol{u} - \boldsymbol{w}) \cdot \boldsymbol{\nabla} \boldsymbol{u} \right) - \boldsymbol{\nabla} \cdot \boldsymbol{\sigma}(\boldsymbol{u},p) = \boldsymbol{f}^{\mathrm{f}} & \text{in} \quad \Omega(t), \\ \boldsymbol{\nabla} \cdot \boldsymbol{u} = 0 & \text{in} \quad \Omega(t). \end{cases} \tag{2.7}$$

The system (2.7) has to be completed with initial conditions:

$$\boldsymbol{u}(0) = \boldsymbol{u}_0 \quad \text{in} \quad \Omega(0)$$

and with boundary conditions on $\partial\Omega(t)$ similar to the ones detailed in (2.2) but now applied to the moving boundaries $\Gamma_{\mathrm{D}}(t)$ and $\Gamma_{\mathrm{N}}(t)$ which form a partition of $\partial\Omega(t)$.

2.3 Coupling strategies

In this section, the different coupling strategies considered in this thesis are presented as well as the assumptions made to obtain them. We start with the description of a complete heart model in Section 2.3.1 before deriving the different simplified approaches obtained from it in Section 2.3.2.

2.3.1 A complete heart model

A complete heart model can be split into three main components which are coupled all together: (i) a 3D blood flow model $\boldsymbol{\mathcal{F}}$ (as the ones described in Section 2.2.2.2), (ii) a 3D myocardium electromechanics model $\boldsymbol{\mathcal{E}}$ and (iii) a complete mechanical model of cardiac valves $\boldsymbol{\mathcal{S}}$. Figure 2.5 depicts the different couplings existing in such a heart model.

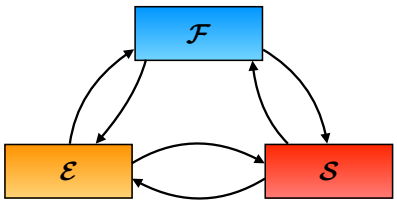

Figure 2.5 – Representation of the different couplings existing in a complete heart model. $\boldsymbol{\mathcal{F}}$, $\boldsymbol{\mathcal{E}}$ and $\boldsymbol{\mathcal{S}}$ represent, respectively, the 3D blood flow model, the 3D myocardium electromechanics model and the complete mechanical model of cardiac valves. Black arrows represent the degree of coupling between all models.

In spite of the physical validity of this approach and of the significant advances achieved

since the beginning of this century (see, e.g., [LP00, vLAdHB04, KHY+17, MSV+16, GFQ+17]), the simulation of a complete heart model, which takes into account all the couplings between its components, remains a complex and challenging problem not easily achievable in practice.

2.3.2 A reduced heart model

In order to overcome the complexity of the previous complete heart model, a common approach consists in modeling $\mathcal{F}$ and $\mathcal{S}$ with simplified models. For instance, as proposed in [SMCCS06, CLMS12], $\mathcal{F}$ is replaced with a 0D lumped model (e.g., adequate Windkessel models), denoted $\mathcal{F}_{\mathbf{0D}}$, and $\mathcal{S}$ is replaced with 0D valves, denoted $\mathcal{V}_{\mathbf{0D}}$, which behave like realistic diodes regulating flow between blood compartments. Figure 2.6 represents the different couplings existing in the resulting reduced heart model.

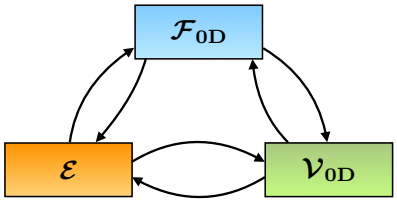

Figure 2.6 – Representation of the different couplings existing in a reduced heart model. $\mathcal{E}$ represent the 3D myocardium electromechanics model. $\mathcal{F}_{\mathbf{0D}}$ and $\mathcal{V}_{\mathbf{0D}}$ represent, respectively, the simplified 0D models of blood flow and valves. Black arrows represent the degree of coupling between all models.

Similarly to the components of the complete heart model (see Figure 2.5), the simplified models $\mathcal{F}_{\mathbf{0D}}$ and $\mathcal{V}_{\mathbf{0D}}$ are still *two-way* coupled with $\mathcal{E}$ and between them. The main benefit of this reduced heart model approach is that it ensures less interlinked solvers and less computational complexity but is still able to provide realistic results (see [SMCCS06, CLMS12]).

In the rest of this work, this reduced heart model will be the framework of reference for the simplified FSI model of the heart. More information about it is provided in Appendix B.

2.3.2.1 Coupling with a 3D blood flow model

In spite of the computational benefits brought by this reduced heart model, the 3D structure of the intraventricular flow cannot be obtained with $\mathcal{F}_{\mathbf{0D}}$ and a 3D blood flow model $\mathcal{F}$ (as the ones described in Section 2.2.2.2) is required for this. Therefore, in order to avoid the computational complexity of a complete heart model (see Figure 2.5) and to be able to compute the full structure of the intraventricular flow in an efficient and not time-consuming way, an *one-way* uncoupling between the reduced heart model (see Figure 2.6) and a 3D blood flow model $\mathcal{F}$ is often assumed (see, e.g., [CCV+15]). This coupling strategy is depicted in Figure 2.7.

A consequence of this *one-way* uncoupling is that the effects of electromechanics on $\mathcal{F}$ are taken into account but that no feedback is considered. In addition of the reduced

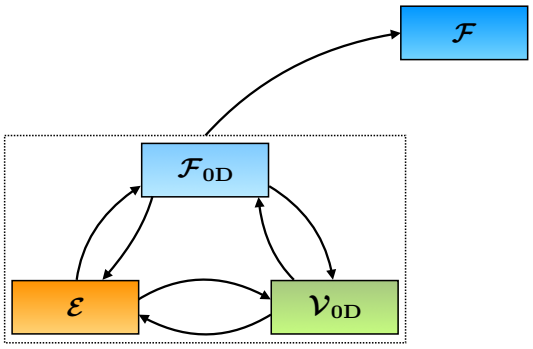

Figure 2.7 – Representation of the *one-way* uncoupling between the reduced heart model and the 3D blood flow model. The dotted box represents the reduced heart model depicted in Figure 2.6. $\mathcal{F}$ represents a 3D blood flow model. Black arrows represent the degree of coupling between all models.

computational complexity compared to the complete heart model (see Figure 2.5), this approach allows the use of different temporal discretization in $\mathcal{E}$ and $\mathcal{F}$.

In this thesis, the approach depicted in Figure 2.7 is primarily used to improve the simulations of cardiac hemodynamics by enhancing them with physiological boundary conditions (as illustrated in the various numerical examples further detailed in Chapters 3, 4 and 7). For instance, we can cite the distortion of the left ventricle surface dictated by the myocardium electromechanics model which is of fundamental interest to be able to compute a correct behavior of blood flow during a heartbeat. Due to the recurring use of this approach, the second section of Appendix B is totally dedicated to this topic. We refer to it for more information about the extraction of results used to improve the simulations of cardiac hemodynamics.

2.3.2.2 Coupling with two different models of cardiac valves

Finally, as regards the modeling of implantable intracardiac devices dedicated to the treatment of MR, a *two-way* coupling of blood flow with a model of cardiac valves is required. This type of coupling allows to compute the reciprocal consequences of the geometry and distortion of the cardiac valves on blood flow. Depending on the nature of the problem, two different models of cardiac valves can be considered:

- The structure of the intraventricular flow is expected to be mainly induced by the geometry of the open configuration of the valve located at the mitral position (see Section 1.2.2.4). Therefore, for a preliminary computation of this flow, a resistive approach of the cardiac valves, where only their open and closed configurations are considered and immersed into the computational domain, is sufficient. This corresponds to the RIS modeling, illustrated in Figure 2.8.
- If more refined problems are investigated (e.g., the study of the mitral prolapse, the study of the influence of the valves geometry on MR or the computation of the constraints applied on their leaflets), a complete mechanical model of cardiac valves

(where their dynamics is taken into account) must be considered. This corresponds to the FSI modeling, illustrated in Figure 2.9.

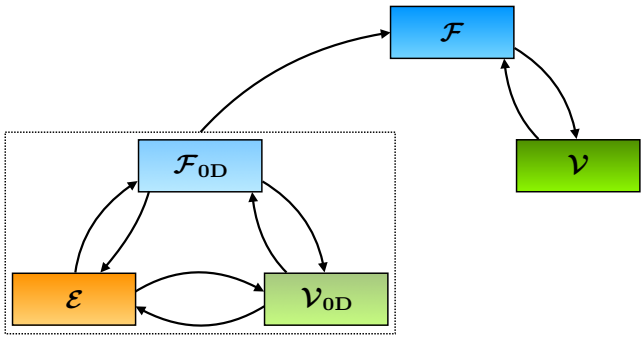

Figure 2.8 – Representation of the different couplings existing in our RIS modeling of cardiac hemodynamics. The dotted box represents the reduced heart model depicted in Figure 2.6. $\mathcal{F}$ and $\mathcal{V}$ represent, respectively, the 3D blood flow model and the resistive immersed model of cardiac valves. Black arrows represent the degree of coupling between all models.

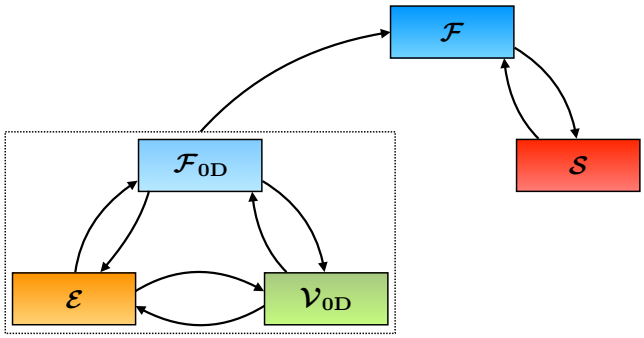

Figure 2.9 – Representation of the different couplings existing in our FSI modeling of cardiac hemodynamics. The dotted box represents the reduced heart model depicted in Figure 2.6. $\mathcal{F}$ and $\mathcal{S}$ represent, respectively, the 3D blood flow model and the complete mechanical model of cardiac valves. Black arrows represent the degree of coupling between all models.

The rest of this chapter is dedicated to the presentation of the above-mentioned $\mathcal{V}$ and $\mathcal{S}$ models ($\mathcal{F}$ has already been introduced in Section 2.2.2.2). In particular, the $\mathcal{F}$-$\mathcal{V}$ and $\mathcal{F}$-$\mathcal{S}$ *two-way* couplings are addressed in Sections 2.4 and 2.5, respectively.

2.4 Resistive Immersed Surfaces method of cardiac valves

In spite of the major advances achieved since the beginning of the 21st century [LP00, vLAdHB04, KHS+15, GFQ+17], the full FSI simulation of cardiac hemodynamics remains a complex and challenging problem. In order to reduce the complexity of this coupled

problem, several alternative models have been proposed in the literature [AHSG12, CMN16, FFDQ17, TDQ17]. The fundamental idea of these simplified approaches consists in combining a reduced modeling of the valves dynamics with a kinematic uncoupling of cardiac hemodynamics and electromechanics (i.e., displacement fields, coming either from measurements or from simulations, are imposed on the boundaries of the fluid cavities), as depicted in Figure 2.8.

The goal of this section is to present one of these approaches dedicated to the simulation of cardiac hemodynamics in the LV, namely the RIS model (see, e.g., [AHSG12]), and to provide its key elements used in Chapter 3 before applying them on 3D realistic numerical examples in Chapter 4.

2.4.1 Original model

In the RIS model proposed in [AHSG12], a cardiac valve is described in a simplified manner by neglecting its dynamics and by only considering its open and closed configurations. These configurations are represented by co-dimension one surfaces (meaning $\subset \mathbb{R}^{d-1}$) which are both immersed in the fluid at the same time (see later Chapters 3 and 4 for illustrations). The fundamental idea of this model consists in introducing a resistive surface term in the fluid momentum equation for each immersed surface. This term is characterized by a time-dependent resistive parameter $R(t)$ which is null when the valve is open and large when the valve is closed. More information about the choice of its value is provided in Section 2.4.3.

In what follows, d is set to 3. We consider the flow of a fluid within a moving domain $\Omega(t) \subset \mathbb{R}^3$ with n immersed valves. The closed configuration of the valves is given in terms of the surfaces $\Sigma_i(t) \subset \Omega$ with $i = 1 \dots n$. The associated open configuration can also coexist with $\Sigma_i(t)$ but is not considered here. Each surface is characterized by a resistive parameter $R_i(t)$ and is assumed to be oriented by a normal $\boldsymbol{n}$. We then define a negative and a positive side via the normal $\boldsymbol{n}^- \overset{\text{def}}{=} \boldsymbol{n}$ and $\boldsymbol{n}^+ \overset{\text{def}}{=} -\boldsymbol{n}^-$. For a given continuous scalar or tensorial field f defined in $\Omega(t)$ (possibly discontinuous across the immersed surface $\Sigma_i(t)$), we define its positive and negative sided restrictions to $\Sigma_i(t)$, denoted respectively by f^+ and f^-, as $f^+(\boldsymbol{x}) \overset{\text{def}}{=} \lim_{\xi \to 0^+} f(\boldsymbol{x} - \xi \boldsymbol{n}^+)$ and $f^-(\boldsymbol{x}) \overset{\text{def}}{=} \lim_{\xi \to 0^+} f(\boldsymbol{x} - \xi \boldsymbol{n}^-)$, for all $\boldsymbol{x} \in \Sigma_i(t)$.

We first recall some notations coming from Section 2.2.2.2 where the immersed valve $\Sigma_i(t)$ is now also considered in the ALE formulation of $\Omega(t)$. The current configuration is denoted by $\Omega(t) = \boldsymbol{\mathcal{A}}(\widehat{\Omega},t)$, where $\widehat{\Omega}$ is the reference configuration and $\boldsymbol{\mathcal{A}} : \widehat{\Omega} \times \mathbb{R}^+ \to \mathbb{R}^3$ is the ALE one-to-one mapping, as depicted in Figure 2.10. This mapping is defined by the fluid domain displacement $\boldsymbol{d}^{\text{f}}$ with the expression $\boldsymbol{\mathcal{A}} \overset{\text{def}}{=} \boldsymbol{I}_{\widehat{\Omega}\times\mathbb{R}^+} + \boldsymbol{d}^{\text{f}}$. Similarly, we have $\partial\Omega(t) \overset{\text{def}}{=} \boldsymbol{\mathcal{A}}(\widehat{\partial\Omega}, t)$ and $\Sigma_i(t) \overset{\text{def}}{=} \boldsymbol{\mathcal{A}}(\widehat{\Sigma_i}, t)$. To simplify notations, in the rest of this section, Ω now refers to $\Omega(t)$, $\partial\Omega$ to $\partial\Omega(t)$, Σ_i to $\Sigma_i(t)$ and R_i to $R_i(t)$.

The displacement field $\boldsymbol{d}^{\text{f}}$ is given in terms of an arbitrary lifting of the exterior boundary displacement $\boldsymbol{d}^{\text{f}}|_{\partial\widehat{\Omega}}$ through the relation $\boldsymbol{d}^{\text{f}} = \boldsymbol{\mathcal{L}}\left(\boldsymbol{d}^{\text{f}}|_{\partial\widehat{\Omega}}\right)$, where $\boldsymbol{\mathcal{L}}$ is a well chosen lifting operator from $\partial\widehat{\Omega}$ to $\widehat{\Omega}$. Moreover, the Lamé parameters of the elements of $\widehat{\Omega}$ are chosen such that the small elements are stiffer than the large ones [STB03, STB04] in order to

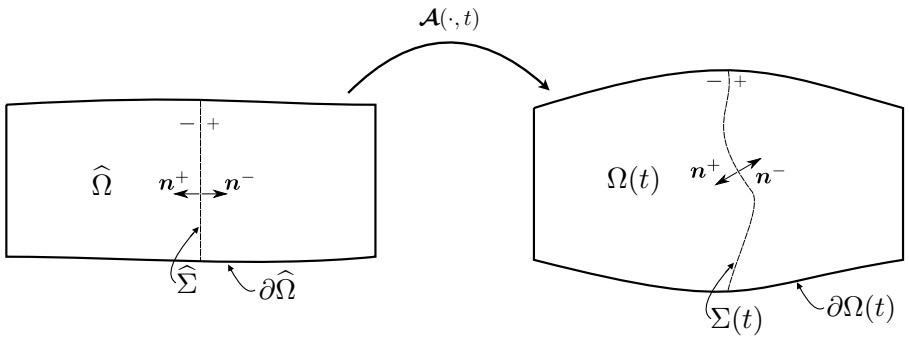

Figure 2.10 – Geometric description with a single valve and a moving domain.

prevent skewed elements. The fluid domain velocity $\boldsymbol{w}$ (i.e., the mesh velocity) is then simply defined from $\boldsymbol{d}^{\mathrm{f}}$ as $\boldsymbol{w} \overset{\text{def}}{=} \dfrac{\partial \boldsymbol{d}^{\mathrm{f}}}{\partial t}$ on Ω.

Using the ALE formulation and defining n individual immersed surfaces $\Sigma_{i=\{1\dots n\}}$ and $\dfrac{\partial \cdot}{\partial t}\Big|_{\boldsymbol{\mathcal{A}}}$ as the ALE time derivative, the RIS problem reads as follows: find the velocity $\boldsymbol{u} = \boldsymbol{u}(\boldsymbol{x},t) : \Omega \times \mathbb{R}^+ \to \mathbb{R}^3$ and the pressure $p = p(\boldsymbol{x},t) : \Omega \times \mathbb{R}^+ \to \mathbb{R}$, such that

$$\begin{cases} \rho^{\mathrm{f}} \left(\dfrac{\partial \boldsymbol{u}}{\partial t}\Big|_{\boldsymbol{\mathcal{A}}} + (\boldsymbol{u} - \boldsymbol{w}) \cdot \boldsymbol{\nabla} \boldsymbol{u} \right) - \boldsymbol{\nabla} \cdot \boldsymbol{\sigma}(\boldsymbol{u},p) + \displaystyle\sum_{i=\{1\dots n\}} \delta_{\Sigma_i} R_i \left(\boldsymbol{u} - \boldsymbol{w} \right) = \boldsymbol{f}^{\mathrm{f}} & \text{in} \quad \Omega, \\ \boldsymbol{\nabla} \cdot \boldsymbol{u} = 0 & \text{in} \quad \Omega, \end{cases} \tag{2.8}$$

where δ_{Σ_i} denotes the Dirac measure on the immersed surface Σ_i. As detailed in further Section 2.4.2, the additional term $\delta_{\Sigma_i} R_i \left(\boldsymbol{u} - \boldsymbol{w} \right)$ in (2.8) ensures the continuity of the velocity $\boldsymbol{u}$ on the moving immersed surface Σ_i and allows jump of the normal stress across it when $R_i \neq 0$. Finally, the system (2.8) has to be completed with initial conditions:

$$\boldsymbol{u}(0) = \boldsymbol{u}_0 \quad \text{in} \quad \Omega$$

and with boundary conditions on $\partial\Omega$. For instance, based on the type of boundary conditions that will be considered in Chapter 4 and based on Figure 2.10, let us consider three sub-parts $\partial\Omega_{\mathrm{N}_1}$, Ω_{N_2} and $\partial\Omega_{\mathrm{s}}$ which form a partition of $\partial\Omega$. A normal stress is applied on $\partial\Omega_{\mathrm{N}_1}$ and on $\partial\Omega_{\mathrm{N}_2}$ to impose the constant static pressures g_1 and g_2, respectively, while a no-slip Dirichlet boundary condition is ensured on $\partial\Omega_{\mathrm{s}}$, as detailed by the following system:

$$\begin{cases} \boldsymbol{\sigma}(\boldsymbol{u},p)\boldsymbol{n} = g_1 \boldsymbol{n} & \text{on} \quad \partial\Omega_{\mathrm{N}_1}, \\ \boldsymbol{\sigma}(\boldsymbol{u},p)\boldsymbol{n} = g_2 \boldsymbol{n} & \text{on} \quad \partial\Omega_{\mathrm{N}_2}, \\ \boldsymbol{u} = \boldsymbol{w} & \text{on} \quad \partial\Omega_{\mathrm{s}}. \end{cases} \tag{2.9}$$

2.4.2 Interface conditions

As pointed out in the original model [AHSG12], if one defines the velocity jump and the stress jump as

$$\begin{aligned} [\![\boldsymbol{u}]\!] &\overset{\text{def}}{=} \boldsymbol{u}^+ - \boldsymbol{u}^-, \\ [\![\boldsymbol{\sigma}(\boldsymbol{u},p)\boldsymbol{n}]\!] &\overset{\text{def}}{=} \boldsymbol{\sigma}(\boldsymbol{u}^-,p^-)\boldsymbol{n}^- + \boldsymbol{\sigma}(\boldsymbol{u}^+,p^+)\boldsymbol{n}^+, \end{aligned} \tag{2.10}$$

then problem (2.8) enforces the following interface conditions:

$$\begin{aligned} [\![\boldsymbol{u}]\!] &= \boldsymbol{0}, \\ [\![\boldsymbol{\sigma}(\boldsymbol{u},p)\boldsymbol{n}]\!] &= -R_i\,(\boldsymbol{u} - \boldsymbol{w}) \end{aligned} \tag{2.11}$$

on Σ_i for $i = \{1 \dots n\}$. Two asymptotic behaviors are then deduced: when R_i is large, $\boldsymbol{u} = \boldsymbol{w}$ is enforced on the moving surface Σ_i, whereas when R_i is close to 0, the flow does not 'see' Σ_i anymore and there is no pressure drop across it. When R_i is between these two extremes, Σ_i acts as a porous surface [FGM08, CFGM11] via the interface Robin condition $(2.11)_2$.

2.4.3 Choice of the resistive parameter

The status (open or closed) of each cardiac valve is fixed by the physics of the problem, and more specifically by the local values of the velocity and pressure fields near the immersed surfaces. When a valve is closed, it will open if there is a positive pressure jump across it. On the opposite, when a valve is open, it will close if there is a backflow detected through its corresponding open surface. The corresponding physical decision criteria are depicted in Figure 2.11. The value of the resistive parameter R_i of each immersed surface varies accordingly to the status of its corresponding valve: when a given valve is closed, the resistive parameter of its closed configuration is large and the one of its open configuration is null; this is the opposite when the valve is open.

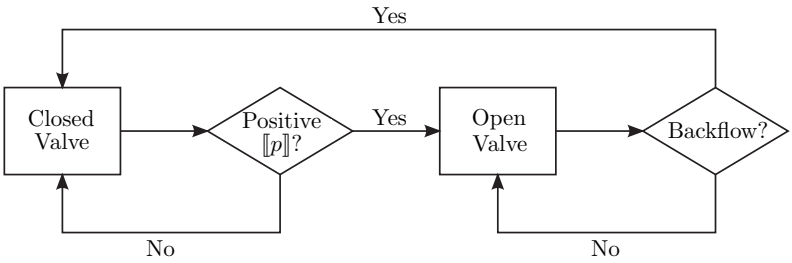

Figure 2.11 – Flow chart representation of the resistive immersed surfaces.

To conclude the presentation of the RIS model, we emphasize the fact that gradual opening and closing of the valve cannot be achieved with the above formulation because only the open and closed configurations of the immersed surfaces are considered. Recent work have introduced a reduced model that handles moving resistive immersed implicit

surfaces to correct this flaw (see, e.g., [FFDQ17]). Despite this improvement, the RIS model considered and used in the rest of this work will be the one introduced in Section 2.4.1.

Last, this formulation allows the simulation of blood flow patterns within the cardiac cavities at a reduced computational cost, but at the price of neglecting parts of the cardiac cycle, such as the isovolumetric phases (i.e., when all the valves of the ventricle are closed). Though short-lasting, these phases play a major role in the preservation of a correct unidirectional blood flow within the heart (see Section 1.3.1). Therefore, their correct computation is crucial for the physiological validity of the results. We will investigate this problem in Chapter 3.

2.5 Fluid-Structure Interactions method of cardiac valves

The numerical simulation of the mechanical interaction between elastic thin structures (i.e., cardiac valves) and an incompressible viscous fluid (i.e., blood) is an essential ingredient in the mathematical modeling of the left heart (as depicted previously in Figure 2.9). The earliest three-dimensional FSI models and simulations of cardiac valves date back to the first decade of the present century (see, e.g., [DPSB03, AGPT09, EKR+04, GLMP09]) and the topic has recently seen a surge of interest in the literature (see, e.g., [MGG+13, HKB+14, KHY+17]).

The purpose of this section is to provide a review of some of the state-of-the-art numerical techniques dedicated to the approximation of such FSI problems and to highlight their specificities and limitations. The key components of the FSI methods considered in the context of this thesis are then presented. Moreover, in all the above-mentioned references, computational cost is recognized as one of the major difficulties in the numerical simulation of such problems, related to the efficiency of the FSI coupling method and, when it is modeled, to the robustness of the contact algorithm (see, e.g., [KXL+18]). These points will be specifically addressed, respectively, in Sections 2.5.3.3 and 2.5.4.

We refer to [Ast10, Lan16] (and the references therein) for general introductions to fluid-structure interaction. Particularly, we refer to [FG09] for an extensive discussion on this topic and for the numerical treatment of the coupled problem. Finally, general reviews of various numerical methods and their associated coupling strategies can be found in [HWL12, Fer11a, vLAvdVS07].

2.5.1 Cardiac valves

In what follows, the choices made for the modeling of the cardiac valves are discussed in Section 2.5.1.1 before providing the resulting model of reference in Section 2.5.1.2.

2.5.1.1 Modeling choices

Numerous studies in the scientific literature are focused on the study of the mechanical properties of cardiac valves, indispensable prerequisite for being able to address their correct mathematical modeling. We mention some references (see, e.g., [YCS05, SB09]) for a general overview of the properties of the artificial valves, such as the ones described

in Section 1.5. For the native valves, described in Section 1.2.2.4, we recall that their structure is characterized by a fibrous tissue network, which is mainly made of collagen and elastin. In the past decade, models have been proposed to take into account these valve tissue characteristics (see, e.g., [WKM05]) but this refined level of description clearly outreaches the scope of this work. Therefore, we will describe the cardiac valves as general nonlinear elastic inert materials without taking into account their fibrous tissue network and associated properties.

Given the ratio thickness/size of their leaflets (see Section 1.2.2.4), an additional common assumption (see, e.g., [dSGB08, AGPT09, Ast10, KHS+15, Lan16]) is to model the cardiac valves as co-dimensional one structures (i.e., $(d-1)$-dimensional models where d is the dimension of the problem under analysis). These simplified (but still realistic) dimensionally reduced problems, that we refer to as thin-walled solid models, represent a fundamental key ingredient of the FSI numerical techniques presented later in Section 2.5.2 and considered in Chapters 5–7.

2.5.1.2 Non-linear Reissner-Mindlin beam model

We refer to Appendix C for the derivation of the thin-walled solid models in the linear framework.

The shear-membrane-bending model (which belongs to the family of the thin-walled solid models and whose derivation is also provided in Appendix C), extended to the non-linear framework, will be the model of reference for the description of the cardiac valves in the rest of this work. This model reads as follows: find the solid mid-surface displacement $\boldsymbol{d} : \Sigma \times \mathbb{R}^+ \to \mathbb{R}^d$, the solid mid-surface velocity $\dot{\boldsymbol{d}} : \Sigma \times \mathbb{R}^+ \to \mathbb{R}^d$ and the director vector $\boldsymbol{a} : \Sigma \times \mathbb{R}^+ \to \mathbb{R}^d$ with unit length, $|\boldsymbol{a}| = 1$, such that

$$\begin{cases} \rho^{\mathrm{s}} \epsilon \partial_t \dot{\boldsymbol{d}} + \boldsymbol{L_d}(\boldsymbol{d},\boldsymbol{a}) = \boldsymbol{T} & \text{on} \quad \Sigma, \\ \boldsymbol{L_a}(\boldsymbol{d},\boldsymbol{a}) = \boldsymbol{0} & \text{on} \quad \Sigma, \\ \dot{\boldsymbol{d}} = \partial_t \boldsymbol{d} & \text{on} \quad \Sigma, \end{cases} \tag{2.12}$$

where ρ^{s} and ϵ represent, respectively, the density of the solid and its thickness (assumed constant). $\boldsymbol{T}$ denotes a given source term (e.g., a force per unit area) and the surface operators $(\boldsymbol{L_d},\boldsymbol{L_a})$ represent the strong formulation of the thin-solid elastic contributions (we refer to Appendix C for their explicit treatment in the linear framework).

Finally, the above problem (2.12) has to be completed with initial conditions:

$$\begin{cases} \boldsymbol{d}(0) = \boldsymbol{d}_0 & \text{on} \quad \Sigma, \\ \dot{\boldsymbol{d}}(0) = \dot{\boldsymbol{d}}_0 & \text{on} \quad \Sigma, \\ \boldsymbol{a}(0) = \boldsymbol{a}_0 & \text{on} \quad \Sigma \end{cases} \tag{2.13}$$

and with boundary conditions (e.g., on $\boldsymbol{d}$ and/or on $\boldsymbol{a}$) on $\partial\Sigma$.

In the rest of this work, we will also refer to (2.12) as the non-linear Reissner-Mindlin beam model. The justification of this terminology is provided in Appendix C.

2.5.2 Fluid-structure coupled problem

We introduce a general FSI problem setting in Section 2.5.2.1 before presenting, in Section 2.5.2.2, the different mathematical models that will be considered through Chapters 5, 6 and 7.

2.5.2.1 Geometric configurations and notation

We consider a fluid-structure interaction problem coupling an incompressible viscous fluid (modeled by the incompressible Navier-Stokes equations (see Section 2.2.2.2) in the Eulerian or in the ALE formalisms) with an immersed thin-walled solid (modeled by a non-linear Reissner-Mindlin beam model (see Section 2.5.1.2) in Lagrangian form). Let $\Sigma \subset \mathbb{R}^d$, where $d = 2$ or 3, be the reference configuration of the solid mid-surface. In the context of a thin-walled solid model, Σ also corresponds to the fluid-structure interface. The current position of the interface, denoted by $\Sigma(t)$, is given in terms of the deformation map $\boldsymbol{\phi} : \Sigma \times \mathbb{R}^+ \to \mathbb{R}^d$ as $\Sigma(t) = \boldsymbol{\phi}(\Sigma,t)$, with $\boldsymbol{\phi} \overset{\text{def}}{=} \boldsymbol{I}_{\Sigma\times\mathbb{R}^+} + \boldsymbol{d}$, where $\boldsymbol{d}$ denotes the displacement of the solid. The structure is supposed to move within a fixed domain $\Omega \subset \mathbb{R}^d$ with boundary $\Gamma \overset{\text{def}}{=} \partial\Omega$. The fluid occupies the time-dependent domain $\Omega(t)$ defined as

$$\Omega(t) \overset{\text{def}}{=} \Omega \backslash \Sigma(t) \subset \mathbb{R}^d,$$

with its boundary being partitioned as $\partial\Omega(t) = \Sigma(t) \cup \Gamma$, as depicted in Figure 2.12.

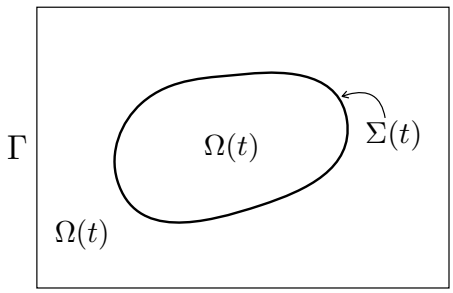

Figure 2.12 – The computational domain Ω.

The interface $\Sigma(t)$ is assumed to be oriented by a unit surface normal vector field denoted by $\boldsymbol{n}_\Sigma$. We can hence define positive and negative sides on $\Sigma(t)$, with respective unit normals $\boldsymbol{n}^+ \overset{\text{def}}{=} \boldsymbol{n}_\Sigma$ and $\boldsymbol{n}^- \overset{\text{def}}{=} -\boldsymbol{n}_\Sigma$. For a given continuous field f defined in Ω (possibly discontinuous across the interface), we define its sided–restrictions to $\Sigma(t)$, denoted by f^+ and f^-, as $f^+(\boldsymbol{x}) \overset{\text{def}}{=} \lim_{\xi\to 0^+} f(\boldsymbol{x} + \xi\boldsymbol{n}^+)$ and $f^-(\boldsymbol{x}) \overset{\text{def}}{=} \lim_{\xi\to 0^+} f(\boldsymbol{x} + \xi\boldsymbol{n}^-)$, for all $\boldsymbol{x} \in \Sigma(t)$. In addition, we also define the following jump and average operators across $\Sigma(t)$:

$$[\![f]\!] \overset{\text{def}}{=} f^+ - f^-, \quad [\![f\boldsymbol{n}]\!] \overset{\text{def}}{=} f^+\boldsymbol{n}^+ + f^-\boldsymbol{n}^-, \quad \{\!\{f\}\!\} \overset{\text{def}}{=} \frac{1}{2}(f^+ + f^-).$$

Finally, in order to ease the presentation, we introduce the notation $\boldsymbol{\phi}_t \overset{\text{def}}{=} \boldsymbol{\phi}(\cdot,t)$, for all field $\boldsymbol{\phi}$ defined in $\Omega \times \mathbb{R}^+$.

2.5.2.2 Coupled problem in different formalisms

In this section, three different formulations of the FSI problem are successively introduced: the Eulerian-Lagrangian, the ALE-Lagrangian and the mixed ALE-Eulerian-Lagrangian ones.

Eulerian-Lagrangian formulation of the coupled problem: Considering the Eulerian form of the Navier-Stokes equations (2.1), the first non-linear coupled problem considered reads as follows: find the fluid velocity and pressure $\boldsymbol{u} : \Omega \times \mathbb{R}^+ \to \mathbb{R}^d$, $p : \Omega \times \mathbb{R}^+ \to \mathbb{R}$, the solid displacement and velocity $\boldsymbol{d} : \Sigma \times \mathbb{R}^+ \to \mathbb{R}^d$, $\dot{\boldsymbol{d}} : \Sigma \times \mathbb{R}^+ \to \mathbb{R}^d$ and the unit director vector $\boldsymbol{a} : \Sigma \times \mathbb{R}^+ \to \mathbb{R}^d$ such that

$$\begin{cases} \rho^{\mathrm{f}} \partial_t \boldsymbol{u} + \rho^{\mathrm{f}} \boldsymbol{u} \cdot \boldsymbol{\nabla} \boldsymbol{u} - \boldsymbol{\nabla} \cdot \boldsymbol{\sigma}(\boldsymbol{u},p) = \boldsymbol{0} & \text{in} \quad \Omega(t), \\ \boldsymbol{\nabla} \cdot \boldsymbol{u} = 0 & \text{in} \quad \Omega(t), \\ \boldsymbol{u} = \boldsymbol{0} & \text{on} \quad \Gamma, \end{cases} \tag{2.14}$$

$$\begin{cases} \rho^{\mathrm{s}} \epsilon \partial_t \dot{\boldsymbol{d}} + \boldsymbol{L_d}(\boldsymbol{d},\boldsymbol{a}) = \boldsymbol{T} & \text{on} \quad \Sigma, \\ \boldsymbol{L_a}(\boldsymbol{d},\boldsymbol{a}) = \boldsymbol{0} & \text{on} \quad \Sigma, \\ \dot{\boldsymbol{d}} = \partial_t \boldsymbol{d} & \text{on} \quad \Sigma, \end{cases} \tag{2.15}$$

$$\begin{cases} \boldsymbol{\phi} = \boldsymbol{I}_{\Sigma \times \mathbb{R}^+} + \boldsymbol{d}, \quad \Sigma(t) = \boldsymbol{\phi}(\Sigma,t), \quad \Omega(t) = \Omega \backslash \Sigma(t), \\ \boldsymbol{u} = \dot{\boldsymbol{d}} \circ \boldsymbol{\phi}_t^{-1} \quad \text{on} \quad \Sigma(t), \\ \displaystyle\int_\Sigma \boldsymbol{T} \cdot \boldsymbol{y} = - \int_{\Sigma(t)} [\![\boldsymbol{\sigma}(\boldsymbol{u},p) \boldsymbol{n}]\!] \cdot \boldsymbol{y} \circ \boldsymbol{\phi}_t^{-1}, \end{cases} \tag{2.16}$$

for all smooth test function $\boldsymbol{y} : \Sigma \to \mathbb{R}^d$. The above problem has to be completed with initial conditions:

$$\begin{cases} \boldsymbol{u}(0) = \boldsymbol{u}_0 & \text{on} \quad \Omega(0), \\ \boldsymbol{d}(0) = \boldsymbol{d}_0 & \text{on} \quad \Sigma, \\ \dot{\boldsymbol{d}}(0) = \dot{\boldsymbol{d}}_0 & \text{on} \quad \Sigma, \\ \boldsymbol{a}(0) = \boldsymbol{a}_0 & \text{on} \quad \Sigma \end{cases} \tag{2.17}$$

and with boundary conditions on Γ and $\partial\Sigma$.

The three lines in (2.16) enforce, respectively, the geometric, the kinematic and the dynamic interface coupling. $(2.16)_1$ represents the fact that the fluid control volume $\Omega(t)$ follows the motion of the interface $\Sigma(t)$. $(2.16)_2$ ensures the continuity of the velocity at the interface $\Sigma(t)$ (as the fluid sticks to it due to its viscosity) and $(2.16)_3$ represents the balance of stresses at the interface $\Sigma(t)$ (also known as Newton's third law).

Remark 2.2

As denoted in Section 2.5.2.1, the solid mid-surface Σ is fully identified with the fluid-structure interface, (i.e., the beam thickness effects are neglected in the interface coupling). This is a commonly used simplification when coupling thin-walled media (see, e.g., [CF03]).

Remark 2.3
The coupled problem (2.14)–(2.16) has an inherent mixed Eulerian-Lagrangian nature, which is a direct consequence of the presence of the maps $\boldsymbol{\phi}_t$ and $\boldsymbol{\phi}_t^{-1}$ in the interface coupling (2.16). This introduces additional (geometrical) non-linearities.

ALE-Lagrangian formulation of the coupled problem: We first recall some notations coming from Section 2.2.2.2. The moving control volume $\Omega(t)$ is assumed to be parametrizable as $\Omega(t) = \boldsymbol{\mathcal{A}}(\widehat{\Omega},t)$, where $\boldsymbol{\mathcal{A}} : \widehat{\Omega} \times \mathbb{R}^+ \to \mathbb{R}^d$ is a one-to-one mapping given by the relation $\boldsymbol{\mathcal{A}} = \boldsymbol{I}_{\widehat{\Omega}\times\mathbb{R}^+} + \boldsymbol{d}^{\mathrm{f}}$, in terms of the fluid domain displacement $\boldsymbol{d}^{\mathrm{f}}$ (see Figure 2.13).

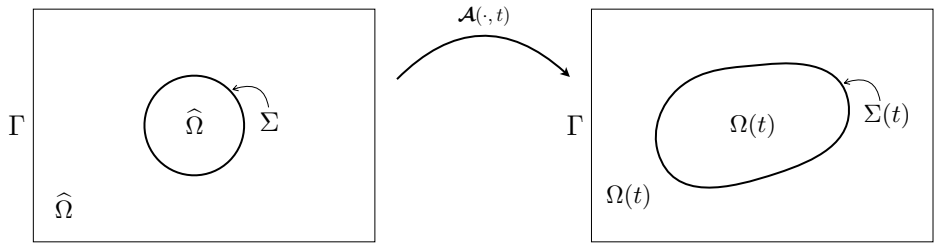

Figure 2.13 – Definition of the ALE map in the ALE-Lagrangian formulation.

The geometrical compatibility between the fluid and solid domains can hence be guaranteed through a relation of the type $\boldsymbol{d}^{\mathrm{f}} = \boldsymbol{\mathcal{L}}(\boldsymbol{d})$, where $\boldsymbol{\mathcal{L}}(\boldsymbol{d})$ represents a suitable lifting of $\boldsymbol{d}$ from Σ to $\widehat{\Omega}$ which vanishes on Γ. Note that $\boldsymbol{d}^{\mathrm{f}}$ can be arbitrarily defined in $\widehat{\Omega}\backslash\Sigma$. We also recall that by a simple use of the chain rule (see Section 2.2.2.2), we have the following relation:

$$\partial_t \boldsymbol{u} = \partial_t|_{\boldsymbol{\mathcal{A}}} \boldsymbol{u} - \boldsymbol{w} \cdot \boldsymbol{\nabla} \boldsymbol{u}, \tag{2.18}$$

where $\partial_t \cdot |_{\boldsymbol{\mathcal{A}}}$ denotes the ALE time derivative and $\boldsymbol{w} \overset{\text{def}}{=} \partial_t \boldsymbol{d}^{\mathrm{f}}$ the fluid domain velocity.

Using the above relations and considering the ALE form of the Navier-Stokes equations (2.7), the second non-linear coupled problem considered reads as follows: find the fluid domain displacement $\boldsymbol{d}^{\mathrm{f}} : \widehat{\Omega} \times \mathbb{R}^+ \to \mathbb{R}^d$, the fluid velocity $\widehat{\boldsymbol{u}} : \widehat{\Omega} \times \mathbb{R}^+ \to \mathbb{R}^d$, the fluid pressure $\widehat{p} : \widehat{\Omega} \times \mathbb{R}^+ \to \mathbb{R}$, the solid mid-surface displacement $\boldsymbol{d} : \Sigma \times \mathbb{R}^+ \to \mathbb{R}^d$, the solid mid-surface velocity $\dot{\boldsymbol{d}} : \Sigma \times \mathbb{R}^+ \to \mathbb{R}^d$ and the unit director vector $\boldsymbol{a} : \Sigma \times \mathbb{R}^+ \to \mathbb{R}^d$, such

that

$$\begin{cases} \rho^{\mathrm{f}}\partial_t|_{\boldsymbol{\mathcal{A}}}\boldsymbol{u} + \rho^{\mathrm{f}}(\boldsymbol{u}-\boldsymbol{w})\cdot\boldsymbol{\nabla}\boldsymbol{u} - \boldsymbol{\nabla}\cdot\boldsymbol{\sigma}(\boldsymbol{u},p) = \boldsymbol{0} & \text{in} \quad \Omega(t), \\ \boldsymbol{\nabla}\cdot\boldsymbol{u} = 0 & \text{in} \quad \Omega(t), \\ \boldsymbol{u} = \boldsymbol{0} & \text{on} \quad \Gamma, \end{cases} \tag{2.19}$$

$$\begin{cases} \rho^{\mathrm{s}}\epsilon\partial_t\dot{\boldsymbol{d}} + \boldsymbol{L_d}(\boldsymbol{d},\boldsymbol{a}) = \boldsymbol{T} & \text{on} \quad \Sigma, \\ \boldsymbol{L_a}(\boldsymbol{d},\boldsymbol{a}) = \boldsymbol{0} & \text{on} \quad \Sigma, \\ \dot{\boldsymbol{d}} = \partial_t\boldsymbol{d} & \text{on} \quad \Sigma, \end{cases} \tag{2.20}$$

$$\begin{cases} \boldsymbol{d}^{\mathrm{f}} = \boldsymbol{\mathcal{L}}(\boldsymbol{d}), \quad \boldsymbol{w} = \partial_t\boldsymbol{d}^{\mathrm{f}}, \quad \boldsymbol{\mathcal{A}} = \boldsymbol{I}_{\widehat{\Omega}\times\mathbb{R}^+} + \boldsymbol{d}^{\mathrm{f}}, \quad \Omega(t) = \boldsymbol{\mathcal{A}}(\widehat{\Omega},t), \\ \boldsymbol{\phi} = \boldsymbol{I}_{\Sigma\times\mathbb{R}^+} + \boldsymbol{d}, \quad \Sigma(t) = \boldsymbol{\phi}(\Sigma,t), \\ \boldsymbol{u} = \dot{\boldsymbol{d}}\circ\boldsymbol{\phi}_t^{-1} = \dot{\boldsymbol{d}}\circ\boldsymbol{\mathcal{A}}_t^{-1} \quad \text{on} \quad \Sigma(t), \\ \displaystyle\int_\Sigma \boldsymbol{T}\cdot\boldsymbol{y} = -\int_{\Sigma(t)}[\![\boldsymbol{\sigma}(\boldsymbol{u},p)\boldsymbol{n}]\!]\cdot\boldsymbol{y}\circ\boldsymbol{\phi}_t^{-1} = -\int_{\Sigma(t)}[\![\boldsymbol{\sigma}(\boldsymbol{u},p)\boldsymbol{n}]\!]\cdot\boldsymbol{y}\circ\boldsymbol{\mathcal{A}}_t^{-1}, \end{cases} \tag{2.21}$$

for all smooth function $\boldsymbol{y}:\Sigma\to\mathbb{R}^d$. The above problem has to be completed with initial conditions similar to (2.17) and with boundary conditions on Γ and $\partial\Sigma$.

Similarly to what has been emphasized for (2.16), the two lines $(2.21)_1$ and $(2.21)_2$ enforce the geometric interface coupling. $(2.21)_3$ and $(2.21)_4$ enforce, respectively, the kinematic and the dynamic interface coupling.

Remark 2.4

The fundamental relation which justifies the terminology "ALE-Lagrangian" used in this formulation is the following:

$$\boldsymbol{\mathcal{A}}_t^{-1} = \boldsymbol{\phi}_t^{-1} \quad \text{on} \quad \Sigma(t). \tag{2.22}$$

Physically speaking, (2.22) represents the fact that $\boldsymbol{d}^{\mathrm{f}}$ is dictated by the distortion of the structure: $\boldsymbol{d}^{\mathrm{f}}$ does match with $\boldsymbol{d}$ on $\Sigma(t)$.

Mixed ALE-Eulerian-Lagrangian formulation of the coupled problem: We now consider a mixed ALE-Eulerian-Lagrangian formulation of the coupled problem. The two main differences with the previous formulations is that (i) a given displacement field $\boldsymbol{d}_{\mathbf{w}}$ is now applied on a sub-part $\Sigma_{\mathrm{wall}}(t)$ of the fluid boundary defined as $\Sigma_{\mathrm{wall}}(t) = \partial\Omega(t)\backslash\Gamma$ (see Figure 2.14) and (ii) the domain $\Omega(t)$ is obtained thanks to a map $\boldsymbol{\mathcal{A}}$ which is independent of the displacement $\boldsymbol{d}$ of the structure.

The moving control volume $\Omega(t)$ is still assumed to be parametrizable as $\Omega(t) = \boldsymbol{\mathcal{A}}(\widehat{\Omega},t)$, where $\boldsymbol{\mathcal{A}}:\widehat{\Omega}\times\mathbb{R}^+\to\mathbb{R}^d$ is a one-to-one mapping given by the relation $\boldsymbol{\mathcal{A}} = \boldsymbol{I}_{\widehat{\Omega}\times\mathbb{R}^+} + \boldsymbol{d}^{\mathrm{f}}$, in terms of the fluid domain displacement $\boldsymbol{d}^{\mathrm{f}}$. $\boldsymbol{d}^{\mathrm{f}}$ is obtained through a relation of the type $\boldsymbol{d}^{\mathrm{f}} = \boldsymbol{\mathcal{L}}_{\mathrm{wall}}(\boldsymbol{d}_{\mathbf{w}})$, where $\boldsymbol{\mathcal{L}}_{\mathrm{wall}}(\boldsymbol{d}_{\mathbf{w}})$ represents a suitable lifting of $\boldsymbol{d}_{\mathbf{w}}$ from Σ_{wall} to $\widehat{\Omega}$ which vanishes on Γ. Note that $\boldsymbol{d}^{\mathrm{f}}$ can be arbitrarily defined in $\widehat{\Omega}\backslash\Sigma_{\mathrm{wall}}$ and does not depend on $\boldsymbol{d}$.

Using the above relations and considering the ALE form of the Navier-Stokes equations (2.7), the third non-linear coupled problem considered reads as follows: find the fluid domain displacement $\boldsymbol{d}^{\mathrm{f}}:\widehat{\Omega}\times\mathbb{R}^+\to\mathbb{R}^d$, the fluid velocity $\widehat{\boldsymbol{u}}:\widehat{\Omega}\times\mathbb{R}^+\to\mathbb{R}^d$, the fluid

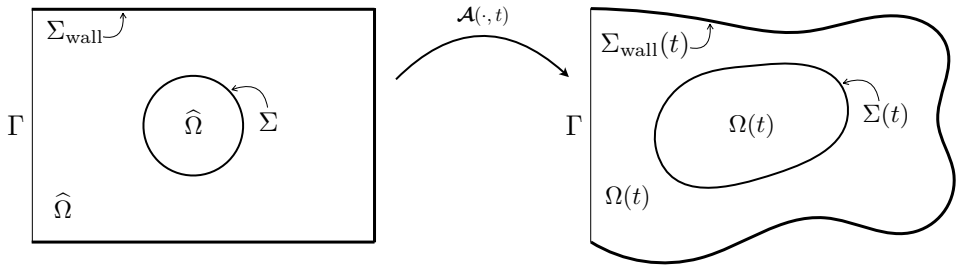

Figure 2.14 – Definition of the ALE map in the mixed ALE-Eulerian-Lagrangian formulation.

pressure $\widehat{p} : \widehat{\Omega} \times \mathbb{R}^+ \to \mathbb{R}$, the solid mid-surface displacement $\boldsymbol{d} : \Sigma \times \mathbb{R}^+ \to \mathbb{R}^d$, the solid mid-surface velocity $\dot{\boldsymbol{d}} : \Sigma \times \mathbb{R}^+ \to \mathbb{R}^d$ and the unit director vector $\boldsymbol{a} : \Sigma \times \mathbb{R}^+ \to \mathbb{R}^d$, such that

$$\begin{cases} \rho^{\mathrm{f}} \partial_t|_{\boldsymbol{\mathcal{A}}} \boldsymbol{u} + \rho^{\mathrm{f}} (\boldsymbol{u} - \boldsymbol{w}) \cdot \boldsymbol{\nabla} \boldsymbol{u} - \boldsymbol{\nabla} \cdot \boldsymbol{\sigma}(\boldsymbol{u},p) = \boldsymbol{0} & \text{in} \quad \Omega(t), \\ \boldsymbol{\nabla} \cdot \boldsymbol{u} = 0 & \text{in} \quad \Omega(t), \\ \boldsymbol{u} = \boldsymbol{0} & \text{on} \quad \Gamma, \\ \boldsymbol{u} = \boldsymbol{w} & \text{on} \quad \Sigma_{\text{wall}}(t), \end{cases} \tag{2.23}$$

$$\begin{cases} \rho^{\mathrm{s}} \epsilon \partial_t \dot{\boldsymbol{d}} + \boldsymbol{L}_{\boldsymbol{d}}(\boldsymbol{d},\boldsymbol{a}) = \boldsymbol{T} & \text{on} \quad \Sigma, \\ \boldsymbol{L}_{\boldsymbol{a}}(\boldsymbol{d},\boldsymbol{a}) = \boldsymbol{0} & \text{on} \quad \Sigma, \\ \dot{\boldsymbol{d}} = \partial_t \boldsymbol{d} & \text{on} \quad \Sigma, \end{cases} \tag{2.24}$$

$$\begin{cases} \boldsymbol{d}^{\mathrm{f}} = \boldsymbol{\mathcal{L}}_{\text{wall}}(\boldsymbol{d}_{\mathbf{w}}), \quad \boldsymbol{w} = \partial_t \boldsymbol{d}^{\mathrm{f}}, \quad \boldsymbol{\mathcal{A}} = \boldsymbol{I}_{\widehat{\Omega} \times \mathbb{R}^+} + \boldsymbol{d}^{\mathrm{f}}, \quad \Omega(t) = \boldsymbol{\mathcal{A}}(\widehat{\Omega},t) \backslash \Sigma(t), \\ \boldsymbol{\psi} = \boldsymbol{I}_{\Sigma_{\text{wall}} \times \mathbb{R}^+} + \boldsymbol{d}_{\mathbf{w}}, \quad \Sigma_{\text{wall}}(t) = \boldsymbol{\psi}(\Sigma_{\text{wall}},t), \\ \boldsymbol{\phi} = \boldsymbol{I}_{\Sigma \times \mathbb{R}^+} + \boldsymbol{d}, \quad \Sigma(t) = \boldsymbol{\phi}(\Sigma,t), \\ \boldsymbol{u} = \dot{\boldsymbol{d}} \circ \boldsymbol{\phi}_t^{-1} \quad \text{on} \quad \Sigma(t), \\ \displaystyle\int_{\Sigma} \boldsymbol{T} \cdot \boldsymbol{y} = - \int_{\Sigma(t)} [\![\boldsymbol{\sigma}(\boldsymbol{u},p) \boldsymbol{n}]\!] \cdot \boldsymbol{y} \circ \boldsymbol{\phi}_t^{-1}, \end{cases} \tag{2.25}$$

for all smooth function $\boldsymbol{y} : \Sigma \to \mathbb{R}^d$. The above problem has to be completed with initial conditions similar to (2.17) and with boundary conditions on Γ and $\partial\Sigma$.

Similarly to what has been emphasized for (2.16), the three lines $(2.25)_1$, $(2.25)_2$ and $(2.25)_3$ enforce the geometric interface coupling. $(2.25)_4$ and $(2.25)_5$ enforce, respectively, the kinematic and the dynamic interface coupling.

Remark 2.5

The fundamental relations which justify the terminology "mixed ALE-Eulerian-Lagrangian"

used in this formulation are the following:

$$\begin{aligned} \boldsymbol{\mathcal{A}}_t^{-1} &\neq \boldsymbol{\phi}_t^{-1} \qquad \text{on} \quad \Sigma(t), \\ \boldsymbol{\mathcal{A}}_t^{-1} &= \boldsymbol{\psi}_t^{-1} \qquad \text{on} \quad \Sigma_{wall}(t). \end{aligned} \tag{2.26}$$

Physically speaking and contrary to (2.22), $(2.26)_1$ *and* $(2.26)_2$ *represent the fact that* $\boldsymbol{d}^{\mathrm{f}}$ *is no more dictated by the distortion of the structure but now by the given distortion of the fluid boundary* $\Sigma_{wall}(t)$*:* $\boldsymbol{d}^{\mathrm{f}}$ *does not match with* $\boldsymbol{d}$ *on* $\Sigma(t)$ *but does match with* $\boldsymbol{d}_{\mathbf{w}}$ *on* $\Sigma_{wall}(t)$*.*

2.5.2.3 Energy balance

From the energetic point of view, we define the system mechanical energy $E(t)$ as

$$E(t) \stackrel{\text{def}}{=} \int_{\Omega(t)} \frac{\rho^{\mathrm{f}}}{2}|\boldsymbol{u}|^2 + \int_{\Sigma} \frac{\rho^{\mathrm{s}}\epsilon}{2}|\dot{\boldsymbol{d}}|^2 + \int_{\Sigma} \frac{1}{2}|\boldsymbol{d}|^2,$$

for all $t \in \mathbb{R}^+$. The first two terms account for the kinetic energy whereas the last one stands for the elastic potential energy. For the three coupled systems (2.14)–(2.16), (2.19)–(2.21) and (2.23)–(2.25), the following proposition holds:

Proposition 2.1
Assuming that the system is isolated, then the following energy inequality holds:

$$E(t) \leq E(0). \tag{2.27}$$

Proof. We refer to [FG09] for the proof of the energy balance (2.27) in the ALE-Lagrangian case. □

2.5.3 Numerical methods

In what follows, various available numerical techniques for this type of coupled problems are reviewed according to two classification criteria: the spatial discretization of the FSI problem (see Section 2.5.3.1) and the nature of the splitting between the fluid and the structure solvers (see Sections 2.5.3.2 and 2.5.3.3).

2.5.3.1 Spatial discretization

The spatial discretization of FSI problems generally depends on the amount of solid displacement within the fluid. Problems featuring moderate interface displacements can be successfully simulated using (moving) fitted meshes with an ALE description of the fluid which follows the motion of the interface (see Figure 2.15). The fact that the fluid and solid meshes fit at their interface guarantees the accurate computation of the transmission conditions. In particular, the discontinuous features of the fluid pressure solution can be straightforwardly incorporated within this framework by duplicating the pressure degrees of freedom at the interface.

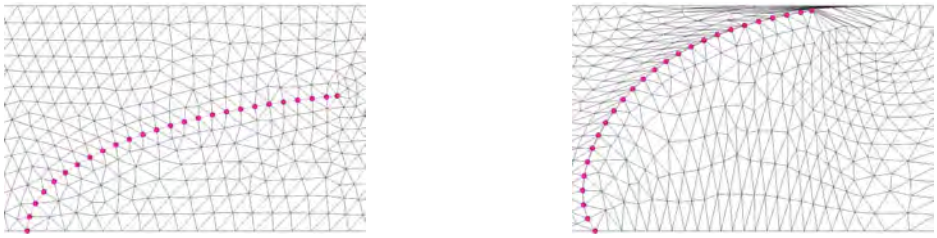

(a) Initial configuration. (b) Displaced configuration.

Figure 2.15 – Illustration of fitted fluid and solid meshes.

Nevertheless, for problems involving large structural deflections with solids that might come into contact (where blood-cardiac valve interaction clearly represents a possible application), the ALE formalism becomes cumbersome (see, e.g., the resulting skewed fluid elements when contact occurs in Figure 2.16b). A preferred approach in this case is to combine an Eulerian formalism in the fluid with an unfitted mesh discretization, in which the fluid-structure interface deforms independently of a background fluid mesh (see Figure 2.16). Among these approaches, we can mention the Immersed Boundary (IB) (see, e.g., [Pes02, BCG11]) and the FD methods (see, e.g., [GPHJ99, Baa01, DPSB03, AGPT09, BCG15, BG17]), which keep a Lagrangian formalism for the solid, and the methodologies based on a fully Eulerian formalism for the fluid (see, e.g., [CMM08, Ric13]).

(a) Initial configuration. (b) Displaced configuration.

Figure 2.16 – Illustration of unfitted fluid and solid meshes.

In general, these unfitted mesh approaches are known to be inaccurate in space, because the discrete treatment of the interface conditions and/or the fluid spatial discretization do/does not allow for discrete discontinuities across the interface, which often yields severe mass loss across the interface. Mesh adaptation can alleviate these issues (e.g., [HFCC13]) but does not cure the problem. The eXtended Finite Element Method (XFEM), which combines a cut-FEM methodology with a local enrichment (see, e.g., [ZL08, GW08, ST11]), overcomes these issues but at the price of introducing additional unknowns (Lagrange multipliers) and a degradation of robustness (with respect to the interface cuts). These difficulties have been recently circumvented by the Nitsche-XFEM method reported in [AFFL16, BF14]. The superior accuracy properties of cut-FEM approaches comes at a price: these methods demand a much more involved computer implementation and require a specific evaluation of the interface intersections (see, e.g., [AFFL16]). In Chapter 5, we will compare the above-mentioned fitted and unfitted meshes methods on a benchmark of 2D numerical examples in order to assess their respective accuracy. The objective is to illustrate and to

discuss the advantages and limitations of each method.

2.5.3.2 Coupling approaches

The content of this section is inspired from [Lan16].

At the discrete level, the above-mentioned numerical methods must satisfy the different transmission conditions (see (2.16), (2.21) or (2.25) depending on the considered formulation), made of the kinematic and dynamic coupling conditions and of the geometrical compatibility between the fluid and solid computational domains. A straightforward way to satisfy them is to simultaneously solve the fluid and the structure subproblems in an unified mathematical framework. This is the monolithic approach (see, e.g., [BQQ08a, RW10, GKW11, CDFQ11, MMH12]), depicted in Figure 2.17.

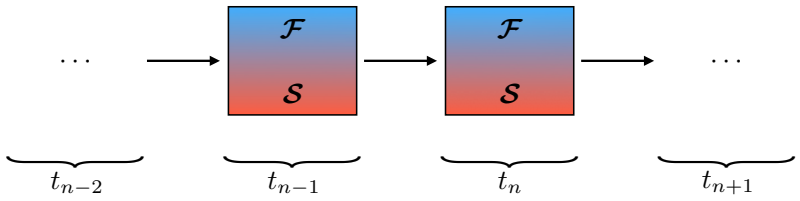

Figure 2.17 – Illustration of the monolithic approach. The fluid $\mathcal{F}$ and the solid $\mathcal{S}$ subproblems are simultaneously solved, in a single block, at a given time-step before proceeding to the next one.

A monolithic method can deliver unconditional stability and optimal accuracy [FG09], but at the price of solving a computationally demanding coupled problem at each time-step. Moreover, this approach results in a global solver which is not easily adaptable. In particular, designing efficient global preconditioners and maintaining state-of-the-art numerical techniques in each of its subproblems becomes quickly cumbersome.

Therefore, a common alternative is to consider two distinct fluid and structure subproblems which are separately solved with their respective mesh and numerical techniques. This is the partitioned approach (see, e.g., [FM05, BNV08, DBHV08, Van11, BK12, NPV13]), depicted in Figure 2.18.

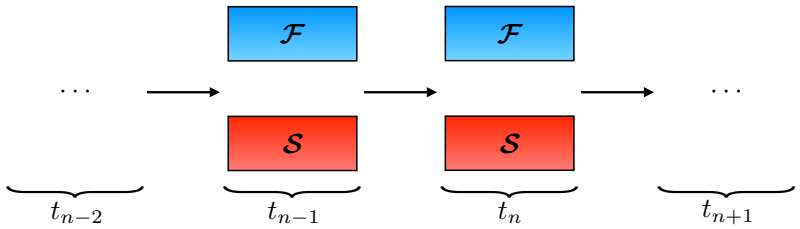

Figure 2.18 – Illustration of the partitioned approach. The fluid $\mathcal{F}$ and the solid $\mathcal{S}$ subproblems are separately solved, in two distinct blocks, at a given time-step before proceeding to the next one.

A partitioned method represents an attractive solution because, within this approach, independent efficient solvers can be easily maintained and coupled together. Nevertheless, from the computational point of view, this modularity does not always mean superior efficiency over the monolithic approach (see, e.g., [BQQ08a, GKW11]). Another major difference between the two above-mentioned approaches concerns the interfacial conditions. In the monolithic approach, the interfacial data is exchanged between homogeneous subproblems coexisting in a single block. In the partitioned approach, this data must be adapted to the heterogeneous nature of the subproblems.

In the rest of this work, we will only consider partitioned procedures, simpler to handle thanks to their versatility.

2.5.3.3 Coupling schemes within the partitioned approach

The way the kinematic-dynamic coupling is enforced between the fluid and solid subsystems determines the so-called coupling scheme: implicit or explicit, as detailed in the following. In Chapter 6, we will provide some examples of such coupling schemes and discuss them in the context of the FD method.

Remark 2.6
No particular treatment of the geometric compatibility condition has been specified so far. In this thesis, this condition will always be treated in an explicit fashion. Therefore, the term "implicit", used in the following, refers to the implicit treatment of the kinematic-dynamic coupling and to the explicit treatment of the geometric coupling.

Implicit coupling: This type of coupling is characterized by the *existence* of inner iterations between the fluid and the solid subproblems at each time-step. Its corresponding workflow is depicted in Figure 2.19.

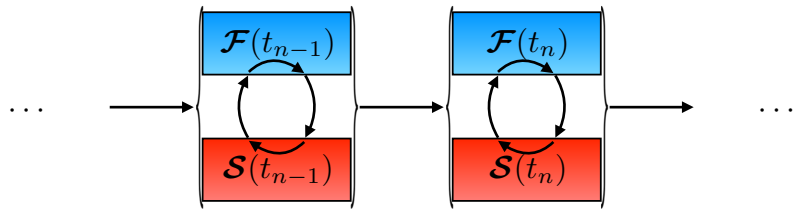

Figure 2.19 – Illustration of the implicit coupling for the partitioned approach. $\mathcal{F}$ and $\mathcal{S}$ represent, respectively, the fluid and the solid subproblems. The arrows in oval shape represent the inners iterations between $\mathcal{F}$ and $\mathcal{S}$ at each time-step. A tolerance parameter (not specified here) controls the number of computed inner iterations before proceeding to the next time-step.

Performing inner iterations at each time-step allows to enforce the transmission conditions with high accuracy [FG09]. Therefore, this type of method is also said to be "strongly coupled".

Explicit coupling: This type of coupling is characterized by the *absence* of inner iterations between the fluid and the solid subproblems at each time-step, contrary to the implicit coupling. Its corresponding workflow is depicted in Figure 2.20.

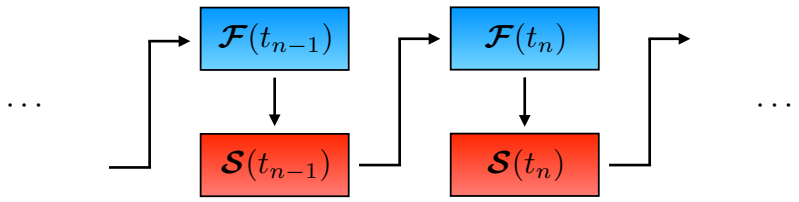

Figure 2.20 – Illustration of the explicit coupling for the partitioned approach. $\mathcal{F}$ and $\mathcal{S}$ represent, respectively, the fluid and the solid subproblems. At a given instant, each subproblem is called only once in a fixed sequential order ($\mathcal{F}$ then $\mathcal{S}$) before proceeding to the next time-step.

The absence of inner iterations at each time-step allows a cheaper approach in terms of computational time, which is particularly interesting for the 3D cardiac hemodynamics simulations investigated in the scope of this work. Nevertheless, the price to pay is that the coupling conditions are no more exactly enforced but now simply approached, resulting in a degradation of accuracy [FG09]. Therefore, this type of coupling is also said to be "weakly coupled".

Another major drawback of this type of explicit scheme is that numerical instabilities are observed in the context of the simulation of cardiac hemodynamics. The origin of these instabilities can be explained by an effect called the added-mass effect [CGN05, FWR07], characterized by the value of the density ratio $\frac{\rho^{\mathrm{s}}}{\rho^{\mathrm{f}}}$. It has been proved in [CGN05] that, for a given geometry, numerical instabilities can be experienced in loosely coupled partitioned algorithms as soon as this ratio is lower than a certain threshold, which is always the case for blood and cardiac valves [CGN05, FWR07, vB09, Ast10].

Over the last decade, significant advances have been achieved in the development and in the analysis of fluid-solid splitting schemes that avoid strong coupling, without compromising stability and accuracy. In the majority of these studies, the spatial discretization is based on body fitted fluid meshes (see, e.g., [FGG07, QQ07, BQQ08b, BF09, GGCC09, BCG+13, Fer13, FMV13, BHS14, FMV15, FLV15, LVCF17]) which makes it become cumbersome or unfeasible in the presence of large interface deflections or of topological changes (e.g., due to contact between solids). In this case, the alternative is to consider an unfitted mesh formulation, in which the fluid mesh is independent of the solid mesh (see, e.g., [Pes02, LCB06, ZL08, GW08, ST11, dSGB08, AGPT09, BCG11, BF14, KHS+15, BCG15, AFFL16, KDP18]). Within the unfitted mesh framework, splitting schemes which avoid strong coupling are rare in the literature. In fact, we are only aware of the methods reported in [BCG11, Ann17, KLC18], using immersed boundary or fictitious domain methods, and in [BF14, AFFL16, KDP18], using unfitted Nitsche based methods with cut-elements. The fundamental drawback of explicit coupling schemes, reported in [BCG11, BF14, KDP18, KLC18], is that their stability/accuracy demands severe time-step restrictions or is limited by the amount of added-mass effect.

These issues have been recently circumvented in [AFFL16, Ann17], by borrowing the ideas of [Fer13, FMV13] where explicit Robin-Neumann schemes are proposed, but at the price of compromising the explicit nature of the coupling scheme. Indeed, the resulting methods are only semi-implicit (see also [FL15]).

Semi-implicit coupling: The type of semi-implicit coupling considered here consists in a fractional-step time-marching in the structure: the contribution of the structure inertial effects are coupled with the fluid in an implicit way whereas the contribution of the structure elastic effects are coupled with the fluid in an explicit way. Its corresponding workflow is depicted in Figure 2.21. Other types of fractional-step time-marching exist in the literature (see, e.g., [GGCC09, Fer11b, BCG+13, LMRHZ13]).

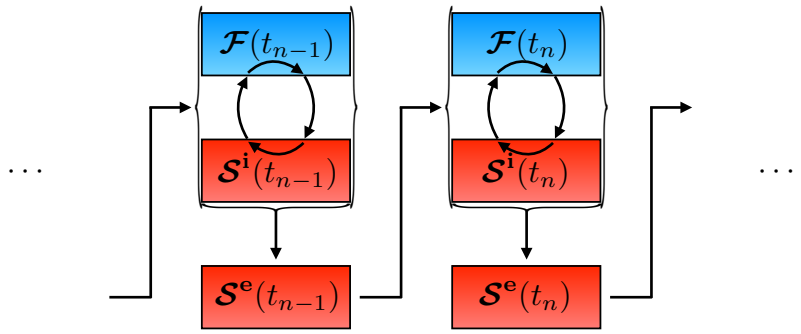

Figure 2.21 – Illustration of the semi-implicit coupling for the partitioned approach. $\mathcal{F}$, $\mathcal{S}^{\mathbf{i}}$ and $\mathcal{S}^{\mathbf{e}}$ represent, respectively, the fluid, the solid inertia and the solid elasticity subproblems. The arrows in oval shape represent the inners iterations between $\mathcal{F}$ and $\mathcal{S}^{\mathbf{i}}$ at each time-step. A tolerance parameter (not specified here) controls the number of computed inner iterations before proceeding to the explicit coupling with $\mathcal{S}^{\mathbf{e}}$. Finally, after one call of $\mathcal{S}^{\mathbf{e}}$, we proceed to the next time-step.

This semi-implicit coupling, enforcing a specific implicit/explicit treatment of the transmissions conditions, represents a stable and less computationally onerous alternative to classical strong coupling approaches [Fer13]. In particular, the implicit part of the coupling guarantees stability, while the explicit one reduces computational complexity.

In Chapter 6, we will introduce and analyze a new explicit coupling scheme for FD approximations of FSI problems in cardiac hemodynamics with immersed thin-walled structures, obtained starting from this semi-implicit coupling scheme and which overcomes the above-mentioned stability and accuracy issues. The definitions of $\mathcal{S}^{\mathbf{i}}$ and $\mathcal{S}^{\mathbf{e}}$ will also be specified.

2.5.4 Contact modeling

As detailed in Section 1.2.2.4, the main function of cardiac valves is to open and close in order to regulate intracardiac blood flow. Therefore, the contact between their leaflets must be necessary taken into account in the FSI models in order to compute physiological numerical simulations. Despite its crucial importance, studies addressing it are still

very preliminary (see, e.g., [vLAvdV06, AGPT09, MPGW10, KXL+18]), highlighting the complexity of this singular problem.

The purpose of this section is to introduce the way the contact is handled in this work. In Section 2.5.4.1, we present the fundamental considered approach for modeling the contact before providing an overview of its numerical implementation in Sections 2.5.4.2 and 2.5.4.3.

In what follows, the contact is assumed to be frictionless and soft, characterized by the fact that only displacements in the normal direction are constrained. Other approaches for the approximation of the contact exist in the literature (see, e.g., [SDL13] for a surface potential framework and [KXL+18] for a repulsive volumetric potential framework) but will not be addressed here. Moreover, no additional forces due to the lubrication of the structures by the surrounding fluid are considered. In spite of these simplifications, this problem is still complex to handle as the induced contact constraints are non-convex, as detailed in Sections 2.5.4.2 and 2.5.4.3.

2.5.4.1 Fundamental approach

The fundamental idea of the contact modeling considered in this work is summarized in what follows. When the distance between a given elastic structure and its respective contact surface (which can be, e.g., a simple straight wall (see Figure 2.22) or another elastic structure (see Figure 2.23)) is greater than a tolerance value ε_g (also termed *gap*), nothing happens. When this tolerance value is reached, a contact force is applied on the structures nodes where this condition is satisfied [dSGB08]. The purpose of this contact force, which coexists with the hydrodynamic forces and which is applied in the same way [dSGB08], is to prevent the structure body to penetrate the contact surface. Contact occurs as long as the tolerance value is reached by at least one single node of the elastic structure (or equivalently, as long as the amplitude of this additional contact force applied on this node is a non-zero value).

The approximation of the contact in the case of a structure colliding with a simple straight wall in 2D is depicted in Figure 2.22.

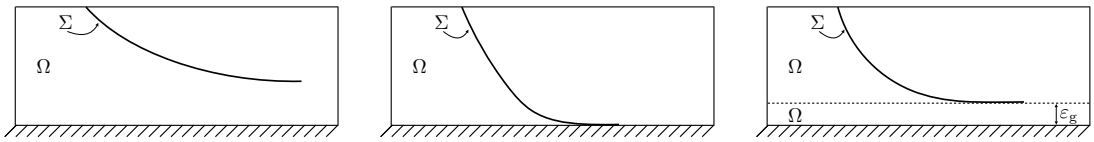

(a) No contact. (b) Realistic contact. (c) Approximated contact.

Figure 2.22 – Two-dimensional illustrations of the way the contact is approximated for the structure-wall case.

A natural extension is to consider the contact between two elastic structures. Acting on the same principle as the simple structure-wall case, the approximation of the contact in the case of a structure colliding with another structure in 2D is depicted in Figure 2.23. We refer to Sections 7.3.1 and 7.3.3 for some illustrations of this structure-structure contact, respectively, in 2D and in 3D.

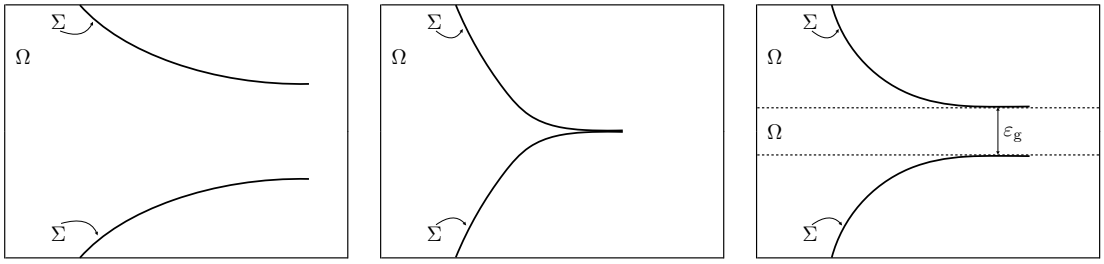

(a) No contact. (b) Realistic contact. (c) Approximated contact.

Figure 2.23 – Two-dimensional illustrations of the way the contact is approximated for the structure-structure case.

Another natural extension of the considered approach consists in the n-structures contact (where $n \geq 3$), not represented here. This type of contact occurs, for instance, in the case of the aortic valve where $n = 3$ leaflets can interact and coapt together. We refer to [AGPT09] and to the numerical experiment of Section 7.3.2 for an illustration of such multi-body contact.

Remark 2.7

The way the contact is approximated, as illustrated above, violates the balance of stresses (also known as Newton's third law) at the interface Σ. As depicted in Figures 2.22b and 2.23b for cases of realistic contact, when contact occurs for some structures nodes, the balance of stresses predicts that the force applied on these nodes is equal to the contact force. As depicted in Figures 2.22c and 2.23c for cases of approximated contact, a thin fluid layer of thickness ε_g remains in the contact zone. This thin layer induces hydrodynamic forces which add up to the contact force resulting in a balance of stresses different from the one obtained with the realistic contact and hence physically wrong.

Recent studies have replaced this thin fluid layer by a porous medium Ω^p (see, e.g., [ASV+18]). This porous medium allows a consistent approach of the fluid-structure-contact interaction where the Newton's third law is ensured [ASV+18]. Illustrations of the previous cases in the presence of an intermediate porous medium Ω^p are provided in Figure 2.24.

Note that the definition of this porous medium Ω^p is straightforward for the structure-wall case (see Figure 2.24a) but becomes very cumbersome for the structure-structure case (see Figure 2.24b) where Ω^p is no more fixed but evolves with the distortion of the leaflets within the fluid domain. This major difficulty justifies the choice of working with the first above-mentioned approach for the contact (depicted in Figures 2.22c and 2.23c), able to provide satisfying results [dSGB08, AGPT09] despite not being realistic from a physical standpoint.

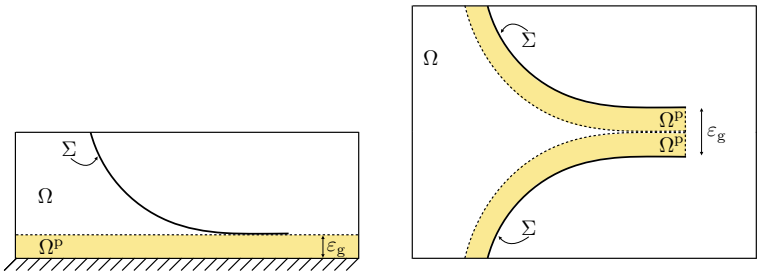

(a) Structure-wall case. (b) Structure-structure case.

Figure 2.24 – Two-dimensional illustrations of the way the contact is approximated for the structure-wall and the structure-structure cases with the use of an intermediate porous medium Ω^{p} colored in yellow.

2.5.4.2 Algorithm and numerical implementation

The content of this section is inspired from [Ast10].

This algorithm has been developed in the context of previous PhD research works (see [dS07, Ast10]) and is dedicated to the contact between the leaflets of a cardiac valve. Only the general ideas are detailed here and we refer the interested reader to [AGPT09, dSGB08] for additional information about the algorithm and to [Pan11] for the mathematical approach of the contact (and more particularly to the definition of the (non-)convex neighborhood $\boldsymbol{\mathcal{U}}$ detailed in what follows).

To describe the main structure of the algorithm, we need to introduce the following notations: $\mathcal{M}$ denotes the family of M immersed solids $\mathcal{M} = (\mathcal{M}_1, \mathcal{M}_2, ..., \mathcal{M}_{\mathrm{M}})$, $\mathcal{T}_H$ a $\mathbb{P}_1$ finite element mesh of $\mathcal{M}$ and $\boldsymbol{X}$ a space of continuous functions defined as

$$\boldsymbol{X} = \left\{ \boldsymbol{\varphi} \in C^0(\mathcal{M}; \mathbb{R}^{\mathrm{d}}), \boldsymbol{\varphi}|_T \in \mathbb{P}_1, \forall T \in \mathcal{T}_H \right\},$$

where d is equal to 2 or 3, depending on the dimension of the problem. $\boldsymbol{\varphi}$ is a function representing the position of the structure and $\boldsymbol{\varphi}_\Sigma$ is its restriction to the interface Σ. This deformation $\boldsymbol{\varphi} : \cup_{i=\{1...\mathrm{M}\}} \mathcal{M}_i \rightarrow \mathbb{R}^{\mathrm{d}}$ is determined by solving at each time-step the following structure minimization problem:

$$\inf_{\boldsymbol{\varphi} \in \boldsymbol{\mathcal{U}}} J(\boldsymbol{\varphi}), \tag{2.28}$$

with

$$\boldsymbol{\mathcal{U}} = \{ \boldsymbol{\varphi} \in \boldsymbol{X}, \mathrm{dist}(\boldsymbol{\varphi}(T_1), \boldsymbol{\varphi}(T_2)) \geq \varepsilon_{\mathrm{g}}, \forall T_1, T_2 \in \mathcal{T}_H \text{ such that } T_1 \cap T_2 = \emptyset \}, \tag{2.29}$$

where $J : \boldsymbol{\mathcal{U}} \rightarrow \mathbb{R}$ stands for the energy of the structure, "dist" the standard Euclidian distance, ε_{g} the considered tolerance gap between and $\boldsymbol{\varphi}(T_i)$ the current position of a finite element mesh $\mathbb{P}_1$ of $\mathcal{M}_i$, where $i \in \{1,...,\mathrm{M}\}$.

Note that the set of constraints (2.29) is clearly non-convex, inducing severe difficulties

in the minimization problem (2.28) for the research of the global minimum. These difficulties can be circumvented by turning this non-convex problem into a sequence of problems with convex constraints, better suited for classical optimization methods. This is made possible thanks to some geometrical assumptions, detailed in [Pan11, AGPT09]), which result into the definition of a convex neighborhood for the above problem (2.28). The price to pay is that at convergence, $\boldsymbol{\varphi}$ does not satisfy *a priori* the optimal conditions of the original problem. However, the induced error is proved to be only of order $\mathcal{O}(h)$ [Pan11].

The proposed algorithm is made of three interlinked loops. The external loop (**Loop 1**) handles the fluid-structure coupling. The first inner loop (**Loop 2**) builds a sequence of convex sets, denoted by $\boldsymbol{\mathcal{C}}(\boldsymbol{\varphi}^k)$, which replaces (2.29) for the resolution of the minimization problem (2.28) handled in the second inner loop (**Loop 3**). Each loop possesses its own stopping criterion. The algorithmic formulation of the above explanation is summarized in [AGPT09] by the following steps:

Loop 1: Fluid-Structure Iterate on j until $\|\boldsymbol{\varphi}_\Sigma^{j+1} - \boldsymbol{\varphi}_\Sigma^{j}\| \leq \varepsilon_{\mathbf{fsi}}$:

1. Solve the fluid problem: given the structures deformation $\boldsymbol{\varphi}_\Sigma^j$, compute the fluid velocity and pressure $(\boldsymbol{u}^j, p^j)$.
2. Compute the load exerted by the fluid $\boldsymbol{\sigma}^{f,j}$.
3. **Loop 2: Sequence of convex minimization problems**
   Iterate on k until $\|\boldsymbol{\varphi}^{j,k+1} - \boldsymbol{\varphi}^{j,k}\| \leq \varepsilon_{\boldsymbol{\mathcal{C}}}$:
   (a) Definition of a convex neighborhood $\boldsymbol{\mathcal{C}}(\boldsymbol{\varphi}^{j,k})$ of $\boldsymbol{\varphi}^{j,k}$.
   (b) **Loop 3: Minimization with convex constraints**
   Uzawa algorithm (tolerance $\varepsilon_{\mathbf{cvx}}$) to solve the convex structure problem

$$\boldsymbol{\varphi}^{j,k+1} = \arg\left(\inf_{\boldsymbol{\psi}\in\boldsymbol{\mathcal{C}}(\boldsymbol{\varphi}^{j,k})} J(\boldsymbol{\psi})\right).$$

More details about the numerical methods considered for the resolution of each loop can be found in [AGPT09]. In what follows, the numerical implementation of the most inner loop – **Loop 3** – is further detailed as its resolution is crucial for the overall efficiency of the whole contact algorithm.

2.5.4.3 Uzawa algorithm for saddle point problems

To solve the most inner loop, various methods – like penalization or relaxation with projection – exist but lead to important changes in the architecture of the existing structure solver. In order to minimize these modifications, the preferred alternative is the maximization of a dual energy thanks to a gradient method with projection.

In what follows, $(\boldsymbol{V}, \|\cdot\|)$ denotes a real Hilbert space, where previous $\boldsymbol{\mathcal{U}}$, given by (2.29), is a subset of $\boldsymbol{V}$. We consider the Lagrangian as a function $\mathcal{L} : \boldsymbol{V} \times (\mathbb{R}^+)^{\mathrm{M}} \to \mathbb{R}$ defined as

$$\mathcal{L}(\boldsymbol{v},\boldsymbol{\mu}) = J(\boldsymbol{v}) + \boldsymbol{\mu}\cdot\boldsymbol{F}(\boldsymbol{v}), \quad (\boldsymbol{v},\boldsymbol{\mu}) \in \boldsymbol{V} \times (\mathbb{R}^+)^{\mathrm{M}},$$

where M is the number of immersed solids and $\boldsymbol{F}$ represents the vector of constraint functions that must verify the following inequalities:

$$F_i(\boldsymbol{v}) \leq 0, \quad \forall i \in \{1,...,\mathrm{M}\}.$$

Physically speaking, for any $i \in \{1,...,\mathrm{M}\}$, μ_i can be interpreted as the Lagrange multiplier associated to the constraint F_i.

The benefits of using $\mathcal{L}$ instead of J is that the resolution of (2.28) can be done on the whole space $\boldsymbol{V}$ instead of the non-convex subset $\boldsymbol{\mathcal{U}}$ as detailed in the following proof.

Proof. If we do define the function $\mathcal{J} : \boldsymbol{V} \supset \boldsymbol{\mathcal{U}} \to \mathbb{R}$ as

$$\mathcal{J}(\boldsymbol{v}) = \sup_{\boldsymbol{\mu} \in (\mathbb{R}^+)^{\mathrm{M}}} \mathcal{L}(\boldsymbol{v}, \boldsymbol{\mu}) = \begin{cases} J(\boldsymbol{v}) & \text{if} \quad F_i(\boldsymbol{v}) \leq 0, \quad \forall i \in \{1,...,\mathrm{M}\}, \\ +\infty & \text{if} \quad \exists\, i \in \{1,...,\mathrm{M}\} \text{ such that } F_i(\boldsymbol{v}) > 0, \end{cases}$$

then it leads directly to the following equalities:

$$\inf_{\boldsymbol{v} \in \boldsymbol{\mathcal{U}}} J(\boldsymbol{v}) = \inf_{\boldsymbol{v} \in \boldsymbol{V}} \mathcal{J}(\boldsymbol{v}) = \inf_{\boldsymbol{v} \in \boldsymbol{V}} \left(\sup_{\boldsymbol{\mu} \in (\mathbb{R}^+)^{\mathrm{M}}} \mathcal{L}(\boldsymbol{v},\boldsymbol{\mu}) \right).$$

The first term with J considers the subset $\boldsymbol{\mathcal{U}}$ whereas the other terms with $\mathcal{J}$ and $\mathcal{L}$ consider the whole space $\boldsymbol{V}$. This completes the proof. □

We also introduce the dual energy $\mathcal{G} : (\mathbb{R}^+)^{\mathrm{M}} \to \mathbb{R}$ as

$$\mathcal{G}(\boldsymbol{\mu}) = \inf_{\boldsymbol{v} \in \boldsymbol{V}} \mathcal{L}(\boldsymbol{v},\boldsymbol{\mu})$$

and the saddle point defined below.

Definition 2.1
$(\boldsymbol{u},\boldsymbol{\lambda})$ is a saddle point of $\mathcal{L}$ in $\boldsymbol{\mathcal{U}} \times (\mathbb{R}^+)^M$ if and only if

$$\mathcal{J}(\boldsymbol{u}) = \inf_{\boldsymbol{v} \in \boldsymbol{V}} \mathcal{J}(\boldsymbol{v}) = \sup_{\boldsymbol{\mu} \in (\mathbb{R}^+)^M} \mathcal{G}(\boldsymbol{\mu}) = \mathcal{G}(\boldsymbol{\lambda}).$$

If we apply the previous definition to our problem, we get the following result:

$$\inf_{\boldsymbol{v} \in \boldsymbol{\mathcal{U}}} J(\boldsymbol{v}) = \inf_{\boldsymbol{v} \in \boldsymbol{V}} \mathcal{J}(\boldsymbol{v}) = \inf_{\boldsymbol{v} \in \boldsymbol{V}} \left(\sup_{\boldsymbol{\mu} \in (\mathbb{R}^+)^{\mathrm{M}}} \mathcal{L}(\boldsymbol{v},\boldsymbol{\mu}) \right) = \sup_{\boldsymbol{\mu} \in (\mathbb{R}^+)^{\mathrm{M}}} \mathcal{G}(\boldsymbol{\mu}),$$

which is of fundamental interest as the projection on an arbitrary convex is generally difficult compared to the one on $(\mathbb{R}^+)^{\mathrm{M}}$.

The two steps of the Uzawa algorithm are detailed below. For the sake of clarity, the superscript j used in the previous Section is omitted here.

1. First, we begin with the primal problem. Let $\boldsymbol{u}(\boldsymbol{\mu})$ be the solution of the following minimization problem without constraints:

$$\boldsymbol{u}(\boldsymbol{\mu}) = \arg\left(\inf_{\boldsymbol{v}\in\boldsymbol{V}} \mathcal{L}(\boldsymbol{v},\boldsymbol{\mu})\right). \tag{2.30}$$

   By definition, we have

$$\mathcal{G}(\boldsymbol{\mu}) = J(\boldsymbol{u}(\boldsymbol{\mu})) + \boldsymbol{\mu}\cdot\boldsymbol{F}(\boldsymbol{u}(\mu))$$

   and, by deriving with respect to $\boldsymbol{\mu}$,

$$\boldsymbol{\mathcal{G}}'(\boldsymbol{\mu}) = \boldsymbol{F}(\boldsymbol{u}(\boldsymbol{\mu})) + \langle\, J'(\boldsymbol{u}(\boldsymbol{\mu})) + \boldsymbol{\mu}\cdot\boldsymbol{F}'(\boldsymbol{u}(\boldsymbol{\mu})), \boldsymbol{u}'(\boldsymbol{\mu})\rangle. \tag{2.31}$$

   As $\boldsymbol{u}$ verifies the following equation:

$$\frac{\partial\mathcal{L}}{\partial\boldsymbol{v}}(\boldsymbol{u},\boldsymbol{\mu}) = 0,$$

   we have

$$J'(\boldsymbol{u}(\boldsymbol{\mu})) + \boldsymbol{\mu}\cdot\boldsymbol{F}'(\boldsymbol{u}(\boldsymbol{\mu})) = 0$$

   and by reinserting this into (2.31), we get

$$\boldsymbol{\mathcal{G}}'(\boldsymbol{\mu}) = \boldsymbol{F}(\boldsymbol{u}(\boldsymbol{\mu})).$$

2. Then, we consider the dual problem. Let $\boldsymbol{\lambda}$ be the solution of the following maximization problem on the closed convex $(\mathbb{R}^+)^{\mathrm{M}}$:

$$\boldsymbol{\lambda} = \arg\left(\sup_{\boldsymbol{\mu}\in(\mathbb{R}^+)^{\mathrm{M}}} \mathcal{G}(\boldsymbol{\mu})\right). \tag{2.32}$$

   $\boldsymbol{\lambda}$ is then obtained thanks to a gradient method with projection on $(\mathbb{R}^+)^{\mathrm{M}}$ denoted by $\Pi_{(\mathbb{R}^+)^{\mathrm{M}}}$:

$$\boldsymbol{\lambda}^{k+1} = \Pi_{(\mathbb{R}^+)^{\mathrm{M}}}\left(\boldsymbol{\lambda}^k + \alpha\boldsymbol{\mathcal{G}}'(\boldsymbol{\lambda}^k)\right),$$

   where α is the step size of the gradient method.

Based on the above description, the whole loop of minimization with convex constraints (**Loop 3**) can be finally summarized by the following two steps:

$$\begin{aligned}
&\text{First step}: \boldsymbol{u}^k = \arg\left(\inf_{\boldsymbol{v}\in\boldsymbol{V}} \mathcal{L}(\boldsymbol{v},\boldsymbol{\lambda}^k)\right),\\
&\text{Second step}: \boldsymbol{\lambda}^{k+1} = \Pi_{(\mathbb{R}^+)^{\mathrm{M}}}\left(\boldsymbol{\lambda}^k + \alpha\boldsymbol{F}(u^k)\right).
\end{aligned} \tag{2.33}$$

Towards a more efficient implementation: The efficiency of resolution of this most inner loop is of major concern as the number of iterations might greatly increase when the computed contact forces are important and the structures thin, which is the case for the

simulation of cardiac valves.

Therefore, despite its ease of implementation, other optimization methods, known to perform better than this gradient method with projection step $(2.33)_2$ where the step size is fixed, have been investigated and used to improve the overall efficiency of the contact algorithm. For this purpose, we have used the Method of Moving Asymptotes (MMA) algorithm available with the NLopt library. NLopt[7] is a free/open-source library for non-linear optimization, providing a common interface for various implementations of optimization routines. MMA[8] is an algorithm dedicated to non-linear constrained gradient-based optimization and we refer to [Sva02] for further information about its implementation.

2.6 Conclusions

In this chapter, the modeling and the simulation of cardiac hemodynamics has been addressed. First, the geometrical description of the left heart as well as standard models of blood flow, key components of realistic simulations, have been presented. It has been physically justified that blood can be assumed to be homogeneous, incompressible and Newtonian and thus governed by the Navier-Stokes equations in their Eulerian or ALE formulations. Then, the preferred coupling strategy considered in this work has been described and its benefits highlighted: it consists in a simplified heart model *one-way* kinematically uncoupled with a 3D blood flow model. This common approach ensures an overall reduced computational complexity compared to fully coupled solutions.

For the purpose of realistic simulations, this blood flow model needs to be *two-way* coupled with a model of cardiac valves. Based on the degree of complexity adopted for their modeling (i.e., whether or not their dynamics is considered), two main methods have been introduced and widely discussed: the RIS and the FSI ones. For each of them and particularly for the latter one, we have reviewed various formulations and associated state-of-the-art numerical techniques in order to assess their respective strengths and limitations. Finally, the contact between several elastic structures, which is specific to the FSI approach, has been addressed. We have detailed the way it is modeled in this work as well as its numerical implementation.

The content of this chapter will be the fundamental mathematical background of the work presented in the rest of this thesis, in Parts II and III, for the RIS and the FSI models, respectively.

[7] See `https://nlopt.readthedocs.io/en/latest/`.
[8] See `https://nlopt.readthedocs.io/en/latest/NLopt_Algorithms/`.

Part II

Simulation of intracardiac blood flow with a simplified model of valves

Chapter 3

Augmented resistive immersed surfaces valve model for the simulation of cardiac hemodynamics with isovolumetric phases

In order to reduce the complexity of cardiac hemodynamics simulations, one-way coupling approaches are often considered for the modeling of the immersed valves as an alternative to complex FSI models. A possible shortcoming of these simplified approaches is the difficulty to correctly capture the pressure dynamics during the isovolumetric phases. In this chapter, we propose an enhanced RIS model of cardiac valves which overcomes this issue. The benefits of the model are investigated and tested in blood flow simulations of the left heart.

The results presented in this chapter have been reported in:

- L. Boilevin-Kayl, A. This, M.A. Fernández and J.F. Gerbeau, **Augmented Resistive Immersed Surfaces valve model for the simulation of cardiac hemodynamics with isovolumetric phases.** *International Journal for Numerical Methods in Biomedical Engineering*, in press, *2019*. Available online: https://hal.inria.fr/hal-01944798.
- L. Boilevin-Kayl, A. This, M.A. Fernández and J.F. Gerbeau, **An efficient valve model based on resistive immersed surfaces enhanced with physiological data.** *CMBE 2017 – 5th International Conference on Computational and Mathematical Biomedical Engineering, April 2017, Pittsburgh, United States.* Available online: https://hal.inria.fr/hal-01519602.

Contents

3.1 Introduction

In this chapter, we propose a new simplified modeling approach which fixes the problem of definition of the isovolumetric phases mentioned in Section 2.4. Starting from the RIS model for valves dynamics [AHSG12] described in Section 2.4.1, we introduce an additional interface term which controls the ventricle pressure when both valves are closed. This term involves ventricle pressure data coming either from measurements or from external electromechanical simulations, hence the terminology *augmented* RIS model. The fundamental idea of the proposed approach is that, under some basic assumptions and for moderate values of the resistive parameters, the simulated fluid pressure within the ventricle can be regulated in terms of the external pressures, the volume variation and the provided pressure data. Two three-dimensional numerical examples are proposed to test the new model and to assess the validity of its related assumptions.

The rest of this chapter is organized as follows. Section 3.2 provides an estimation of the pressure within an enclosed cavity obtained with the original RIS model and introduces the new augmented one. In Section 3.3, two three-dimensional numerical examples are presented. Finally, a summary of the main results are given in Section 3.4.

3.2 Problem setting and mathematical models

In this section, we first briefly recall the original RIS model [FGM08, AHSG12] as well as its spatial and temporal discretization in the context of its application to a moving cavity enclosed by multiple immersed valves. Then, an estimate of the intracavity pressure in the resulting setting is provided. This analysis motivates the derivation of the ARIS model, whose goal is to properly control this intracavity pressure during the isovolumetric phases.

3.2.1 Original RIS model

We refer to Section 2.4.1 for the description of the original RIS model, given by (2.8). For the sake of clarity, in the rest of this chapter, we remind that Ω will refer to $\Omega(t)$, $\partial\Omega$ to $\partial\Omega(t)$, Σ_i to $\Sigma_i(t)$ and R_i to $R_i(t)$. We also recall that $[\![\cdot]\!]$ represents the jump operator, initially introduced in $(2.10)_1$, whereas $[\![\cdot]\!]_{\Sigma_i}$ represents its specific application on the immersed surface Σ_i.

The fully discrete approximation of (2.8)–(2.9) is detailed in what follows. We denote $\tau > 0$ the time-step length and we define $t_n \overset{\text{def}}{=} n\tau$ for $n \in \mathbb{N}$. For any tensorial field $\boldsymbol{q}$, we denote $\boldsymbol{q}^n$ the value of this field evaluated at time t_n for $n \in \mathbb{N}$. For the sake of clarity, $\boldsymbol{f}^{\mathrm{f}}$ is assumed to be equal to $\mathbf{0}$.

As regards the discretization in space, a stabilized finite element method is considered, namely the couple of finite elements $\mathbb{P}_1/\mathbb{P}_1$. To this purpose, we consider a family of $\{\mathcal{T}_h\}_{0<h<1}$ of the reference fluid domain Ω which are fitted to the (reference) valve surfaces Σ_i. The discrete space for the velocity $\boldsymbol{V}_h \subset [H^1(\Omega)]^3$ is the standard Lagrange finite element space of continuous piece-wise affine functions. The pressure space $Q_h \subset L^2(\Omega)$ is also made of piece-wise affine functions which are globally continuous except across Σ_i.

This allows to correctly capture the pressure jumps when the cardiac valves, represented by Σ_i, are closed [AHSG12]. This has been achieved by considering fluid meshes which are fitted to these immersed surfaces.

Finally, combining the temporal and spatial discretization, we get the following fully discrete method of (2.8)–(2.9): find $(\widehat{\boldsymbol{u}}_h^n, \widehat{p}_h^n) \in \boldsymbol{V}_h \times Q_h$, with $\widehat{\boldsymbol{u}}_h^n|_{\partial\Omega_\mathrm{s}} = \boldsymbol{w}_h^n$, such that

$$\begin{aligned}\frac{\rho^\mathrm{f}}{\tau}\left[\int_{\Omega^n} \boldsymbol{u}_h^n \cdot \boldsymbol{v}_h - \int_{\Omega^{n-1}} \boldsymbol{u}_h^{n-1} \cdot \boldsymbol{v}_h\right] + a^\mathrm{f}_{\Omega^n,h}\big(\boldsymbol{u}_h^{n-1} - \boldsymbol{w}_h^n; (\boldsymbol{u}_h^n,p_h^n),(\boldsymbol{v}_h,q_h)\big)\\ - \rho^\mathrm{f}\int_{\Omega^n} (\boldsymbol{\nabla}\cdot\boldsymbol{w}_h^n)\boldsymbol{u}_h^n\cdot\boldsymbol{v}_h + \sum_{i=\{1\dots n\}} R_i^n \int_{\Sigma_i^n} (\boldsymbol{u}_h^n - \boldsymbol{w}_h^n)\cdot\boldsymbol{v}_h\\ = -\int_{\partial\Omega^n_{\mathrm{N}_1}} g_1^n \boldsymbol{n}\cdot\boldsymbol{v}_h - \int_{\partial\Omega^n_{\mathrm{N}_2}} g_2^n \boldsymbol{n}\cdot\boldsymbol{v}_h, \quad (3.1)\end{aligned}$$

for all $(\widehat{\boldsymbol{v}}_h, \widehat{q}_h) \in \boldsymbol{V}_h \times Q_h$, with $\widehat{\boldsymbol{v}}_h|_{\partial\Omega_\mathrm{s}} = \boldsymbol{0}$. The discrete Navier-Stokes trilinear form $a^\mathrm{f}_{\Omega^n,h}$ is given by

$$\begin{aligned}a^\mathrm{f}_{\Omega^n,h}\big(\boldsymbol{z}_h; (\boldsymbol{u}_h,p_h),(\boldsymbol{v}_h,q_h)\big) &= \rho^\mathrm{f}\int_{\Omega^n}(\boldsymbol{z}_h\cdot\boldsymbol{\nabla}\boldsymbol{u}_h)\cdot\boldsymbol{v}_h + \frac{\rho^\mathrm{f}}{2}\int_{\Omega^n}(\boldsymbol{\nabla}\cdot\boldsymbol{z}_h)\boldsymbol{u}_h\cdot\boldsymbol{v}_h\\ &+ \int_{\Omega^n}\boldsymbol{\sigma}(\boldsymbol{u}_h,p_h):\boldsymbol{\nabla}\boldsymbol{v}_h + \int_{\Omega^n} q_h\boldsymbol{\nabla}\cdot\boldsymbol{u}_h\\ &+ \sum_{K\in\mathcal{T}_h^n}\int_K \delta_h\left(\rho^\mathrm{f}(\boldsymbol{z}_h\cdot\boldsymbol{\nabla})\boldsymbol{u}_h + \boldsymbol{\nabla}p_h\right)\cdot\left(\rho^\mathrm{f}(\boldsymbol{z}_h\cdot\boldsymbol{\nabla})\boldsymbol{v}_h + \boldsymbol{\nabla}q_h\right),\end{aligned}$$

where the last term stands for the Streamline Upwind Petrov-Galerkin (SUPG)/Pressure-Stabilized Petrov-Galerkin (PSPG) stabilization (see, e.g., [Tez91]).

REMARK 3.1
Note that in (3.1), the dissipative terms read as follows:

$$\left\langle R_i^n \boldsymbol{u}_h^n \delta_{\Sigma_i^n}, \boldsymbol{v}_h\right\rangle = \int_{\Sigma_i^n} R_i^n \boldsymbol{u}_h^n\cdot\boldsymbol{v}_h = R_i^n\int_{\Sigma_i^n}\boldsymbol{u}_h^n\cdot\boldsymbol{v}_h, \quad \forall i\in\{1\dots n\},$$

illustrating the way the $\delta_{\Sigma_i^n}$ function (Dirac measure) associated to the surface Σ_i^n is numerically handled.

REMARK 3.2
In (3.1), the fluid integrals in the current configuration involve the composition with the corresponding discrete ALE map provided in Section 2.4.1. For instance, the second term is given by

$$\int_{\Omega^{n-1}}\boldsymbol{u}_h^{n-1}\cdot\boldsymbol{v}_h = \int_{\Omega^{n-1}}(\widehat{\boldsymbol{u}}_h^{n-1}\circ(\boldsymbol{\mathcal{A}}_h^{n-1})^{-1})\cdot(\widehat{\boldsymbol{v}}_h\circ(\boldsymbol{\mathcal{A}}_h^{n-1})^{-1}).$$

In the rest of this chapter and for the sake of clarity, further models are derived and

described only in strong formulation.

3.2.2 Estimate of the pressure within an enclosed cavity

Based on the original RIS model (2.8), let Ω denote a moving domain, composed of three fluid sub-domains $\Omega \overset{\text{def}}{=} \Omega_1 \cup \Omega_2 \cup \Omega_3$, as depicted in Figure 3.1. We assume that Ω_1 shares an interface with Ω_2, denoted as Σ_{12}, and that Ω_2 also shares another interface with Ω_3, denoted as Σ_{23}. The domains Ω_1 and Ω_3 do not share any interface. The opening and closing dynamics of Σ_{12} and Σ_{23} are described using the RIS model.

The exterior boundary of Ω is divided into non-overlapping subsets $\partial\Omega_{\cdot,\mathrm{D}}$ and $\partial\Omega_{\cdot,\mathrm{N}}$ as depicted in Figure 3.1. No-slip Dirichlet boundary conditions are imposed on $\partial\Omega_{\cdot,\mathrm{D}} = \partial\Omega_{1,\mathrm{D}} \cup \partial\Omega_{2,\mathrm{D}} \cup \partial\Omega_{3,\mathrm{D}}$ and Neumann normal boundary conditions are imposed on $\partial\Omega_{\cdot,\mathrm{N}} = \partial\Omega_{1,\mathrm{N}} \cup \partial\Omega_{3,\mathrm{N}}$. The body force $\boldsymbol{f}^{\mathrm{f}}$ is assumed to be equal to $\mathbf{0}$.

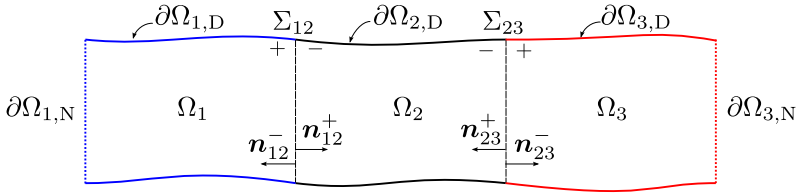

Figure 3.1 – Geometrical domain Ω considered for the problems (3.2) and (3.9).

The following problem is therefore considered: find the velocity $\boldsymbol{u} = \boldsymbol{u}(\boldsymbol{x},t) : \Omega \times \mathbb{R}^+ \to \mathbb{R}^3$ and the pressure $p = p(\boldsymbol{x},t) : \Omega \times \mathbb{R}^+ \to \mathbb{R}$, such that

$$
\begin{cases}
\rho^{\mathrm{f}} \left(\left. \dfrac{\partial \boldsymbol{u}}{\partial t} \right|_{\boldsymbol{\mathcal{A}}} + (\boldsymbol{u} - \boldsymbol{w}) \cdot \boldsymbol{\nabla} \boldsymbol{u} \right) - \boldsymbol{\nabla} \cdot \boldsymbol{\sigma}(\boldsymbol{u},p) \\
\qquad + \displaystyle\sum_{i=\{12,23\}} R_i \delta_{\Sigma_i} (\boldsymbol{u} - \boldsymbol{w}) = \mathbf{0} \quad \text{in} \quad \Omega, \\
\qquad\qquad \boldsymbol{\nabla} \cdot \boldsymbol{u} = 0 \quad \text{in} \quad \Omega, \\
\qquad\qquad \boldsymbol{u} = \boldsymbol{w} \quad \text{on} \quad \partial\Omega_{1,\mathrm{D}} \cup \partial\Omega_{2,\mathrm{D}} \cup \partial\Omega_{3,\mathrm{D}}, \\
\qquad\qquad \boldsymbol{\sigma}(\boldsymbol{u},p)\boldsymbol{n} = \boldsymbol{g_1} \quad \text{on} \quad \partial\Omega_{1,\mathrm{N}}, \\
\qquad\qquad \boldsymbol{\sigma}(\boldsymbol{u},p)\boldsymbol{n} = \boldsymbol{g_3} \quad \text{on} \quad \partial\Omega_{3,\mathrm{N}}.
\end{cases}
\tag{3.2}
$$

The above system has to be completed with initial conditions:

$$\boldsymbol{u}(0) = \boldsymbol{u}_0 \quad \text{in} \quad \Omega.$$

The main difficulty which arises in the description of the isovolumetric phases using an uncoupling approach is that the ventricular pressure is defined up to a constant, since the fluid velocity is prescribed on the boundary of the enclosed cavity. This issue is circumvented in the original RIS model (2.8) thanks to the interface Robin condition $(2.11)_2$, for moderate values of R_i. However, as we shall discuss below, this results in an arbitrarily fixed internal pressure.

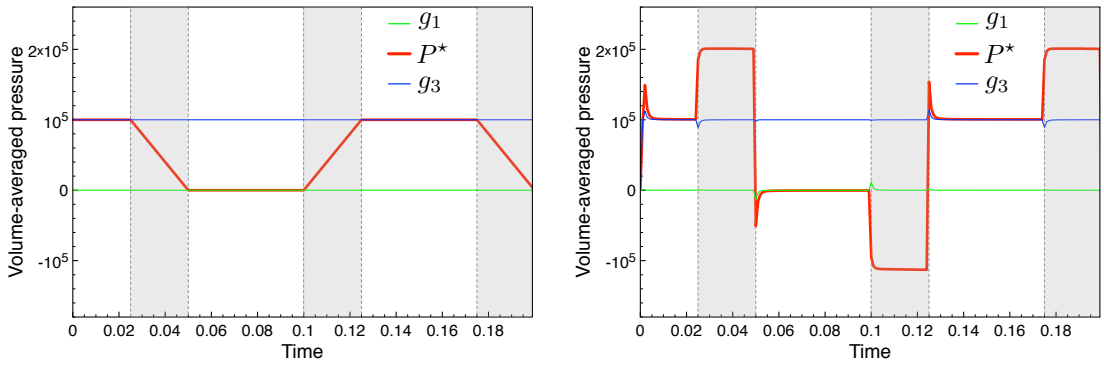

(a) Expected results.

(b) Side view.

Figure 3.2 – Time history of the pressures. The grey areas delimit the isovolumetric phases.

For instance, Figures 3.2a–3.2b depict, respectively, the expected pressures and the typical computed ones, in a simple toy problem based on the domain depicted in Figure 3.1 and described later in Section 3.3.1. Results portrayed in Figure 3.2b have been obtained by using the setting (3.2). Outside the chosen isovolumetric phases delimited by the gray areas, the computed pressures match the reference ones depicted in Figure 3.2a. On the other hand, when the middle cavity Ω_2 is closed, its inner computed volume-averaged pressure $\overline{P_{\Omega_2}}$ is clearly different from the expected one. It can be noted that, during these isovolumetric phases, $\overline{P_{\Omega_2}}$ reaches an arbitrary value, outside of the interval $\left[\overline{P_{\Omega_1}}, \overline{P_{\Omega_3}}\right]$.

In the following analysis, we provide an estimate of the resulting pressure inside Ω_2 in the situation where both R_{12} and R_{23} belong to $]0, +\infty[$. We consider two simplifying assumptions:

(H1) the viscous contribution to the normal stress is considered negligible on the valves.

(H2) the pressure inside the cavities are considered approximately constant in space when the valves are closed, namely,

$$p(\boldsymbol{x},t) \simeq P_{\Omega_i}(t), \quad \forall (\boldsymbol{x},i) \in \Omega_i \times \{1,2,3\}.$$

PROPOSITION 3.1

Under assumptions (H1) and (H2), the pressure inside the cavity Ω_2 can be estimated as

$$P_{\Omega_2} \simeq \frac{\varepsilon_{12}|\Sigma_{12}|}{K} P_{\Omega_1} + \frac{\varepsilon_{23}|\Sigma_{23}|}{K} P_{\Omega_3} - \frac{1}{K} \int_{\partial\Omega_2} \boldsymbol{w} \cdot \boldsymbol{n}, \tag{3.3}$$

where $\varepsilon_i \overset{\text{def}}{=} \dfrac{1}{R_i}$, $K \overset{\text{def}}{=} (\varepsilon_{12}|\Sigma_{12}| + \varepsilon_{23}|\Sigma_{23}|)$ and $|\Sigma_i|$ stands for the measure of the surface Σ_i, where $i = \{12,23\}$.

Proof. We consider the following interface condition (see $(2.11)_2$) on Σ_i:

$$[\![\boldsymbol{\sigma}(\boldsymbol{u},p)\boldsymbol{n}]\!] = -R_i\,(\boldsymbol{u} - \boldsymbol{w})\,. \tag{3.4}$$

Using assumption (H1) and rearranging the terms, we obtain

$$\boldsymbol{u} \simeq \boldsymbol{w} + \frac{1}{R_i}\left(p^- \boldsymbol{n}^- + p^+ \boldsymbol{n}^+\right) \quad \text{on} \quad \Sigma_i.$$

Multiplying by $\boldsymbol{n}^-$ and integrating over Σ_i, we get

$$\int_{\Sigma_i} \boldsymbol{u}\cdot\boldsymbol{n}^- \simeq \int_{\Sigma_i} \boldsymbol{w}\cdot\boldsymbol{n}^- + \frac{1}{R_i}\int_{\Sigma_i}\left(p^- - p^+\right).$$

Using assumption (H2), we finally obtain

$$\int_{\Sigma_i} \boldsymbol{u}\cdot\boldsymbol{n}^- \simeq \int_{\Sigma_i} \boldsymbol{w}\cdot\boldsymbol{n}^- + \frac{1}{R_i}\left(p^- - p^+\right)|\Sigma_i|.$$

In particular, for Σ_{12} and Σ_{23}, we get the following expressions:

$$\int_{\Sigma_{12}} \boldsymbol{u}\cdot\boldsymbol{n}^- \simeq \int_{\Sigma_{12}} \boldsymbol{w}\cdot\boldsymbol{n}^- + \frac{1}{R_{12}}\left(P_{\Omega_2} - P_{\Omega_1}\right)|\Sigma_{12}|, \tag{3.5}$$

$$\int_{\Sigma_{23}} \boldsymbol{u}\cdot\boldsymbol{n}^- \simeq \int_{\Sigma_{23}} \boldsymbol{w}\cdot\boldsymbol{n}^- + \frac{1}{R_{23}}\left(P_{\Omega_2} - P_{\Omega_3}\right)|\Sigma_{23}|. \tag{3.6}$$

Applying the divergence theorem on $(3.2)_2$, we have

$$\int_{\Omega_2} \boldsymbol{\nabla}\cdot\boldsymbol{u} \;= 0 \quad \Leftrightarrow \quad \int_{\partial\Omega_{2,\mathrm{D}}} \boldsymbol{u}\cdot\boldsymbol{n}^- + \int_{\Sigma_{12}} \boldsymbol{u}\cdot\boldsymbol{n}^- + \int_{\Sigma_{23}} \boldsymbol{u}\cdot\boldsymbol{n}^- = 0. \tag{3.7}$$

Finally, by substituting (3.5), (3.6) and $(3.2)_3$ into (3.7), we obtain

$$\int_{\partial\Omega_2} \boldsymbol{w}\cdot\boldsymbol{n}^- \; + \frac{1}{R_{12}}\left(P_{\Omega_2} - P_{\Omega_1}\right)|\Sigma_{12}| + \frac{1}{R_{23}}\left(P_{\Omega_2} - P_{\Omega_3}\right)|\Sigma_{23}| \simeq 0.$$

Rearranging the equation, we get the the estimation (3.3). This completes the proof. □

It is worth noting that, when the cavity is closed and if the assumptions hold, the pressure P_{Ω_2} is regulated both by the exterior pressures (i.e., with P_{Ω_1} and P_{Ω_3}) and by the change of the volume of Ω_2. In the case of a perfectly incompressible cavity (i.e., when $\int_{\partial\Omega_2} \boldsymbol{w}\cdot\boldsymbol{n} = 0$), a balance of the exterior pressures is reached and is regulated both by the surface area of the immersed surfaces – $|\Sigma_{12}|$ and $|\Sigma_{23}|$ – and by the value of their corresponding resistive parameters R_i.

If the volume of the closed cavity is undergoing change (i.e., $\int_{\partial\Omega_2} \boldsymbol{w}\cdot\boldsymbol{n} \neq 0$), its pressure will also evolve. Noting that $\boldsymbol{n}$ is the outgoing normal, the dilatation of the cavity (i.e., $\int_{\partial\Omega_2} \boldsymbol{w}\cdot\boldsymbol{n} > 0$) would induce a negative pressure contribution. On the opposite, a contracting cavity (i.e., $\int_{\partial\Omega_2} \boldsymbol{w}\cdot\boldsymbol{n} < 0$) would result in a positive pressure contribution. Moreover, this pressure change is proportional to R_i and inversely proportional to the surface area of the immersed surfaces. This behavior is coherent with the fact that the original RIS formulation has been designed to model porous media. In the case of an increasing porous surface area, more fluid would pass through, resulting in a lower pressure

jump across the surface. On the other hand, in the case of a decreasing porosity, less fluid would pass through, resulting in a higher pressure jump.

While the intracavity pressure has been estimated in a situation where both R_{12} and R_{23} are different from 0, it has to be noted that this estimation becomes singular when both R_{12} and R_{23} converge to $+\infty$. In this asymptotic case, the fact that the velocity is prescribed on the whole cavity boundary leaves the pressure undetermined and might not be compatible with the incompressibility constraint.

3.2.3 Augmented Resistive Immersed Surface model

As shown in Section 3.2.2, an estimation of the pressure P_{Ω_2} has been proposed. This expression involves the distal pressures, the wall velocity, the surface area of the immersed surfaces as well as the value of their resistive parameters. In this section, given a reference time-dependent pressure $P^\star = P^\star(t)$, the objective is to modify the RIS model in order to enforce $P_{\Omega_2} \simeq P^\star$.

The proposed approach consists in considering an additional normal stress term on each of the immersed surfaces so that the corresponding interface condition (3.4) becomes

$$[\![\boldsymbol{\sigma}(\boldsymbol{u},p)\boldsymbol{n}]\!]_{\Sigma_i} = -R_i\,(\boldsymbol{u}-\boldsymbol{w}) + g_{\Sigma_i}\boldsymbol{n}. \tag{3.8}$$

The proposed approach will be referred to as the ARIS model. Assuming the same setting as the one in Section 3.2.2 and applying this model on the immersed surfaces Σ_{12} and Σ_{23}, we consider the following problem: find the velocity $\boldsymbol{u} = \boldsymbol{u}(\boldsymbol{x},t) : \Omega \times \mathbb{R}^+ \to \mathbb{R}^3$ and the pressure $p = p(\boldsymbol{x},t) : \Omega \times \mathbb{R}^+ \to \mathbb{R}$, such that

$$\begin{cases} \rho^{\mathrm{f}}\left(\left.\dfrac{\partial \boldsymbol{u}}{\partial t}\right|_{\boldsymbol{\mathcal{A}}} + (\boldsymbol{u}-\boldsymbol{w})\cdot\boldsymbol{\nabla}\boldsymbol{u}\right) - \boldsymbol{\nabla}\cdot\boldsymbol{\sigma}(\boldsymbol{u},p) \\ \qquad\qquad + \displaystyle\sum_{i=\{12,23\}} R_i\delta_{\Sigma_i}\,(\boldsymbol{u}-\boldsymbol{w}) = \sum_{i=\{12,23\}} g_i\delta_{\Sigma_i}\boldsymbol{n} \quad \text{in} \quad \Omega, \\ \qquad\qquad\qquad\qquad \boldsymbol{\nabla}\cdot\boldsymbol{u} = 0 \quad \text{in} \quad \Omega, \\ \qquad\qquad\qquad\qquad \boldsymbol{u} = \boldsymbol{w} \quad \text{on} \quad \partial\Omega_{1,\mathrm{D}} \cup \partial\Omega_{2,\mathrm{D}} \cup \partial\Omega_{3,\mathrm{D}}, \\ \qquad\qquad\qquad\qquad \boldsymbol{\sigma}(\boldsymbol{u},p)\boldsymbol{n} = \boldsymbol{g_1} \quad \text{on} \quad \partial\Omega_{1,\mathrm{N}}, \\ \qquad\qquad\qquad\qquad \boldsymbol{\sigma}(\boldsymbol{u},p)\boldsymbol{n} = \boldsymbol{g_3} \quad \text{on} \quad \partial\Omega_{3,\mathrm{N}}. \end{cases} \tag{3.9}$$

The above system has to be completed with an appropriate initial condition. The following interface conditions are then satisfied:

$$\begin{aligned} [\![\boldsymbol{u}]\!]_{\Sigma_i} &= \boldsymbol{0}. \\ [\![\boldsymbol{\sigma}(\boldsymbol{u},p)\boldsymbol{n}]\!]_{\Sigma_i} &= -R_i\,(\boldsymbol{u}-\boldsymbol{w}) + g_{\Sigma_i}\boldsymbol{n}. \end{aligned} \tag{3.10}$$

Proposition 3.2
Let $P^\star = P^\star(t)$ be a given time-depend function. Using the ARIS model with the stress terms $g_{\Sigma_{12}}$ and $g_{\Sigma_{23}}$ defined as

$$g_{12} \overset{\text{def}}{=} P_{\Omega_1} - P^\star - \frac{1}{K}\int_{\partial\Omega_2} \boldsymbol{w}\cdot\boldsymbol{n} \quad \text{and} \quad g_{23} \overset{\text{def}}{=} P_{\Omega_3} - P^\star - \frac{1}{K}\int_{\partial\Omega_2} \boldsymbol{w}\cdot\boldsymbol{n}, \tag{3.11}$$

we have the following estimation of the pressure inside the cavity Ω_2:

$$P_{\Omega_2} \simeq P^\star. \tag{3.12}$$

Proof. By reproducing the proof of Section 3.2.2 using the interface condition resulting of the proposed ARIS model as a starting point, the pressure estimate P_{Ω_2} obtained is

$$P_{\Omega_2} \simeq \frac{\varepsilon_{12}|\Sigma_{12}|}{K}\left(P_{\Omega_1} - g_{\Sigma_{12}}\right) + \frac{\varepsilon_{23}|\Sigma_{23}|}{K}\left(P_{\Omega_3} - g_{\Sigma_{23}}\right) - \frac{1}{K}\int_{\partial\Omega_2} \boldsymbol{w}\cdot\boldsymbol{n}. \tag{3.13}$$

Substituting (3.11) into (3.13), one readily obtains (3.12). This completes the proof. □

Remark 3.3
Looking at the pressure estimate (3.13), it is clear that one can find an infinite amount of pairs $\{g_{\Sigma_{12}}, g_{\Sigma_{23}}\}$ for which $P_{\Omega_2} \simeq P^\star$. The proposed pair (3.11) is nevertheless intuitive as each corrective term counteracts the contribution of the exterior pressure related to the immersed surface on which this term is applied. Moreover, the term related to the cavity volume change is counteracted by both $g_{\Sigma_{12}}$ and $g_{\Sigma_{23}}$ at the same time.

3.3 Numerical experiments

As the core motivation of the present chapter is the simulation of the isovolumetric phases in the LV, two three-dimensional examples mimicking the behavior of such a system are considered. To assess the efficiency of the ARIS model introduced in Section 3.2.3, prescribed reference pressure will be compared with the simulated one in different formulations of the pressure corrective term (3.11). Finally, the choice of the resistive parameter R_i is crucial and requires a specific care. The determination of its value will be discussed, for each numerical example, in the next paragraphs.

In this section and in the rest of this work, the ARIS model (3.9) is discretized in space by using $\mathbb{P}_1/\mathbb{P}_1$ SUPG/PSPG stabilized finite elements for the velocity and the pressure unknowns (see, e.g., [Tez91]). All the numerical experiments presented in what follows have been computed by using the finite element library FELiScE[1]. All the units are expressed in the CGS system, unless specified otherwise.

[1] See https://gforge.inria.fr/projects/felisce/.

3.3.1 Toy problem

A simple academic case is designed to reproduce the setting and the problems described in Section 3.2. The simplified geometry of the fluid domain is given by Ω, which has the shape of a cylinder, as depicted in Figure 3.3a. The domain is divided into 3 parts, successively denoted as Ω_1, Ω_2 and Ω_3, as depicted in Figure 3.3b. Their dimensions are respectively given by $\{r_{\Omega_1} = 1, l_{\Omega_1} = 2\}$, $\{r_{\Omega_2} = 1, l_{\Omega_2} = 6\}$ and $\{r_{\Omega_3} = 1, l_{\Omega_3} = 2\}$, where r and l stand for, respectively, the radius and the length of the cylindric subdomain. Two identical planes surfaces are immersed inside the domain: Σ_{12} is the interface between Ω_1 and Ω_2 whereas Σ_{23} is the interface between Ω_2 and Ω_3, as shown in Figure 3.3b.

The physical parameters for the fluid are $\rho^{\mathrm{f}} = 1.06$ and $\mu = 0.04$. The simulations are carried out for a total time of $t = 0.2$ with a time-step $\tau = 10^{-3}$. The fluid is initially at rest. The whole computational domain Ω is made of 7 375 tetrahedra. Both immersed surface, Σ_{12} and Σ_{23}, are made of 95 triangles.

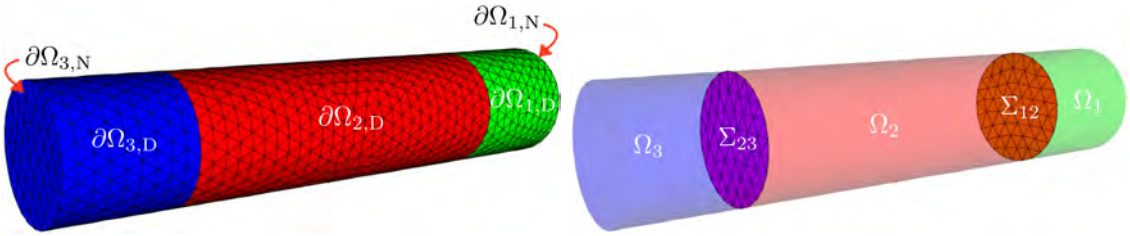

(a) Exterior of the fluid domain.

(b) Interior of the fluid domain.

Figure 3.3 – Computational domains used for the toy problem model.

A no-slip boundary condition is enforced on the solid wall of the large cylinder $\partial\Omega_{1,\mathrm{D}} \cup \partial\Omega_{2,\mathrm{D}} \cup \partial\Omega_{3,\mathrm{D}}$. The following Neumann conditions are prescribed on the inlet and outlet boundaries:

$$\begin{aligned} \boldsymbol{\sigma}(\boldsymbol{u},p)\boldsymbol{n} &= \mathbf{0} \quad && \text{on} \quad \partial\Omega_1, \\ \boldsymbol{\sigma}(\boldsymbol{u},p)\boldsymbol{n} &= -10^5\boldsymbol{n} \quad && \text{on} \quad \partial\Omega_3. \end{aligned}$$

Moreover, a reference pressure $P^\star$, which should be obtained for P_{Ω_2}, is used in the pressure corrective term (3.11). All these pressures have been analytically generated to imitate the main simplified characteristics of a human left heart [FL08] and are depicted in Figure 3.4.

The surface of the middle cavity $\partial\Omega_{2,\mathrm{D}}$ is displaced to mimic the typical behavior of a LV during a heartbeat. In order to address different situations where the incompressibility constraint is broken or not, three different surface velocities, denoted $\boldsymbol{w}_0$, $\boldsymbol{w}_{\text{iso}}$ and $\boldsymbol{w}_{\text{not-iso}}$, evolving with time, are considered. The corresponding displacement field is then obtained thanks to a simple backward Euler method. The motion of the full domain is computed by extending the imposed surface displacements within the domain Ω using an appropriate non-linear lifting operator [LVCF17] (denoted $\boldsymbol{\mathcal{L}}$ in Section 3.2.1). The surface velocities

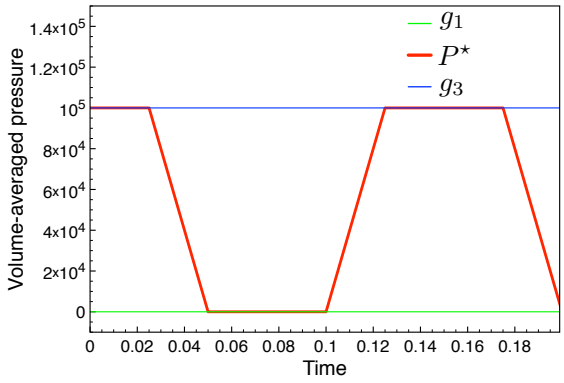

Figure 3.4 – Time history of the reference pressures used for each cavity of the toy problem model.

are given by the following expressions, for all $\boldsymbol{x} \in \partial\Omega_{2,\mathrm{D}}$:

$$\boldsymbol{w}_0(\boldsymbol{x},t) = \quad \mathbf{0}, \qquad \forall t \in \mathbb{R}^+.$$

$$\boldsymbol{w}_{\mathrm{iso}}(\boldsymbol{x},t) = \begin{cases} \mathbf{0}, & \forall t \in \mathbb{R}^+ \mid (R_{12}(t) \neq 0 \text{ and } R_{23}(t) \neq 0)\,, \\ \boldsymbol{r}(\boldsymbol{x},t), & \forall t \in \mathbb{R}^+ \mid (R_{12}(t) = 0 \text{ or } R_{23}(t) = 0)\,. \end{cases}$$

$$\boldsymbol{w}_{\text{not-iso}}(\boldsymbol{x},t) = \begin{cases} \boldsymbol{r}(\boldsymbol{x},t)/10, & \forall t \in \mathbb{R}^+ \mid (R_{12}(t) \neq 0 \text{ and } R_{23}(t) \neq 0)\,, \\ \boldsymbol{r}(\boldsymbol{x},t), & \forall t \in \mathbb{R}^+ \mid (R_{12}(t) = 0 \text{ or } R_{23}(t) = 0)\,. \end{cases}$$

$\boldsymbol{r}$ is a periodic function of period $T = 0.15$, mimicking contraction and dilatation of a pumping heart and tailored to produce a radial displacement. To obtain a negligible shift of the vertices at the immersed surface level, a gaussian profile is prescribed to get a greater displacement at the center of Ω_2 compared with its extremities.

Figures 3.5a–3.5c present some typical snapshots of the displacement field obtained with $\boldsymbol{w}_{\mathrm{iso}}$ and applied to the computational domain, respectively, at $t = 0$ (initial state), $t = 0.04$ (maximum contraction state) and $t = 0.115$ (maximum dilatation state).

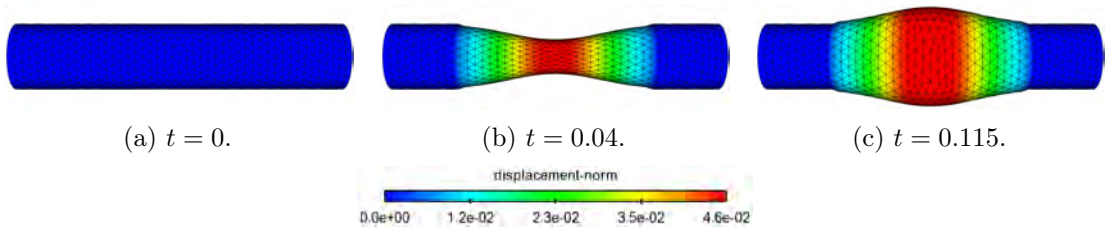

(a) $t = 0$. (b) $t = 0.04$. (c) $t = 0.115$.

Figure 3.5 – Snapshots of the displacement magnitude of the computational domain obtained with $\boldsymbol{w}_{\mathrm{iso}}$ for the toy problem model. The amplitude of the deformation field has been amplified by 10 to increase its visibility.

In this toy problem model, the values of R_{12} and R_{23} are arbitrarily prescribed. Figure 3.6a depicts the evolution of the status of the valves and Figure 3.6b relates it to the evolution of the volume of the cavity Ω_2. Long contraction and dilatation phases are

interspersed with three short isovolumetric phases (respectively defined by the time intervals $[t = 0.025, t = 0.05]$, $[t = 0.1, t = 0.125]$ and $[t = 0.175, t = 0.2]$). During the contraction and dilatation phases, at least one of the two valves is open, while both valves are closed during isovolumetric phases.

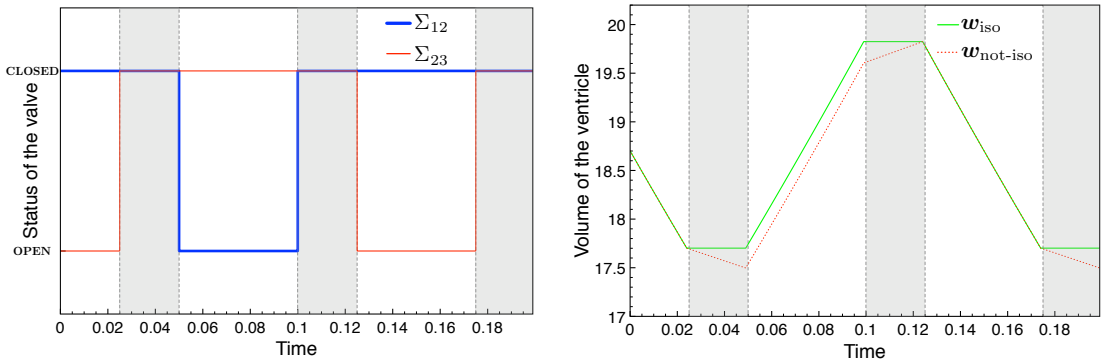

(a) Time history of the status of the valves. (b) Time history of the volume of the cavity Ω_2.

Figure 3.6 – Description of the isovolumetric phases considered for the toy problem model. The grey areas delimit the isovolumetric phases.

The representation of the volume curves corresponding to $\boldsymbol{w}_{\text{iso}}$ and $\boldsymbol{w}_{\text{not-iso}}$ is given in Figure 3.6b. $\boldsymbol{w}_0$ represents the simple case where the computational domain is not moving. On the other hand, $\boldsymbol{w}_{\text{iso}}$ represents a case with perfect isovolumetric phases while $\boldsymbol{w}_{\text{not-iso}}$ reflects non-perfect isovolumetric phases where a slight residual is introduced when both valves are closed – between $t = 0.025$ and $t = 0.05$ and between $t = 0.1$ and $t = 0.125$ – hence inducing a violation of the incompressibility constraint.

The pressure correction is tested using successively the following two terms:

- $g_{\Sigma_i,\text{pc}} \overset{\text{def}}{=} p^+ - P^\star$ on Σ_i: the partial corrective term which only accounts for the contribution of the distal pressures.
- $g_{\Sigma_i,\text{c}} \overset{\text{def}}{=} g_{\Sigma_i,\text{pc}} - \dfrac{1}{K}\int_{\partial\Omega_2} \boldsymbol{w}\cdot\boldsymbol{n}$ on Σ_i: the full corrective term, defined by (3.11), which accounts for both the distal pressures contribution and the residual volume change of the cavity.

An investigation is first provided to evaluate the influence of the resistive term R_i on the efficiency of the pressure correction. For this purpose, a case with no cavity motion (i.e., when $\boldsymbol{w}(t)|_{\partial\Omega_{2,\text{D}}} = \boldsymbol{w_0}(\boldsymbol{x}, t)$) is considered and the term $g_{\Sigma_i,\text{pc}}$ is used to correct the intracavity pressure. The set of values used for the resistive parameter R_i is

$$R_i = \{10^i, \quad i = 0 \dots 10\}.$$

Defining $Q(t)$ as the inlet flow rate and $Q_0(t)$ as the inlet flow rate of a reference case in which no valve model is used, we define the logarithmic scaled residual flow rate Q_{res} as

$$Q_{res}(t) = \log_{10}\left(\frac{Q(t)}{Q_0(t)}\right). \tag{3.14}$$

Its value is reported to quantify the actual flow reduction provided by the resistive immersed surfaces. For each value of R_i, the average pressure inside the cavity Ω_2, denoted $\overline{P_{\Omega_2}}$, is compared with the reference pressure $P^\star$ to evaluate how good the intracavity pressure is corrected.

Following this first investigation, the best value of R_i is then empirically fixed and used for all cases described in the following Table 3.1:

Case	$\boldsymbol{w}\|_{\partial\Omega_{2,\mathrm{D}}}$	$g_{\Sigma_{12}}$	$g_{\Sigma_{23}}$
$T_{1,\mathrm{NC}}$	$\boldsymbol{w}_0(\boldsymbol{x},t)$	0	0
$T_{1,\mathrm{C}}$	$\boldsymbol{w}_0(\boldsymbol{x},t)$	$g_{\Sigma_{12},pc}$	$g_{\Sigma_{23},pc}$
$T_{2,\mathrm{NC}}$	$\boldsymbol{w}_{\mathrm{iso}}(\boldsymbol{x},t)$	0	0
$T_{2,\mathrm{C}}$	$\boldsymbol{w}_{\mathrm{iso}}(\boldsymbol{x},t)$	$g_{\Sigma_{12},pc}$	$g_{\Sigma_{23},pc}$
$T_{3,\mathrm{NC}}$	$\boldsymbol{w}_{\text{not-iso}}(\boldsymbol{x},t)$	0	0
$T_{3,\mathrm{PC}}$	$\boldsymbol{w}_{\text{not-iso}}(\boldsymbol{x},t)$	$g_{\Sigma_{12},pc}$	$g_{\Sigma_{23},pc}$
$T_{3,\mathrm{C}}$	$\boldsymbol{w}_{\text{not-iso}}(\boldsymbol{x},t)$	$g_{\Sigma_{12},c}$	$g_{\Sigma_{23},c}$

Table 3.1 – Cases of pressure correction considered for the toy problem model.

Cases T_1 are designed in order to test the pressure correction in a simple, non-moving domain. Cases T_2 are designed to test the pressure correction in a more complex setting involving domain motion. Cases T_3 are designed to test the pressure correction in an even more challenging setting involving domain motion and breaking of the incompressibility constraint. The subscripts NC, PC and C denote, respectively, "**N**o **C**orrection", "**P**artial **C**orrection", and "**C**orrection". Note that for the cases T_1 and T_2, there is no distinction between partial correction and correction as the cavity is not undergoing volume change during the isovolumetric phases (i.e., when $\int_{\partial\Omega_2} \boldsymbol{w}\cdot\boldsymbol{n} = 0$). The average pressure $\overline{P_{\Omega_2}}$ inside the cavity Ω_2 is systematically computed in these different cases and compared with the prescribed pressure $P^\star$ to quantify the effectiveness of the pressure correction.

3.3.1.1 Results

Sensitivity analysis of the resistance parameter

Figure 3.7 depicts the evolution of $Q_{\mathrm{res}}(t)|_{t=0.17}$ with respect to the resistance value R_i. The time instant $t = 0.17$ has been chosen to allow the flow rate Q_0 to be fully developed in the open channel. Moreover, it represents a time instant where only one valve of the toy problem model is closed, hence allowing to properly quantify the flow reduction of Q compared to Q_0. It is noted that, as the resistance increases, the flow rate through the valves decreases, as expected from the standard RIS model. This result tends to justify the choice of a high value for the resistance R_i.

In Figure 3.8, the pressures $\overline{P_{\Omega_2}}$ and $P^\star$ are compared, with respect to the time, using several values of R_i. From $R_i = 10^0$ to $R_i = 10^6$, the prescribed pressure $P^\star$ and computed pressure $\overline{P_{\Omega_2}}$ match properly during the isovolumetric phases depicting a successful behavior of the pressure correction. One can also notice that for $R_i = \{10^5,10^6\}$, the RIS model is

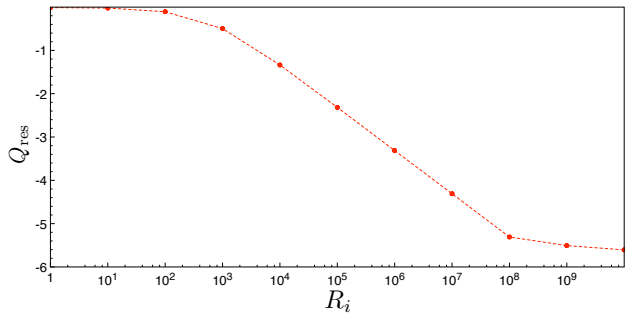

Figure 3.7 – Log relative flow rate through the valves with respect to R_i for the toy problem model.

impermeable enough to also ensure proper pressure values outside the isovolumetric phases. For higher values of R_i, the pressure corrective term cannot ensure a good fit anymore. This justifies the choice of a resistance R_i below 10^6.

In conclusion, it is shown that a trade-off has to be made to ensure that the intracavity pressure is well corrected by the ARIS model while ensuring a good impermeability of the valve. In this specific setting, using $R_i = \{10^5, 10^6\}$ satisfies both conditions: the pressure inside Ω_2 is properly corrected while ensuring a small residual flow rate compared with the open channel flow rate (i.e., Q lower than 1% of Q_0). Based on this study, in the following, the value of the resistance R_i is set to 10^5.

Evaluation of the pressure correction for cases T_1, T_2 and T_3

Figures 3.9a–3.9b depict the results coming from, respectively, the cases $T_{1,\text{NC}}$ and $T_{1,\text{C}}$, for which no motion of the domain is imposed. In the case $T_{1,\text{NC}}$, no pressure correction is applied. During the phases where both valves are closed, it is observed that the average pressure $\overline{P_{\Omega_2}}$ is approximately equal to $5 \cdot 10^4$. This result is coherent with the pressure estimation described by (3.3). Indeed, as $R_{12} = R_{23}$ and $|\Sigma_{12}| = |\Sigma_{23}|$, (3.3) can be reformulated as $P_{\Omega_2} = \frac{1}{2}P_{\Omega_1} + \frac{1}{2}P_{\Omega_3} \simeq 5 \cdot 10^4$, given that $P_{\Omega_1} \simeq 0$ and $P_{\Omega_3} \simeq 10^5$ due to the considered applied Neumann normal boundary conditions. For the corrected case $T_{1,\text{C}}$ (i.e., when we are using the corrective term $g_{\Sigma_i,\text{pc}}$), the intracavity pressure is successfully corrected during the isovolumetric phases, with less than 0.1% difference compared to the reference value.

Figures 3.10a–3.10b depict the results coming from, respectively, the cases $T_{2,\text{NC}}$ and $T_{2,\text{C}}$. In those cases, a domain motion keeping the intracavity volume constant during the isovolumetric phases is imposed. Spurious pressure peaks are noticed after valve transitions (e.g., $t = 0.025$ or $t = 0.05$). These pressure peaks quickly decay (less than five time iterations) toward stable values. As a side note, these spurious pressures are visible even in the non-corrected case. Similar to the cases T_1, the average intracavity pressure is properly predicted by the theoretical analysis (3.3) in case $T_{2,\text{NC}}$. For the case $T_{2,\text{C}}$, using the corrective term $g_{\Sigma_i,\text{pc}}$ allows to get the expected intracavity pressure during the isovolumetric phases.

Finally, Figures 3.11a–3.11c depict the results coming from, respectively, the cases

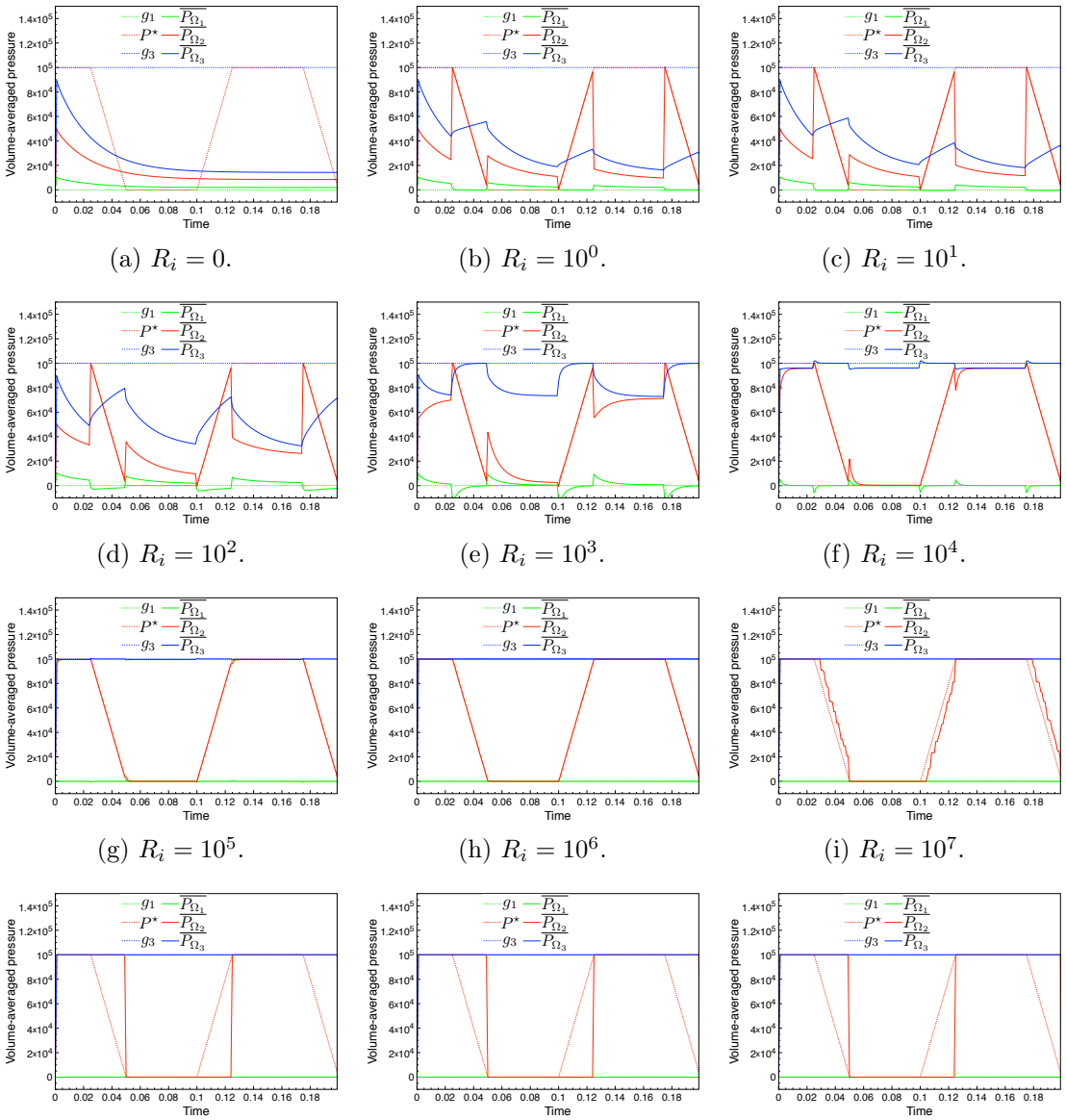

(a) $R_i = 0$. (b) $R_i = 10^0$. (c) $R_i = 10^1$.

(d) $R_i = 10^2$. (e) $R_i = 10^3$. (f) $R_i = 10^4$.

(g) $R_i = 10^5$. (h) $R_i = 10^6$. (i) $R_i = 10^7$.

(j) $R_i = 10^8$. (k) $R_i = 10^9$. (l) $R_i = 10^{10}$.

Figure 3.8 – Time history of the computed pressures obtained with pressure correction for different values of R_i for the toy problem model.

$T_{3,\mathrm{NC}}$, $T_{3,\mathrm{PC}}$ and $T_{3,\mathrm{C}}$. In these cases, an additional difficulty is addressed by considering a residual motion imposed during the isovolumetric phases. Compared to the previous cases $T_{1,\cdot}$ and $T_{2,\cdot}$, a major difference is observed for the intracavity pressure for the non corrected case $T_{3,\mathrm{NC}}$. Indeed, the pressure is strongly offset during the non-perfect isovolumetric phases: positively when the residual motion induces a contraction of the cavity and negatively when it induces a dilatation. This behavior has been predicted by the analysis provided in the discussion of Section 3.2.2. In the partially corrected case $T_{3,\mathrm{PC}}$, it may also be noted that the corrective term $g_{\Sigma_i,\mathrm{pc}}$ is not enough to correct the

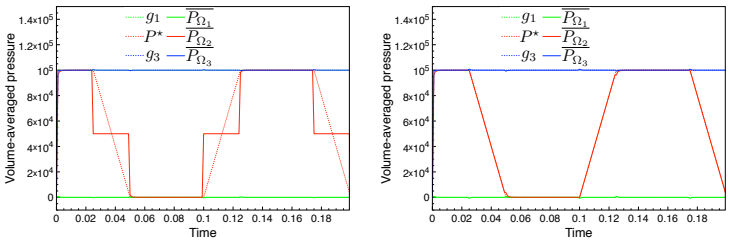

(a) Without correction. (b) With partial correction.

Figure 3.9 – Time history of the computed pressures obtained for the cases T_1.

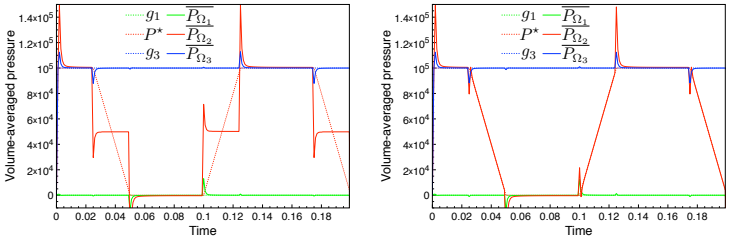

(a) Without correction. (b) With partial correction.

Figure 3.10 – Time history of the computed pressures obtained for the cases T_2.

intracavity pressure as the residual motion of the cavity is not taken into account into the correction. On the opposite, using the complete corrective term $g_{\Sigma_i,\mathrm{c}}$, the intracavity pressure is corrected much more efficiently. In this case, it is observed that both the overall behavior of the intracavity pressure and its value match the prescribed pressure $P^\star$. Nevertheless, a small gap between the two pressure curves is observed, probably caused by the non-perfect validity of the simplifying assumptions (H1) and (H2).

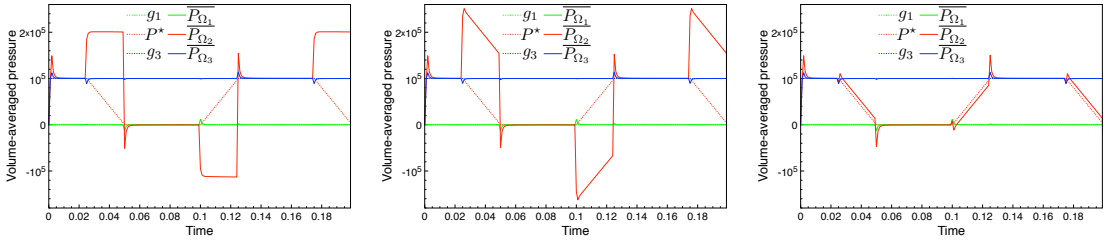

(a) Without correction. (b) With partial correction. (c) With correction.

Figure 3.11 – Time history of the computed pressures obtained for the cases T_3.

3.3.2 Simplified heart model

Since the pressure correction introduced in Section 3.2 has proved its benefits in correcting the intraventricular pressure of the toy problem model in several settings, we now use the ARIS model to assess its robustness and to confirm its benefits in a more realistic setting. In particular, we consider a case involving a simplified geometry of the

human left heart with physical values comparable to quantities that can be observed in a physiological setting. Therefore, in this section, the term realistic and physiological will be used to refer to this case, even though it is admitted that it is a simplification of reality.

We consider, for the fluid domain Ω, a simplified anatomically realistic portion of the human heart, as depicted in Figure 3.12a. For simplicity, we will use the physiological terminology of the cardiology to designate the different parts of the considered computational domain. Based on the previous notations of Section 3.2, the computational domains Ω_1, Ω_2, Ω_3 correspond, respectively, to the portion of the atrium, to the full ventricle and to the portion of the aorta, as shown in Figure 3.12b. The geometry comes from a CT scan realized by Zygote (see Section 2.2.1) and has been processed as follows.

The right side of the heart has been removed. The volumes corresponding to the left ventricle, to the left atrium and to the aortic root have been extracted from the rest of the geometry. The pulmonary veins and aorta openings have been closed using a planar surface. The endocardial surface has been smoothed to remove the trabeculae and papillary muscles. Two immersed resistive valves, Σ_{12} and Σ_{23}, corresponding, respectively, to the mitral valve (see Figure 3.12c) and to the aortic valve (see Figure 3.12d) have been inserted into the geometry. The former has been designed with the 3-matic software[2] based on physiological *in vivo* data [RLWS70, RSE52, DPM64, N+16, VCV+08] whereas the latter was already included in the Zygote model. More information about the geometry of the mitral valve is provided in Appendix A. Then, each volume – namely, 1) the left atrium, 2) the cavity defined by the open and closed configurations of the mitral valve, 3) the left ventricle and 4) the aortic root – have been meshed using the 3D meshing software GHS3D[3] [GHS90] ensuring that surface meshes shared by two adjacent volumes are conformal. Finally, all the resulting volume meshes have been fused together. Typical dimension of the resulting simplified left heart model can be found in Appendix B.

The physical parameters for the fluid are $\rho^{\mathrm{f}} = 1.06$ and $\mu = 0.04$. The simulations are carried out for a total time of $t = 0.85$, based on averaged physiological values for the heartbeat of a young adult [Har15], with a time-step $\tau = 10^{-3}$. The fluid is initially at rest. The whole computational domain Ω is made of 326 090 tetrahedra. The immersed surfaces, Σ_{12} and Σ_{23} are made of, respectively, 816 and 1 474 triangles.

In order to enhance the physiological validity of the considered numerical example, an electromechanical simulation [CFG+09, CLMS12] was used in order to prescribe some boundary conditions of the fluid simulation. We refer to Appendix B for more information about electromechanics. The surface displacement $\boldsymbol{d}|_{\partial\Omega_{2,\mathrm{D}}}$ obtained from the electromechanical simulation is extended throughout the domain Ω using the ALE framework. A no-slip boundary condition on the velocity is enforced on $\partial\Omega_{1,\mathrm{D}} \cup \partial\Omega_{2,\mathrm{D}} \cup \partial\Omega_{3,\mathrm{D}}$. The pressure is prescribed on the inlet $\partial\Omega_{1,\mathrm{N}}$ – corresponding to the cut ends of the pulmonary veins – as well as on the outlet $\partial\Omega_{3,\mathrm{N}}$ – corresponding to the lower cut section of the aorta

[2] See https://www.materialise.com/.
[3] See https://team.inria.fr/gamma3/gamma-software/ghs3d/.

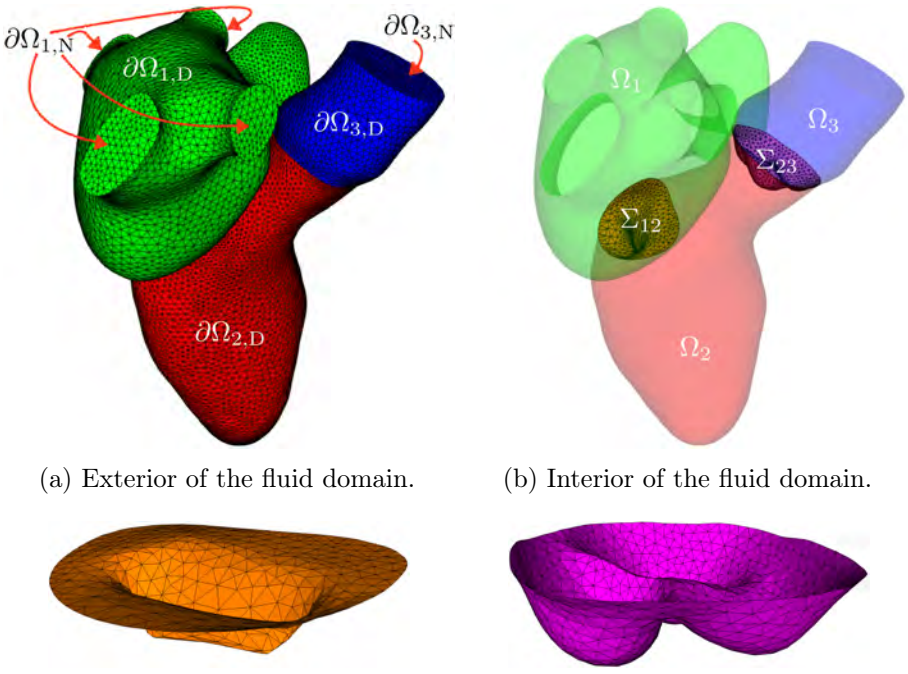

(a) Exterior of the fluid domain.

(b) Interior of the fluid domain.

(c) Immersed surface Σ_{12}.

(d) Immersed surface Σ_{23}.

Figure 3.12 – Computational domains used for the realistic model.

– using the following Neumann normal boundary conditions:

$$\begin{aligned} \boldsymbol{\sigma}(\boldsymbol{u},p)\boldsymbol{n} &= -g_1\boldsymbol{n} \quad \text{on} \quad \partial\Omega_1, \\ \boldsymbol{\sigma}(\boldsymbol{u},p)\boldsymbol{n} &= -g_3\boldsymbol{n} \quad \text{on} \quad \partial\Omega_3. \end{aligned}$$

The amplitude of these pressures, respectively denoted g_1 and g_3, as well as the intraventricular pressure $P^\star$ used in the corrective term (3.11), are given by time-dependent values obtained from Windkessel models which are coupled to the electromechanical model [SMCCS06] (see Appendix B). Their values are depicted in Figure 3.13. Finally, a backflow stabilization based on a local regularization of the fluid velocity along the tangential directions on the Neumann boundaries [MBH+11] is applied on $\partial\Omega_{1,\mathrm{N}}$ and on $\partial\Omega_{3,\mathrm{N}}$.

The surface displacement prescribed on $\partial\Omega_{2,\mathrm{D}}$ is extended to the rest of the domain using an appropriate non-linear lifting operator [LVCF17] (denoted $\boldsymbol{\mathcal{L}}$ in Section 3.2.1). Figures 3.14a–3.14c present some typical snapshots of the resulting displacement field, applied to the computational domain, respectively, at $t = 0$ (initial state), $t = 0.2$ (maximum dilatation state) and $t = 0.5$ (maximum contraction state).

In this example, the temporal evolutions of R_{12} and R_{23} are not manually prescribed anymore. Instead, we now consider the instantaneous opening and closing dynamics of the original RIS model as detailed in previous Figure 2.11. For the immersed surface Σ_{12}, a positive pressure jump and an existing backflow mean, respectively, $p^+ - p^- > 0$ on Σ_{12} and $\int_{\Sigma_{12}} \boldsymbol{u}\cdot\boldsymbol{n}^+ < 0$. For the immersed surface Σ_{23}, it means, respectively, $p^- - p^+ > 0$ on Σ_{23}

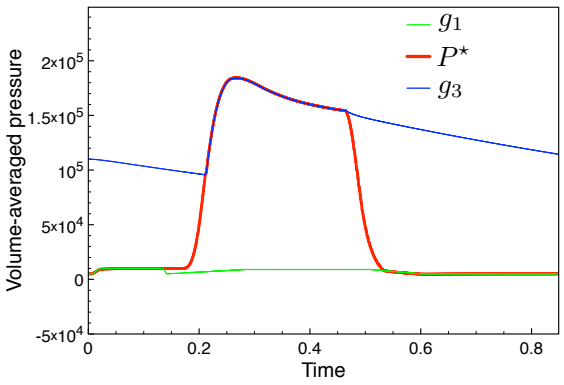

Figure 3.13 – Time history of the reference pressures used for each cavity of the realistic model.

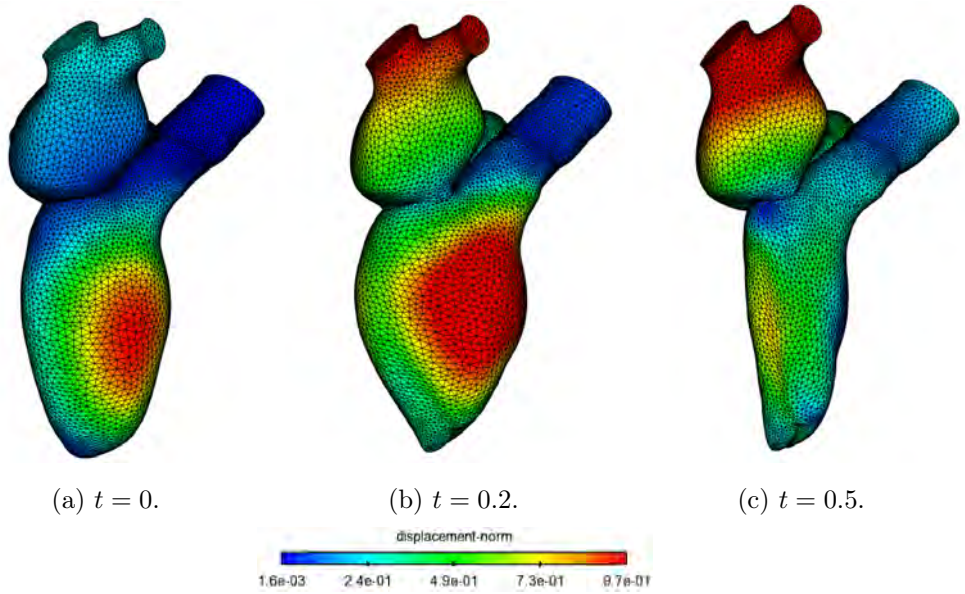

(a) $t = 0$. (b) $t = 0.2$. (c) $t = 0.5$.

Figure 3.14 – Snapshots of the displacement magnitude of the computational domain obtained for the realistic model.

and $\int_{\Sigma_{23}} \boldsymbol{u} \cdot \boldsymbol{n}^- < 0$. A refractory time, typically set to a few time-steps, is introduced to prevent the valve from changing its status immediately after a first switch. This given constraint ensures a full development of the flow physics near the valve before a possible second switch.

Based on the pressure values previously depicted in Figure 3.13, two short isovolumetric phases (respectively defined by the time intervals $[t = 0.135, t = 0.215]$ and $[t = 0.465, t = 0.533]$) are then expected. The evolution of the volume of the cavity Ω_2, given by the previous mentioned electromechanical simulation (see Appendix B), is portrayed in Figure 3.15. As observed in real physiological cases [WBWW78], the dilatation of the ventricle lasts longer than its contraction. Two zooms (the blue arrows) show that the incompressibility constraint is not perfectly verified during the isovolumetric phases.

Therefore, the full pressure correction (3.13) is expected to be mandatory to compute the correct values of the pressures and thus the correct behavior of the resistive immersed valves.

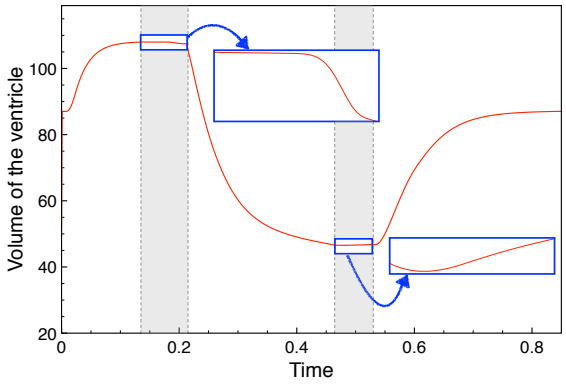

Figure 3.15 – Time history of the volume of the ventricle for the realistic model. The grey areas delimit the expected isovolumetric phases.

In the following, the ARIS model is applied on this realistic model and the results obtained without pressure correction are compared with the ones obtained by using the corrective term given by (3.11).

To assess the sensitivity of the efficiency of the pressure correction with respect to the parameter R_i and to confirm our previous choice, the same analysis, as the one described in Section 3.3.1, is carried on here. The set of values used for the resistive parameter R_i is still

$$R_i = \{10^i, \quad i = 0 \dots 10\}.$$

Eventually, as the structure of the flow dynamics inside the ventricle can be used as a predictor of diseases or malfunction [DQCP07, CMN16], it is crucial to ensure that the new pressure correction does not perturb the velocity field. A comparative study of the velocity and pressure fields obtained during the first isovolumetric phase, with and without the pressure correction, is undertaken in order to highlight the absence of disruption. The first phase is the most pertinent for this comparison as its correct computation is crucial and mandatory to not perturb the physics of the developed flow and thus the next time-steps of the simulation.

3.3.2.1 Results

In Figure 3.16, the matching of the evolution of the pressures $\overline{P_{\Omega_2}}$ and $P^\star$, obtained with the pressure correction, is compared for several values of R_i with respect to the time. The goal is to determine suitable value for the resistive parameter.

Firstly, positive and negative peak values are observed for $\overline{P_{\Omega_2}}$, respectively, at $t = 0.21$ and at $t = 0.54$ (i.e., respectively, just after the first and the second isovolumetric phases), on all cases. This behavior is similar to what has been observed for the toy model in Section 3.3.1.1. Moreover, even for a case where the pressure correction is not applied (i.e., when $R_i = 0$), the same pressure peaks are obtained, as depicted in Figure 3.16a. This

highlights the fact that these local quickly decaying extrema for $\overline{P_{\Omega_2}}$ are not induced by the introduced pressure correction. A possible explanation would be that the resistance changes, due to valve opening and closing, are explicitly imposed to the fluid. As a result, some time-steps are required for the fluid to adapt to these topological changes, inducing pressure oscillations. We refer the reader to Section 4.4 for some perspectives on how to tackle this behavior.

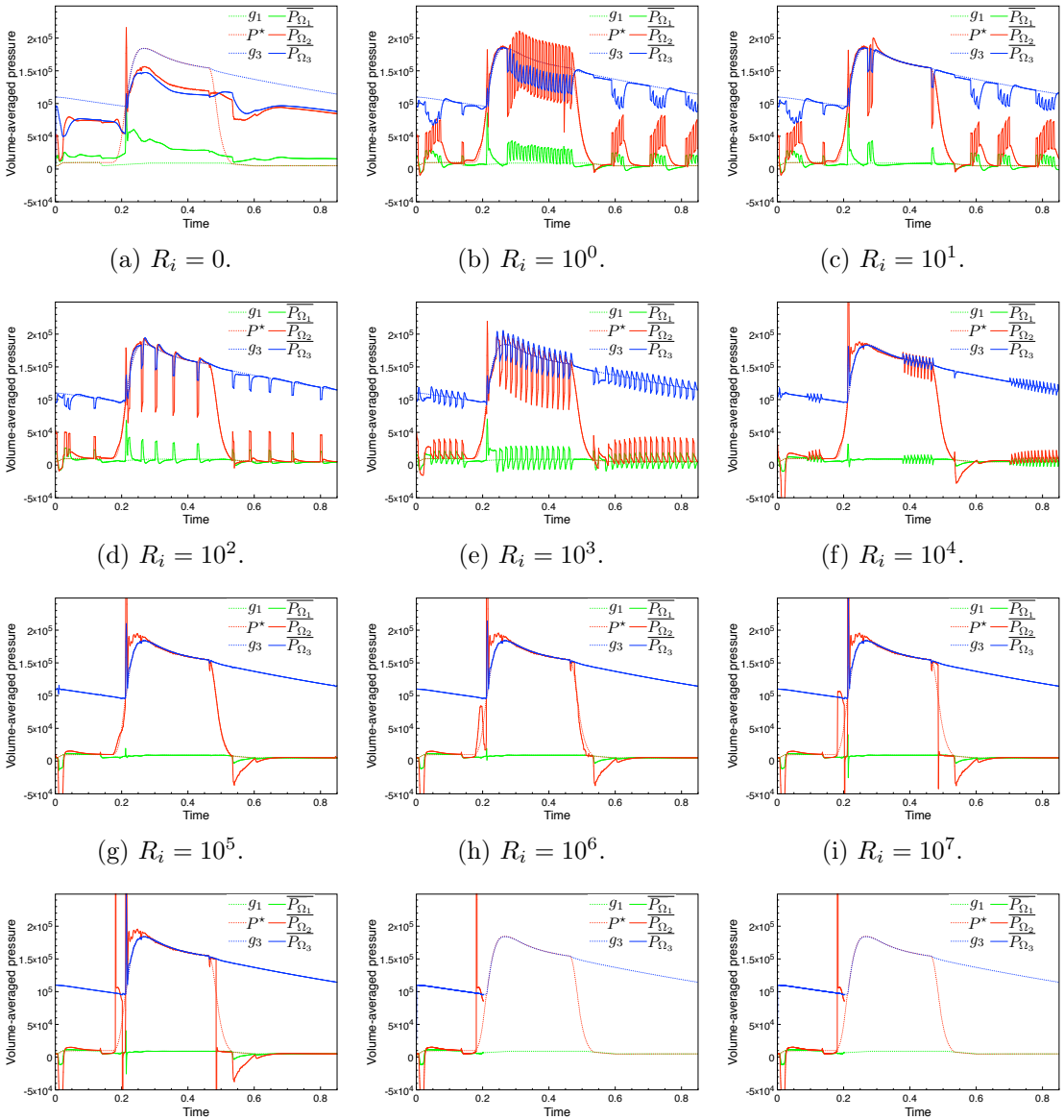

(a) $R_i = 0$. (b) $R_i = 10^0$. (c) $R_i = 10^1$.

(d) $R_i = 10^2$. (e) $R_i = 10^3$. (f) $R_i = 10^4$.

(g) $R_i = 10^5$. (h) $R_i = 10^6$. (i) $R_i = 10^7$.

(j) $R_i = 10^8$. (k) $R_i = 10^9$. (l) $R_i = 10^{10}$.

Figure 3.16 – Time history of the computed pressures obtained with pressure correction for different values of R_i for the realistic model.

Figure 3.16a depicts the case where no immersed valve is used (as R_i is set to 0) and where the matching of the pressures is hence, obviously, impossible to obtain. The

computed pressure $\overline{P_{\Omega_2}}$ of Figures 3.16b–3.16f fail to match the reference $P^\star$ outside the isovolumetric phases, due to the bad behavior of the immersed valves which keep fluctuating quickly between their closed and open configurations. This phenomenon is illustrated by the pressures oscillations. Among all the cases, the best pressure matching is obtained for $R_i = 10^5$, as observed in Figure 3.16g. When the resistance is increased beyond this value, the intraventricular pressure is not matching the reference pressure anymore, especially for the first isovolumetric phase, as depicted in Figures 3.16h–3.16j. For the case $R_i = 10^6$, portrayed in Figure 3.16h, even if $\overline{P_{\Omega_2}}$ is confined between $\overline{P_{\Omega_1}}$ and $\overline{P_{\Omega_3}}$, it is not monotonous, as it should be in a physiological case. For the two following cases, due to the inaccurate computed physics, and more precisely the wrong intraventricular pressure, the valve status change several time during the isovolumetric phases while they were supposed to keep being closed. Beyond the case of $R_i = 10^8$, where $\overline{P_{\Omega_2}}$ present very strong oscillations for $t \in [0.135, 0.215]$ and for $t \in [0.465, 0.533]$, as represented in Figure 3.16j, the other cases fail to converge and the simulations stops around $t = 0.2$, as portrayed in Figures 3.16k–3.16l. Based on this study, in the following, the value of the resistance R_i is now set to 10^5.

Figures 3.17a–3.17b depict the pressure curves coming from, respectively, the case without and with the use of the corrective term (3.11), both for the optimized value of $R_i = 10^5$. It must be noted that, except for the isovolumetric phases, the computed pressures between both cases are almost perfectly identical. This underlines the fact that the corrective term, only used during the isovolumetric phases, does not have an impact on the other instants of the simulation, as expected.

As portrayed in Figure 3.17a, for the case without correction, $\overline{P_{\Omega_2}}$ is not well-defined when both valves are closed and get arbitrary values. Therefore, this induces wrong behaviors of the immersed valves. On the opposite, when the corrective term is applied, $\overline{P_{\Omega_2}}$ is now correctly defined and the computed pressures match the reference ones, as highlighted in Figure 3.17b.

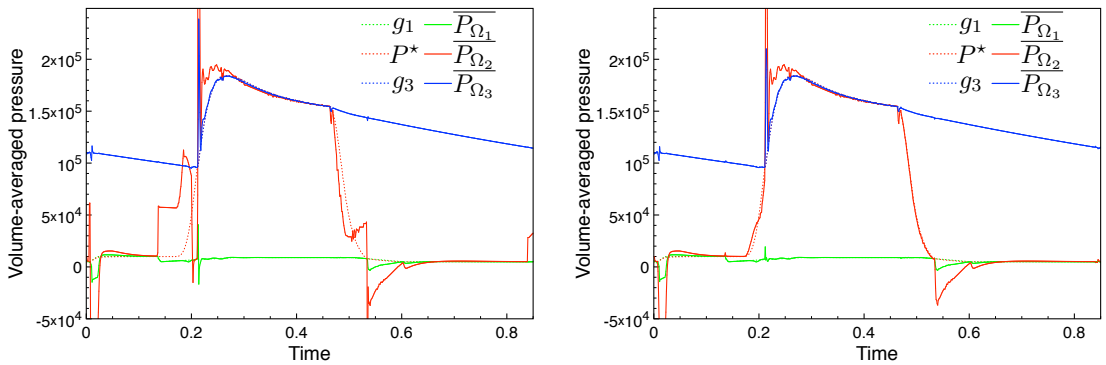

(a) Without correction.

(b) With correction.

Figure 3.17 – Time history of the computed pressures for the optimized value of $R_i = 10^5$ for the realistic model.

The time history of the valves status of each immersed surface Σ_{12} and Σ_{23} obtained for the cases without and with pressure correction are depicted, respectively, in Figures 3.18a–

3.18b. Major differences are observed during the first isovolumetric phase: non physiological changes of configuration of each valve are obtained when no pressure correction is applied while the expected correct behavior, similar to the one used for the toy model in Figure 3.6a, is get with the pressure correction. This difference of behavior is crucial to correct as a wrong isovolumetric phase will induce a erroneous computation of the flow characteristics during the rest of the simulation.

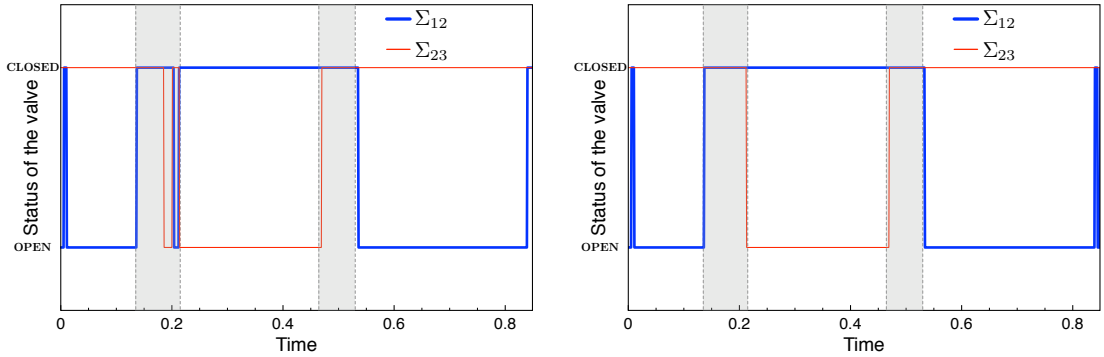

(a) Without correction.

(b) With correction.

Figure 3.18 – Time history of the status of the valves obtained for the realistic model. The grey areas delimit the expected isovolumetric phases.

Figures 3.19a–3.19b present the snapshots of the velocity field obtained during the middle of the first isovolumetric phase, at $t = 0.185$, respectively, for the case without and with pressure correction. The same typical features of the velocity field, especially its vorticity, are obtained for the two cases, illustrating the fact that the additional normal stress term (3.8), applied on the immersed surfaces, keeps the velocity field comparable. To quantitatively compare these two fields, the normalized Root Mean Square (RMS) of the difference of velocities in the ventricular cavity is depicted in Figure 3.20 for the first portion of the cardiac cycle, for which the time history of the valve status are comparable. In particular, during the isovolumetric phase (starting at $t = 0.135$), the differences between the two flow fields is less than 4% (corresponding to an absolute RMS of approximately 0.35).

Snapshots of the pressure fields obtained without and with ARIS pressure correction are given in Figures 3.21a–3.21b, respectively. On both figures, observation of the ventricular cavity reveals that even though P_{Ω_2} is not perfectly homogeneous on the scale of the ventricle – as it is assumed in (H2) – the pressure values near the first immersed surface Σ_{12} and near the second immersed surface Σ_{23} are approximately equal. This observation highlights the fact that using the same value P_{Ω_2} for the negative sided–restrictions of the pressure p^- in (3.5) and (3.6), respectively, for both immersed surfaces Σ_{12} and Σ_{23}, is coherent.

Based on the reference pressures of Figure 3.13, $\overline{P_{\Omega_2}}$ is expected, at $t = 0.185$, to belong to the interval of values $\left[\overline{P_{\Omega_1}}, \overline{P_{\Omega_3}}\right]$. The intraventricular pressure is correctly computed when pressure correction is applied whereas, when there is no correction, its value is overestimated and even exceed the aortic one, as illustrated in Figure 3.21a. This

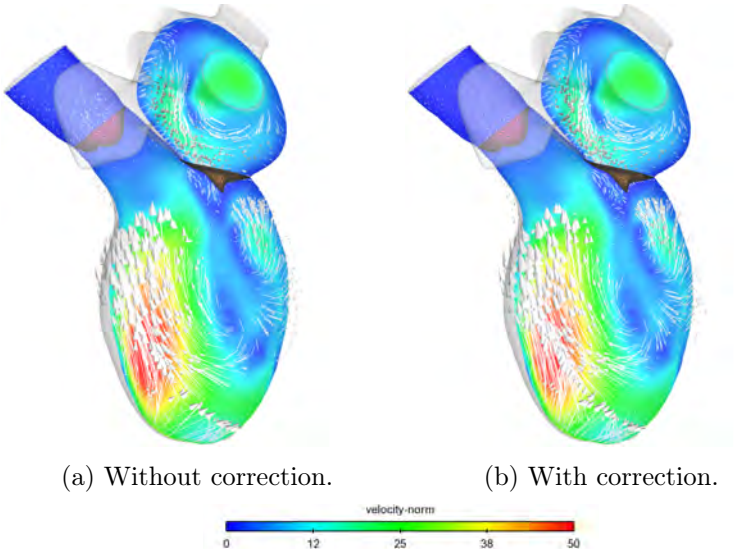

(a) Without correction. (b) With correction.

Figure 3.19 – Snapshots of the velocity field obtained at $t = 0.185$ for the realistic model.

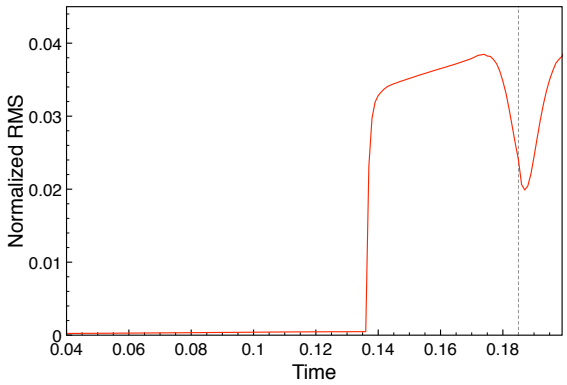

Figure 3.20 – Time history of the normalized RMS, restricted to the portion of the cardiac cycle where the time history of the valve status are comparable. The vertical gray dotted line represents the time instant at which the two velocity fields depicted in Figure 3.19 are compared.

highlights the benefits brought by the pressure corrective term (3.11) for the computation of the correct transitional pressure during the isovolumetric phases.

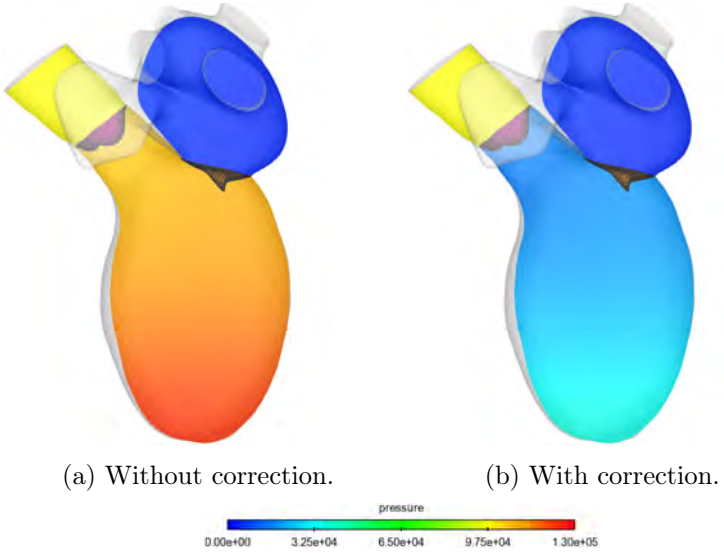

(a) Without correction. (b) With correction.

Figure 3.21 – Snapshots of the pressure field obtained at $t = 0.185$ for the realistic model.

3.4 Conclusions

In this chapter, a new reduced model for heart valves has been introduced for the description of the isovolumetric phases within an uncoupling approach.

The generic problem of a fluid cavity enclosed by two closed RIS valves has been considered by providing an estimate of the internal pressure in Section 3.2.2. A simplified expression estimating the pressure of the cavity has been derived, highlighting that its value depends on several parameters including the exterior pressures, the resistive term of the RIS model and the wall cavity velocities. This analysis proved why realistic isovolumetric phases could not be obtained with the standard RIS model. In Section 3.2.3, the new reduced model, called ARIS, has been presented. An additional normal stress term was introduced in order to counteract the contributions of the exterior pressures and wall velocities.

In Section 3.3, two numerical examples have been considered to illustrate the benefits of this new approach. First, a toy model with a simplified geometry has been designed to reproduce the main characteristics of more complex heart simulations. Arbitrary pressure values and several different domain motions have been prescribed to test the efficiency of the ARIS model in different configurations. The second numerical example has consisted of a physiological left heart geometry where the pressure values and domain motions were provided by an external electromechanical simulation. In all those cases, the original RIS model failed to properly model the intracavity pressures and the valves behavior during the isovolumetric phases. These experiments highlighted that the intracavity pressure could be computed using the pressure estimate described by (3.3). It also highlighted that the violation of the incompressibility constraint and its correction is a key challenge to compute the correct intraventricular pressure during the isovolumetric phases.

In both numerical examples, an analysis of the influence of the valve resistive parameter R_i showed that a trade-off had to be made between a proper correction of the intracavity pressure and an acceptable impermeability of the valves. Indeed, the introduced corrective term benefits from the fact that the RIS model is penalizing the fluid on the immersed surfaces and is only enforcing Dirichlet boundary conditions in a weak sense. However, as the resistive term keeps increasing, the RIS model converges toward a singular problem equivalent to imposing only Dirichlet boundary conditions. In this setting, the pressure correction was not working anymore.

A suitable value of R_i has been empirically determined in each example and its use in the ARIS model led to strong improvements in the physiological validity of the numerical simulations compared to the traditional RIS model. In the cardiac test case, it was shown that the ARIS model was able to control the left ventricular pressure during the isovolumetric phases resulting in a better physiological behavior of the valves. Moreover, the ARIS model properly corrected the intracavity pressure without alteration of the velocity field and its main features.

The proposed approach therefore offers a good compromise between standard uncoupling and complex FSI models. By expanding the original RIS formulation with an additional reference value, a realistic behavior of the intracavity pressure during the isovolumetric phases is partially recovered without using fully coupled fluid-structure models. We further

illustrate the possibilities offered by this resulting ARIS model in Chapter 4, in the context of the numerical simulation of implantable intracardiac devices.

Acknowledgements: The authors wish to thank D. Chapelle, P. Moireau, R. Chabiniok, G. Bureau and colleagues, from the M3DISIM Inria project-team, for providing data on displacements and pressure of the left ventricle, used in Section 3.3.2, and for their support with the mechanical simulations. The research has been partially supported by a CIFRE Ph.D convention established between INRIA Paris and Philips Research, France.

Chapter 4

Simulation of implantable cardiovascular devices with the augmented resistive immersed surfaces valve model

In this chapter, we illustrate the capabilities of the ARIS model, introduced in Chapter 3, by considering the numerical simulation of the implantable cardiovascular devices mentioned in Chapter 1. The goal here is to highlight the benefits brought by this model when considering realistic cases, despite its simplicity compared to FSI approaches.

Some of the results on mitral regurgitation presented in this chapter have been reported in:

- A. This, L. Boilevin-Kayl, H. Morales, O. Bonnefous, P. Allain, M.A. Fernández and J.F. Gerbeau, **One Mesh To Rule Them All: Registration-Based Personalized Cardiac Flow Simulations.** *FIMH 2017 – 9th International Conference on Functional Imaging and Modeling of the Heart, June 2017, Toronto, Canada.* Available online: `https://hal.inria.fr/hal-01512309`.

Contents

4.1 Introduction

The performance and benefits of bioprosthetic valves, designed for the treatment of MR, are usually evaluated on clinical values (e.g., effective orifice area, para-valvular leakage, transvalvular pressure drop, ...) accessible by echocardiography [Bac97]. The

most commonly used artifical valve is the trileaflet one which has clinically been proven to ensure long-term durability [V+10]. Recent studies showed that the intraventricular flow can be significantly altered after the implantation of such an artificial valve at the mitral position [F+10, PDT10]. This can be explained by modifications of the left ventricular hemodynamics induced by factors not yet clinically evaluated, such as valve geometry and orientation [SLG16]. In fact, the structure of the flow vortex during the filling phase is an indicator of cardiac health [GRK+06, ACK+13] and abnormal flow behaviors can be used to predict early development of cardiac diseases [PD15, PLCAT14]. This explains the strong clinical interest for efficient predictive numerical simulations able to reproduce such physiological phenomena. This chapter aims at illustrating the capabilities of the RIS and ARIS models, introduced in Chapters 2 and 3, to model hemodynamics of MR and of its treatment.

For this purpose, as a first numerical example, a simplified simulation of MR is computed with the original RIS model and is compared to its corresponding healthy configuration simulated with the ARIS model. Then, numerical simulations computed with the ARIS model are used to assess the impact of two different artificial valves on hemodynamics of the LV in a context of Mitral Valve Replacement (MVR). The goal is to numerically point out that the structure of intraventricular blood flow obtained with the D-shape monoleaflet valve from Epygon is much more physiological than the one induced by the tricuspid valve (also known as trileaflet valve) which is however used in many surgeries (see, e.g., [BCM60, RGDRC17]). In both numerical experiments, the native valve case computed with the ARIS model will be considered as the reference for the comparison of results.

The rest of this chapter is organized as follows. Section 4.2 introduces the geometries and configurations of the immersed valves considered through this chapter as well as additional elements of modeling for the numerical simulations. In Section 4.3, the two studies on MR and MVR, whose purpose is detailed above, are computed and their results are discussed. Finally, the main results obtained with the ARIS model are summarized in Section 4.4.

4.2 Problem setting

In this section, the mathematical models and notations are those of Chapter 3. In the following, we will refer to the native mitral valve by “native valve”, to the bioprosthetic tricuspid valve by “tricuspid valve” and to the D-shape monoleaflet valve from Epygon by “Epygon valve”.

4.2.1 Immersed valves configurations

The fluid domain Ω is the same as the one depicted in Figure 3.12a. The immersed valve Σ_{23}, which represents the aortic valve, is identical to the one depicted in Figure 3.12b and is located in the same place. Only the immersed valve Σ_{12}, which represents the mitral valve, is different. Its open and closed configurations are depicted in Figure 4.1 for the three different valves.

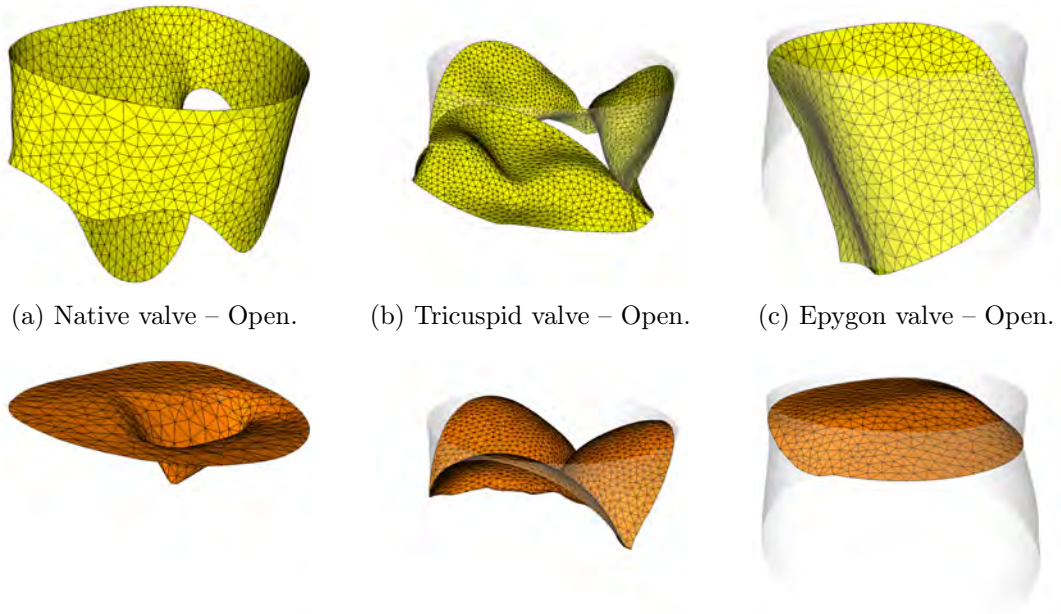

(a) Native valve – Open. (b) Tricuspid valve – Open. (c) Epygon valve – Open.

(d) Native valve – Closed. (e) Tricuspid valve – Closed. (f) Epygon valve – Closed.

Figure 4.1 – Computational domains configurations used for the different immersed valves. The open configurations, colored in yellow, are expected to have an important impact on the structure of the intraventricular flow. The closed configurations are colored in orange and the immersed walls, linking the valves to the mitral annulus (see Figure 4.2c below), in transparent light grey.

The open and closed configurations of the native valve have been designed using physiological data. The closed configuration of the tricuspid valve is coming from a previous work. Its corresponding open configuration has been computed in a FSI framework starting from the closed configuration and using a following pressure. Finally, the open and closed configurations of the D-shape monoleaflet valve have been directly provided by Epygon, thanks to digitization of its existing device. More information about the geometry of each valve as well as their associated references, when available, are provided in Appendix A.

A particular point of attention is the upper part of the LV surface which must fit the immersed mitral valve. Note that the geometry of this part slightly changes with the considered valve in order to match the corresponding annulus, as depicted in Figure 4.2. An electromechanical simulation must be run for each type of valve in order to provide a displacement field matching the associated upper part of the LV surface in the further fluid simulations. More information about this matching and the extraction of results are provided in Appendix B.

Finally, the spatial discretization of all the fluid computational domains Ω, Σ_{12} (in open and closed configurations) and Σ_{23} are given in the following Table 4.1 for the different valves cases:

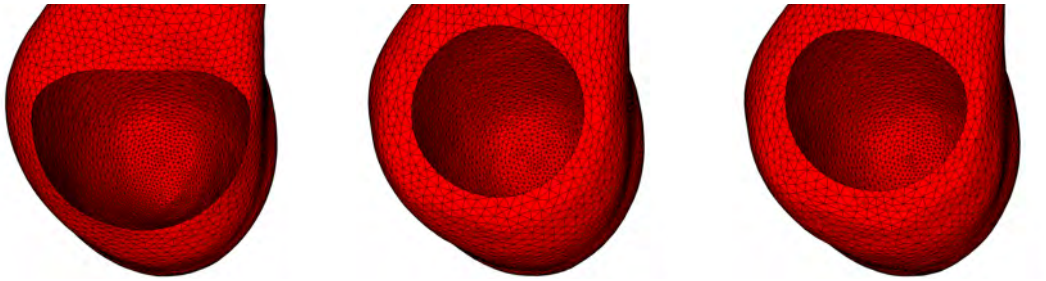

(a) Native valve. (b) Tricuspid valve. (c) Epygon valve.

Figure 4.2 – Upper part of the ventricle surface of the considered computational domain for the different valves.

Case	Ω	Σ_{12} – open	Σ_{12} – closed	Σ_{23}
Native valve	316 100 tetrahedra	1 867 triangles	816 triangles	1 474 triangles
Tricuspid valve	409 244 tetrahedra	4 277 triangles	3 177 triangles	1 474 triangles
Epygon valve	335 848 tetrahedra	1 054 triangles	815 triangles	1 474 triangles

Table 4.1 – Size of all the computational domains Ω, Σ_{12} and Σ_{23} for the different immersed valves.

4.2.2 Simulation time and boundary conditions

The boundary conditions and physical parameters considered here for all the numerical simulations through this chapter are identical to the ones provided in Section 3.3.2. The only difference between the two examples concerns the total time of the simulation: for the comparison of cardiac hemodynamics between the different valves (and, in particular, of the intraventricular flow during the diastole), instead of considering one single heartbeat, the simulation is run for a total time $t = 2.55$, corresponding to three full heartbeats of a young adult. The idea is to get a periodic behavior independent of the initial conditions. On the opposite, for the simulation of MR, computing one heartbeat is enough since the purpose here is simply to highlight the differences occurring during the systole between two healthy and regurgitant configurations.

In the following, only the native valve case is depicted as this geometry is the same in both numerical examples. In addition, the computational domains for the tricuspid and the Epygon valves being almost identical, depicting them would be unduly redundant. Figures 4.3a–4.3i present some typical snapshots of the resulting displacement field, obtained for the case of the native valve, at different instants of the three heartbeats. Compared to Figure 3.14, major differences can be observed for the atrium. They are discussed later in Section 4.2.3.

The corresponding LV volume is depicted with respect to the time for the case of the native valve in Figure 4.4. Note that the consideration of several heartbeats allows a clear definition of the atrial systole (described in Section 1.3.1) which was not previously observed in Figure 3.15.

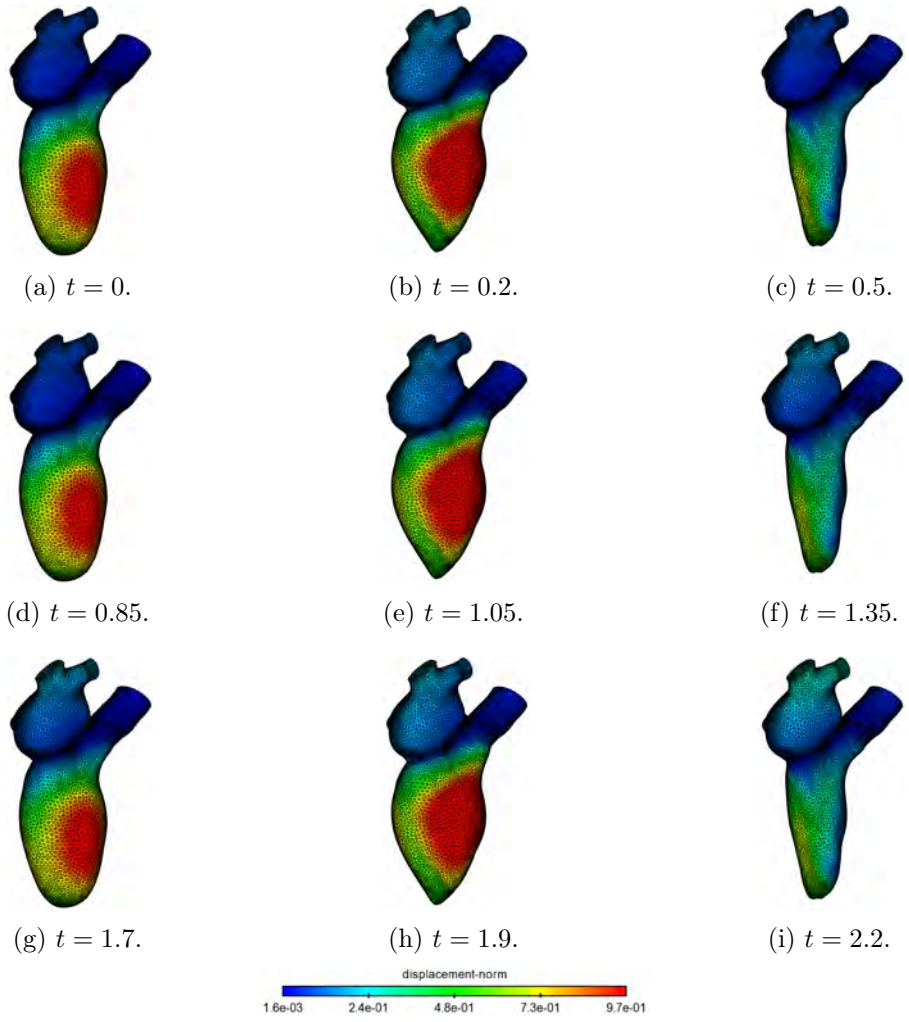

(a) $t = 0$. (b) $t = 0.2$. (c) $t = 0.5$.

(d) $t = 0.85$. (e) $t = 1.05$. (f) $t = 1.35$.

(g) $t = 1.7$. (h) $t = 1.9$. (i) $t = 2.2$.

Figure 4.3 – Snapshots of the displacement magnitude obtained for the case of the native valve at different instants of the three heartbeats. Each line corresponds to a heartbeat. For a given heartbeat (meaning, for a given line), the first column corresponds to the initial state, the second one corresponds to the maximum contraction state and the last one corresponds to the maximum dilatation state.

The amplitude of the pressures considered for the boundary conditions and for the pressure correction in the context of the native valve case, are depicted with respect to the time in Figure 4.5.

4.2.3 Stiffening of the immersed valves

As mentioned in Section 4.2.1, the open configuration of the immersed mitral valve is expected to have an important impact on the structure of the intraventricular flow. Based on the displacement field applied on the LV surface, the edge belonging to the mitral valve, which is linked to the mitral annulus, may be subject to important deformations as

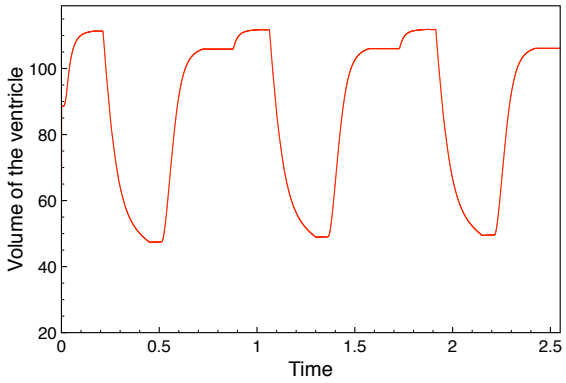

Figure 4.4 – Time history of the volume of the ventricle for the case of the native valve.

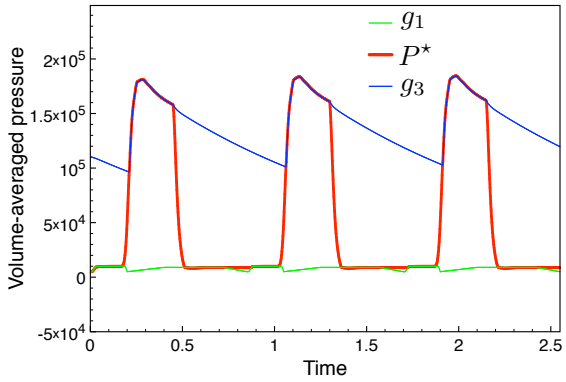

Figure 4.5 – Time history of the reference pressures used for each cavity for the case of the native valve.

the LV is greatly distorted during the simulated heartbeats. In order to counteract this phenomenon, a stiffening (based on an original idea from [STB03, STB04]) is applied to the tetrahedra of the fluid domain which are in the vicinity of the mitral valve. This is done by multiplying their associated Lamé coefficients, that are used in the expression of the lifting operator $\boldsymbol{\mathcal{L}}$ (see Section 3.3.2), by 200.

This stiffening ensures that the open configurations of the immersed valves (see Figure 4.1) are indeed the ones inducing the structure of the computed intraventricular flow and not arbitrary deformations of them. This choice is also supported by the fact that, for the Epygon valve, the stent wrapping the flexible leaflet (see Figure 1.14) is supposed to be rigid and thus not distorted during its lifespan.

Several consequences flow from this stiffening. First, as noticed in Section 4.2.2, the displacement field of the atrium, now linked to a less distorted annulus, is smaller than before (see Figure 4.3 compared to previous Figure 3.14). Second, the ventricle is more constrained than before as its upper part near the mitral annulus, linked to the stiffed elements, is prevented to distort as dictated by the displacement field coming from the electromechanical simulations (see Appendix B). This may induce strong distortions in the first layer of finite elements of the LV surface near the mitral annulus, leading to

degradations in the matching of the computed pressures with the reference ones, as detailed in Section 4.3, compared to what has been computed in Chapter 3.

4.2.4 Modeling of mitral regurgitation

The modeling of MR is based on an original idea from [Ale19], where a sphere of given dimensions is used to define the regurgitating region (see Figure 4.6a). The elements of the closed mitral valve intersected by the sphere (colored in light green in Figure 4.6b) are the ones used for simulating the leak towards the atrium: when the valve is closed, the resistance R_i of its elements is set to its usual optimal value except for the intersected ones whose resistive parameter is set to 0. This null value locally disables the porosity, allowing the fluid to flow through them.

(a) Considered sphere for the marking. (b) Resulting marked region.

Figure 4.6 – Region marking strategy for the native valve in closed configuration. The light green triangles represent the finite elements where the porosity is disabled. Images from [Ale19].

Note that this simplified approach for the modeling of MR does not correspond to one of the cases listed into the Carpentier's functional classification (see Figure 1.9) but has the main benefit of considering the same computational domain as the one used for the healthy configuration. Therefore, no additional mesh generation is required. Finally, it is worth noting that this region marking strategy has been only applied to the closed configuration of the immersed mitral valve: it has been assumed that the effects of the regurgitating region on the open configuration are not interesting for our comparison study and can hence be neglected.

4.3 Numerical experiments

All the following results have been obtained with the ARIS model whose pressure correction (detailed in Section 3.2.3) has been enabled during isovolumetric phases. For the simulation of MR (denoted by "regurgitant case"), such phases do not exist due to the regurgitation and the use of pressure correction does not make sense. Thus, the results about MR have been obtained with the original RIS model (introduced in Section 2.4.1). All the units are expressed in the CGS system, unless specified otherwise.

4.3.1 Mitral regurgitation simulation

In this section and in the context of the native mitral valve, a healthy case is computed with the ARIS model and is used as a reference to evaluate the main differences obtained with a regurgitant case computed with the RIS model. For this purpose, the matching of the evolution of the pressure $\overline{P_{\Omega_2}}$ and $P^\star$ is depicted in Figure 4.7 for both cases. Figure 4.7a depicts a good overall pressures matching for the healthy case. On the contrary, for the regurgitant case, the simulation is characterized by a pressure $\overline{P_{\Omega_2}}$ strongly offset from $P^\star$, as pictured in Figure 4.7b. In particular, during the time interval defined by $[t = 0.215, t = 0.465]$, $\overline{P_{\Omega_2}}$ keeps decreasing towards $\overline{P_{\Omega_1}}$, consequence of blood leakage into the atrium. It is worth recalling that for the regurgitant case, $P^\star$ is simply illustrative and does not represent a target value as no pressure correction is used with MR.

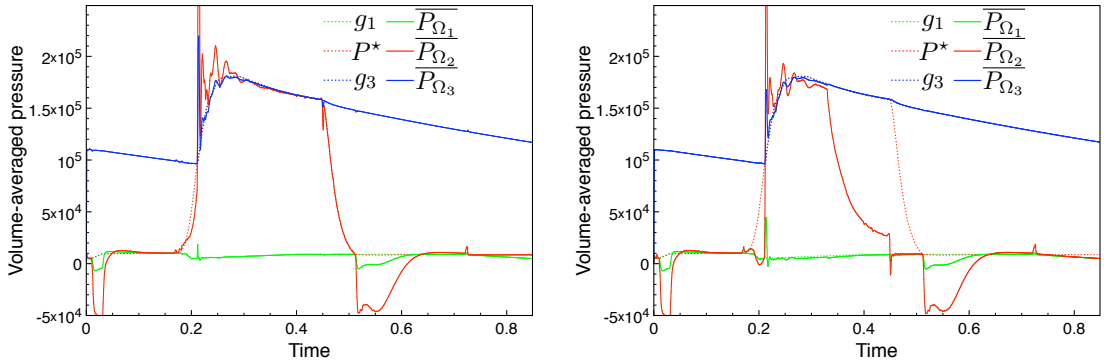

(a) Healthy case.

(b) Regurgitant case.

Figure 4.7 – Time history of the computed pressures obtained for the healthy and regurgitant cases.

Figure 4.8 presents some snapshots of the velocity field, obtained in the early moments of the simulation, for both healthy and regurgitant cases. At $t = 0.05$ and $t = 0.125$, the results between both cases are the same as the regurgitating region only exists when the mitral valve is in its closed configuration (i.e., when $t > 0.215$). Figure 4.8f depicts the velocity field when MR occurs. An important blood flow coming back into the atrium through the defined orifice is observed and hits the atrial upper wall before following its curvature by rotating. Meanwhile, the flow rate though the aorta is reduced compared to the healthy case (see Figure 4.8e).

Snapshots of the pressure fields obtained for both healthy and regurgitant cases are given in Figure 4.9. As depicted in Figures 4.9a–4.9d, small differences between both cases are observed at $t = 0.185$ and $t = 0.2$. These differences are explained by the fact that no pressure correction is considered for the regurgitant case (we recall that the first isovolumetric phase is roughly defined by the time interval $[t = 0.135, t = 0.215]$). The most important differences are obtained at $t = 0.35$ (see Figures 4.9e and 4.9f) when the regurgitating region is active (i.e., when MR occurs).

Finally, snapshots of some pathlines are given in Figure 4.10. As detailed for the velocity field, the results between both cases are the same at $t = 0.05$ and $t = 0.125$.

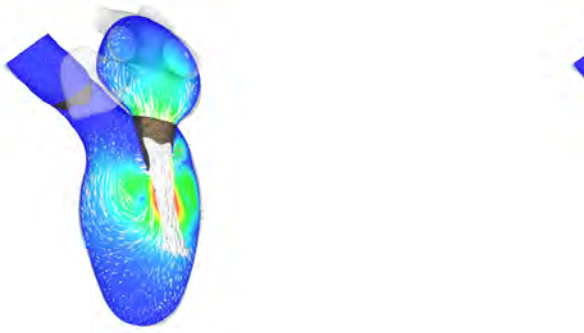

(a) Healthy case – $t = 0.05$.

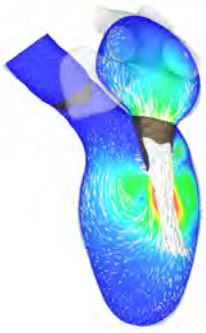

(b) Regurgitant case – $t = 0.05$.

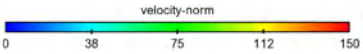

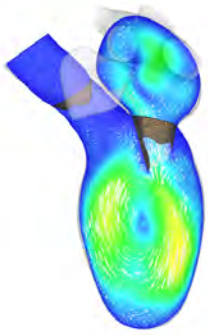

(c) Healthy case – $t = 0.125$.

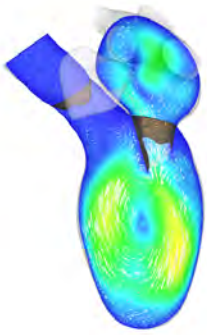

(d) Regurgitant case – $t = 0.125$.

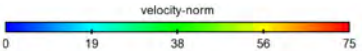

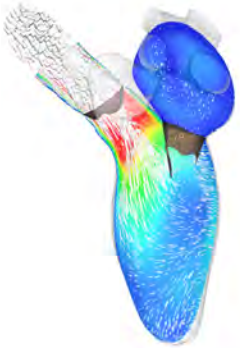

(e) Healthy case – $t = 0.25$.

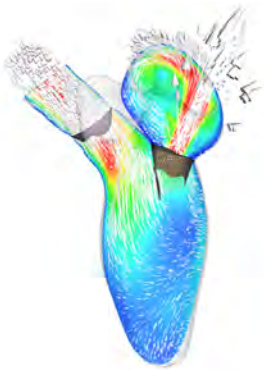

(f) Regurgitant case – $t = 0.25$.

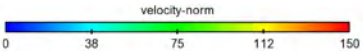

Figure 4.8 – Snapshots of the velocity field obtained at different early moments of the simulation for the healthy and regurgitant cases.

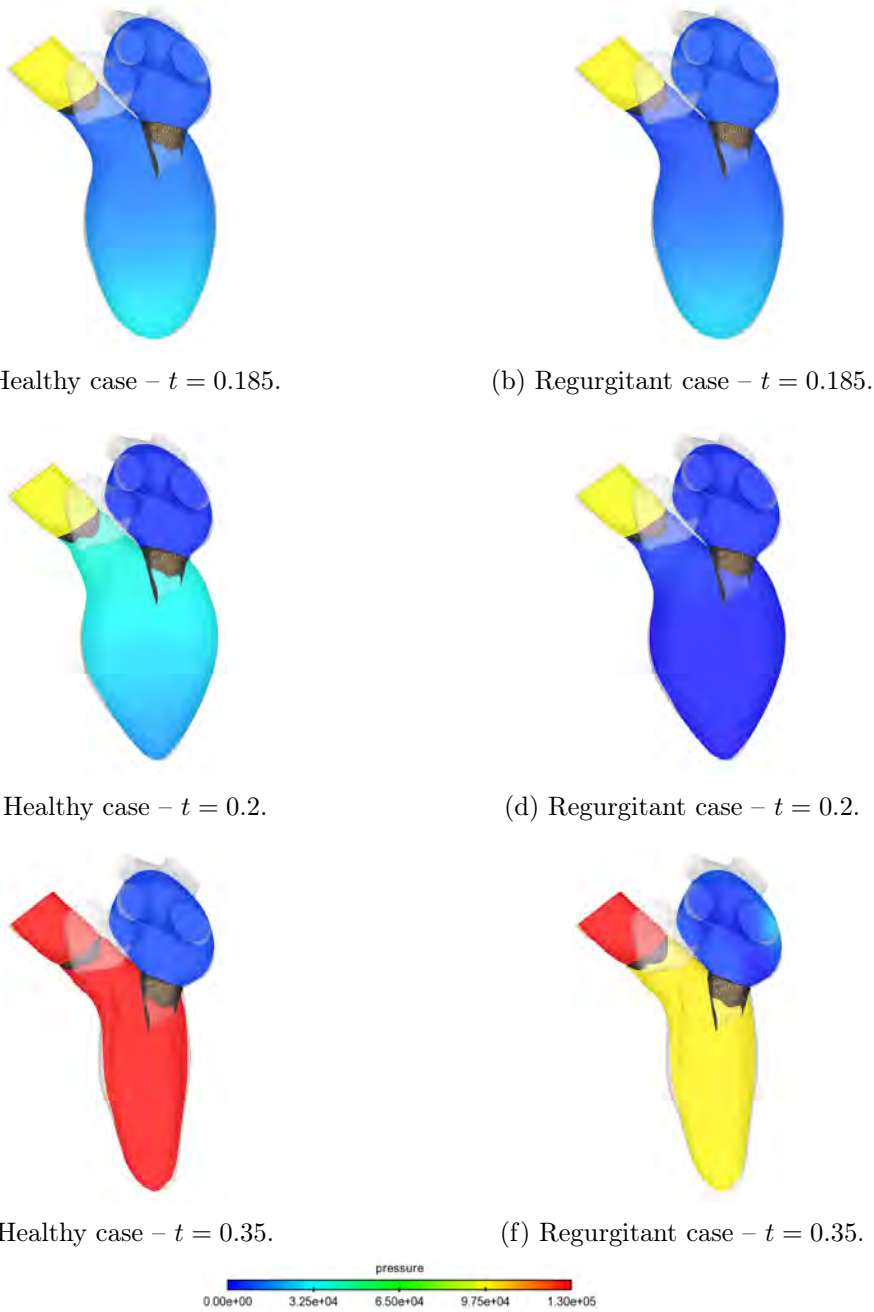

(a) Healthy case – $t = 0.185$.

(b) Regurgitant case – $t = 0.185$.

(c) Healthy case – $t = 0.2$.

(d) Regurgitant case – $t = 0.2$.

(e) Healthy case – $t = 0.35$.

(f) Regurgitant case – $t = 0.35$.

Figure 4.9 – Snapshots of the pressure field obtained at various instants for the healthy and regurgitant cases. As regards the first isovolumetric phase, the first, second and third lines correspond to instants, respectively, just before, during and after this phase.

Nevertheless, a clear difference of behavior is observed at $t = 0.25$ where blood leakage is obtained for the regurgitant case, characterized by some particles flowing back into the atrium (see in Figure 4.10f).

(a) Healthy case – $t = 0.05$.

(b) Regurgitant case – $t = 0.05$.

(c) Healthy case – $t = 0.125$.

(d) Regurgitant case – $t = 0.125$.

(e) Healthy case – $t = 0.25$.

(f) Regurgitant case – $t = 0.25$.

Figure 4.10 – Snapshots of some pathlines obtained at various instants for the healthy and regurgitant cases.

4.3.2 Cardiac hemodynamics simulations for different artificial valves

The time history of the pressures $\overline{P_{\Omega_2}}$ and $P^\star$ are depicted in Figure 4.11 for the three different types of mitral valve (namely, the native one, the Epygon one and the tricuspid one). A good overall matching is obtained for the different cases, independently of the considered heartbeat.

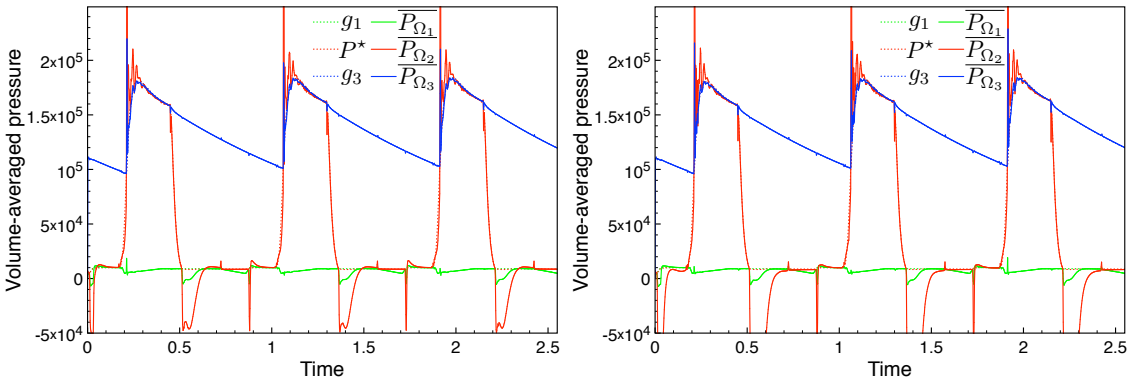

(a) Native valve.

(b) Tricuspid valve.

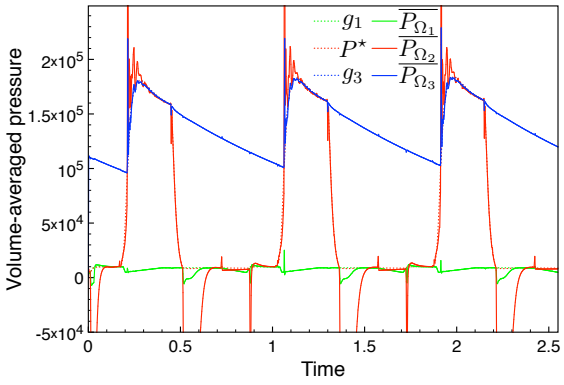

(c) Epygon valve.

Figure 4.11 – Time history of the computed pressures obtained for the different valves.

Figure 4.12 presents some snapshots of the velocity field, obtained at various instants of the second heartbeat for the different valves. At $t = 1.1$, during the systole phase, the three velocity fields broadly exhibit the same behavior, as observed in Figures 4.12a–4.12c. Only the Epygon case is slightly different due to its immersed rigid and impermeable stent which forces blood to circumvent it and to leave the LV by a section more narrowed than the one of the native and tricuspid cases. Figures 4.12d–4.12f depict the velocity field when the ventricle filling is just beginning. The aperture angle of the peak flow is clearly the widest for the tricuspid case. Moreover, as detailed in Section 1.5.3, the physiological diastolic asymmetric flow oriented towards the posterior wall is observed for the Epygon valve and not for the tricuspid one, highlighting its superiority. Finally, this remark is also supported by Figures 4.12g–4.12i where the fully developed velocity field is depicted for the different valves. One can clearly observe that, for the Epygon case, its structure is closer to the native one than the tricuspid one, even if it is slightly accelerated (intended effect described in [Epy]). In particular, the rotation of the flow for the tricuspid valve is in the opposite direction compared to the physiological one [TKHL16].

Snapshots of the kinetic energy field, obtained at various instants of the second heartbeat, are given in Figure 4.13 for the different valves. The corresponding snapshots for the vorticity field are depicted in Figure 4.14. Remarks previously made for the velocity also

apply to these physical values. In particular, Figures 4.13e and 4.13f clearly highlight the difference between both artificial valves in terms of flow structure: symmetric (i.e., non-physiological) for the tricuspid one and asymmetric (i.e., physiological) for the Epygon one. In a healthy native case, the kinetic energy loss is expected to be minimized during the diastole. This ensures the conservation of the energy provided by the peak flow rate [KYW+00]. As observed in Figures 4.14g–4.14i, the vorticity field generated by the Epygon valve, even if displaying greater values, is the closest to the native one.

For the purpose of completeness, Figure 4.15 presents the corresponding snapshots for the pressure field. The three cases exhibit the exact same behavior. Similarities between Figures 4.15a–4.15c and Figure 3.21b are clearly noticeable, highlighting the proper functioning of the pressure correction for the three valves.

Figure 4.16 presents snapshots of some pathlines, obtained at various instants of the second heartbeat for the different valves. As already discussed in the context of the velocity field, the particles are not flowing in the physiological direction for the tricuspid case. Pathlines follow the same tendency in terms of structure between native and Epygon cases. The Epygon pathlines are always ahead of the native ones (as observed by comparing Figure 4.16f with Figure 4.16d and Figure 4.16i with Figure 4.16g), consequence of the coveted physiological flow acceleration of blood inside the LV [Epy].

Finally, the residence time of three particles in the LV are given in Table 4.2 for the different valves cases. As consistent with what has been highlighted in the previous comparisons of the different physical fields, a clear correlation between the native case and the Epygon case is observed. The delay obtained for the tricuspid valve can be explained by the fact that the particles are not flowing in the physiological direction and are then much farther away from the aortic valve when systole begins than the ones of the native case. The advance of particle 1 for the Epygon case compared to the native case is also a consequence of the coveted physiological blood flow acceleration inside the LV [Epy].

Case	Particle 1	Particle 2	Particle 3
Native valve	553 ms	562 ms	612 ms
Tricuspid valve	563 ms	611 ms	704 ms
Relative gap with respect to the native case	+ 1.8 %	+ 8.7 %	+ 15.0 %
Epygon valve	533 ms	567 ms	613 ms
Relative gap with respect to the native case	- 3.6 %	+ 0.9 %	+ 0.2 %

Table 4.2 – Residence time of three particles in the LV for the different valves. The initial position of each particle has been picked up on the surface defined by the mitral annulus and has been kept the same between each case.

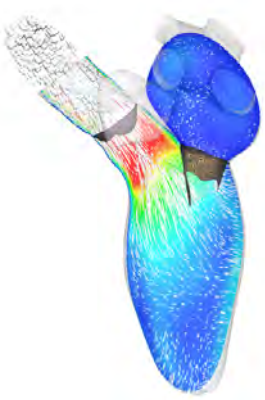

(a) Native valve – $t = 1.1$.

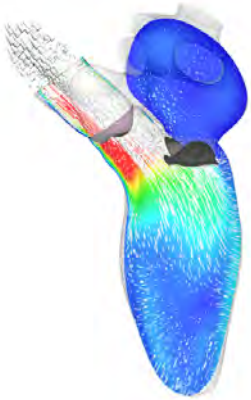

(b) Tricuspid valve – $t = 1.1$.

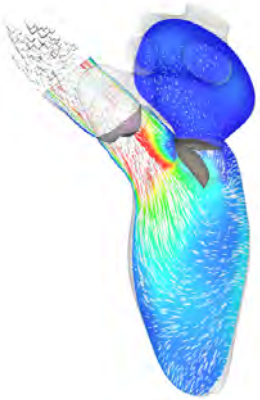

(c) Epygon valve – $t = 1.1$.

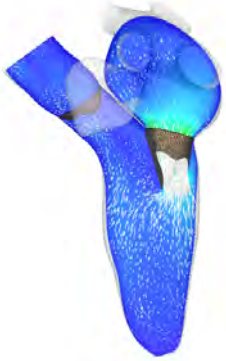

(d) Native valve – $t = 1.37$.

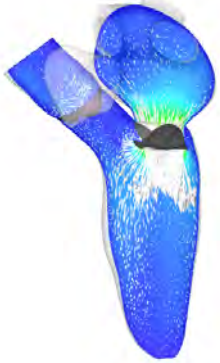

(e) Tricuspid valve – $t = 1.37$.

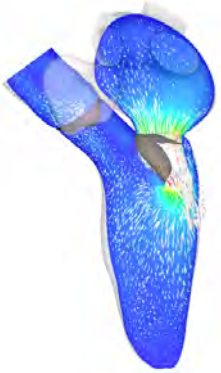

(f) Epygon valve – $t = 1.37$.

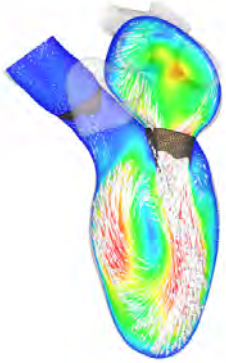

(g) Native valve – $t = 1.45$.

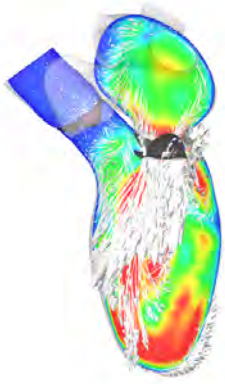

(h) Tricuspid valve – $t = 1.45$.

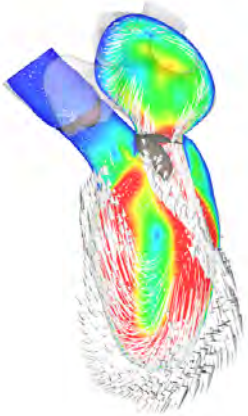

(i) Epygon valve – $t = 1.45$.

Figure 4.12 – Snapshots of the velocity field obtained at various instants of the second heartbeat for the different valves.

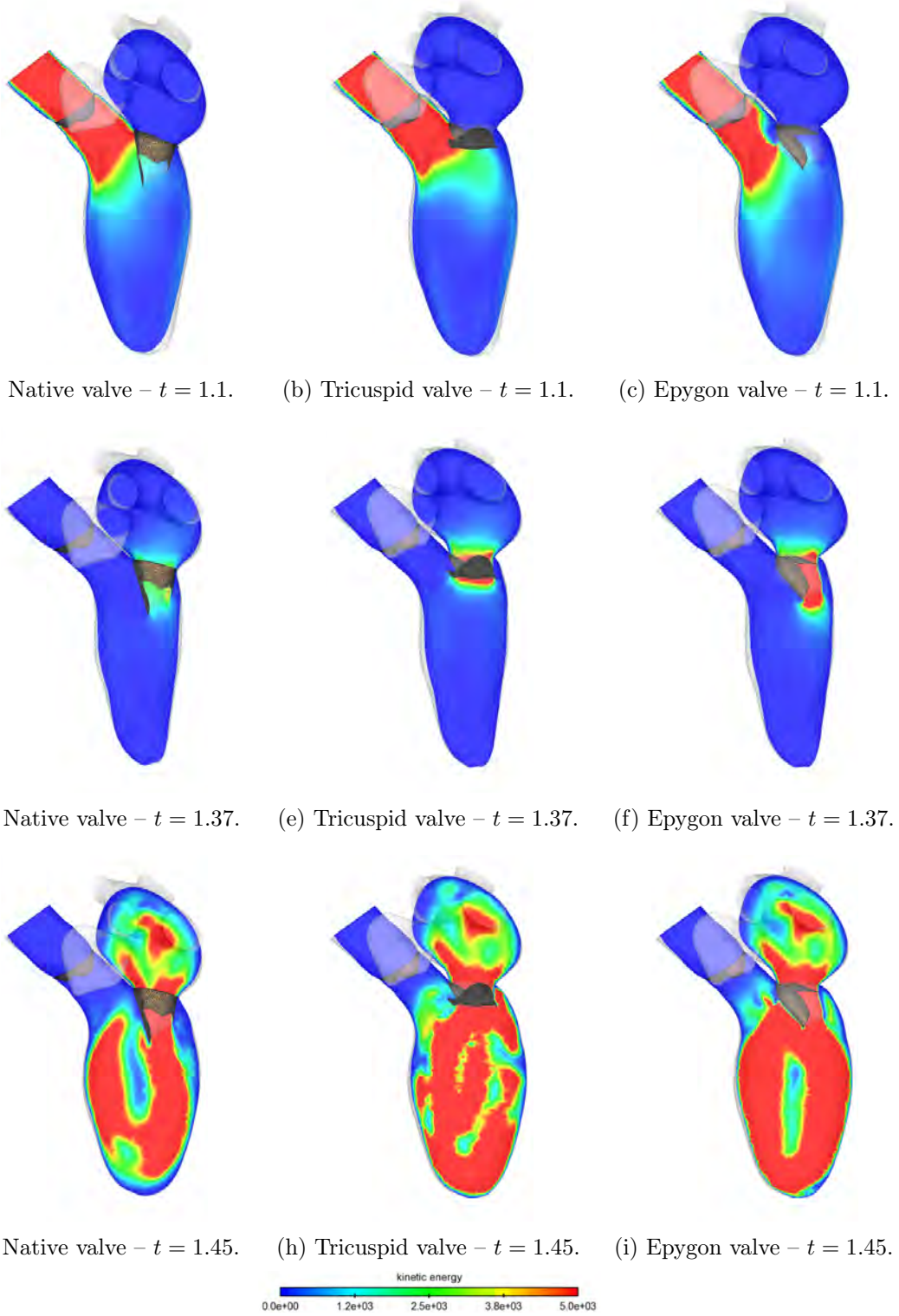

(a) Native valve – $t = 1.1$. (b) Tricuspid valve – $t = 1.1$. (c) Epygon valve – $t = 1.1$.

(d) Native valve – $t = 1.37$. (e) Tricuspid valve – $t = 1.37$. (f) Epygon valve – $t = 1.37$.

(g) Native valve – $t = 1.45$. (h) Tricuspid valve – $t = 1.45$. (i) Epygon valve – $t = 1.45$.

Figure 4.13 – Snapshots of the kinetic energy field obtained at various instants of the second heartbeat for the different valves.

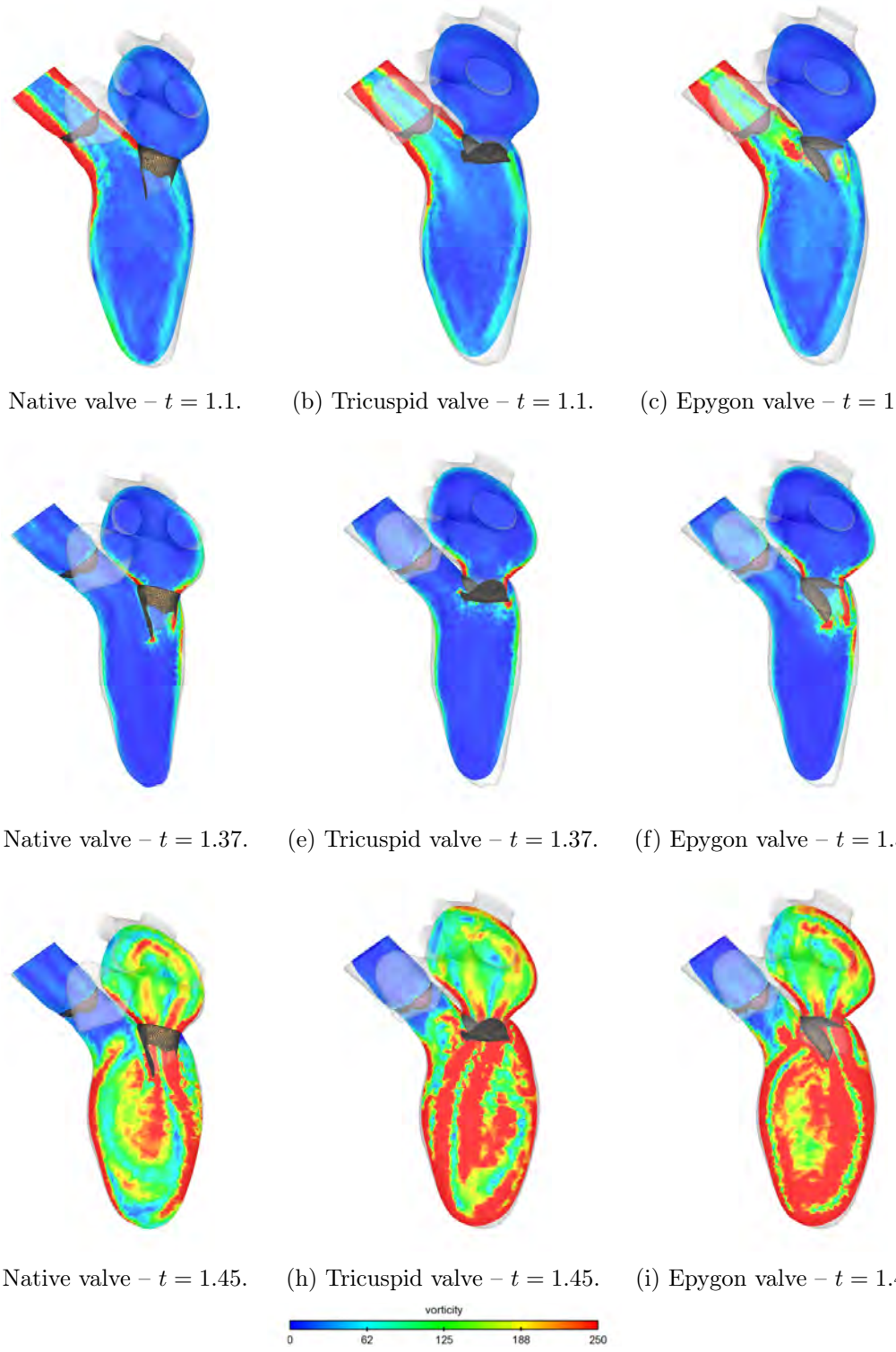

(a) Native valve – $t = 1.1$. (b) Tricuspid valve – $t = 1.1$. (c) Epygon valve – $t = 1.1$.

(d) Native valve – $t = 1.37$. (e) Tricuspid valve – $t = 1.37$. (f) Epygon valve – $t = 1.37$.

(g) Native valve – $t = 1.45$. (h) Tricuspid valve – $t = 1.45$. (i) Epygon valve – $t = 1.45$.

Figure 4.14 – Snapshots of the vorticity field obtained at various instants of the second heartbeat for the different valves.

(a) Native valve – $t = 1.035$. (b) Tricuspid valve – $t = 1.035$. (c) Epygon valve – $t = 1.035$.

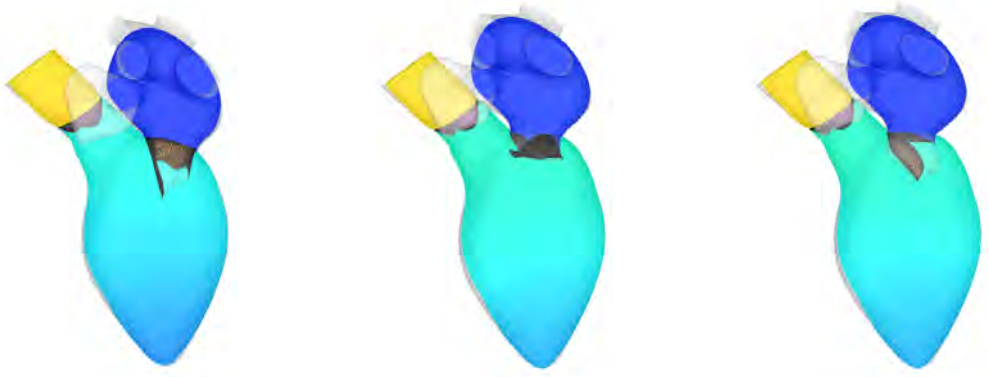

(d) Native valve – $t = 1.05$. (e) Tricuspid valve – $t = 1.05$. (f) Epygon valve – $t = 1.05$.

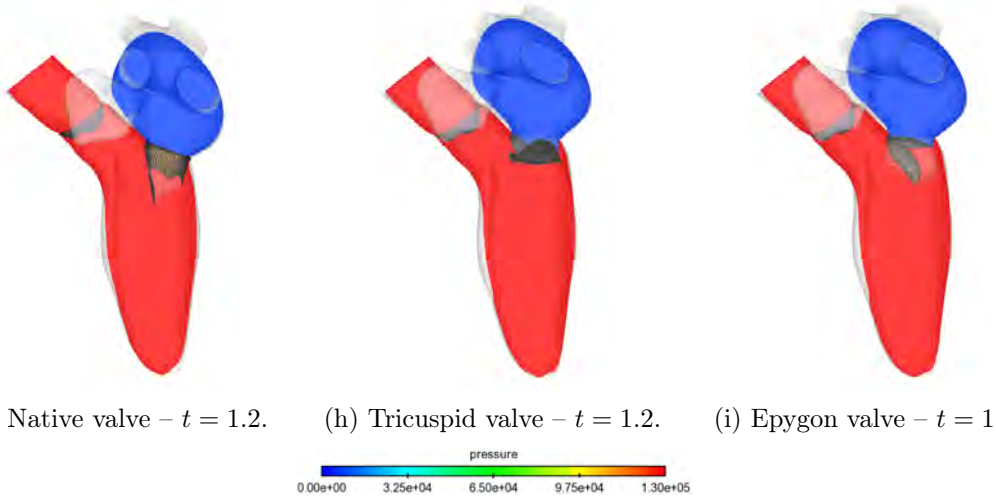

(g) Native valve – $t = 1.2$. (h) Tricuspid valve – $t = 1.2$. (i) Epygon valve – $t = 1.2$.

Figure 4.15 – Snapshots of the pressure field obtained at various instants of the second heartbeat for the different valves.

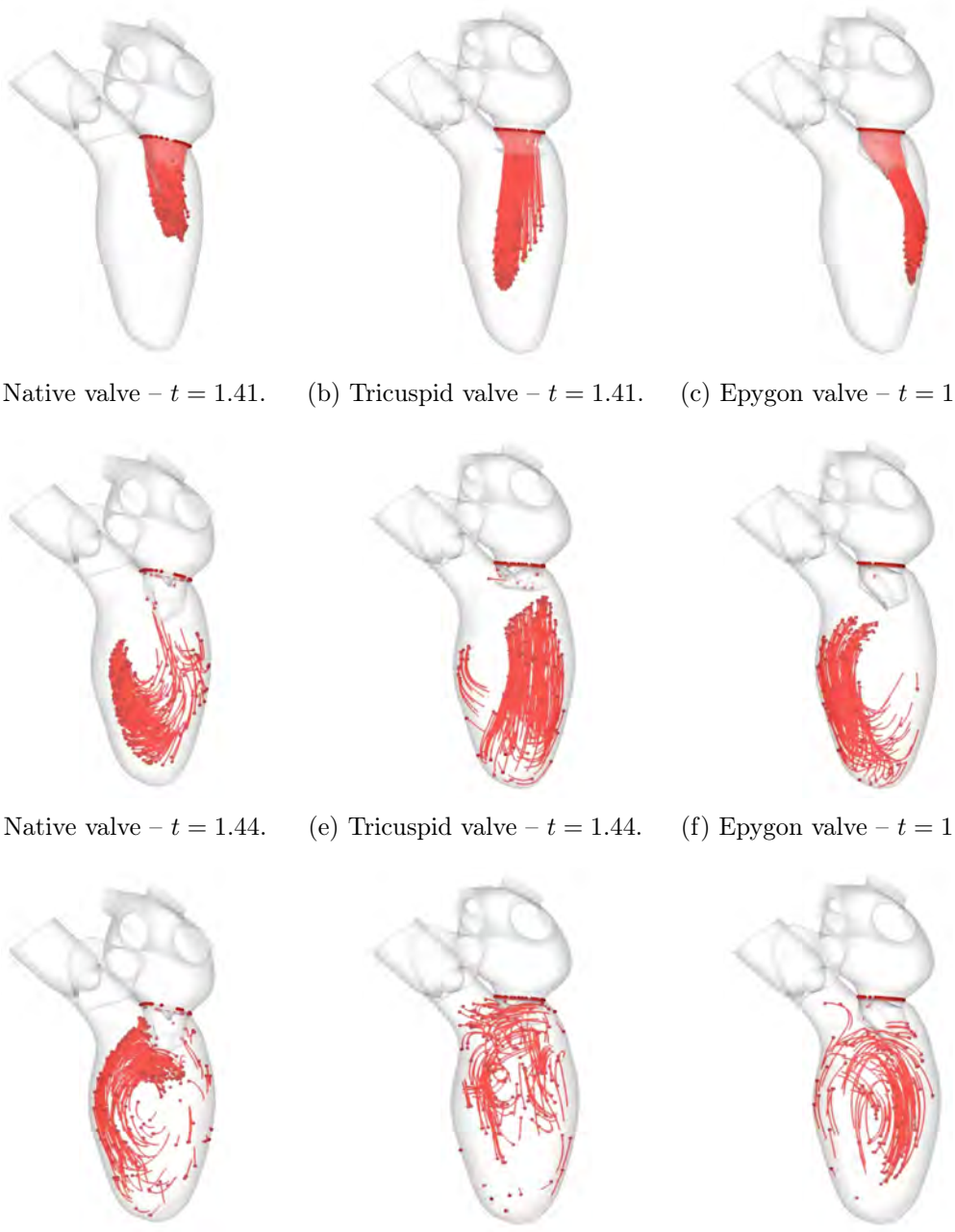

(a) Native valve – $t = 1.41$. (b) Tricuspid valve – $t = 1.41$. (c) Epygon valve – $t = 1.41$.

(d) Native valve – $t = 1.44$. (e) Tricuspid valve – $t = 1.44$. (f) Epygon valve – $t = 1.44$.

(g) Native valve – $t = 1.47$. (h) Tricuspid valve – $t = 1.47$. (i) Epygon valve – $t = 1.47$.

Figure 4.16 – Snapshots of some pathlines obtained at various instants of the second heartbeat for the different valves.

4.4 Conclusions

The RIS and ARIS models, in spite of their simplicity, have provided interesting illustrations and results in the context of realistic cases. First, a simple model of MR has been computed on a physiological geometry and has been compared to the corresponding healthy configuration, emphasizing the possibilities offered by the RIS approach to assess its severity. Then, with the ARIS model, we have highlighted that, contrary to the bioprosthetic tricuspid valve, the intraventricular flow generated by the Epygon valve presents important similarities with the native one, highlighting its superiority. This can be explained by the presence of the D-shaped annulus combined with the single anterior valve leaflet, empowering the asymmetry of the downstream flow inside the LV. Studies on other artificial valves with similar geometrical properties have also observed the same benefits (see, e.g., [FPK15]).

Several limitations to the presented model can however be mentioned. First, the ARIS model requires the availability of a reference pressure data. While obtainable in an uncoupled electromechanical/fluid framework, as presented in Section 3.3.2, *in vivo* recovery of the intraventricular pressure by catheterization is an invasive procedure and might not always be feasible. Secondly, the ARIS model is based on a reduced valve model and therefore inherits from all its limitations. In particular, we can mention the fact that the valve instantaneously switches between its open and closed configurations, which is a simplification of reality. A second limitation of the reduced valve model is dictated by the arbitrary displacement of the immersed surfaces, resulting from the lifting operator of the ALE framework: the immersed valve surfaces displacements are not driven by any physical considerations. Finally, due to the explicit treatment of the valve model, pressure oscillations can be observed during transition phases, as mentioned in Section 3.3.2.1. This last issue might be circumvented by formulating the valve dynamics as a non-linear constraint on the fluid velocity.

An interesting extension of this work would be to compare the results coming from the ARIS model with the ones coming from a fully coupled FSI framework in order to quantify the potential inaccuracies induced by the current approach. Moreover, while a simplified left heart geometry (described in Section 3.3.2) was considered, using a richer geometry (including, e.g., papillary muscles or chordae tendineae) could help evaluating the proposed approach in a more realistic setting.

Last, the ARIS model is too simplistic to reproduce the most complex phenomena occurring during a heartbeat. In particular, the dynamics aspects of the flow, induced by the gradual opening and closing of the valve, cannot be obtained with this reduced modeling of the immersed surfaces. Even if recent works introducing an implicit valve description have been proposed to bypass this open/closed duality (see, e.g., [FFDQ17]), the computation of some specific phenomena are still out ot reach with this simplified model. We can mention, for instance, the study of the relationship between the mitral annular shape and the mitral valve prolapse (see, e.g., [LTHW87]). For this type of problems, more sophisticated models taking into account a full description of the dynamics of the structures interacting with the fluid, including the management of the contact between the leaflets, need to be considered. These more complex models will be considered in Part III

where the simulation of intracardiac blood flow and implantable cardiovascular devices with a complete fluid-structure interaction model is investigated.

Part III

Simulation of intracardiac blood flow with a complete fluid-structure interaction model

Chapter 5

Numerical methods for immersed fluid-structure interaction with thin-walled structures

As detailed in Section 2.5, the numerical simulation of a thin-walled structure immersed in an incompressible fluid can be addressed by various FSI methods. In this chapter, three of them are considered: the ALE method, the FD/Lagrange multipliers method and the Nitsche-eXtended Finite Element Method (NXFEM) method. Taking ALE as a reference, the advantages and limitations of FD and Nitsche-XFEM are carefully discussed on three benchmark test cases which have been chosen to be representative of typical difficulties encountered in cardiac valves simulations.

The results presented in this chapter have been reported in:

- L. Boilevin-Kayl, M.A. Fernández and J.F. Gerbeau, **Numerical methods for immersed FSI with thin-walled structures.** *Computers & Fluids*, DOI: 10.1016/j.compfluid.2018.05.024, *2019*. Available online: `https://hal.inria.fr/hal-01704575`.

Contents

5.1 Introduction

Unfitted mesh methods for FSI are rarely compared between them in the literature. It is hence unclear to what extend cut-FEM methodologies are appealing in practice, with respect to more standard IB or FD methods. The first contribution of this chapter consists in providing insight into this problem. To this purpose, we compare and validate some of the unfitted mesh methods mentioned in Section 2.5 in a series of 2D FSI benchmarks with dynamics interfaces undergoing large deflections. We consider an archetypal sample of unfitted mesh methods: the FD method as implemented in [dSGB08], an enhanced variant from [KHS+15] and the Nitsche-XFEM method introduced in [AFFL16]. The numerical approximation provided by an ALE fitted mesh approach is used as reference for the comparisons. The second contribution of this work has to do with the above referenced unfitted Nitsche-XFEM method, which is here formulated and validated, for the first time, in a fully non-linear framework, involving a general thin-wall solid model for large displacements and rotations. The numerical results reported in [AFFL16] were limited to moderate (normal) displacements using a simple string model.

The rest of the chapter is organized as follows. Section 5.2 recalls the different mathematical models and formulations considered through the chapter. The numerical methods are described in Section 5.3. Section 5.4 presents the comparisons of the results obtained with the three FSI benchmarks tests. Finally, a summary of the main conclusions is given in Section 5.6.

5.2 Problem setting and mathematical formulations

In what follows, the fluid is modeled by the incompressible Navier-Stokes equations in the Eulerian or in the ALE formalisms. The thin-walled solid is described by a non-linear Reissner-Mindlin beam model in Lagrangian form. We refer to Sections 2.2.2.2 and 2.5.1.2 for more information about these models.

The geometric configurations and notations are those of Section 2.5.2.1. Then, for the coupled problem with Eulerian formalism in the fluid, we refer to (2.14)–(2.16) in previous Section 2.5.2.2. For the coupled problem with ALE formalism in the fluid, we refer to (2.19)–(2.21) in previous Section 2.5.2.2.

5.3 Numerical methods

Though the coupled problems (2.14)–(2.16) and (2.19)–(2.21) are equivalent at the continuous level, their discretization generally leads to different numerical approaches.

In what follows, $\tau > 0$ denotes the time-step length, $t_n \overset{\text{def}}{=} n\tau$ for $n \in \mathbb{N}$, and $\partial_\tau x^n \overset{\text{def}}{=} \frac{1}{\tau}\big(x^n - x^{n-1}\big)$ stands for the first-order backward difference. We will also make use of the standard Sobolev spaces $H^m(\omega)$ $(m \geq 0)$. The closed subspaces $H^1_\Gamma(\omega)$, of functions in $H^1(\omega)$ with zero trace on Γ, and $L^2_0(\omega)$, of functions in $L^2(\omega)$ with zero mean in ω, will also be used. The scalar product in $L^2(\omega)$ is denoted by $(\cdot,\cdot)_\omega$. We consider $\boldsymbol{V} \overset{\text{def}}{=} [H^1_\Gamma(\Omega)]^d$

and $Q \stackrel{\text{def}}{=} L^2_0(\Omega)$ as the fluid velocity and pressure functional spaces, respectively. The space of admissible displacements is denoted by $\boldsymbol{Y} \subset [H^1(\Sigma)]^d$. The trial set for the unitary director vectors is denoted by $\boldsymbol{S}$ and its variations are taken in the space $\Theta \subset H^1(\Sigma)$.

5.3.1 Fitted mesh methods

By using the parametrization of the fluid domain, given by the one-to-one mapping $\boldsymbol{\mathcal{A}}$, we can consider as fluid unknowns

$$\widehat{\boldsymbol{u}} \stackrel{\text{def}}{=} \boldsymbol{u} \circ \boldsymbol{\mathcal{A}}_t \quad \text{and} \quad \widehat{p} \stackrel{\text{def}}{=} p \circ \boldsymbol{\mathcal{A}}_t,$$

instead of $\boldsymbol{u} = \widehat{\boldsymbol{u}} \circ \boldsymbol{\mathcal{A}}_t^{-1}$ and $p = \widehat{p} \circ \boldsymbol{\mathcal{A}}_t^{-1}$. The coupled problem (2.19)–(2.21) hence admits the following variational formulation (see, e.g., [FG09]): for $t > 0$, find $\big(\widehat{\boldsymbol{u}},\widehat{p},\boldsymbol{d},\boldsymbol{a}\big) \in \boldsymbol{V} \times Q \times \boldsymbol{Y} \times \boldsymbol{S}$, with $\dot{\boldsymbol{d}} = \partial_t \boldsymbol{d}$ and $\widehat{\boldsymbol{u}}|_\Sigma = \dot{\boldsymbol{d}}$, such that the geometric compatibility $(2.21)_1$ holds and

$$\left\{ \begin{aligned} \rho^{\mathrm{f}} \frac{\mathrm{d}}{\mathrm{d}t}\big(\boldsymbol{u},\boldsymbol{v}\big)_{\Omega(t)} - \rho^{\mathrm{f}}\big((\boldsymbol{\nabla}\cdot\boldsymbol{w})\boldsymbol{u},\boldsymbol{v}\big)_{\Omega(t)} + a^{\mathrm{f}}_{\Omega(t)}\big(\boldsymbol{u}-\boldsymbol{w};(\boldsymbol{u},p),(\boldsymbol{v},q)\big) \\ + \rho^{\mathrm{s}}\epsilon\big(\partial_\tau \dot{\boldsymbol{d}},\boldsymbol{y}\big)_\Sigma + a^{\mathrm{s}}\big((\boldsymbol{d},\boldsymbol{a}),(\boldsymbol{y},\theta)\big) = 0, \end{aligned} \right. \tag{5.1}$$

for all $(\widehat{\boldsymbol{v}},\widehat{q},\boldsymbol{y},\theta) \in \boldsymbol{V} \times Q \times \boldsymbol{Y} \times \Theta$, with $\widehat{\boldsymbol{v}}|_\Sigma = \boldsymbol{y}$. Here, the trilinear fluid form $a^{\mathrm{f}}_{\Omega(t)}$ is defined by

$$a^{\mathrm{f}}_{\Omega(t)}\big(\boldsymbol{z};(\boldsymbol{u},p),(\boldsymbol{v},q)\big) \stackrel{\text{def}}{=} c_{\Omega(t)}(\boldsymbol{z},\boldsymbol{u},\boldsymbol{v}) + a_{\Omega(t)}\big((\boldsymbol{u},p),(\boldsymbol{v},q)\big),$$

with

$$a_{\Omega(t)}\big((\boldsymbol{u},p),(\boldsymbol{v},q)\big) \stackrel{\text{def}}{=} 2\mu\big(\boldsymbol{\epsilon}(\boldsymbol{u}),\boldsymbol{\epsilon}(\boldsymbol{v})\big)_{\Omega(t)} - (p,\boldsymbol{\nabla}\cdot\boldsymbol{v})_{\Omega(t)} + (q,\boldsymbol{\nabla}\cdot\boldsymbol{u})_{\Omega(t)},$$

$$c_{\Omega(t)}(\boldsymbol{z},\boldsymbol{u},\boldsymbol{v}) \stackrel{\text{def}}{=} \rho^{\mathrm{f}}(\boldsymbol{z}\cdot\boldsymbol{\nabla}\boldsymbol{u},\boldsymbol{v})_{\Omega(t)}.$$

The term a^{s} represents the weak form of the solid operators $\boldsymbol{L_d}$ and $\boldsymbol{L_a}$.

The coupled variational problem (5.1) is particularly well adapted to the discretization with fitted meshes. We hence consider a family of triangulations of $\{\mathcal{T}^{\mathrm{f}}_h\}_{0<h<1}$ of the reference fluid domain Ω which are fitted to the family of triangulations $\{\mathcal{T}^{\mathrm{s}}_h\}_{0<h<1}$ of Σ. In other words, the fluid and solid meshes match at the interface. The discrete spaces $\boldsymbol{V}_h \subset \boldsymbol{V}$, $\boldsymbol{Y}_h \subset \boldsymbol{Y}$ and $\Theta_h \subset \Theta$ are the standard Lagrange finite element space of continuous piecewise affine functions, so that we have $\boldsymbol{Y}_h = \boldsymbol{V}_h|_\Sigma$. The pressure space $Q_h \subset Q$ is also made of piece-wise affine functions which are continuous on each sub-domain Ω_i, $i = \{1,2\}$, but which can be discontinuous across Σ.

The geometric coupling condition $(2.21)_1$ is treated in an explicit fashion as follows. For a given discrete displacement $\boldsymbol{d}_h^{n-1} \in \boldsymbol{Y}_h$ at time level t_{n-1}, we define the ALE map $\boldsymbol{\mathcal{A}}_h^n$ as

$$\boldsymbol{d}_h^{\mathrm{f},n} = \boldsymbol{\mathcal{L}}_h\left(\boldsymbol{d}_h^{n-1}\right) \quad \text{and} \quad \boldsymbol{\mathcal{A}}_h^n = \boldsymbol{I}_\Omega + \boldsymbol{d}_h^{\mathrm{f},n}.$$

The resulting numerical method is detailed in Algorithm 5.1. Here, we have used the

Algorithm 5.1 Fitted mesh ALE method.

For $n \geq 1$,

1. Fluid mesh update:

$$\boldsymbol{d}_h^{\mathrm{f},n} = \boldsymbol{\mathcal{L}}_h\left(\boldsymbol{d}_h^{n-1}\right), \quad \boldsymbol{w}_h^n = \partial_\tau \boldsymbol{d}_h^{\mathrm{f},n}, \quad \boldsymbol{\mathcal{A}}_h^n = \boldsymbol{I}_\Omega + \boldsymbol{d}_h^{\mathrm{f},n}, \quad \Omega_h^n = \boldsymbol{\mathcal{A}}_h^n(\Omega).$$

2. Find $\left(\widehat{\boldsymbol{u}}_h^n, \widehat{p}_h^n, \boldsymbol{d}_h^n, \boldsymbol{a}_h^n\right) \in \boldsymbol{V}_h \times Q_h \times \boldsymbol{Y}_h \times \boldsymbol{S}_h$, with $\dot{\boldsymbol{d}}_h = \partial_\tau \boldsymbol{d}_h^n$ and $\widehat{\boldsymbol{u}}_h^n|_\Sigma = \dot{\boldsymbol{d}}_h^n$, such that

$$\begin{cases} \dfrac{\rho^{\mathrm{f}}}{\tau}\left[\left(\boldsymbol{u}_h^n, \boldsymbol{v}_h\right)_{\Omega_h^n} - \left(\boldsymbol{u}_h^{n-1}, \boldsymbol{v}_h\right)_{\Omega_h^{n-1}}\right] - \rho^{\mathrm{f}}\left((\boldsymbol{\nabla}\cdot\boldsymbol{w}_h^n)\boldsymbol{u}_h^n, \boldsymbol{v}_h\right)_{\Omega_h^n} \\ + a^{\mathrm{f}}_{\Omega_h^n,h}\left(\boldsymbol{u}_h^{n-1} - \boldsymbol{w}_h^n; (\boldsymbol{u}_h^n, p_h^n), (\boldsymbol{v}_h, q_h)\right) \\ + \rho^{\mathrm{s}}\epsilon\left(\partial_\tau \dot{\boldsymbol{d}}_h^n, \boldsymbol{y}_h\right)_\Sigma + a_h^{\mathrm{s}}\left((\boldsymbol{d}_h^n, \boldsymbol{a}_h^n), (\boldsymbol{y}_h, \theta_h)\right) = 0, \end{cases} \tag{5.2}$$

for all $(\widehat{\boldsymbol{v}}_h, \widehat{q}_h, \boldsymbol{y}_h, \theta_h) \in \boldsymbol{V}_h \times Q_h \times \boldsymbol{Y}_h \times \Theta_h$, with $\boldsymbol{v}_h|_\Sigma = \boldsymbol{y}_h$.

standard notation

$$\begin{aligned} a^{\mathrm{f}}_{\Omega_h^n,h}\left(\boldsymbol{z}_h; (\boldsymbol{u}_h, p_h), (\boldsymbol{v}_h, q_h)\right) &\stackrel{\mathrm{def}}{=} c_h^n(\boldsymbol{z}_h; \boldsymbol{u}_h, \boldsymbol{v}_h) + a_{\Omega_h^n}\left((\boldsymbol{u}_h, p_h), (\boldsymbol{v}_h, q_h)\right) \\ &\quad + s_{\Omega_h^n,h}(\boldsymbol{z}_h; \boldsymbol{u}_h, \boldsymbol{v}_h), \end{aligned}$$

with the convective trilinear form given by

$$c_h^n(\boldsymbol{z}_h; \boldsymbol{u}_h, \boldsymbol{v}_h) \stackrel{\mathrm{def}}{=} c_{\Omega_h^n}(\boldsymbol{z}_h; \boldsymbol{u}_h, \boldsymbol{v}_h) + \frac{\rho^{\mathrm{f}}}{2}\left((\boldsymbol{\nabla}\cdot\boldsymbol{z}_h)\boldsymbol{u}_h, \boldsymbol{v}_h\right)_{\Omega_h^n}.$$

The form $s_{\Omega_h^n,h}$ corresponds to the SUPG/PSPG and grad-div stabilizations (see, e.g., [Tez91]) and is given by

$$\begin{aligned} s_{\Omega_h^n,h}(\boldsymbol{z}_h; \boldsymbol{u}_h, \boldsymbol{v}_h) &\stackrel{\mathrm{def}}{=} \sum_{K\in\mathcal{T}_h^{\mathrm{f}}} \int_K \frac{\lambda_{\mathrm{C}} h^2}{\delta_h} (\boldsymbol{\nabla}\cdot\boldsymbol{u}_h)(\boldsymbol{\nabla}\cdot\boldsymbol{v}_h) \\ &\quad + \sum_{K\in\mathcal{T}_h^{\mathrm{f}}} \int_K \delta_h \left(\rho^{\mathrm{f}}\left(\boldsymbol{z}_h\cdot\boldsymbol{\nabla}\right)\boldsymbol{u}_h + \boldsymbol{\nabla} p_h\right)\cdot\left(\rho^{\mathrm{f}}\left(\boldsymbol{z}_h\cdot\boldsymbol{\nabla}\right)\boldsymbol{v}_h + \boldsymbol{\nabla} q_h\right), \\ \delta_h &\stackrel{\mathrm{def}}{=} \lambda_{\mathrm{M}}\left(\rho^{\mathrm{f}}\sqrt{\frac{4}{\tau^2} + \frac{16\mu^2}{h^4(\rho^{\mathrm{f}})^2} + \frac{4|\boldsymbol{z}_h|^2}{h^2}}\right)^{-1}, \end{aligned} \tag{5.3}$$

with $\lambda_{\mathrm{M}}, \lambda_{\mathrm{C}} > 0$ user-defined parameters. At last, the solid term a_h^{s} denotes the linear Mixed Interpolation of Tensorial Components (MITC) approximation of a^{s} (see, e.g., [Bat96]), involving 3 degrees of freedom per node in the increments (two displacements and one rotation).

Remark 5.1

In (5.2), the fluid integrals in the current configurations involve the composition with the

corresponding discrete ALE map. For instance, the second term is given by

$$\big(\boldsymbol{u}_h^{n-1},\boldsymbol{v}_h\big)_{\Omega_h^{n-1}} = \big(\widehat{\boldsymbol{u}}_h^{n-1}\circ(\boldsymbol{\mathcal{A}}_h^{n-1})^{-1},\widehat{\boldsymbol{v}}_h\circ(\boldsymbol{\mathcal{A}}_h^{n-1})^{-1}\big)_{\Omega_h^{n-1}}.$$

The main drawback of Algorithm 5.1 comes from the motion of the fluid domain mesh in step 1. Indeed, the viability and efficiency of the whole numerical method strongly depends on the capability of the discrete lifting operator $\boldsymbol{\mathcal{L}}_h$ to deliver a correct deformed fluid mesh which maintains a reasonable quality. This contraint often becomes a challenging problem in the case of large interface deflections (see, e.g., [STB03, Wic11, Ala14]). In this chapter, we consider the non-linear lifting operator introduced in [LVCF17] which is simply an incremental variant of the approach reported in [STB03].

5.3.2 Unfitted mesh methods

The coupled problem (2.14)–(2.16) is often discretized with an unfitted mesh method to circumvent the above-mentioned limitation of Algorithm 5.1. In this chapter, we consider two different unfitted methods which are discussed in the next two paragraphs.

5.3.2.1 Fictitious domain method

The basic idea of the so-called Fictitious Domain method, is to consider the kinematic condition $(2.16)_2$ as a constraint in the fluid problem which is enforced through Lagrange multipliers, viz.,

$$b\big(\boldsymbol{\mu},\boldsymbol{u}\circ\boldsymbol{\phi}\big) = b\big(\boldsymbol{\mu},\dot{\boldsymbol{d}}\big),\quad \forall\boldsymbol{\mu}\in\boldsymbol{\Lambda},$$

where $\boldsymbol{\Lambda}$ denotes the Lagrange multiplier space and $b:\boldsymbol{\Lambda}\times[H^{\frac{1}{2}}(\Sigma)]^d\to\mathbb{R}$ is a continuous bilinear form, such that $b(\boldsymbol{\mu},\boldsymbol{z})=0$, for all $\boldsymbol{\mu}\in\boldsymbol{\Lambda}$, yields $\boldsymbol{z}=\boldsymbol{0}$ on Σ. For instance, we can take $\boldsymbol{\Lambda}=([H^{\frac{1}{2}}(\Sigma)]^d)'$ and $b(\boldsymbol{\mu},\boldsymbol{z})=\langle\boldsymbol{\mu},\boldsymbol{z}\rangle$, where $\langle\cdot,\cdot\rangle$ represents the duality pairing between $([H^{\frac{1}{2}}(\Sigma)]^d)'$ and $[H^{\frac{1}{2}}(\Sigma)]^d$ (see, e.g., [Pat11, BG17]).

Hence, in weak form the coupled problem (2.14)–(2.16) can be formulated as follows: for $t>0$, find $\big(\boldsymbol{u},p,\boldsymbol{\lambda},\boldsymbol{d},\boldsymbol{a}\big)\in\boldsymbol{V}\times Q\times\boldsymbol{\Lambda}\times\boldsymbol{Y}\times\boldsymbol{S}$, with $\dot{\boldsymbol{d}}=\partial_t\boldsymbol{d}$, such that the geometric compatibility $(2.16)_1$ holds and

$$\begin{cases}\rho^{\mathrm{f}}\big(\partial_t\boldsymbol{u},\boldsymbol{v}\big)_\Omega + a_\Omega^{\mathrm{f}}\big(\boldsymbol{u};(\boldsymbol{u},p),(\boldsymbol{v},q)\big) + \rho^{\mathrm{s}}\epsilon\big(\partial_t\dot{\boldsymbol{d}},\boldsymbol{y}\big)_\Sigma + a^{\mathrm{s}}\big((\boldsymbol{d},\boldsymbol{a}),(\boldsymbol{y},\theta)\big)\\ \qquad + b(\boldsymbol{\lambda},\boldsymbol{v}\circ\boldsymbol{\phi}_t-\boldsymbol{y}) - b\big(\boldsymbol{\mu},\boldsymbol{u}\circ\boldsymbol{\phi}_t-\dot{\boldsymbol{d}}\big)=0,\end{cases}\tag{5.4}$$

for all $(\boldsymbol{v},q,\boldsymbol{\mu},\boldsymbol{y},\theta)\in\boldsymbol{V}\times Q\times\boldsymbol{\Lambda}\times\boldsymbol{Y}\times\Theta$.

At the discrete level, the fluid velocity is searched for in the same space $\boldsymbol{V}_h$ as in the fitted mesh formulation of Section 5.3.1. Nevertheless, the fluid mesh is now fixed and the pressure space Q_h is made of globally continuous functions. For the solid, we consider the same discretization as in Section 5.3.1. As approximation space for the Lagrange

Algorithm 5.2 Fictitious domain method (from [dSGB08]).

For $n \geq 1$,

1. Interface update:

$$\boldsymbol{\phi}_h^n = \boldsymbol{I}_\Sigma + \boldsymbol{d}_h^{n-1}, \quad \Sigma_h^n = \boldsymbol{\phi}_h^n(\Sigma), \quad \Omega_h^n = \Omega \backslash \Sigma_h^n. \tag{5.5}$$

2. Find $\left(\boldsymbol{u}_h^n, p_h^n, \boldsymbol{\lambda}_h^n, \boldsymbol{d}_h^n, \boldsymbol{a}_h^n\right) \in \boldsymbol{V}_h \times Q_h \times \boldsymbol{\Lambda}_h \times \boldsymbol{Y}_h \times \boldsymbol{S}_h$, with $\dot{\boldsymbol{d}}_h = \partial_\tau \boldsymbol{d}_h^n$, such that

$$\begin{cases} \rho^{\mathrm{f}}\left(\partial_\tau \boldsymbol{u}_h^n, \boldsymbol{v}_h\right)_\Omega + a_{\Omega,h}^{\mathrm{f}}\left(\boldsymbol{u}_h^{n-1}; (\boldsymbol{u}_h^n, p_h^n), (\boldsymbol{v}_h, q_h)\right) \\ + \rho^{\mathrm{s}} \epsilon \left(\partial_\tau \dot{\boldsymbol{d}}_h^n, \boldsymbol{y}_h\right)_\Sigma + a^{\mathrm{s}}\left((\boldsymbol{d}_h^n, \boldsymbol{a}_h^n), (\boldsymbol{y}_h, \theta_h)\right) \\ + b\left(\boldsymbol{\lambda}_h^n, \boldsymbol{v}_h \circ \boldsymbol{\phi}_h^n - \boldsymbol{y}_h\right) - b\left(\boldsymbol{\mu}_h, \boldsymbol{u}_h^n \circ \boldsymbol{\phi}_h^n - \dot{\boldsymbol{d}}_h^n\right) = 0, \end{cases} \tag{5.6}$$

for all $(\boldsymbol{v}_h, q_h, \boldsymbol{\mu}_h, \boldsymbol{y}_h, \theta_h) \in \boldsymbol{V}_h \times Q_h \times \boldsymbol{\Lambda}_h \times \boldsymbol{Y}_h \times \Theta_h$.

multipliers, we take

$$\boldsymbol{\Lambda}_h = \left\{ \boldsymbol{\mu}_h = \sum_{i=1}^{N_h^{\mathrm{s}}} \boldsymbol{\mu}_i \delta_{\boldsymbol{x}_i^{\mathrm{s}}} \Big/ \boldsymbol{\mu}_i \in \mathbb{R}^d, \quad \forall i \in \{1, \ldots, N_h^{\mathrm{s}}\} \right\}, \tag{5.7}$$

where $\{\boldsymbol{x}_i^{\mathrm{s}}\}_{i=1}^{N_h^{\mathrm{s}}}$ denotes the points of the triangulation $\mathcal{T}_h^{\mathrm{s}}$ and $\delta_{\boldsymbol{x}_i^{\mathrm{s}}}$ stands for the Dirac's measure at point $\boldsymbol{x}_i^{\mathrm{s}}$. This non-conforming approximation was used for example in [GPHJ99, dSGB08] and analyzed in [FM14]. The discrete method is hence obtained from the approximation of the weak form (5.4), as detailed in Algorithm 5.2. Note that the geometric compatibility condition $(2.16)_1$ is treated explicitly via the first step (5.5).

From (5.7), the discrete treatment of the kinematic constraint in (5.6), namely,

$$b\left(\boldsymbol{\mu}_h, \boldsymbol{u}_h^n \circ \boldsymbol{\phi}_h^n - \dot{\boldsymbol{d}}_h^n\right) = 0, \quad \forall \boldsymbol{u}_h \in \boldsymbol{\Lambda}_h,$$

simply reads

$$\boldsymbol{u}_h^n \circ \boldsymbol{\phi}_h^n(\boldsymbol{x}_i^{\mathrm{s}}) - \dot{\boldsymbol{d}}_h^n(\boldsymbol{x}_i^{\mathrm{s}}) = 0, \quad \forall i \in \{1, \ldots, N_h^{\mathrm{s}}\}. \tag{5.8}$$

The present computer implementation of this method is performed by penalization (omitted in the concise description of Algorithm 5.2 for the sake of clarity). Let $\varepsilon > 0$ be a given (non-dimensionless) parameter, the kinematic coupling condition (5.8) is hence replaced by

$$\boldsymbol{u}_h^n \circ \boldsymbol{\phi}_h^n(\boldsymbol{x}_i^{\mathrm{s}}) - \dot{\boldsymbol{d}}_h^n(\boldsymbol{x}_i^{\mathrm{s}}) = \varepsilon \boldsymbol{\lambda}_i^n, \quad \forall i \in \{1, \ldots, N_h^{\mathrm{s}}\}. \tag{5.9}$$

Owing to the choice of $\boldsymbol{\Lambda}_h$, the elimination of the Lagrange multipliers obtained with the penalization can be done without affecting the sparse pattern of the matrix of the fluid problem. This property makes the approach very convenient from a computer implementation point of view. The influence of the penalty parameter ε on the accuracy of the method will be discussed in Section 5.4, devoted to the numerical experiments. The choice here is to enforce relation (5.9) at every time-step, but let us mention an interesting

alternative which consists in introducing a time dynamics for the Lagrange multiplier, in the spirit of what is done for the pressure in pseudo-compressibility methods. This approach is adopted in [KHS+15], and further analyzed in [KHY+17] in a scalar case.

The main sources of inaccuracies in Algorithm 5.2 come from the choice of the Lagrange multiplier space (5.7) and from the continuous nature of the pressure approximation across the interface. While the impact of the former can be mitigated via mesh refinement, the latter is known to yield major mass conservation issues across the interface. It is worth noting that similar poor mass conservation was encountered with the original immersed boundary method using finite difference approximations in space (see, e.g., [PP93, BDG+17]). In the variational setting of Algorithm 5.2, the use of alternative spatial approximations, based on globally discontinuous pressures and higher order polynomials for the velocities, has been investigated in [Baa01, BCGG12b, BCGG12a, BCG15] with the purpose of overcoming this issue. In this chapter, we follow the approach considered in [KHS+15] (see also [GLRW12, CBCG17]), with which the original (low-order) velocity/pressure approximation is preserved by simply modifying the SUPG/PSPG and grad-div stabilizations in a neighborhood ω_h^n of the interface Σ_h^n (typically 2 layers of fluid elements on each side). More precisely, in (5.3) we take

$$\lambda_{\mathrm{C}} = 1 \quad \text{in} \quad \Omega, \quad \lambda_{\mathrm{M}} = \begin{cases} 1 & \text{in} \quad \Omega \backslash \omega_h^n, \\ \varepsilon_{\mathrm{M}} & \text{in} \quad \omega_h^n, \end{cases}$$

with $0 < \varepsilon_{\mathrm{M}} \ll 1$ a user-defined parameter. Thus, the idea of the method consists in boosting the grad-div stabilization while reducing the SUPG/PSPG stabilization near the interface. The first improves mass conservation while the second limits the impact of the local residual inconsistencies.

5.3.2.2 Nitsche-XFEM method

As in Algorithm 5.2, the geometric compatibility condition $(2.16)_1$ is treated in an explicit fashion and we consider the same discretization of the solid. For the construction of the fluid approximation spaces, we introduce two family of meshes $\{\mathcal{T}_{h,i}^n\}_{0<h<1}$, $i = \{1,2\}$, where each $\mathcal{T}_{h,i}^n$ covers the i^{th} fluid region defined by Σ_h^n. Each mesh $\mathcal{T}_{h,i}^n$ is fitted to the exterior boundary Γ but not to Σ_h^n (see Figure 5.1). Furthermore for every element $K \in \mathcal{T}_{h,1}^n \cap \mathcal{T}_{h,2}^n$ we assume that $K \cap \Sigma_h^n \neq \emptyset$. Note that $\mathcal{T}_{h,1}^n \cup \mathcal{T}_{h,2}^n$ is a triangulation of the whole fluid domain Ω. We denote by $\Omega_{h,i}^n$ the domain covered by $\mathcal{T}_{h,i}^n$, viz.,

$$\Omega_{h,i}^n \overset{\text{def}}{=} \operatorname{int}\left(\cup_{K \in \mathcal{T}_{h,i}^n} K\right).$$

We can hence introduce the following time-dependent spaces of continuous piecewise affine functions:

$$X_{h,i}^n \overset{\text{def}}{=} \left\{ v_h \in C^0(\overline{\Omega_{h,i}^n}) \,/\, v_{h|K} \in \mathbb{P}_1(K), \quad \forall K \in \mathcal{T}_{h,i}^n \right\},$$

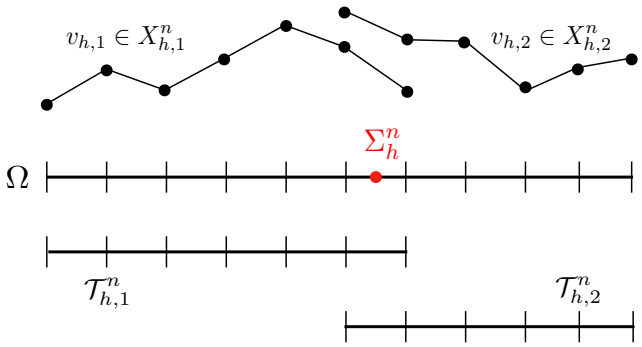

Figure 5.1 – One-dimensional illustration of the construction of the discrete spaces $X^n_{h,i}$.

for $i = \{1,2\}$. For the approximation of the fluid velocity and pressure we will consider the product spaces $\boldsymbol{V}^n_h$ and Q^n_h defined as

$$\boldsymbol{V}^n_h \overset{\text{def}}{=} \big([X^n_{h,1}]^d \times [X^n_{h,2}]^d\big) \cap \boldsymbol{V} \quad \text{and} \quad Q^n_h \overset{\text{def}}{=} (X^n_{h,1} \times X^n_{h,2}) \cap Q.$$

Note that interfacial (strong and weak) discontinuities are now incorporated at the discrete level. Indeed, the functions of these spaces are continuous in the fluid domain $\Omega^n_h \overset{\text{def}}{=} \Omega \backslash \Sigma^n_h$, but discontinuous across the moving interface Σ^n_h (see Figure 5.1).

In this framework, the kinematic/dynamic fluid-solid coupling $(2.16)_{2,3}$ can be enforced in a consistent fashion (and Lagrange multipliers free) through a fluid-sided Nitsche's mortaring (see [AFFL16, BF14]). The resulting numerical method is detailed in Algorithm 5.3.

Here, $\gamma > 0$ denotes the Nitsche's penalty parameter and the fluid trilinear form $a^{\text{f},n}_h$ is given by the following expression:

$$\begin{aligned} a^{\text{f},n}_h\big(\boldsymbol{z}_h;(\boldsymbol{u}_h,p_h),(\boldsymbol{v}_h,q_h)\big) \overset{\text{def}}{=} c^n_h(\boldsymbol{z}_h;\boldsymbol{u}_h,\boldsymbol{v}_h) + a_{\Omega^n_h}\big((\boldsymbol{u}_h,p_h),(\boldsymbol{v}_h,q_h)\big) \\ + s^n_{\text{v},h}(\boldsymbol{z}_h;\boldsymbol{u}_h,\boldsymbol{v}_h) + s^n_{\text{p},h}(\boldsymbol{z}_h;p_h,q_h) + g^n_h(\boldsymbol{u}_h,\boldsymbol{v}_h). \end{aligned} \tag{5.11}$$

In this expression, the convective term is defined as

$$\begin{aligned} c^n_h(\boldsymbol{z}_h;\boldsymbol{u}_h,\boldsymbol{v}_h) \overset{\text{def}}{=} c_{\Omega^n_h}(\boldsymbol{z}_h;\boldsymbol{u}_h,\boldsymbol{v}_h) + \frac{\rho^{\text{f}}}{2}\big((\boldsymbol{\nabla}\cdot\boldsymbol{z}_h)\boldsymbol{u}_h,\boldsymbol{v}_h\big)_{\Omega^n_h} \\ - \rho^{\text{f}}\big(\{\!\{\boldsymbol{z}_h\}\!\}\cdot\boldsymbol{n}[\![\boldsymbol{u}_h]\!],\{\!\{\boldsymbol{v}_h\}\!\}\big)_{\Sigma^n_h} - \frac{\rho^{\text{f}}}{2}\big([\![\boldsymbol{z}_h\cdot\boldsymbol{n}]\!],\{\!\{\boldsymbol{u}_h\cdot\boldsymbol{v}_h\}\!\}\big)_{\Sigma^n_h}, \end{aligned}$$

where the last two (consistent) terms are introduced for stability purposes to guarantee that $c^n_h(\boldsymbol{z}_h;\boldsymbol{v}_h,\boldsymbol{v}_h) = 0$.

The terms in $s^n_{\text{v},h}$ and $s^n_{\text{p},h}$ in (5.11) correspond to the continuous interior penalty (CIP)

Algorithm 5.3 Nitsche-XFEM method (from [AFFL16]).

For $n \geq 1$,

1. Interface update:

$$\boldsymbol{\phi}_h^n = \boldsymbol{I}_\Sigma + \boldsymbol{d}_h^{n-1}, \quad \Sigma_h^n = \boldsymbol{\phi}_h^n(\Sigma), \quad \Omega_h^n = \Omega \backslash \Sigma_h^n.$$

2. Find $\left(\boldsymbol{u}_h^n, p_h^n, \boldsymbol{d}_h^n, \boldsymbol{a}_h^n\right) \in \boldsymbol{V}_h^n \times Q_h^n \times \boldsymbol{Y}_h \times \boldsymbol{S}_h$, with $\dot{\boldsymbol{d}}_h = \partial_\tau \boldsymbol{d}_h^n$, such that

$$\begin{cases} \rho^{\mathrm{f}}\left(\partial_\tau \boldsymbol{u}_h^n, \boldsymbol{v}_h\right)_{\Omega_h^n} + a_h^{\mathrm{f},n}\left(\boldsymbol{u}_h^{n-1}; (\boldsymbol{u}_h^n, p_h^n), (\boldsymbol{v}_h, q_h)\right) \\ + \rho^{\mathrm{s}} \epsilon \left(\partial_\tau \dot{\boldsymbol{d}}_h^n, \boldsymbol{y}_h\right)_\Sigma + a_h^{\mathrm{s}}\left((\boldsymbol{d}_h^n, \boldsymbol{a}_h^n), (\boldsymbol{y}_h, \theta_h)\right) \\ - \displaystyle\sum_{i=1}^{2} \left(\boldsymbol{\sigma}(\boldsymbol{u}_{h,i}^n, p_{h,i}^n)\boldsymbol{n}_i, \boldsymbol{v}_{h,i} - \boldsymbol{y}_h\right)_{\Sigma_h^n} \\ - \displaystyle\sum_{i=1}^{2} \left(\boldsymbol{u}_{h,i}^n - \dot{\boldsymbol{d}}_h^n, \boldsymbol{\sigma}(\boldsymbol{v}_{h,i}, -q_{h,i})\boldsymbol{n}_i\right)_{\Sigma_h^n} \\ + \dfrac{\gamma\mu}{h} \displaystyle\sum_{i=1}^{2} \left(\boldsymbol{u}_{h,i}^n - \dot{\boldsymbol{d}}_h^n, \boldsymbol{v}_{h,i} - \boldsymbol{y}_h\right)_{\Sigma_h^n} = 0, \end{cases} \tag{5.10}$$

for all $(\boldsymbol{v}_h, q_h, \boldsymbol{y}_h, \theta_h) \in \boldsymbol{V}_h^n \times Q_h^n \times \boldsymbol{Y}_h \times \Theta_h$.

stabilization (see [BFH06]) given by

$$\begin{aligned} s_{\mathrm{v},h}^n(\boldsymbol{z}_h; \boldsymbol{u}_h, \boldsymbol{v}_h) &\stackrel{\mathrm{def}}{=} \gamma_{\mathrm{v}} h^2 \sum_{i=1}^{2} \sum_{F \in \mathcal{F}_{h,i}^n} \xi_F(\boldsymbol{z}_h) \|\boldsymbol{z}_h \cdot \boldsymbol{n}\|_{L^\infty(F)} \left([\![\boldsymbol{\nabla} \boldsymbol{u}_h]\!]_F, [\![\boldsymbol{\nabla} \boldsymbol{v}_h]\!]_F\right)_F, \\ s_{\mathrm{p},h}^n(\boldsymbol{z}_h; p_h, q_h) &\stackrel{\mathrm{def}}{=} \gamma_{\mathrm{p}} h^2 \sum_{i=1}^{2} \sum_{F \in \mathcal{F}_{h,i}^n} \frac{\xi_F(\boldsymbol{z}_h)}{\|\boldsymbol{z}_h\|_{L^\infty(F)}} \left([\![\boldsymbol{\nabla} p_h]\!]_F, [\![\boldsymbol{\nabla} q_h]\!]_F\right)_F, \end{aligned} \tag{5.12}$$

where $\mathcal{F}_{h,i}^n$ denotes the set of interior edges (for $d = 2$) or faces (for $d = 3$) of $\mathcal{T}_{h,i}^n$, the symbol $[\![\cdot]\!]_F$ stands for the jump operator across the edge or face F, the function ξ_F is defined by

$$\xi_F(\boldsymbol{z}_h) \stackrel{\mathrm{def}}{=} \min\{1, \mathrm{Re}_F(\boldsymbol{z}_h)\} \quad \text{and} \quad \mathrm{Re}_F(\boldsymbol{z}_h) \stackrel{\mathrm{def}}{=} \frac{\rho^{\mathrm{f}} \|\boldsymbol{z}_h\|_{L^\infty(F)} h}{\mu}$$

and $\gamma_{\mathrm{p}}, \gamma_{\mathrm{v}} > 0$ are user-defined parameters. The main reason of using the CIP stabilization (5.12) (instead of (5.3)) is that it is strongly consistent in the whole computational domain $\Omega_{h,1}^n \times \Omega_{h,2}^n$, while (5.3) it is strongly consistent only in the physical domain Ω_h^n due to its residual-based nature (see [AFFL16] for a discussion).

At last, the term g_h^n in (5.11) corresponds to the so-called ghost-penalty stabilization operator which guarantees the robustness of the method with respect to the way the

interface Σ_h^n cuts the fluid elements. It is given by the following expression (see [Bur10]):

$$g_h^n(\boldsymbol{u}_h,\boldsymbol{v}_h) \overset{\text{def}}{=} \gamma_{\text{g}}\mu h \sum_{i=1}^{2} \sum_{F\in\mathcal{F}_{h,i}^{n,\Sigma}} \left(\llbracket \boldsymbol{\nabla} \boldsymbol{u}_{h,i} \rrbracket_F, \llbracket \boldsymbol{\nabla} \boldsymbol{v}_{h,i} \rrbracket_F\right)_F,$$

where $\mathcal{F}_{h,i}^{n,\Sigma}$ denotes the set of interior edges or faces of the elements of $\mathcal{T}_{h,i}^n$ intersected by Σ_h^n and $\gamma_{\text{g}} > 0$ is a user-defined parameter.

It should be noted that, for consistency, all the fluid bulk terms in (5.10) are evaluated only in the physical zones of $\Omega_{h,i}^n$ (i.e., the integrals are evaluated over cut-elements). Furthermore, the interface integrals on Σ_h^n involve the products of fields defined on different meshes. Hence, in comparison with Algorithm 5.2, Algorithm 5.3 requires a non-standard computer implementation and a specific evaluation of all the interface intersections. We refer to [AFFL16] (and the references therein) for a critical review on this point.

5.4 Numerical experiments

The purpose of this section is to illustrate and compare, via a series of 2D numerical examples (i.e., the above-mentioned dimension d is set to 2), the accuracy of the unfitted methods described in Section 5.3.2. To this purpose, we consider as reference solution the one provided by the fitted mesh method (Algorithm 5.1) using a highly refined space-time grid. The accuracy of the unfitted mesh methods will be then evaluated by comparing the results obtained with three successive levels of mesh refinement in space and in time.

Through this section, the acronyms ALE, FD and NXFEM respectively refer to Algorithms 5.1, 5.2 and 5.3. Moreover, the variant of Algorithm 5.2 discussed in Section 5.3.2.1, with enhanced interfacial mass conservation, will be referred to as FD_{stab}. Table 5.1 summarizes the different user-defined parameters involved in each method, with some prescribed values.

ALE	FD	FD_{stab}	NXFEM
$\lambda_{\text{C}} = 0$	$\lambda_{\text{C}} = 0$	$\lambda_{\text{C}} = 1$	$\gamma = 10^2$
$\lambda_{\text{M}} = 1$	$\lambda_{\text{M}} = 1$	$\lambda_{\text{M}} = \begin{cases} 1 & \text{in} \quad \Omega\backslash\omega_h^n \\ \varepsilon_{\text{M}} & \text{in} \quad \omega_h^n \end{cases}$	$\gamma_{\text{v}} = \gamma_{\text{p}} = 10^{-2}$
	ε	ε	$\gamma_{\text{g}} = 1$

Table 5.1 – Free parameters of the numerical methods.

For the FD and FD_{stab} methods, the choice of the penalty parameter ε and (for the latter only) of the stabilization parameter ε_{M} requires a specific care which will be discussed in the next paragraphs. More information about the way the penalty parameter ε is chosen and the neighborhood ω_h^n is defined are provided, respectively, in Appendices D and E.

In this section and in the rest of this work, the different fluid problems are discretized in space by using $\mathbb{P}_1/\mathbb{P}_1$ SUPG/PSPG stabilized finite elements for the velocity and the

pressure unknowns (see, e.g., [Tez91]), unless otherwise stated. The spatial discretization of the solid problem is based on linear MITC elements (see, e.g., [Bat96]). Last, all the numerical experiments presented in what follows have been computed by using the finite element library FELiScE[1]. All the units are expressed in the CGS system, unless specified otherwise.

5.4.1 Open valve

As first example, we consider the heart-valve-inspired benchmark problem proposed in [KHS+15, GABH13, HGAB12, Wic14]. Due to the symmetric properties of the problem, only half of the domain is simulated with appropriate symmetry boundary conditions. The problem consists of one cantilevered elastic beam immersed in a 2D channel filled with an incompressible Newtonian fluid, as shown in Figure 5.2.

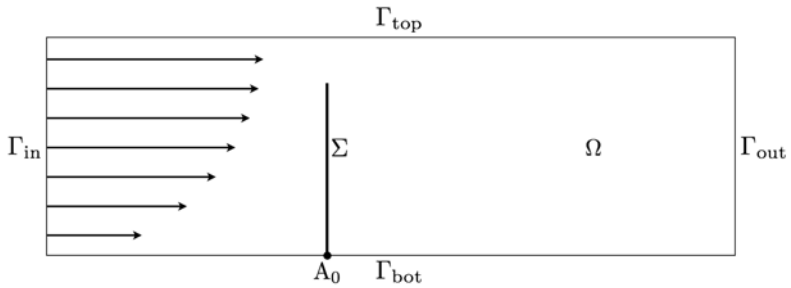

Figure 5.2 – Geometric configuration of the first numerical example.

The geometry of the fluid domain is given by $\Omega = [0, 8] \times [0, 0.805]$. The reference configuration of the solid is the segment with endpoints $(2, 0)$ and $(2, 0.7)$ (see Figure 5.2). The physical parameters for the fluid are $\rho^f = 100$ and $\mu = 10$. For the solid, we have $\rho^s = 100$, $\epsilon = 0.0212$, with Young's modulus $E = 5.6 \cdot 10^7$ and Poisson's ratio $\nu = 0.4$.

As regards the boundary conditions for the fluid, a no-slip boundary condition is enforced on Γ_{bot} while a symmetry boundary condition is imposed on Γ_{top}. Zero traction is enforced on the lateral boundary Γ_{out}. The velocity is prescribed on Γ_{in}, as a half parabolic profile whose maximum amplitude is defined by a positive time-dependent function $u_{max}(t)$ given by the following expression:

$$u_{max}(t) = \ 5 \cdot (0.805)^2 \cdot (\sin(2\pi t) + 1.1)\,, \quad \forall t \in \mathbb{R}^+.$$

The beam is fully clamped at its bottom endpoint. The fluid and the solid are initially at rest.

5.4.1.1 Spatial and temporal discretization

A reference solution has been generated using Algorithm 5.1 with a high space-time grid resolution. The solid mesh is made of 59 segments and the body-fitted fluid mesh of

[1] See https://gforge.inria.fr/projects/felisce/.

48 706 quadrilaterals which are refined around the interface. The initial configuration of the fitted meshes is depicted in Figure 5.3a.

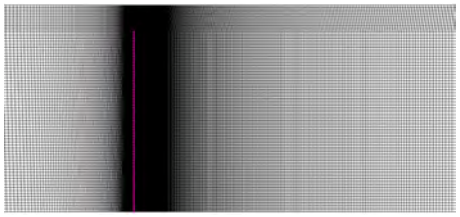

(a) Fitted meshes - Reference.

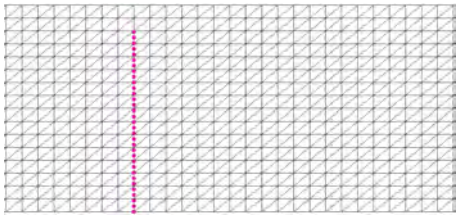

(b) Unfitted meshes - M_1.

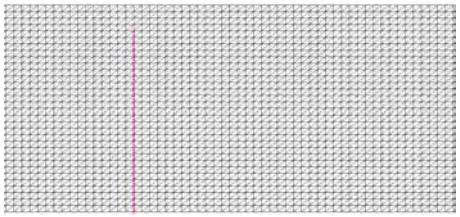

(c) Unfitted meshes - M_2.

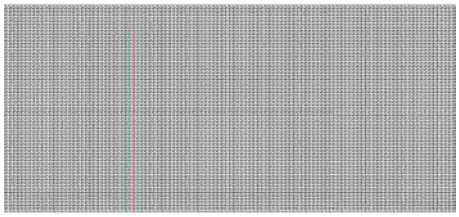

(d) Unfitted meshes - M_3.

Figure 5.3 – Zoom on the fluid and solid meshes at time $t = 0$.

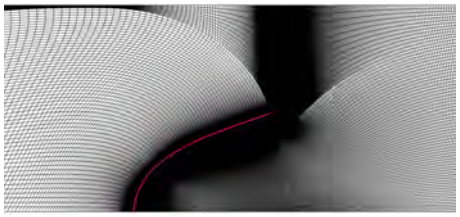

(a) Fitted meshes - Reference.

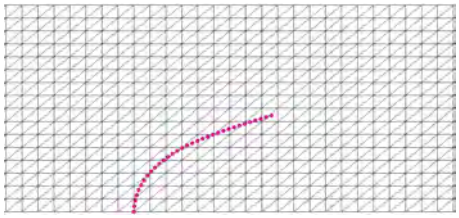

(b) Unfitted meshes - M_1.

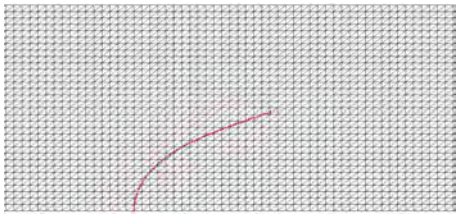

(c) Unfitted meshes - M_2.

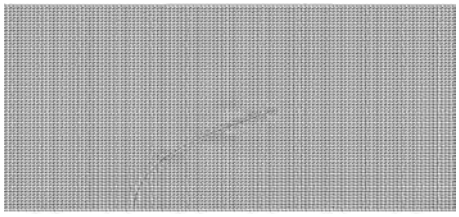

(d) Unfitted meshes - M_3.

Figure 5.4 – Zoom on the fluid and solid meshes at time $t = 0.5$.

Here, the fluid velocity and pressure fields are approximated using $\mathbb{Q}_1$ finite elements. The time-step is $\tau = 10^{-3}$ and the final time is $t = 3$, corresponding to around 3 full cycles of oscillations of the structure. A snapshot of the resulting deformed mesh at time $t = 0.5$ is shown in Figure 5.4a.

The first level of refinement for the unfitted meshes, which we refer to as M_1, divides the fluid domain into 4 096 triangles and the structure domain into 32 segments. The corresponding time-step is $\tau = 10^{-2}$. The two subsequent space-time grids, respectively noted M_2 and M_3, are uniform refinements of M_1 with a factor of, respectively, 2 and 4

along the spatial and temporal directions. Hence, M_2 is made of 16 384 triangles and M_3 of 65 536 triangles. Their corresponding structure domains are respectively divided into 64 and 128 segments. The time-steps are $\tau = 5 \cdot 10^{-3}$ in M_2 and $\tau = 2.5 \cdot 10^{-3}$ in M_3. For illustration purposes, M_1, M_2 and M_3 at $t = 0$ are shown in Figures 5.3b–5.3d and at $t = 0.5$ in Figures 5.4b–5.4d (obtained with the NXFEM method).

5.4.1.2 Comparison of results

The values of the penalty parameter ε for the FD method are equal to 10^{-5} with M_1, 10^{-6} with M_2 and 10^{-6} with M_3. The motivation of these choices will be discussed in Section 5.4.1.3 below. For this example, the results obtained with the FD_{stab} variant method are very close to those obtained with the FD method and thus are omitted.

Figures 5.5 and 5.6 present snapshots of the interface location and fluid velocity magnitude near the leaflet at $t = 0.5$ for the three levels of refinement and for the NXFEM and FD methods, respectively. Overall, a good agreement of the velocity field with the ALE method is already observed for the coarsest grid M_1. Note that the correct computation of the induced vortex after the leaflet requires more refinement and it is better captured by the NXFEM method.

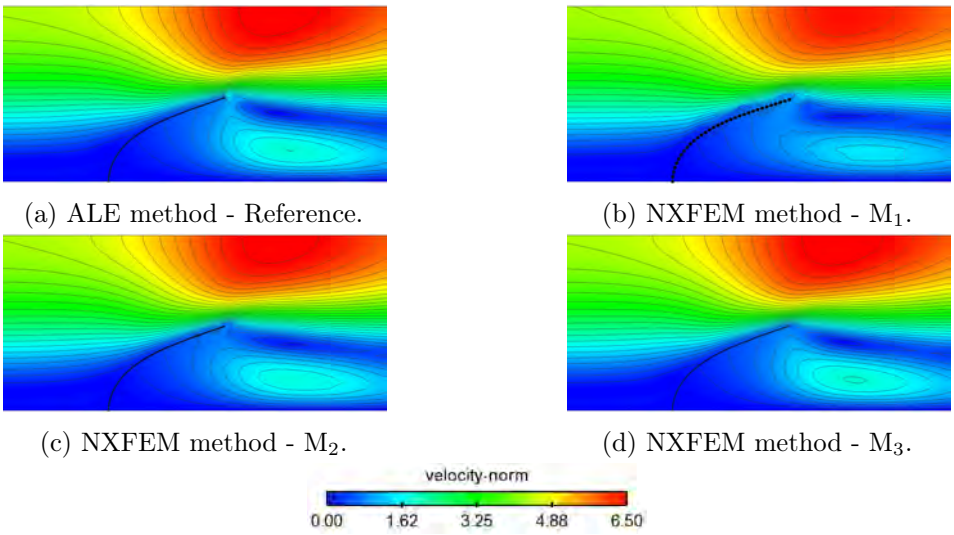

(a) ALE method - Reference.

(b) NXFEM method - M_1.

(c) NXFEM method - M_2.

(d) NXFEM method - M_3.

Figure 5.5 – Snapshots of the fluid velocity magnitude at $t = 0.5$ obtained with NXFEM.

The results for the pressure are given in Figures 5.7 and 5.8, respectively for the NXFEM and FD methods. The NXFEM method gets the correct shape of the pressure field, even with the coarsest grid resolution. After refinement, the agreement with the ALE method is very good in both approaches. For the FD method, comparisons between M_1 and M_3 clearly indicates that mesh refinement improves the results.

Figure 5.9 reports a comparison of the time history of the x-solid displacement at the upper leaflet tip obtained with the NXFEM and FD methods. The NXFEM method shows better agreement with the ALE method. Nevertheless, the overall agreement of the FD methods is satisfying for the M_2 and M_3 refinement levels.

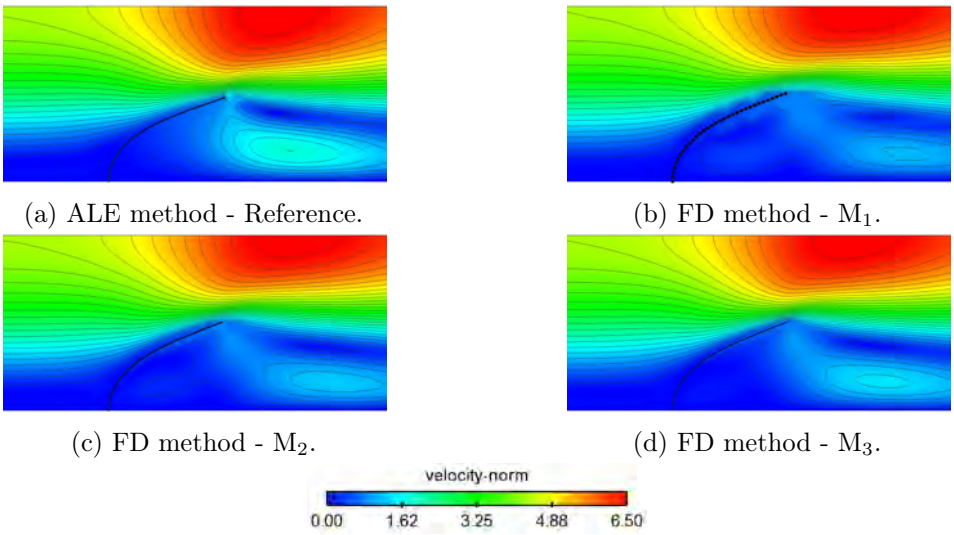

(a) ALE method - Reference. (b) FD method - M_1.

(c) FD method - M_2. (d) FD method - M_3.

Figure 5.6 – Snapshots of the fluid velocity magnitude at $t = 0.5$ obtained with FD.

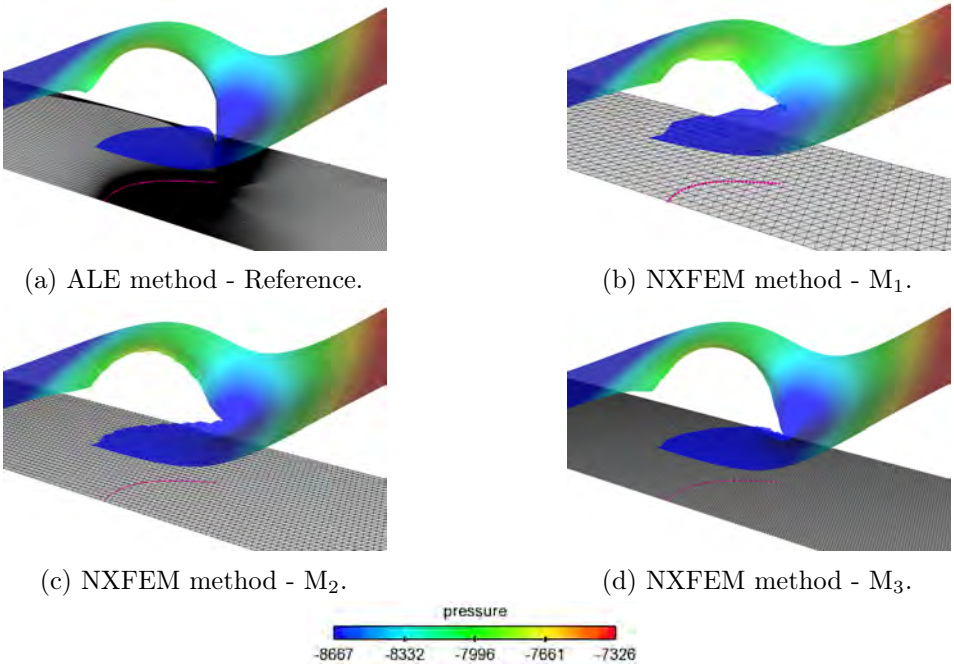

(a) ALE method - Reference. (b) NXFEM method - M_1.

(c) NXFEM method - M_2. (d) NXFEM method - M_3.

Figure 5.7 – Snapshots of the fluid elevated pressure at $t = 0.5$ obtained with NXFEM.

Similar observations can be made from Figure 5.10, which reports the time history of the y-solid displacement of the upper leaflet tip. Note that the convergence of the FD method towards the reference solution is clearly visible, but slower than for the NXFEM method.

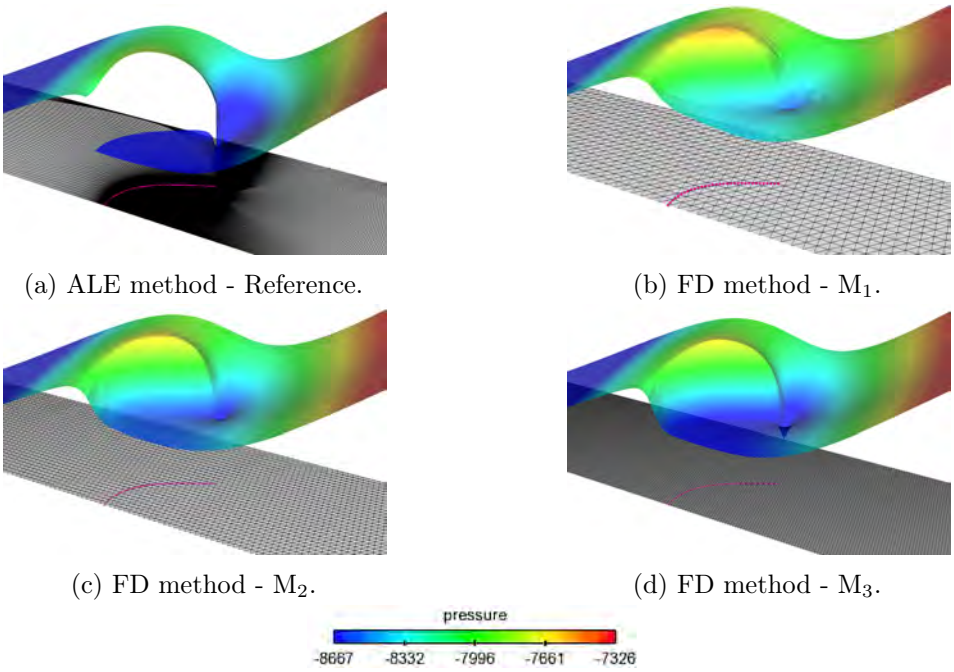

(a) ALE method - Reference. (b) FD method - M_1.

(c) FD method - M_2. (d) FD method - M_3.

Figure 5.8 – Snapshots of the fluid elevated pressure at $t = 0.5$ obtained with FD.

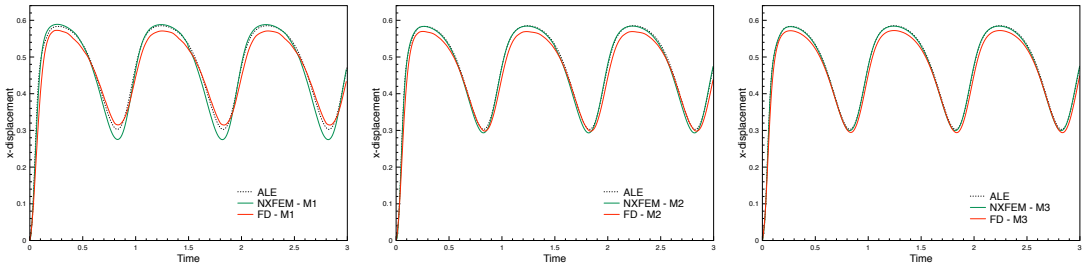

(a) M_1 vs. Reference. (b) M_2 vs. Reference. (c) M_3 vs. Reference.

Figure 5.9 – Time history of the x-displacement of the upper leaflet tip.

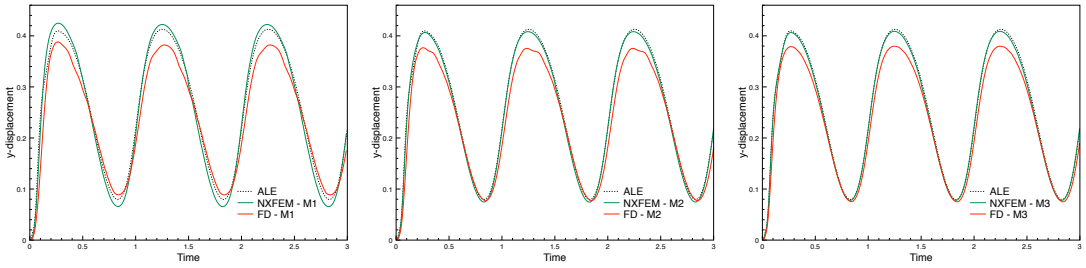

(a) M_1 vs. Reference. (b) M_2 vs. Reference. (c) M_3 vs. Reference.

Figure 5.10 – Time history of the y-displacement of the upper leaflet tip.

5.4.1.3 Choice of the penalty parameters for the fictitious domain methods

For the FD method introduced in Algorithm 5.2, the critical parameter to fix is the penalization coefficient ε. The choice of the values of penalty parameters is usually delicate and arbitrary (see, e.g., [ZS14, RAB07]). Here, we present the workflow we carried on to determine a range of admissible values for the penalization coefficient ε. Our approach is similar to the one used in [ZS14]: a given simulation has been run with a large range of values for the penalty parameter ε. The value is initially 10^{-1} and is reduced until the convergence is lost due to ill-conditioning problems of the system. A physical value, characterizing the current case, is then computed with respect to the time. This convergence study is done on for each level of refinement.

The physical value of interest here is the displacement magnitude of the immersed upper leaflet tip. The set of values used for ε is given by

$$\varepsilon = \begin{cases} \{10^{-i}, \quad i = 1 \dots 6\}, & \text{for } M_1, \\ \{10^{-i}, \quad i = 1 \dots 7\}, & \text{for } M_2, \\ \{10^{-i}, \quad i = 1 \dots 7\}, & \text{for } M_3. \end{cases}$$

The corresponding results for the levels of refinement M_1, M_2 and M_3 are respectively shown in Figures 5.11a–5.11c.

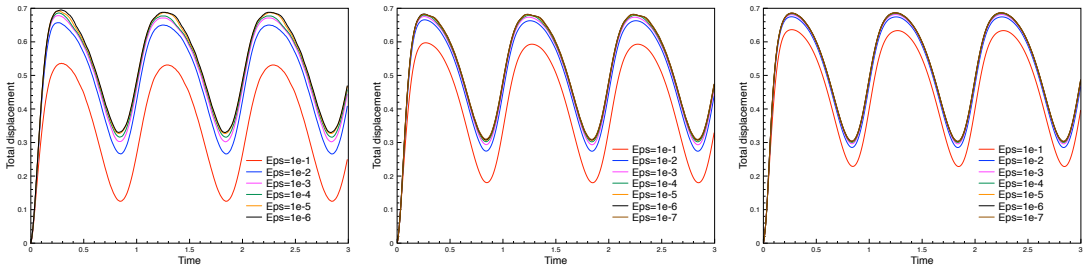

(a) M_1. (b) M_2. (c) M_3.

Figure 5.11 – Convergence study of the penalty parameter ε.

As expected, all the curves have the same behavior, independently of the penalization or the refinement of the meshes. The penalty parameter ε has an impact on the amplitude of the displacement: when the penalization is stronger, the different curves convergence towards the same value. As the penalization of the immersed structure appears in the fluid problem under the form $\frac{1}{\varepsilon}$, a small penalty parameter may induce ill-conditioning of the system and then, low convergence rate. This is why we assumed that, once a good over-all convergence has been achieved and the results are independent of the values of ε, it is no more useful to further reduce it. More information about the convergence study of the penalty parameter ε for this case are provided in Appendix D for the different levels of refinement.

5.4.2 Closed valve

As second example, we consider a benchmark problem mimicking the behavior of a closed valve (see, e.g., [KHS+15, vLAdHB04]). The main difficulty here are the correct evaluation of the pressure jump and the conservation of mass across the valve.

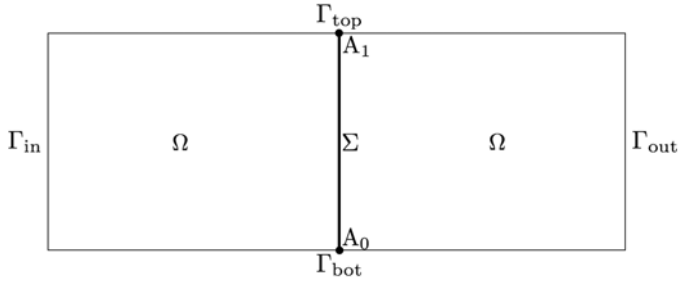

Figure 5.12 – Geometric configuration of the second numerical example.

The problem consists of an elastic beam clamped on its endpoints and immersed in a 2D channel filled with an incompressible Newtonian fluid, as shown in Figure 5.12. The geometry of the fluid domain is given by $\Omega = [0, 4] \times [0, 1]$. The reference configuration for the solid is defined as the segment with endpoints $(2, 0)$ and $(2, 1)$ (see Figure 5.12). The physical parameters for the fluid are $\rho^f = 100$ and $\mu = 10$. For the solid, we have $\rho^s = 100$, $\epsilon = 0.0212$, with Young's modulus $E = 5.6 \cdot 10^7$ and Poisson's ratio $\nu = 0.4$.

As regards the boundary conditions for the fluid, a no-slip boundary condition is enforced on Γ_{bot} and Γ_{top}. Zero traction is enforced on the lateral boundary Γ_{out}, while on Γ_{in}, traction is imposed in terms of the following positive time-dependent pressure function $p_{in}(t)$, given by the following expression:

$$p_{in}(t) = \ 3 \cdot 10^5 \cdot \operatorname{atanh}(10 \cdot t), \quad \forall t \in \mathbb{R}^+.$$

The structure is fully clamped at its endpoints A_0 and A_1. The fluid and the solid are initially at rest. As the prescribed pressure builds up, the solid starts to bend and elongate. After this brief transition phase, the system reaches a steady state with a pressure jump across the interface. The fluid and solid velocities vanish and the pressure is a piecewise constant function taking the value $3 \cdot 10^5$ and zero on each side of the interface, respectively.

5.4.2.1 Spatial and temporal discretization

A reference solution has been generated using Algorithm 5.1 with a high space-time grid resolution. The solid mesh is made of 80 segments and the body-fitted fluid mesh of 25 600 quadrilaterals. The initial configuration of the fitted meshes is depicted in Figure 5.13a.

Here, the fluid velocity and pressure fields are approximated using $\mathbb{Q}_1$ finite elements. The time-step is $\tau = 10^{-3}$ and the final time is $t = 3$, corresponding to the time required by the structure to reach its steady state. A snapshot of the resulting deformed mesh at time $t = 0.125$ is shown in Figure 5.14a.

The first level of refinement for the unfitted meshes, M_1, divides the fluid domain into

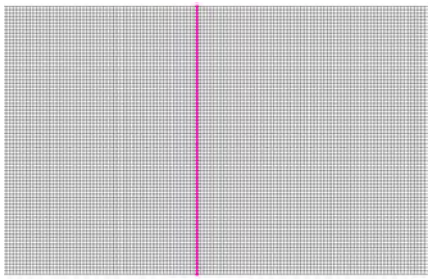

(a) Fitted meshes - Reference.

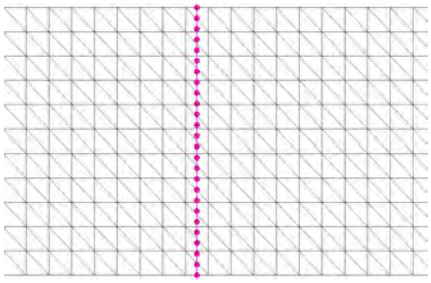

(b) Unfitted meshes - M_1.

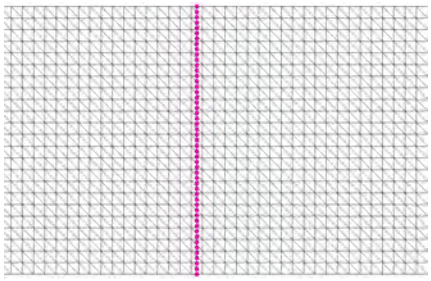

(c) Unfitted meshes - M_2.

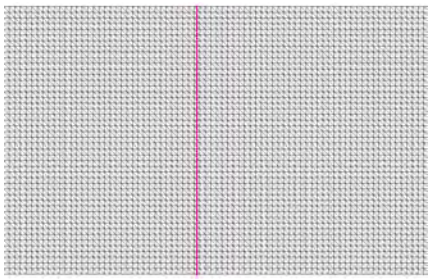

(d) Unfitted meshes - M_3.

Figure 5.13 – Zoom on the fluid and solid meshes at time $t = 0$.

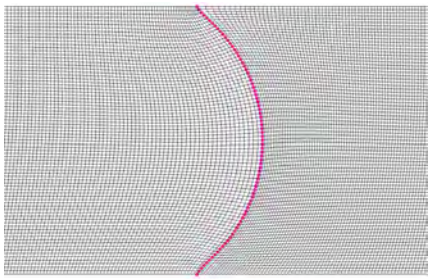

(a) Fitted meshes - Reference.

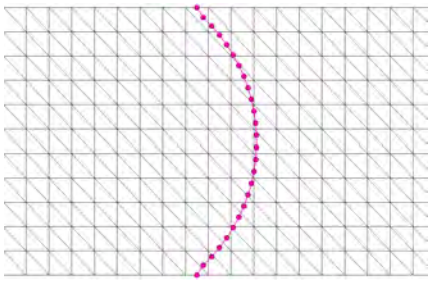

(b) Unfitted meshes - M_1.

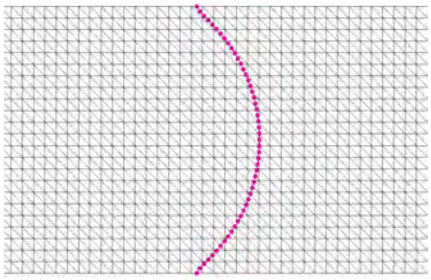

(c) Unfitted meshes - M_2.

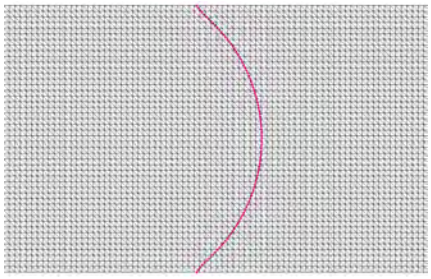

(d) Unfitted meshes - M_3.

Figure 5.14 – Zoom on the fluid and solid meshes at time $t = 0.125$.

1 034 triangles and the structure domain into 25 segments. The corresponding time-step is $\tau = 2 \cdot 10^{-3}$. As in the previous example, the two subsequent space-time grids are uniform refinements of M_1: M_2 is made of 4 370 triangles and M_3 of 17 954 triangles. Their corresponding structure domains are respectively divided into 50 and 100 segments. The

time-steps are $\tau = 10^{-3}$ in M_2 and $\tau = 5 \cdot 10^{-4}$ in M_3. For illustration purposes, M_1, M_2 and M_3 at $t = 0$ are shown in Figures 5.13b–5.13d and at $t = 0.125$ in Figures 5.14b–5.14d (obtained with the NXFEM method).

5.4.2.2 Comparison of results

For all the refinement levels, we have taken $\varepsilon = 10^{-5}$ in the FD and FD_{stab} methods. In the latter, the stabilization parameter is set to $\varepsilon_M = 10^{-4}$. The motivation of these choices will be discussed in Section 5.4.2.3 below.

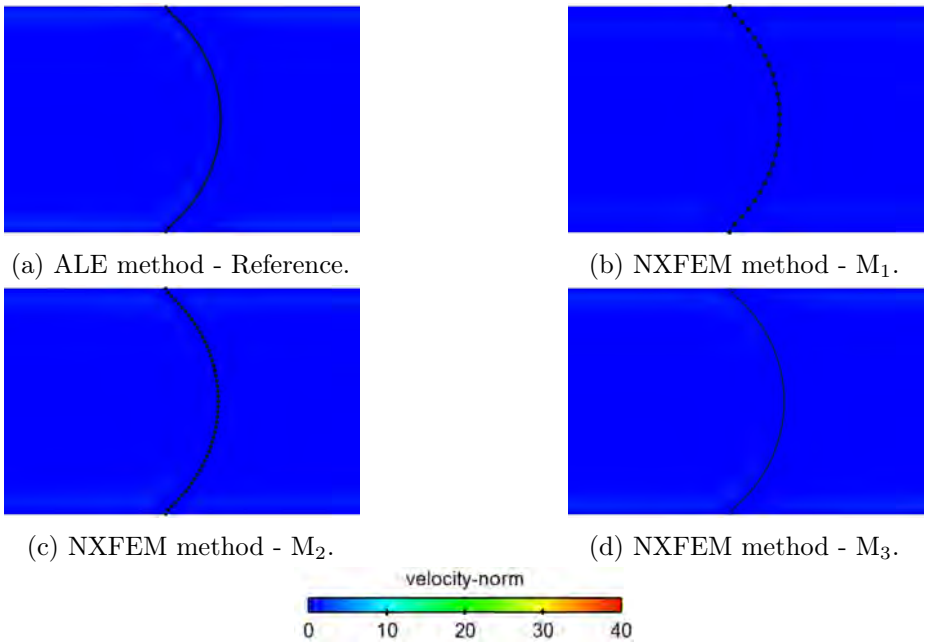

(a) ALE method - Reference.
(b) NXFEM method - M_1.
(c) NXFEM method - M_2.
(d) NXFEM method - M_3.

Figure 5.15 – Snapshots of the fluid velocity magnitude at $t = 0.125$ obtained with NXFEM.

Figures 5.15–5.17 present, respectively for the NXFEM, FD and FD_{stab} methods, the snapshots of the interface location and the fluid velocity magnitude near the leaflet at $t = 0.125$ for the three levels of refinement. The NXFEM method retrieves the negligible velocity field of the reference ALE solution in all the grid refinement levels. The color palette has been kept the same for the three figures in order to highlight the loss of mass featured by the FD method. In Figure 5.16, no matter what level of refinement is used, a significant spurious flow is observed through the channel. This phenomenon is an important limitation of the FD method with continuous pressure approximations (see, e.g., [Baa01, KHS+15]), which guarantees global but not local mass conservation (i.e., on each side of the interface). Figure 5.17 shows, on the contrary, that the FD_{stab} variant is able to significantly reduce this leak across the interface, which highlights the benefits of the modified SUPG/PSPG and grad-div stabilizations proposed in [KHS+15].

The results for the pressure are reported in Figures 5.18–5.20, respectively for the NXFEM, FD and FD_{stab} methods. Once more, the NXFEM method gets the correct pressure jump, particularly with the grid refinement levels M_2 and M_3. On the opposite,

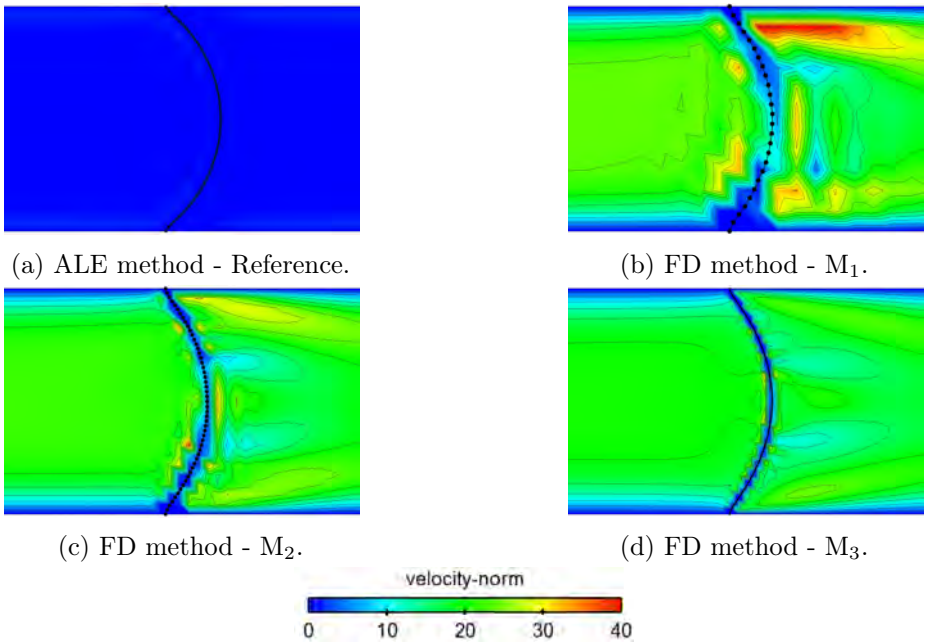

(a) ALE method - Reference. (b) FD method - M_1.

(c) FD method - M_2. (d) FD method - M_3.

Figure 5.16 – Snapshots of the fluid velocity magnitude at $t = 0.125$ obtained with FD.

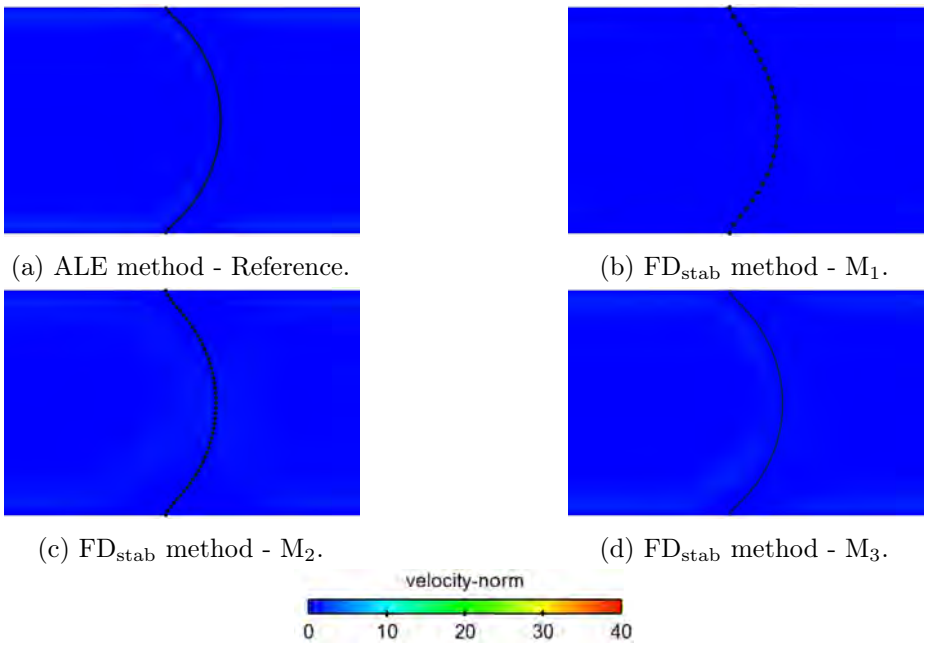

(a) ALE method - Reference. (b) FD_{stab} method - M_1.

(c) FD_{stab} method - M_2. (d) FD_{stab} method - M_3.

Figure 5.17 – Snapshots of the fluid velocity magnitude at $t = 0.125$ obtained with FD_{stab}.

the FD method struggles to correctly compute the pressure jump, which is largely underestimated compared to the reference solution. The FD_{stab} method shows a very good correction of the pressure jump across the valve compared to the FD method. Moreover, the fact that the prediction of the pressure jump improves with the refinement is much

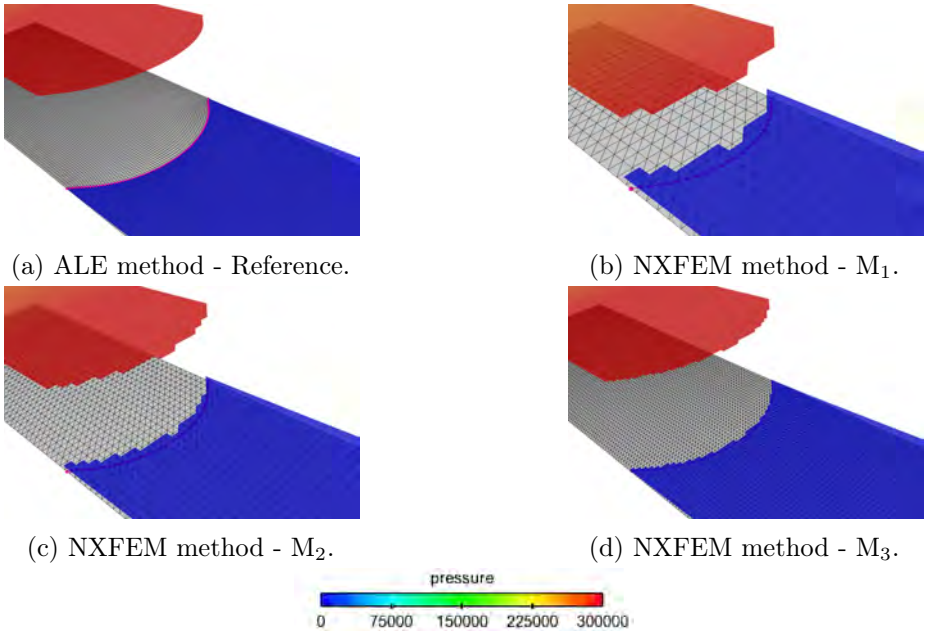

(a) ALE method - Reference. (b) NXFEM method - M_1.

(c) NXFEM method - M_2. (d) NXFEM method - M_3.

Figure 5.18 – Snapshots of the fluid elevated pressure at $t = 0.125$ obtained with NXFEM.

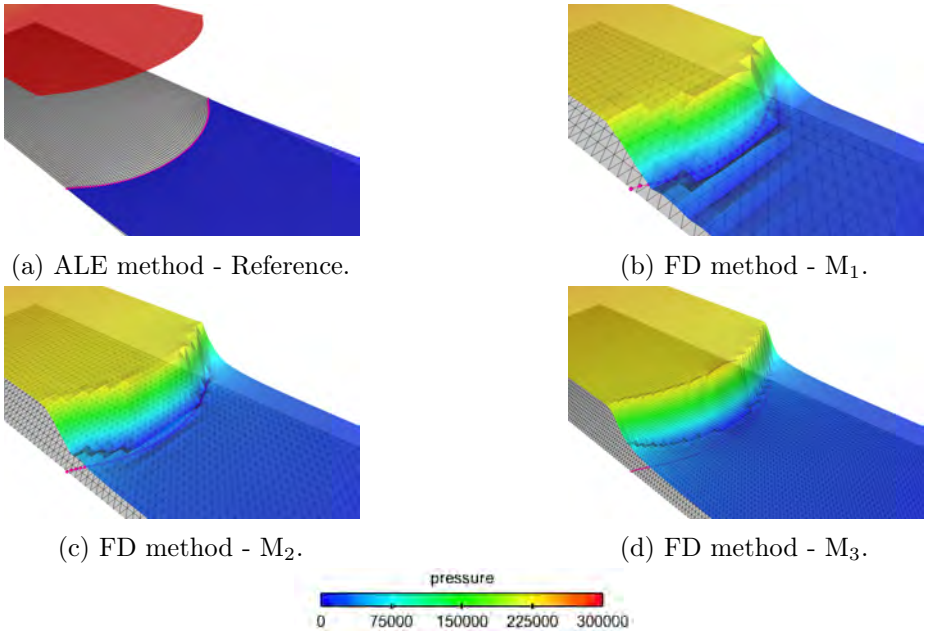

(a) ALE method - Reference. (b) FD method - M_1.

(c) FD method - M_2. (d) FD method - M_3.

Figure 5.19 – Snapshots of the fluid elevated pressure at $t = 0.125$ obtained with FD.

more striking in Figure 5.20.

Figure 5.21 reports a comparison of the time history of the x-solid displacement of the valve mid-point obtained with the NXFEM, FD and FD_{stab} methods. Similar observations can be made from these results. The NXFEM and FD_{stab} methods shows better agreement with the reference solution than with the FD method. One particular point of interest

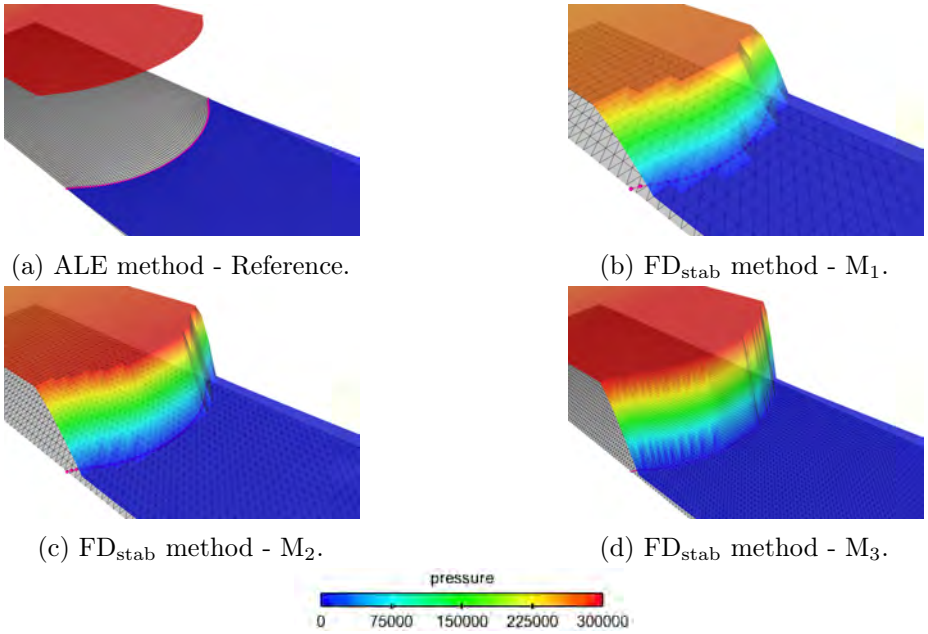

(a) ALE method - Reference. (b) FD_{stab} method - M_1.

(c) FD_{stab} method - M_2. (d) FD_{stab} method - M_3.

Figure 5.20 – Snapshots of the fluid elevated pressure at $t = 0.125$ obtained with FD_{stab}.

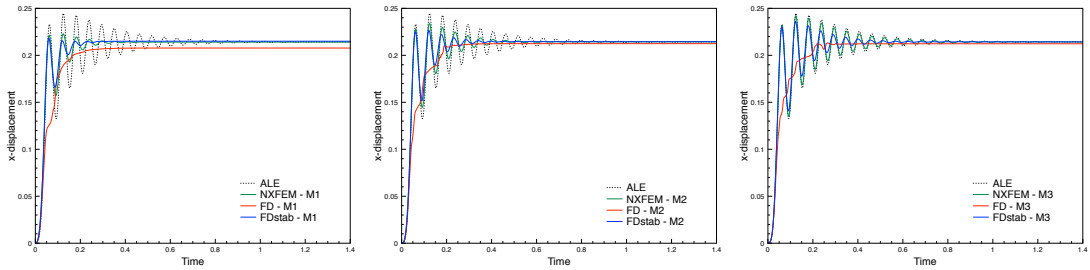

(a) M_1 vs. Reference. (b) M_2 vs. Reference. (c) M_3 vs. Reference.

Figure 5.21 – Time history of the x-displacement of the valve mid-point.

is the computation of the dynamics of the valve, characterized by the oscillations of the x-value around the reference steady state. The FD method is clearly unable to compute the initial dynamics of the valve, no matter what level of refinement is used. On the contrary, the NXFEM and FD_{stab} predict the dynamics of the closed and show convergence to the reference after grid refinement.

5.4.2.3 Choice of the penalty parameters for the fictitious domain methods

As explained in Section 5.4.1.3, we carried on the same convergence study with respect to the penalty parameter ε, appearing in the FD method. The physical value of interest here is the x-displacement of the valve mid-point. For each level of refinement, the case has been run several times with a large panel of values for ε. The same behaviors as the ones described in Section 5.4.1.3 have also been observed here. The chosen values of ε are based on the previous mentioned criteria of convergence. More information about the

convergence study of the penalty parameter ε for this case are provided in Appendix D for the different levels of refinement.

For the sake of illustration, the interfacial zone in which the modified $\mathrm{FD}_{\mathrm{stab}}$ acts, is depicted at $t = 0.125$ in Figures 5.22a–5.22c, respectively for the meshes M_1, M_2 and M_3. In order to choose the values of ε_{M}, the same kind of convergence study as the one

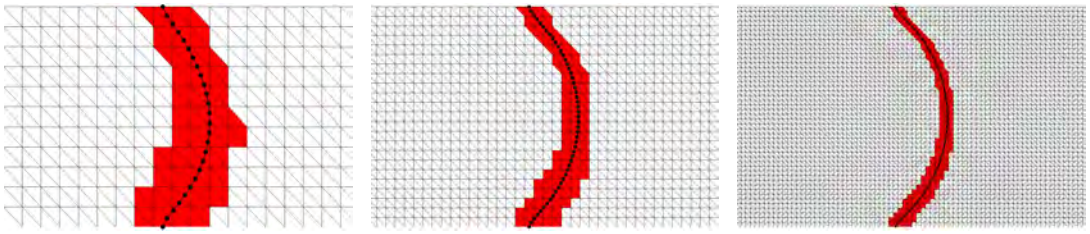

(a) M_1. (b) M_2. (c) M_3.

Figure 5.22 – The neighborhood ω_h^n at time $t = 0.125$.

described in Section 5.4.1.3 for ε has been carried on. For each case M_1, M_2 and M_3, ε is equal to the value given by the convergence study and the case is run several times with a large range of values for the user-defined parameter ε_{M}. The set of values used for ε_{M} is given by

$$\varepsilon_{\mathrm{M}} = \begin{cases} \{10^{-i}, \quad i = 0 \dots 4\}, & \text{for } M_1, \\ \{10^{-i}, \quad i = 0 \dots 4\}, & \text{for } M_2, \\ \{10^{-i}, \quad i = 0 \dots 4\}, & \text{for } M_3. \end{cases}$$

The lowest value, which do not compromise the convergence of the simulation, is chosen. More information about the definition of ω_h^n for this case are provided in Appendix E for the different levels of refinement.

5.4.3 Vesicle in lid-driven cavity flow

As last example, we consider the lid-driven cavity benchmark problem (inspired from, e.g., [RHC15, WZ10, Gri12, GL17]) with an immersed elastic circle, as shown in Figure 5.23.

The geometry of the fluid domain is given by $\Omega = [0, 0] \times [1, 1]$. The reference solid configuration is a circle of radius $R = 0.2$ centred at $(0.6, 0.5)$ (see Figure 5.23). The physical parameters for the fluid are $\rho^{\mathrm{f}} = 100$ and $\mu = 10$. For the solid, we have $\rho^{\mathrm{s}} = 100$, $\epsilon = 0.0212$, with Young's modulus $E = 5.6 \cdot 10^3$ and Poisson's ratio $\nu = 0.4$.

As regards the boundary conditions for the fluid, a no-slip boundary condition is enforced on Γ_{bot} and Γ_{wall}. Zero traction is enforced on the lateral boundaries Γ_{in} and Γ_{out}. The velocity is prescribed on Γ_{top}, as a positive velocity whose amplitude is constant and equal to 1. Both the fluid and the solid are initially at rest.

5.4.3.1 Spatial and temporal discretization

The reference ALE solution has been generated using a solid mesh made of 200 segments and a body-fitted fluid mesh of 46 078 triangles. The initial configuration of the fitted

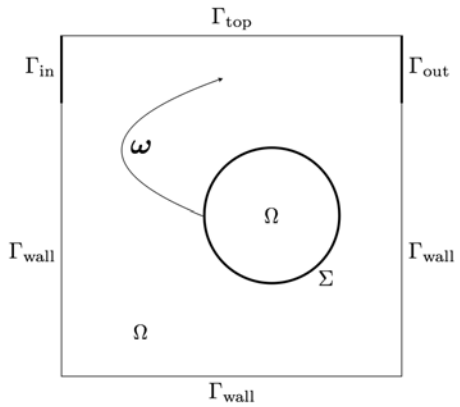

Figure 5.23 – Geometric configuration of the third numerical example.

meshes is depicted in Figure 5.24a. The time-step is $\tau = 2.5 \cdot 10^{-3}$ and the final time is $t = 10$, approximately corresponding to a full turn of the vesicle. A snapshot of the resulting deformed mesh at time $t = 6$ is shown in Figure 5.25a . We consider that $t = 6$ is the upper limit where we can still refer to the ALE solution as the reference (close to the break-down of the mesh motion procedure).

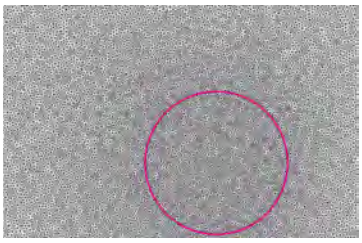

(a) Fitted meshes - Reference.

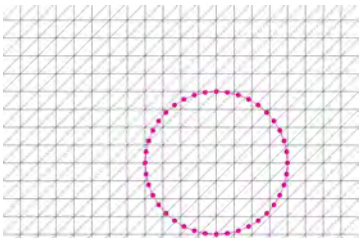

(b) Unfitted meshes - M_1.

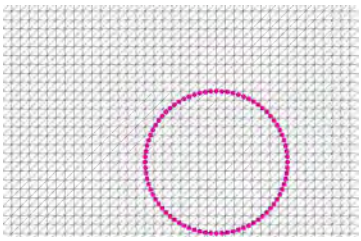

(c) Unfitted meshes - M_2.

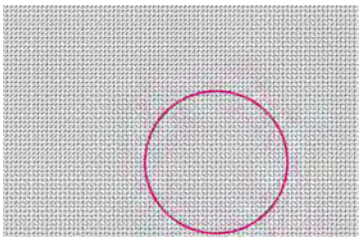

(d) Unfitted meshes - M_3.

Figure 5.24 – Zoom on the fluid and solid meshes at time $t = 0$.

The first level of refinement for the unfitted meshes, M_1, divides the fluid domain into 800 triangles and the structure domain into 40 segments. The corresponding time-step is $\tau = 10^{-2}$. As in two previous test cases, the two subsequent space-time grids, denoted by M_2 and M_3 respectively, are uniform refinements of M_1. Thus, M_2 is made of 3 200 triangles and M_3 of 12 800 triangles. Their corresponding structure domains are divided into 80 and 160 segments respectively. The time-steps are $\tau = 5 \cdot 10^{-3}$ in M_2 and $\tau = 2.5 \cdot 10^{-3}$ in M_3. For illustration purposes, M_1, M_2 and M_3 at $t = 0$ are shown in Figures 5.24b–5.24d

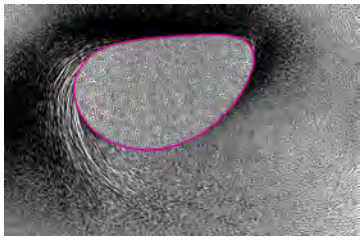

(a) Fitted meshes - Reference.

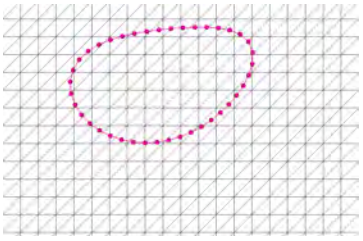

(b) Unfitted meshes - M_1.

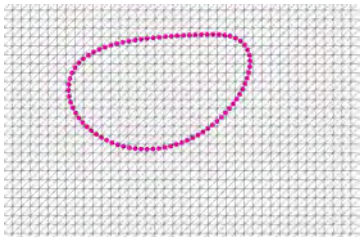

(c) Unfitted meshes - M_2.

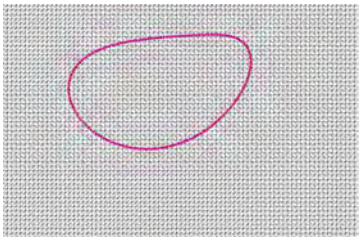

(d) Unfitted meshes - M_3.

Figure 5.25 – Zoom on the fluid and solid meshes at time $t = 6$.

and at $t = 6$ in Figures 5.25b–5.25d (obtained with the NXFEM method).

5.4.3.2 Comparison of results

The penalty parameter ε for the FD and FD_{stab} methods is $\varepsilon = 10^{-4}$ for all levels of refinement. As regards the stabilization parameter ε_{M}, we have $\varepsilon_{\text{M}} = 1$ with M_1, $\varepsilon_{\text{M}} = 10^{-1}$ with M_2 and $\varepsilon_{\text{M}} = 10^{-4}$ with M_3. These optimal choices will be discussed in Section 5.4.3.3 below.

Figures 5.26–5.28 present the snapshots of the fluid velocity magnitude near the vesicle and its location, at $t = 6$, for the three levels of refinement and for the NXFEM, FD and FD_{stab} methods, respectively. Note that some slight oscillations in the isolines of the reference ALE solution are visible, which can be related to the distortion of the deformed fluid mesh (see Figure 5.25a). We can clearly observe that the NXFEM method is able to predict the correct location of the interface even with the coarsest approximation (see Figure 5.26b). The situation is much more delicate for the FD method which, at all grid levels, shows major mass losses across the interface. In other words, the area of the vesicle significantly evolves during the simulation. This unphysical phenomenon is corrected by the FD_{stab} after grid refinement (see Figure 5.28d). This issue is explicitly measured in Figure 5.29, which reports the time history of the relative vesicle area for the three unfitted mesh methods. As expected, the area of the vesicle obtained with ALE method is practically constant over time. Note that the reference simulation breaks down at $t = 6.0275$, due to the stretching of fluid elements around the interface. Area changes are negligible with the NXFEM method and, after reasonable grid refinement, with the FD_{stab} method.

Some pressures snapshots are given in Figures 5.30–5.32, respectively for the NXFEM, FD and FD_{stab} methods. Note that the FD method does not predict any significant

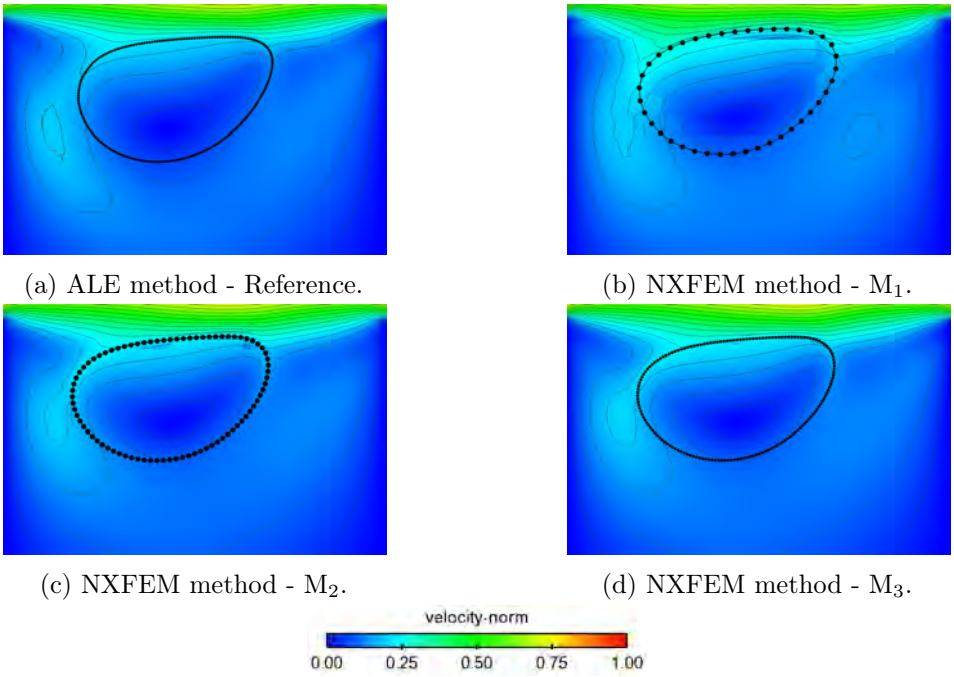

(a) ALE method - Reference. (b) NXFEM method - M_1.

(c) NXFEM method - M_2. (d) NXFEM method - M_3.

Figure 5.26 – Snapshots of the fluid velocity magnitude at $t = 6$ obtained with NXFEM.

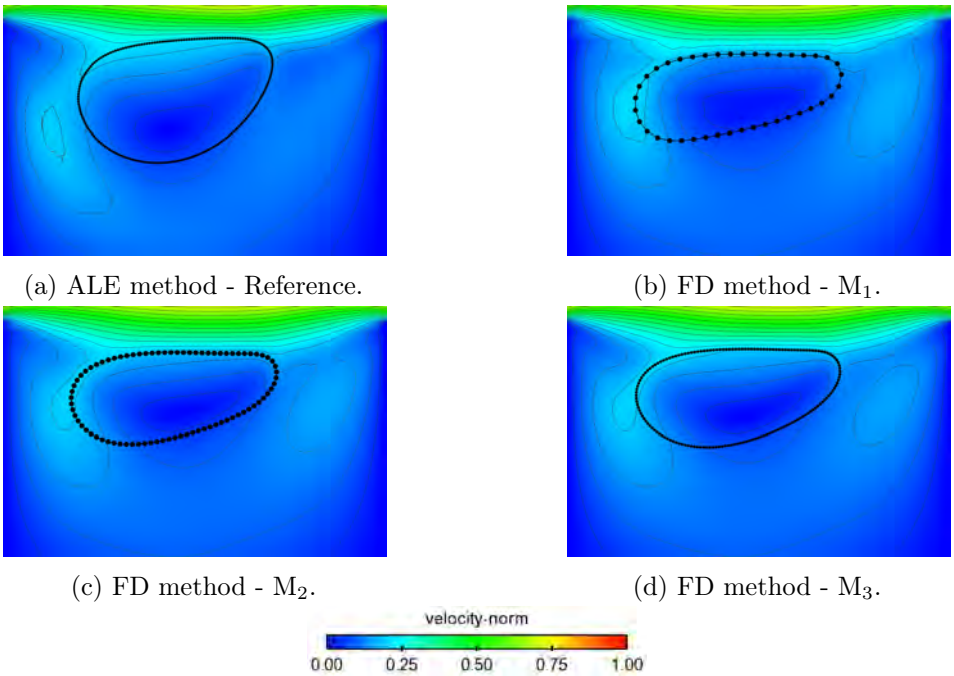

(a) ALE method - Reference. (b) FD method - M_1.

(c) FD method - M_2. (d) FD method - M_3.

Figure 5.27 – Snapshots of the fluid velocity magnitude at $t = 6$ obtained with FD.

pressure jump between the inner vesicle and the rest of the cavity, no matter what level of refinement is used. On the contrary, the NXFEM method is able to predict it and it also improves after refinement. A similar behavior can be observed from M_2 with the

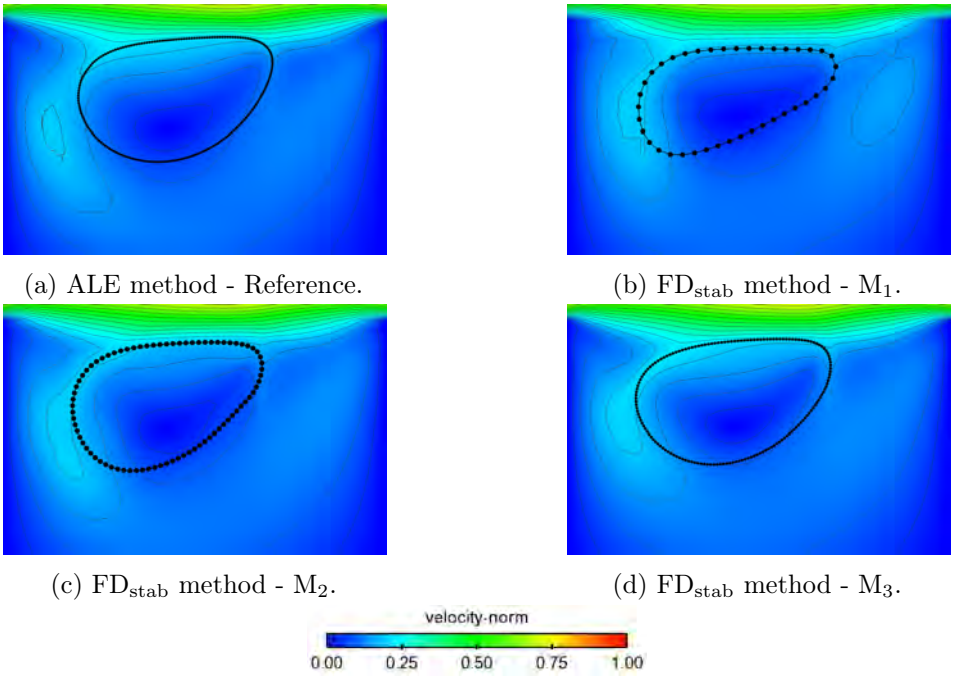

(a) ALE method - Reference. (b) FD_{stab} method - M_1.

(c) FD_{stab} method - M_2. (d) FD_{stab} method - M_3.

Figure 5.28 – Snapshots of the fluid velocity magnitude at $t = 6$ obtained with FD_{stab}.

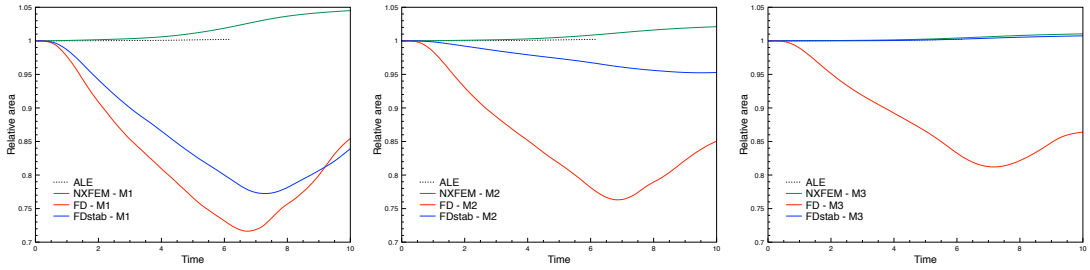

(a) M_1 vs. Reference. (b) M_2 vs. Reference. (c) M_3 vs. Reference.

Figure 5.29 – Time history of the relative area of the vesicle.

FD_{stab} variant. Particularly noticeable is the very good agreement between the NXFEM and FD_{stab} approximations with the reference solution, for the highest level of refinement.

Similar observations can be made from Figure 5.33, which reports the time history of the trajectory of the bottom of the vesicle. Again, the FD method presents shifted trajectories compared to the other methods, consequence of the continuous pressure approximation.

5.4.3.3 Choice of the penalty parameters for the fictitious domain methods

As explained in Section 5.4.1.3, we carried on the same convergence study with respect to the penalty parameter ε, appearing in the FD method. The physical value of interest here is the displacement magnitude of the bottom of the vesicle. For each level of refinement, the case has been run several times with a large panel of values for ε. The same behaviors as the ones described in Section 5.4.1.3 and Section 5.4.2.3 have also been observed here.

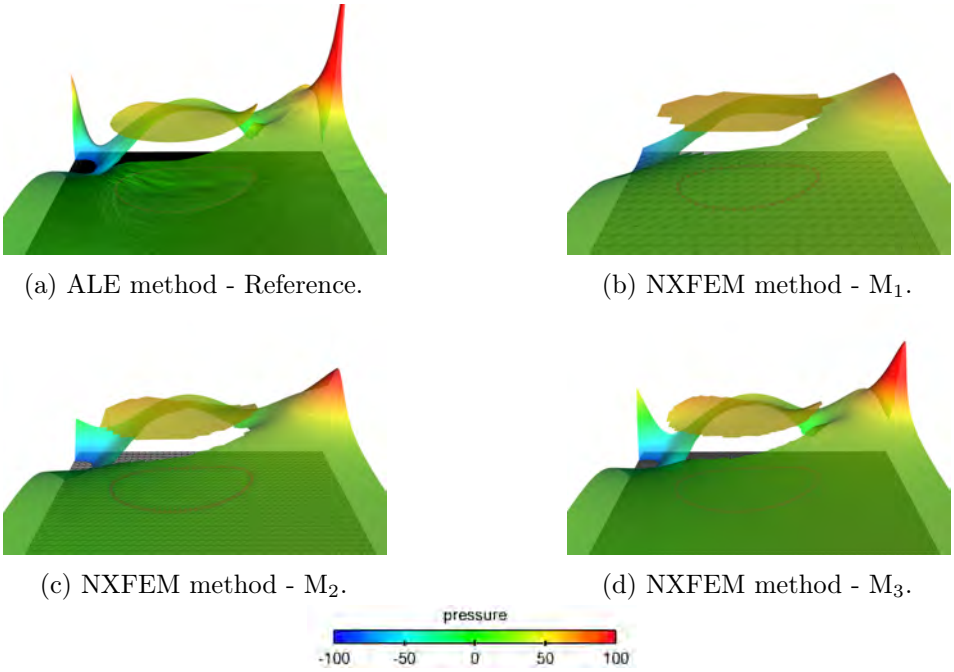

(a) ALE method - Reference.

(b) NXFEM method - M_1.

(c) NXFEM method - M_2.

(d) NXFEM method - M_3.

Figure 5.30 – Snapshots of the fluid elevated pressure at $t = 6$ obtained with NXFEM.

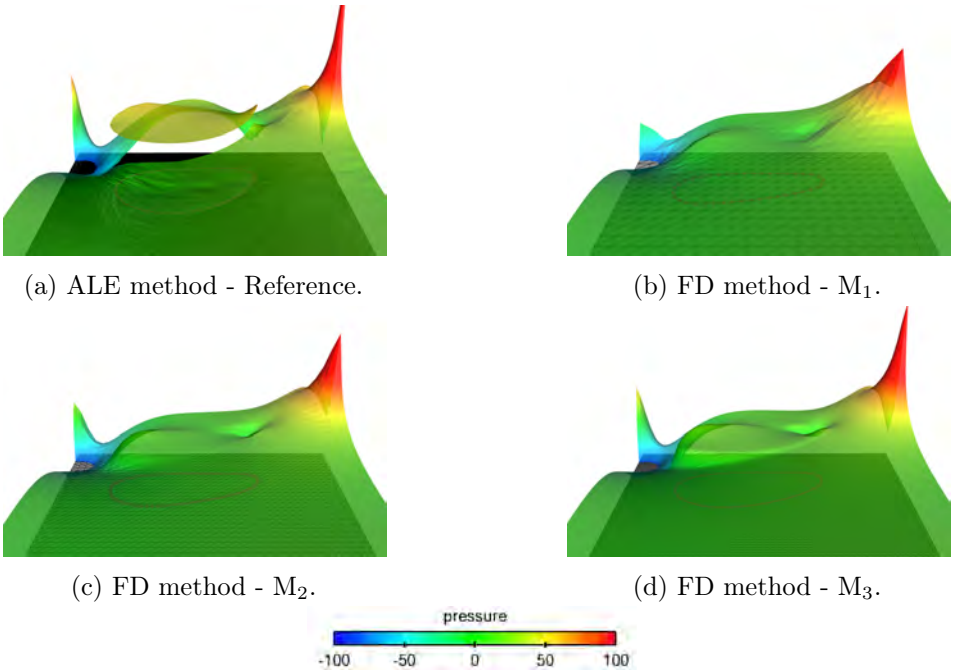

(a) ALE method - Reference.

(b) FD method - M_1.

(c) FD method - M_2.

(d) FD method - M_3.

Figure 5.31 – Snapshots of the fluid elevated pressure at $t = 6$ obtained with FD.

The chosen values of ε are based on the previous mentioned criteria of convergence. More information about the convergence study of the penalty parameter ε for this case are provided in Appendix D for the different levels of refinement.

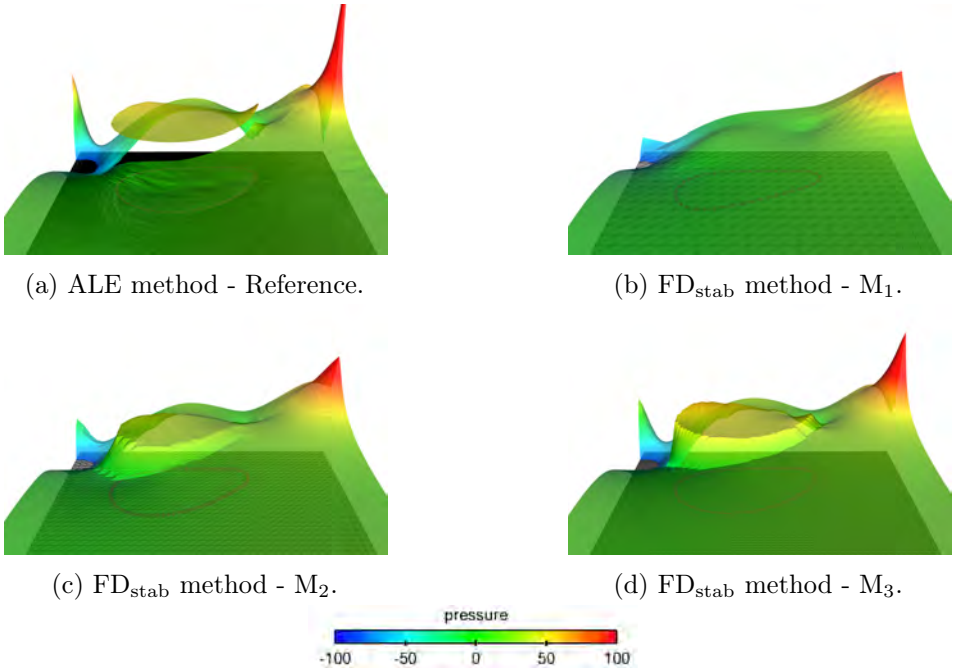

(a) ALE method - Reference.

(b) FD_{stab} method - M_1.

(c) FD_{stab} method - M_2.

(d) FD_{stab} method - M_3.

Figure 5.32 – Snapshots of the fluid elevated pressure at $t = 6$ obtained with FD_{stab}.

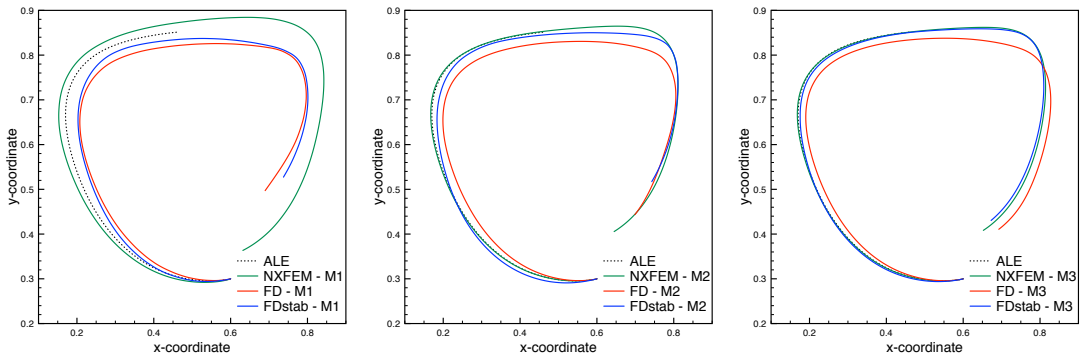

(a) M_1 vs. Reference.

(b) M_2 vs. Reference.

(c) M_3 vs. Reference.

Figure 5.33 – Time history of the trajectory of the bottom of the vesicle.

In order to choose the values of ε_M, we carried on the same kind of convergence study as the one described in Section 5.4.2.3. The possible values taken by this parameter are dependent on the size of the area where the stabilization is modified and thus of the level of refinement. This explains why ε_M is lower for more refined space-time grids. More information about the definition of ω_h^n for this case are provided in Appendix E for the different levels of refinement.

5.5 An alternative approach to the $\mathrm{FD}_{\mathrm{stab}}$ method

The previous $\mathrm{FD}_{\mathrm{stab}}$ method, introduced in Section 5.3.2.1 and investigated in Section 5.4, shows very good results when the space-time grid refinement is reasonable enough. Nevertheless, its main limitation is the degradation of the conditioning of the stiffness matrix, induced by the grad-div penalty used in some layers of fluid elements near the interface.

Therefore, the main motivation here is to propose an alternative grad-div free method (in order to avoid these ill-conditioning issues) but still able to ensure the interfacial mass conservation. In Section 5.5.1, we detail its fundamental idea which consists in removing the inconsistency of the pressure jumps by making the pressure stabilization coefficient vanish within a h-dependent vicinity of the interface. Then, in Section 5.5.2, the benefits of this alternative approach are illustrated on the same numerical examples previously investigated in this chapter.

5.5.1 Fundamental idea

A new approach based on a stabilized low-order mixed $\mathbb{P}_1/\mathbb{P}_0$ approximation for the fluid mesh is investigated here. This couple of finite elements is known to not respect the inf-sup condition and thus needs to be stabilized in terms of pressure. The global pressure stabilization (see, e.g., [HF87, TV96]) is given by

$$\frac{\gamma_{\mathrm{p}} h}{\mu} \sum_{F \in \mathcal{F}_h} \int_F [\![p_h]\!][\![q_h]\!],$$

where γ_{p} denotes a non-dimensional stability constant, h the mesh parameter, μ the fluid dynamic viscosity, $\mathcal{F}_h$ the set of interior edges (for $d = 2$) or faces (for $d = 3$) and $[\![\cdot]\!]$ the jump operator. p_h and q_h represent, respectively, the pressure unknown and the associated test function, which do belong to an appropriate pressure space made of globally continuous functions, as the one defined in Section 5.3.2.

To achieve stability, it has been proved that stabilizing on macro-patches is sufficient (see, e.g., [KS92]). The new approach we propose consists in considering a new macro-patch with a pressure stabilization coefficient which vanishes within a h-dependent vicinity of the interface, in order to remove the inconsistency of the pressure jumps. The different pressure sub-regions induced by the definition of this new macro-patch, starting from an initial configuration of unfitted meshes depicted in Figure 5.34a, are represented in Figure 5.34b.

5.5.2 Illustrations of the benefits

In terms of numerical implementation, the alternative approach requires (i) to detect the different fluid finite elements which have at least one inner edge or face intersected by the interface and (ii) to remove the pressure stabilization coefficient on the other inner edges or faces of this given subset of elements. In what follows, in the context of the numerical experiments described in Section 5.4, various illustrations about this detection

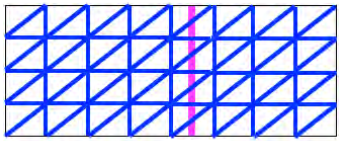

(a) Initial meshes configurations.

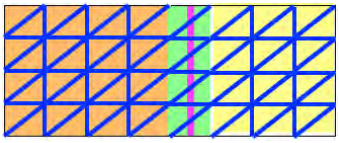

(b) Induced definition of the three sub-regions.

Figure 5.34 – Two-dimensional representation of the pressure sub-regions induced by the definition of the new macro-patch. The stabilized inner fluid edges are colored in blue and the interface is colored in fuchsia. On the left, the pressure stabilization is applied on all inner edges. On the right, the elements colored in green have at least one inner edge intersected by the interface and the pressure stabilization has been removed from their other inner edges (note that the two vertical blue lines of edges on each side of the interface have disappeared). This induces the definition of two other pressure sub-regions (colored in orange and yellow) on each side of the interface.

are provided and the results of this alternative approach are compared to the ones obtained with the FD_{stab} method.

Through this section, "FD_{stab} – $\mathbb{P}_1/\mathbb{P}_1$ grad-div" refers to the previous FD_{stab} method whereas "FD_{stab} – $\mathbb{P}_1/\mathbb{P}_0$" or "$FD_{stab}$ grad-div free" both refer to the alternative approach developed in Section 5.5.1.

5.5.2.1 Closed valve

Figures 5.35a–5.35c represent the new macro-patch of pressure stabilization considered in the context of the FD_{stab} methods and for the case of the closed valve, for, respectively, the three levels of refinement M_1, M_2 and M_3, defined in associated Section 5.4.2.

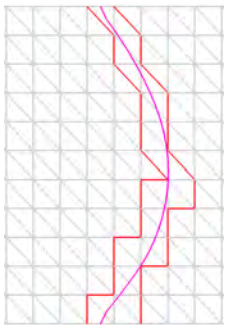

(a) M_1.

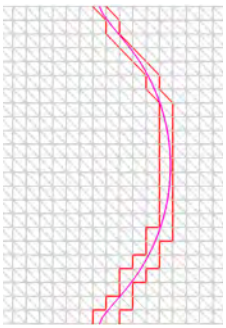

(b) M_2.

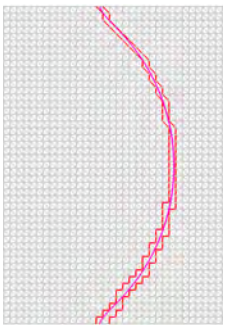

(c) M_3.

Figure 5.35 – Representation of the new macro-patch of pressure stabilization at time $t = 0.125$ for the case of the closed valve. The inner edges colored in red are the ones where the pressure stabilization has been removed.

The physical value of interest here is the x-displacement magnitude of the valve mid-point. The time-history of this value obtained with different methods is depicted in Figure 5.36 for the second level of refinement M_2. Note how the FD_{stab} grad-div free method (red curve) is closer to the NXFEM reference solution (green curve) compared to

the classical FD_{stab} method (blue curve) whose grad-div penalty term might also spoil the conditioning of the fluid problem.

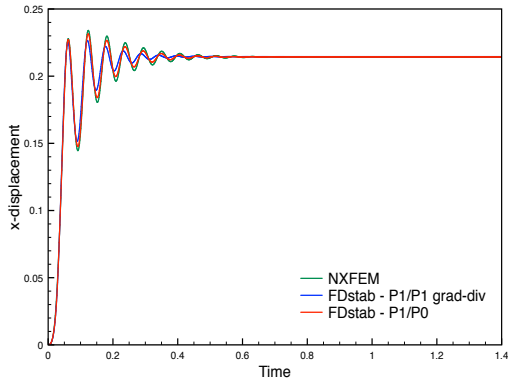

Figure 5.36 – Time-history of the x-displacement magnitude of the valve mid-point for the case of the closed valve for the second level of refinement M_2.

5.5.2.2 Vesicle in lid-driven cavity flow

Figures 5.37a–5.37c represent the macro-patch of pressure stabilization considered in the context of the FD_{stab} methods and for the case of the vesicle in lid-driven cavity flow, for, respectively, the three levels of refinement M_1, M_2 and M_3, defined in associated Section 5.4.3.

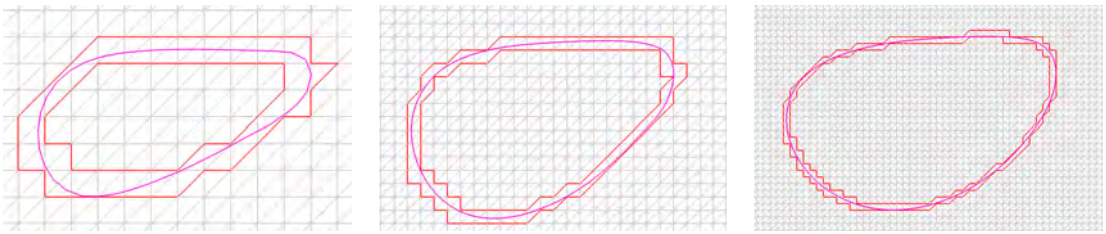

(a) M_1. (b) M_2. (c) M_3.

Figure 5.37 – Representation of the new macro-patch of pressure stabilization at time $t = 6$ for the case of the vesicle in lid-driven cavity flow. The inner edges colored in red are the ones where the pressure stabilization has been removed.

The physical value of interest here is the relative area of the vesicle. The time-history of this value obtained with different methods is depicted in Figure 5.38 for the second level of refinement M_2. As already observed in Section 5.5.2.1, the FD_{stab} grad-div free method is the closest one to the reference solution.

5.6 Conclusions

Different unfitted mesh methods for immersed FSI have been compared and validated in a series of 2D benchmarks involving fully non-linear models and large interface deflections.

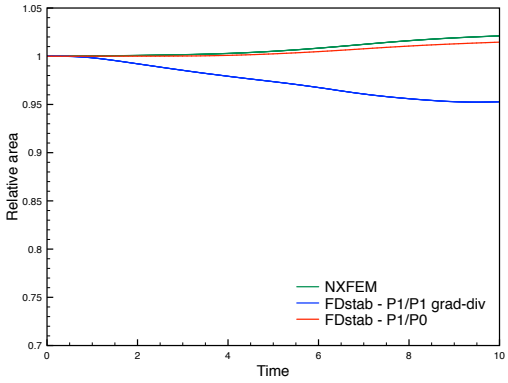

Figure 5.38 – Time-history of the relative area for the case of the vesicle in lid-driven cavity flow for the second level of refinement M_2.

All the methods discussed here are based on low-order first-order Lagrange spatial approximations, both in the fluid and in the solid. *A priori*, the main strengths and weaknesses of the methods can be summarized as follows:

- The FD methods based on Dirac's Lagrange multipliers and globally continuous fluid approximations are very appealing in practice, particularly for 3D applications, since their computer implementation demands relatively simple modifications on existing fluid solvers. The price to pay is the accuracy issues and the condition number degradation due to penalty terms.
- The Nitsche-XFEM method is based on recent mathematically sound results (fully consistent treatment of the interface coupling, optimal error estimates). However, in practice, this method requires major intrusive modifications on existent fluid solvers, due in particular to the dynamic nature of the cut-FEM methodology, that can be challenging in 3D with non-structured meshes (a recent study in this direction can be found in [ZVF18], see also [MLL13, KDP18]).

The detailed comparisons of Section 5.4 showed that, for a given mesh refinement, the best accuracy is obtained with the Nitsche-XFEM method. Another salient result of the present study is that, whenever present, the inaccuracies of the FD method are mainly driven by artificial interfacial mass losses notably in the case of closed domains, rather than by the sub-optimal treatment of the interface coupling. This observation is supported by the very goods results obtained with the FD_{stab} variant and a reasonable space-time grid refinement. The main limitation of this approach is the degradation of the stiffness matrix conditioning induced by the grad-div penalty near the interface.

These ill-conditioning issues can be circumvented by considering either divergence-conforming approximations (see [KHY+17, CBCGZ17] within the immersogeometric framework) or globally discontinuous pressures with higher order polynomials for the velocities (see [Baa01, BCGG12b, BCGG12a, BCG15] within the finite element framework). An interesting extension of this work could be the development of alternative fictitious domain methods with enhanced interfacial mass conservation which preserve, for convenience, the low-order nature of the finite element fluid approximations. The results presented in

Section 5.5 have highlighted the fact that the FD_{stab} grad-div free method appears to be an interesting candidate. Its main benefits are the use of mixed $\mathbb{P}_1/\mathbb{P}_0$ finite elements and the absence of ill-conditioning issues for the fluid problem while ensuring good interfacial mass conservation. Therefore, we believe that this alternative method should be seriously considered and used in future works.

Chapter 6

A loosely coupled scheme for fictitious domain approximations of fluid-structure interaction problems with immersed thin-walled structures

FD approximations of FSI problems are generally discretized in time using strongly coupled schemes. This guarantees unconditional stability but at the price of solving a computationally demanding coupled system at each time-step. The design of loosely coupled schemes (i.e., methods that invoke the fluid and solid solvers only once per time-step) is of fundamental interest, especially for three-dimensional simulations, but the existing approaches are known to suffer from severe stability and/or time accuracy issues. In this chapter, we propose a new approach that overcomes these difficulties in the case of the coupling with immersed thin-walled structures.

The results presented in this chapter have been reported in:

- L. Boilevin-Kayl, M.A. Fernández and J.F. Gerbeau, **A loosely coupled scheme for fictitious domain approximations of fluid-structure interaction problems with immersed thin-walled structures.** *SIAM Journal on Scientific Computing*, DOI: 10.1137/18M1192779, *2019*. Available online: https://hal.inria.fr/hal-01811290.

Contents

6.1 Introduction

In this chapter, we introduce and analyze a new loosely coupled scheme for FD approximations of FSI problems with immersed thin-walled structures which overcomes the above-mentioned issues. Our starting point is the semi-implicit coupling scheme reported in [Ann17] and described in Section 2.5.3.3. We show that the combination of an appropriate choice of the Lagrange multipliers space (equivalent to a collocation method) with a mass lumping approximation in the solid yield a loosely coupled scheme. We also present a general stability result which proves that the scheme is unconditionally stable in the energy norm. Numerical experiments in a series of representative two-dimensional examples, involving large interface deflections and topology changes in the fluid domain, illustrate the performance of the proposed approach.

The rest of the chapter is organized as follows. Section 6.2 recalls the coupled problem considered through this chapter. The FD spatial approximation is introduced in Section 6.3. Section 6.4 presents the new coupling scheme and its stability analysis. The numerical experiments are reported in Section 6.5. Finally, a summary of the main results obtained is provided in Section 6.6.

6.2 Problem setting

In what follows, the fluid is modeled by the incompressible Navier-Stokes equations in the Eulerian formalism. No ALE formalism is considered in this chapter. The thin-walled solid is still described by a non-linear Reissner-Mindlin beam model in Lagrangian form. We refer to Sections 2.2.2.2 and 2.5.1.2 for more information about these models.

The geometric configurations and notations are those of Section 2.5.2.1. Then, for the coupled problem with Eulerian formalism in the fluid, we refer to (2.14)–(2.16) in previous Section 2.5.2.2.

6.3 Weak form and spatial discretization

Most of the material presented in this section has already been introduced in previous Section 5.3. Nevertheless, for the purpose of completeness with respect to the couplings schemes described in next Section 6.4, key components are recalled here.

In what follows, the closed subspaces $H^1_\Gamma(\omega)$, of functions in $H^1(\omega)$ with zero trace on Γ, and $L^2_0(\omega)$, of functions in $L^2(\omega)$ with zero mean in ω, will be used. The scalar product in $L^2(\omega)$ is denoted by $(\cdot,\cdot)_\omega$, and we set $(\cdot,\cdot) \overset{\text{def}}{=} (\cdot,\cdot)_\Omega$.

We consider $\boldsymbol{V} \overset{\text{def}}{=} [H^1_\Gamma(\Omega)]^d$ and $Q \overset{\text{def}}{=} L^2_0(\Omega)$ as the fluid velocity and pressure functional spaces, respectively. The standard Navier-Stokes trilinear form a^{f} defined as

$$a^{\text{f}}\big(\boldsymbol{z};(\boldsymbol{u},p),(\boldsymbol{v},q)\big) \overset{\text{def}}{=} \rho^{\text{f}}\big(\boldsymbol{z}\cdot\boldsymbol{\nabla}\boldsymbol{u},\boldsymbol{v}\big) + 2\mu\big(\boldsymbol{\epsilon}(\boldsymbol{u}),\boldsymbol{\epsilon}(\boldsymbol{v})\big) - (p,\boldsymbol{\nabla}\cdot\boldsymbol{v}) + (q,\boldsymbol{\nabla}\cdot\boldsymbol{u}) \tag{6.1}$$

will also be used. The space of solid admissible displacements is denoted by $\boldsymbol{Y} \subset [H^1(\Sigma)]^d$. The weak form of the solid operators $\boldsymbol{L_d}$ and $\boldsymbol{L_a}$ will be represented by an application

$a^{\mathrm{s}} : \boldsymbol{Y} \times \boldsymbol{Y} \to \mathbb{R}$ which is assumed to be linear only with respect to the second argument.

In the spirit of [BG17] (see also [dSGB08, Baa01]), we introduce a space of Lagrange multipliers $\boldsymbol{\Lambda}$ and a continuous bilinear form $b : \boldsymbol{\Lambda} \times [H^{\frac{1}{2}}(\Sigma)]^d \to \mathbb{R}$, such that $b(\boldsymbol{\mu},\boldsymbol{z}) = 0$, for all $\boldsymbol{\mu} \in \boldsymbol{\Lambda}$, implies $\boldsymbol{z} = \boldsymbol{0}$ on Σ. As an example, we can take $\boldsymbol{\Lambda} = ([H^{\frac{1}{2}}(\Sigma)]^d)'$ and $b(\boldsymbol{\mu},\boldsymbol{z}) = \langle \boldsymbol{\mu}, \boldsymbol{z} \rangle$, where $\langle \cdot, \cdot \rangle$ represents the duality pairing between $([H^{\frac{1}{2}}(\Sigma)]^d)'$ and $[H^{\frac{1}{2}}(\Sigma)]^d$ (see, e.g., [BG17, Pat11]).

The weak form of the linear coupled problem (2.14)–(2.16) reads therefore as follows: for $t > 0$, find $(\boldsymbol{u},p,\boldsymbol{d},\boldsymbol{\lambda}) \in \boldsymbol{V} \times Q \times \boldsymbol{Y} \times \boldsymbol{\Lambda}$, with $\dot{\boldsymbol{d}} = \partial_t \boldsymbol{d}$, such that the geometric compatibility $(2.16)_1$ holds and

$$\begin{aligned} \rho^{\mathrm{f}}\big(\partial_t \boldsymbol{u},\boldsymbol{v}\big) + a^{\mathrm{f}}\big(\boldsymbol{u};(\boldsymbol{u},p),(\boldsymbol{v},q)\big) + b(\boldsymbol{\lambda}, \boldsymbol{v} \circ \boldsymbol{\phi} - \boldsymbol{y}) \\ + \rho^{\mathrm{s}}\epsilon\big(\partial_t \dot{\boldsymbol{d}}, \boldsymbol{y}\big)_\Sigma + a^{\mathrm{s}}(\boldsymbol{d}, \boldsymbol{y}) - b\big(\boldsymbol{\mu}, \boldsymbol{u} \circ \boldsymbol{\phi} - \dot{\boldsymbol{d}}\big) = 0, \end{aligned} \tag{6.2}$$

for all $(\boldsymbol{v},q,\boldsymbol{y},\boldsymbol{\mu}) \in \boldsymbol{V} \times Q \times \boldsymbol{Y} \times \boldsymbol{\Lambda}$.

We now consider a family $\{\mathcal{T}_h^{\mathrm{f}}\}_{0<h<1}$ of triangulations of Ω. The mesh $\mathcal{T}_h^{\mathrm{f}}$ is fitted to the exterior boundary Γ but, in general, not to Σ. For the solid, we consider a family $\{\mathcal{T}_h^{\mathrm{s}}\}_{0<h<1}$ of triangulations of Σ. We introduce the following standard spaces of continuous piecewise affine functions:

$$\begin{aligned} X_h^{\mathrm{f}} &\stackrel{\mathrm{def}}{=} \left\{ v_h \in C^0(\overline{\Omega}) \,/\, v_{h|K} \in \mathbb{P}_1(K), \quad \forall K \in \mathcal{T}_h^{\mathrm{f}} \right\}, \\ X_h^{\mathrm{s}} &\stackrel{\mathrm{def}}{=} \left\{ v_h \in C^0(\overline{\Sigma}) \,/\, v_{h|K} \in \mathbb{P}_1(K), \quad \forall K \in \mathcal{T}_h^{\mathrm{s}} \right\}. \end{aligned} \tag{6.3}$$

For the approximations of the fluid velocity and pressure, we will consider the spaces

$$\boldsymbol{V}_h \stackrel{\mathrm{def}}{=} [X_h^{\mathrm{f}}]^d \cap \boldsymbol{V} \quad \text{and} \quad Q_h \stackrel{\mathrm{def}}{=} X_h^{\mathrm{f}} \cap Q, \tag{6.4}$$

respectively. Furthermore, we consider the following discrete counterpart of (6.1):

$$\begin{aligned} a_h^{\mathrm{f}}\big(\boldsymbol{z}_h;(\boldsymbol{u}_h,p_h),(\boldsymbol{v}_h,q_h)\big) \stackrel{\mathrm{def}}{=} a^{\mathrm{f}}\big(\boldsymbol{z}_h;(\boldsymbol{u}_h,p_h),(\boldsymbol{v}_h,q_h)\big) + \frac{\rho^{\mathrm{f}}}{2}\big((\boldsymbol{\nabla}\cdot\boldsymbol{z}_h)\boldsymbol{u}_h, \boldsymbol{v}_h\big) \\ + s_h(\boldsymbol{z}_h;\boldsymbol{u}_h,\boldsymbol{v}_h), \end{aligned}$$

where the form s_h corresponds to the SUPG/PSPG and grad-div stabilizations (see, e.g., [Tez91, KHS+15]) given by

$$\begin{aligned} s_h(\boldsymbol{z}_h;\boldsymbol{u}_h,\boldsymbol{v}_h) &\stackrel{\mathrm{def}}{=} \sum_{K\in\mathcal{T}_h^{\mathrm{f}}} \int_K \frac{\lambda_C h^2}{\delta_h} (\boldsymbol{\nabla}\cdot\boldsymbol{u}_h)(\boldsymbol{\nabla}\cdot\boldsymbol{v}_h) \\ &\quad + \sum_{K\in\mathcal{T}_h^{\mathrm{f}}} \int_K \delta_h \left(\rho^{\mathrm{f}}\left(\boldsymbol{z}_h\cdot\boldsymbol{\nabla}\right)\boldsymbol{u}_h + \boldsymbol{\nabla} p_h\right)\cdot\left(\rho^{\mathrm{f}}\left(\boldsymbol{z}_h\cdot\boldsymbol{\nabla}\right)\boldsymbol{v}_h + \boldsymbol{\nabla} q_h\right), \\ \delta_h &\stackrel{\mathrm{def}}{=} \lambda_{\mathrm{M}} \left(\rho^{\mathrm{f}}\sqrt{\frac{4}{\tau^2} + \frac{16\mu^2}{h^4(\rho^{\mathrm{f}})^2} + \frac{4|\boldsymbol{z}_h|^2}{h^2}}\right)^{-1}, \end{aligned} \tag{6.5}$$

with $\lambda_{\mathrm{M}} > 0$ and $\lambda_{\mathrm{C}} \geq 0$ user-defined parameters.

In order to overcome the artificial interfacial mass losses induced by the continuous nature of the pressure approximations considered in (6.4), we will consider (notably when dealing with enclosed fluid domains) the approach proposed in [KHS+15] for an immersogeometric method, which consists in boosting the grad-div stabilization while reducing the SUPG/PSPG stabilization near the interface (see also [CBCG17]) by taking

$$\lambda_{\mathrm{C}} = 1 \quad \text{in} \quad \Omega, \quad \lambda_{\mathrm{M}} = \begin{cases} 1 & \text{in} \quad \Omega \backslash \omega_h^n, \\ \varepsilon_{\mathrm{M}} & \text{in} \quad \omega_h^n, \end{cases} \tag{6.6}$$

where $0 < \varepsilon_{\mathrm{M}} \ll 1$ is a user-defined (dimensionless) parameter and ω_h^n a neighborhood of the interface Σ_h^n (typically 2 layers of fluid elements on each of its side). The motivation of the first choice is that it improves local mass conservation while the second reduces the impact of the local residual inconsistencies near the interface. More information about the way ω_h^n is defined are provided in Appendix E.

The solid displacement and velocity are approximated in $\boldsymbol{Y}_h \overset{\text{def}}{=} [X_h^{\mathrm{s}}]^d \cap \boldsymbol{Y}$. For the approximation of the Lagrange multiplier, we consider the following non-conforming approximation space (see, e.g., [BTT97, dSGB08, GPHJ99, FM14]):

$$\boldsymbol{\Lambda}_h = \left\{ \boldsymbol{\mu}_h = \sum_{i=1}^{N_h^{\mathrm{s}}} \boldsymbol{\mu}_i \delta_{\boldsymbol{x}_i^{\mathrm{s}}} \Big/ \boldsymbol{\mu}_i \in \mathbb{R}^d, \quad \forall i \in \{1, \ldots, N_h^{\mathrm{s}}\} \right\}, \tag{6.7}$$

where $\{\boldsymbol{x}_i^{\mathrm{s}}\}_{i=1}^{N_h^{\mathrm{s}}}$ denotes the points of the triangulation $\mathcal{T}_h^{\mathrm{s}}$ and $\delta_{\boldsymbol{x}_i^{\mathrm{s}}}$ stands for the Dirac's measure at point $\boldsymbol{x}_i^{\mathrm{s}}$. For alternative approximation spaces, the reader is referred to [Baa01, Ann17, BG17] for instance. Due to the non-conforming nature of the approximation (6.7), we introduce the discrete bilinear form $b_h : \boldsymbol{\Lambda}_h \times [C^0(\Sigma)]^d \to \mathbb{R}$, defined by

$$b_h(\boldsymbol{\mu}_h, \boldsymbol{z}) \overset{\text{def}}{=} \sum_{i=1}^{N_h^{\mathrm{s}}} \boldsymbol{\mu}_i \cdot \boldsymbol{z}(\boldsymbol{x}_i^{\mathrm{s}}), \tag{6.8}$$

for all $(\boldsymbol{\mu}_h, \boldsymbol{z}) \in \boldsymbol{\Lambda}_h \times [C^0(\Sigma)]^d$. This amounts to enforce the kinematic constraint $(2.16)_2$ as in a collocation method (see, e.g., [BTT97, GPHJ99]). The spatial semi-discrete approximation of (6.2) reads therefore as follows: for $t > 0$, find $(\boldsymbol{u}_h, p_h, \boldsymbol{d}_h, \boldsymbol{\lambda}_h) \in \boldsymbol{V}_h \times Q_h \times \boldsymbol{Y}_h \times \boldsymbol{\Lambda}_h$, with $\dot{\boldsymbol{d}}_h = \partial_t \boldsymbol{d}_h$ and $\boldsymbol{\phi}_h = \boldsymbol{I}_\Sigma + \boldsymbol{d}_h$, such that

$$\begin{aligned} \rho^{\mathrm{f}}\big(\partial_t \boldsymbol{u}_h, \boldsymbol{v}_h\big) + a_h^{\mathrm{f}}\big(\boldsymbol{u}_h; (\boldsymbol{u}_h, p_h), (\boldsymbol{v}_h, q_h)\big) + b_h(\boldsymbol{\lambda}_h, \boldsymbol{v}_h \circ \boldsymbol{\phi}_h - \boldsymbol{y}_h) \\ + \rho^{\mathrm{s}} \epsilon\big(\partial_t \dot{\boldsymbol{d}}_h, \boldsymbol{y}_h\big)_\Sigma + a^{\mathrm{s}}(\boldsymbol{d}_h, \boldsymbol{y}_h) - b_h(\boldsymbol{\mu}_h, \boldsymbol{u}_h \circ \boldsymbol{\phi}_h - \dot{\boldsymbol{d}}_h) = 0, \end{aligned} \tag{6.9}$$

for all $(\boldsymbol{v}_h, q_h, \boldsymbol{y}_h, \boldsymbol{\mu}_h) \in \boldsymbol{V}_h \times Q_h \times \boldsymbol{Y}_h \times \boldsymbol{\Lambda}_h$.

6.4 Time-discretization: coupling schemes

This section is devoted to the discretization in time of (6.9). In what follows, the parameter $\tau > 0$ stands for the time-step length and $t_n \overset{\text{def}}{=} n\tau$, for $n \in \mathbb{N}$. For a given time-dependent field $x(t)$, the symbol x^n denotes an approximation of $x(t_n)$ and $\partial_\tau x^n \overset{\text{def}}{=} (x^n - x^{n-1})/\tau$, the first-order backward difference. For simplicity, we consider a first-order time-discretization of the bulk terms in the fluid and in the solid.

We first introduce the strongly coupled scheme reported in Algorithm 6.1 (see, e.g., [BG17, BCG11]). The method implicitly treats the kinematic–dynamic coupling through the Lagrange multiplier, but the geometric coupling is treated in an explicit fashion. This yields unconditional stability but at the price of solving the coupled system (6.12) below at each time-step, which can be costly and cumbersome (e.g., when the fluid and the solid are solved in separate codes).

Owing to (6.8), the discrete kinematic constraint in (6.12) writes

$$\boldsymbol{u}_h^n \circ \boldsymbol{\phi}_h^n(\boldsymbol{x}_i^{\mathrm{s}}) - \dot{\boldsymbol{d}}_h^n(\boldsymbol{x}_i^{\mathrm{s}}) = 0, \quad \forall i \in \{1, \dots, N_h^{\mathrm{s}}\}. \tag{6.10}$$

This is also equivalent to consider in (6.12) (and in (6.9)) the conforming space of Lagrange multipliers $\boldsymbol{\Lambda}_h = [X_h^{\mathrm{s}}]^d$ and the discrete bilinear form $b_h(\boldsymbol{\mu}_h, \boldsymbol{z}) = (\boldsymbol{\mu}_h, \boldsymbol{z})_{\Sigma,h}$. The symbol $(\cdot,\cdot)_{\Sigma,h}$ denotes the lumped-mass approximation of the L^2-inner product $(\cdot,\cdot)_\Sigma$, namely, the surface integral over Σ is approximated using nodal quadrature. Note that (6.10) avoids the need for the evaluation of interface integrals with quantities defined on unfitted meshes. Actually, only localization of the solid nodes within the fluid mesh is required. Little is known however on the discrete inf-sup conditions guaranteeing the existence, uniqueness and convergence of the approximation provided by (6.12), for these choices of the Lagrange multipliers spaces.

REMARK 6.1

In this regard, we are only aware of two theoretical results. The first concerns the convergence analysis reported in [FM14] for the primal variable of a saddle-point problem involving the Poisson equation, provided that the local size of the solid mesh is of the same order as the local size of the fluid mesh. More recently, a complete analysis is given in [BG17] for the choice $\boldsymbol{\Lambda}_h = [X_h^{\mathrm{s}}]^d$ and $b_h(\boldsymbol{\mu}_h, \boldsymbol{z}) = b(\boldsymbol{\mu}_h, \boldsymbol{z})$ (i.e., without quadrature approximation of the interface integral), under the assumption that the fluid mesh is sufficiently refined with respect to the solid mesh.

In other to avoid the lack of inf-sup stability result for (6.12), we follow the penalty strategy considered in [dSGB08] for the computer implementation of Algorithm 6.1, which consists in relaxing (6.10) to

$$\boldsymbol{u}_h^n \circ \boldsymbol{\phi}_h^n(\boldsymbol{x}_i^{\mathrm{s}}) - \dot{\boldsymbol{d}}_h^n(\boldsymbol{x}_i^{\mathrm{s}}) = \varepsilon \boldsymbol{\lambda}_i^n, \quad \forall i \in \{1 \dots, N_h^{\mathrm{s}}\}, \tag{6.11}$$

where $\varepsilon > 0$ is a small (non-dimensionless) parameter. This enables the elimination of the Lagrange multipliers, with the convenient property of preserving the sparse pattern of the matrix of the fluid problem. The fundamental drawbacks of this approach lie in

the choice of the parameter ε (which needs be tuned depending on the mesh size) and in the ill-conditioning issues induced by the resulting penalty term in the fluid momentum equation. More information about the way the penalty parameter ε is determined are provided in Appendix D.

Algorithm 6.1 Strongly coupled scheme.

For $n \geq 1$,

1. Interface update:
$$\boldsymbol{\phi}_h^n = \boldsymbol{I}_\Sigma + \boldsymbol{d}_h^{n-1}.$$
2. Find $(\boldsymbol{u}_h^n, p_h^n, \boldsymbol{d}_h^n, \boldsymbol{\lambda}_h^n) \in \boldsymbol{V}_h \times Q_h \times \boldsymbol{Y}_h \times \boldsymbol{\Lambda}_h$, with $\partial_\tau \boldsymbol{d}_h^n = \dot{\boldsymbol{d}}_h^n$, such that
$$\begin{aligned}\rho^{\mathrm{f}}\big(\partial_\tau \boldsymbol{u}_h^n, \boldsymbol{v}_h\big)_\Omega + a_h^{\mathrm{f}}\big(\boldsymbol{u}_h^{n-1}; (\boldsymbol{u}_h^n, p_h^n), (\boldsymbol{v}_h, q_h)\big) + b_h\big(\boldsymbol{\lambda}_h^n, \boldsymbol{v}_h \circ \boldsymbol{\phi}_h^n - \boldsymbol{y}_h\big) \\ + \rho^{\mathrm{s}}\epsilon\big(\partial_\tau \dot{\boldsymbol{d}}_h^n, \boldsymbol{y}_h\big)_\Sigma + a^{\mathrm{s}}\big(\boldsymbol{d}_h^n, \boldsymbol{y}_h\big) - b_h\big(\boldsymbol{\mu}_h, \boldsymbol{u}_h^n \circ \boldsymbol{\phi}_h^n - \dot{\boldsymbol{d}}_h^n\big) = 0, \quad (6.12)\end{aligned}$$
for all $(\boldsymbol{v}_h, q_h, \boldsymbol{y}_h, \boldsymbol{\mu}_h) \in \boldsymbol{V}_h \times Q_h \times \boldsymbol{Y}_h \times \boldsymbol{\Lambda}_h$.

We now consider the alternative numerical method reported in Algorithm 6.2 which is not strongly coupled and thus, less computationally demanding than Algorithm 6.1. This scheme, introduced in [Ann17] for a different choice of $\boldsymbol{\Lambda}_h$, extends the ideas of [Fer13, AFFL16] to the unfitted mesh formulation (6.9). Basically, this scheme treats implicitly the coupling of the fluid with the solid inertia and explicitly the coupling with the solid elastic effects. The former guarantees stability (by avoiding the explicit treatment of the added-mass) while the latter reduces the computational complexity with respect to Algorithm 6.1.

Algorithm 6.2 Semi-implicit scheme (not strongly coupled).

For $n \geq 1$,

1. Interface update:
$$\boldsymbol{\phi}_h^n = \boldsymbol{I}_\Sigma + \boldsymbol{d}_h^{n-1}.$$
2. Fluid with solid inertia step: find $(\boldsymbol{u}_h^n, p_h^n, \dot{\boldsymbol{d}}_h^{n-\frac{1}{2}}, \boldsymbol{\lambda}_h^n) \in \boldsymbol{V}_h \times Q_h \times \boldsymbol{Y}_h \times \boldsymbol{\Lambda}_h$, such that
$$\begin{aligned}\rho^{\mathrm{f}}\big(\partial_\tau \boldsymbol{u}_h^n, \boldsymbol{v}_h\big) + a_h^{\mathrm{f}}\big(\boldsymbol{u}_h^{n-1}; (\boldsymbol{u}_h^n, p_h^n), (\boldsymbol{v}_h, q_h)\big) + b_h\big(\boldsymbol{\lambda}_h^n, \boldsymbol{v}_h \circ \boldsymbol{\phi}_h^n - \boldsymbol{y}_h\big) \\ + \frac{\rho^{\mathrm{s}}\epsilon}{\tau}\big(\dot{\boldsymbol{d}}_h^{n-\frac{1}{2}} - \dot{\boldsymbol{d}}_h^{n-1}, \boldsymbol{y}_h\big)_\Sigma - b_h\big(\boldsymbol{\mu}_h, \boldsymbol{u}_h^n \circ \boldsymbol{\phi}_h^n - \dot{\boldsymbol{d}}_h^{n-\frac{1}{2}}\big) \\ = -a^{\mathrm{s}}\big(\boldsymbol{d}_h^{n-1}, \boldsymbol{y}_h\big), \quad (6.13)\end{aligned}$$
for all $(\boldsymbol{v}_h, q_h, \boldsymbol{y}_h, \boldsymbol{\mu}_h) \in \boldsymbol{V}_h \times Q_h \times \boldsymbol{Y}_h \times \boldsymbol{\Lambda}_h$.
3. Solid update: find $\boldsymbol{d}_h^n \in \boldsymbol{Y}_h$, with $\dot{\boldsymbol{d}}_h^n = \partial_\tau \boldsymbol{d}_h^n$, such that
$$\rho^{\mathrm{s}}\epsilon\big(\partial_\tau \dot{\boldsymbol{d}}_h^n, \boldsymbol{y}_h\big)_\Sigma + a^{\mathrm{s}}(\boldsymbol{d}_h^n, \boldsymbol{y}_h) = b_h(\boldsymbol{\lambda}_h^n, \boldsymbol{y}_h), \quad (6.14)$$
for all $\boldsymbol{y}_h \in \boldsymbol{Y}_h$.

REMARK 6.2
Alternative extrapolations (e.g., zero-order or second-order) could be considered for the last term of (6.13), as reported in [Fer13, AFFL16, Ann17]. Nevertheless, in the present work, we limit the discussion to first-order extrapolation since it guarantees both unconditional stability (Theorem 6.1) and first-order time accuracy.

Note that Algorithm 6.2 uncouples the computation of the fluid and solid unknowns $(\boldsymbol{u}_h^n,p_h^n,\boldsymbol{\lambda}_h^n)$ and $(\dot{\boldsymbol{d}}_h^n,\boldsymbol{d}_h^n)$. The price to pay for this splitting is the introduction of a new unknown in step (6.13), the so-called intermediate solid velocity $\dot{\boldsymbol{d}}_h^{n-\frac{1}{2}}$. Similar difficulties arise in the semi-implicit scheme reported in [AFFL16] for a Nitsche-XFEM unfitted mesh method (Lagrange multipliers free).

6.4.1 A new loosely coupled scheme

The first fundamental idea of the present chapter is that, if we choose $\boldsymbol{\Lambda}_h$ as in (6.7), both the intermediate velocity $\dot{\boldsymbol{d}}_h^{n-\frac{1}{2}}$ and the Lagrange multiplier $\boldsymbol{\lambda}_h^n$ can be eliminated in terms of the standard fluid unknown $(\boldsymbol{u}_h^n,p_h^n)$. To this purpose, we introduce the fluid-to-solid Lagrange interpolation operator $\boldsymbol{B}_h : [C^0(\Sigma)]^d \to \boldsymbol{Y}_h$ and we state the following result in Lemma 6.1.

LEMMA 6.1
Let the discrete space $\boldsymbol{\Lambda}_h$ be given by (6.7). We have

$$b_h\big(\boldsymbol{\mu}_h,\boldsymbol{v}_h\circ\boldsymbol{\phi}_h^n\big) = b_h\big(\boldsymbol{\mu}_h,\boldsymbol{B}_h(\boldsymbol{v}_h\circ\boldsymbol{\phi}_h^n)\big), \quad \forall \boldsymbol{v}_h \in \boldsymbol{V}_h. \tag{6.15}$$

Furthermore, the relations

$$b_h\big(\boldsymbol{\mu}_h,\boldsymbol{v}_h\circ\boldsymbol{\phi}_h^n - \boldsymbol{y}_h\big) = 0, \quad \forall \boldsymbol{\mu}_h \in \boldsymbol{\Lambda}_h \tag{6.16}$$

and

$$\boldsymbol{y}_h = \boldsymbol{B}_h\big(\boldsymbol{v}_h\circ\boldsymbol{\phi}_h^n\big) \tag{6.17}$$

are equivalent.

Proof. From (6.8), we have

$$\begin{aligned} b_h\big(\boldsymbol{\mu}_h,\boldsymbol{v}_h\circ\boldsymbol{\phi}_h^n\big) = \sum_{i=1}^{N_h^{\mathrm{s}}} \boldsymbol{\mu}_i\cdot\boldsymbol{v}_h(\boldsymbol{\phi}_h^n(\boldsymbol{x}_i^{\mathrm{s}})) &= \sum_{i=1}^{N_h^{\mathrm{s}}} \boldsymbol{\mu}_i\cdot\boldsymbol{B}_h\big(\boldsymbol{v}_h\circ\boldsymbol{\phi}_h^n\big)(\boldsymbol{x}_i^{\mathrm{s}}) \\ &= b_h\big(\boldsymbol{\mu}_h,\boldsymbol{B}_h(\boldsymbol{v}_h\circ\boldsymbol{\phi}_h^n)\big). \end{aligned}$$

On the other hand, owing to (6.16), we get

$$\sum_{i=1}^{N_h^{\mathrm{s}}} \boldsymbol{\mu}_i\cdot\big(\boldsymbol{B}_h\big(\boldsymbol{v}_h\circ\boldsymbol{\phi}_h^n\big)(\boldsymbol{x}_i^{\mathrm{s}}) - \boldsymbol{y}_h(\boldsymbol{x}_i^{\mathrm{s}})\big) = 0,$$

for all $\boldsymbol{\mu}_i \in \mathbb{R}^d$, or, equivalently,

$$\boldsymbol{B}_h\big(\boldsymbol{v}_h \circ \boldsymbol{\phi}_h^n\big)(\boldsymbol{x}_i^{\mathrm{s}}) = \boldsymbol{y}_h(\boldsymbol{x}_i^{\mathrm{s}}),$$

for $i \in \{1,\dots,N_h^{\mathrm{s}}\}$, which yields (6.17) and completes the proof. □

The next result shows that the coupled system (6.13) can be formulated exclusively in terms of a pure fluid problem without additional unknowns.

Lemma 6.2
For $n \geq 1$, let $(\boldsymbol{u}_h^n, p_h^n, \dot{\boldsymbol{d}}_h^{n-\frac{1}{2}}, \boldsymbol{\lambda}_h^n) \in \boldsymbol{V}_h \times Q_h \times \boldsymbol{Y}_h \times \boldsymbol{\Lambda}_h$ be solution of (6.13), then we have:

- $\dot{\boldsymbol{d}}_h^{n-\frac{1}{2}} = \boldsymbol{B}_h\big(\boldsymbol{u}_h^n \circ \boldsymbol{\phi}_h^n\big)$.
- $(\boldsymbol{u}_h^n, p_h^n) \in \boldsymbol{V}_h \times Q_h$ *satisfy*

$$\begin{aligned}
&\rho^{\mathrm{f}}\big(\partial_\tau \boldsymbol{u}_h^n, \boldsymbol{v}_h\big) + a_h^{\mathrm{f}}\big(\boldsymbol{u}_h^{n-1}; (\boldsymbol{u}_h^n, p_h^n), (\boldsymbol{v}_h, q_h)\big) \\
&+ \frac{\rho^{\mathrm{s}}\epsilon}{\tau}\big(\boldsymbol{B}_h\big(\boldsymbol{u}_h^n \circ \boldsymbol{\phi}_h^n\big), \boldsymbol{B}_h\big(\boldsymbol{v}_h \circ \boldsymbol{\phi}_h^n\big)\big)_\Sigma \\
&= \frac{\rho^{\mathrm{s}}\epsilon}{\tau}\big(\dot{\boldsymbol{d}}_h^{n-1}, \boldsymbol{B}_h\big(\boldsymbol{v}_h \circ \boldsymbol{\phi}_h^n\big)\big)_\Sigma - a^{\mathrm{s}}\big(\boldsymbol{d}_h^{n-1}, \boldsymbol{B}_h\big(\boldsymbol{v}_h \circ \boldsymbol{\phi}_h^n\big)\big),
\end{aligned} \tag{6.18}$$

  for all $(\boldsymbol{v}_h, q_h) \in \boldsymbol{V}_h \times Q_h$.
- $\boldsymbol{\lambda}_h^n \in \boldsymbol{\Lambda}_h$ *satisfies*

$$b\big(\boldsymbol{\lambda}_h^n, \boldsymbol{y}_h\big) = \frac{\rho^{\mathrm{s}}\epsilon}{\tau}\big(\boldsymbol{B}_h\big(\boldsymbol{u}_h^n \circ \boldsymbol{\phi}_h^n\big) - \dot{\boldsymbol{d}}_h^{n-1}, \boldsymbol{y}_h\big)_\Sigma + a^{\mathrm{s}}\big(\boldsymbol{d}_h^{n-1}, \boldsymbol{y}_h\big), \tag{6.19}$$

  for all $\boldsymbol{y}_h \in \boldsymbol{Y}_h$.

The reciprocal also holds.

Proof. From (6.13) with $(\boldsymbol{v}_h, q_h, \boldsymbol{y}_h) = (\boldsymbol{0}, 0, \boldsymbol{0})$, we have

$$b_h\big(\boldsymbol{\mu}_h, \boldsymbol{u}_h^n \circ \boldsymbol{\phi}_h^n - \dot{\boldsymbol{d}}_h^{n-\frac{1}{2}}\big) = 0, \quad \forall \boldsymbol{\mu}_h \in \boldsymbol{\Lambda}_h$$

and

$$\begin{aligned}
\rho^{\mathrm{f}}\big(\partial_\tau \boldsymbol{u}_h^n, \boldsymbol{v}_h\big) + a_h^{\mathrm{f}}\big(\boldsymbol{u}_h^{n-1}; (\boldsymbol{u}_h^n, p_h^n), (\boldsymbol{v}_h, q_h)\big) + b_h\big(\boldsymbol{\lambda}_h^n, \boldsymbol{v}_h \circ \boldsymbol{\phi}_h^n - \boldsymbol{y}_h\big) \\
+ \frac{\rho^{\mathrm{s}}\epsilon}{\tau}\big(\dot{\boldsymbol{d}}_h^{n-\frac{1}{2}} - \dot{\boldsymbol{d}}_h^{n-1}, \boldsymbol{y}_h\big)_\Sigma = -a^{\mathrm{s}}\big(\boldsymbol{d}_h^{n-1}, \boldsymbol{y}_h\big),
\end{aligned}$$

for all $(\boldsymbol{v}_h, q_h, \boldsymbol{y}_h) \in \boldsymbol{V}_h \times Q_h \times \boldsymbol{Y}_h$. Owing to Lemma 6.1, these relations can respectively be formulated as

$$\boldsymbol{B}_h\big(\boldsymbol{u}_h^n \circ \boldsymbol{\phi}_h^n\big) = \dot{\boldsymbol{d}}_h^{n-\frac{1}{2}} \tag{6.20}$$

and

$$\rho^{\mathrm{f}}\big(\partial_\tau \boldsymbol{u}_h^n,\boldsymbol{v}_h\big) + a_h^{\mathrm{f}}\big(\boldsymbol{u}_h^{n-1};(\boldsymbol{u}_h^n,p_h^n),(\boldsymbol{v}_h,q_h)\big) + b_h\big(\boldsymbol{\lambda}_h^n,\boldsymbol{B}_h\big(\boldsymbol{v}_h\circ\boldsymbol{\phi}_h^n\big)-\boldsymbol{y}_h\big) + \frac{\rho^{\mathrm{s}}\epsilon}{\tau}\big(\dot{\boldsymbol{d}}_h^{n-\frac{1}{2}}-\dot{\boldsymbol{d}}_h^{n-1},\boldsymbol{y}_h\big)_\Sigma = -a^{\mathrm{s}}\big(\boldsymbol{d}_h^{n-1},\boldsymbol{y}_h\big), \quad (6.21)$$

for all $(\boldsymbol{v}_h,q_h,\boldsymbol{y}_h)\in \boldsymbol{V}_h\times Q_h\times \boldsymbol{Y}_h$. Note that the intermediate solid velocity can be eliminated via (6.20). In order to also eliminate the Lagrange multipliers, we take $\boldsymbol{y}_h = \boldsymbol{B}_h\big(\boldsymbol{v}_h\circ\boldsymbol{\phi}_h^n\big)$ in (6.21), which yields (6.18). Finally, the relation (6.19) simply follows from (6.20) and (6.21) with $(\boldsymbol{v}_h,q_h)=(\boldsymbol{0},0)$.

Conversely, we assume now that (6.18) and (6.19) hold. From (6.19), there follows that

$$b\big(\boldsymbol{\lambda}_h^n,\boldsymbol{B}_h\big(\boldsymbol{v}_h\circ\boldsymbol{\phi}_h^n\big)-\boldsymbol{y}_h\big) - \frac{\rho^{\mathrm{s}}\epsilon}{\tau}\big(\boldsymbol{B}_h\big(\boldsymbol{u}_h^n\circ\boldsymbol{\phi}_h^n\big)-\dot{\boldsymbol{d}}_h^{n-1},\boldsymbol{B}_h\big(\boldsymbol{v}_h\circ\boldsymbol{\phi}_h^n\big)-\boldsymbol{y}_h\big)_\Sigma = a^{\mathrm{s}}\big(\boldsymbol{d}_h^{n-1},\boldsymbol{B}_h\big(\boldsymbol{v}_h\circ\boldsymbol{\phi}_h^n\big)-\boldsymbol{y}_h\big),$$

for all $(\boldsymbol{v}_h,\boldsymbol{y}_h)\in \boldsymbol{V}_h\times\boldsymbol{Y}_h$. By adding this expression to (6.18), we get

$$\rho^{\mathrm{f}}\big(\partial_\tau \boldsymbol{u}_h^n,\boldsymbol{v}_h\big) + a_h^{\mathrm{f}}\big(\boldsymbol{u}_h^{n-1};(\boldsymbol{u}_h^n,p_h^n),(\boldsymbol{v}_h,q_h)\big) + b_h\big(\boldsymbol{\lambda}_h^n,\boldsymbol{B}_h\big(\boldsymbol{v}_h\circ\boldsymbol{\phi}_h^n\big)-\boldsymbol{y}_h\big) + \frac{\rho^{\mathrm{s}}\epsilon}{\tau}\big(\boldsymbol{B}_h\big(\boldsymbol{u}_h^n\circ\boldsymbol{\phi}_h^n\big)-\dot{\boldsymbol{d}}_h^{n-1},\boldsymbol{y}_h\big)_\Sigma = -a^{\mathrm{s}}\big(\boldsymbol{d}_h^{n-1},\boldsymbol{y}_h\big),$$

for all $(\boldsymbol{v}_h,q_h,\boldsymbol{y}_h)\in \boldsymbol{V}_h\times Q_h\times\boldsymbol{Y}_h$. We finally retrieve (6.13) by setting $\dot{\boldsymbol{d}}_h^{n-\frac{1}{2}} = \boldsymbol{B}_h\big(\boldsymbol{u}_h^n\circ\boldsymbol{\phi}_h^n\big)$ and by applying Lemma 6.1. This completes the proof. □

REMARK 6.3

Note that (6.18) is a pure fluid problem, with a specific non-negative bilinear term acting on the interface. It is therefore well-posed. Furthermore, owing to the reciprocal part of Lemma 6.2, problem (6.13) admits also a unique solution.

REMARK 6.4

The system (6.18) can be viewed as a fluid problem with an immersed interface condition which generalizes the Robin-base splitting reported in [Fer13, FMV13, LVCF17] to the case of unfitted meshes. Alternative interface Robin conditions (see, e.g., [NV08, GGCC09, BCG+13] with fitted meshes) can also be generalized with the present approach.

The fundamental difficulty of (6.18) is that, in general, the interfacial term introduces non-standard coupling terms in the fluid matrix. Even more, the stencil of the resulting matrix depends on the location of the interface at each time-step. In order to overcome these drawbacks, we propose to replace the canonic L^2-inner product $(\cdot,\cdot)_\Sigma$ in Algorithm 6.2 by its lumped-mass approximation $(\cdot,\cdot)_{\Sigma,h}$ (see, e.g., [Tho06]). We can then establish the following result.

Lemma 6.3
The term

$$\big(\boldsymbol{B}_h(\boldsymbol{u}_h^n \circ \boldsymbol{\phi}_h^n), \boldsymbol{B}_h(\boldsymbol{v}_h \circ \boldsymbol{\phi}_h^n)\big)_{\Sigma,h} \tag{6.22}$$

preserves the sparsity of the original fluid matrix.

Proof. Let $i,j \in \mathbb{N}$ be the indices of two fluid nodes which do not share the same edge (see Figure 6.1). We will show that its corresponding matrix entry in each block of (6.22) vanishes. The matrix associated with (6.22) has a diagonal block structure, for instance,

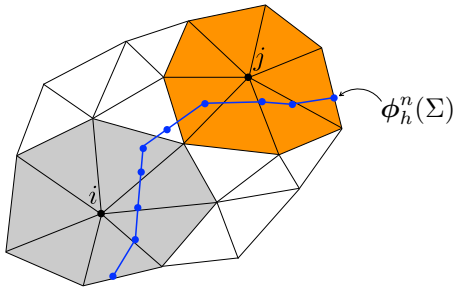

Figure 6.1 – Two-dimensional illustration of the support of two fluid shape functions (in grey and in orange) intersected by the interface $\boldsymbol{\phi}_h^n(\Sigma)$ where i and j do not share the same edge.

in 2D we have

$$\mathrm{R}^n \overset{\text{def}}{=} \begin{bmatrix} (\mathrm{B}^n)^{\mathrm{T}}\mathrm{M}\mathrm{B}^n & 0 \\ 0 & (\mathrm{B}^n)^{\mathrm{T}}\mathrm{M}\mathrm{B}^n \end{bmatrix},$$

where $\mathrm{M} \in \mathbb{R}^{N_h^{\mathrm{s}} \times N_h^{\mathrm{s}}}$ denotes the (scalar) lumped-mass matrix of the solid and $\mathrm{B}^n \in \mathbb{R}^{N_h^{\mathrm{s}} \times N_h^{\mathrm{f}}}$ the (scalar) Lagrange interpolation matrix from the fluid mesh to the solid mesh of the current configuration $\boldsymbol{\phi}_h^n(\Sigma)$. Therefore, it suffices to discuss only the diagonal blocks of R^n.

Since the lumped-mass matrix is diagonal, we have $\mathrm{M}_{lk} = \alpha_l \delta_{lk}$, with $\alpha_l \in \mathbb{R}$ and δ_{lk} standing for the Kronecker delta. Let $\mathrm{e}_i, \mathrm{e}_j$ be the canonical basis vectors of $\mathbb{R}^{N^{\mathrm{f}}}$ associated with the nodes i,j. We have

$$\begin{aligned}\big((\mathrm{B}^n)^{\mathrm{T}}\mathrm{M}\mathrm{B}^n\big)_{ij} &= \big(\mathrm{B}^n\mathrm{e}_i\big)^{\mathrm{T}}\mathrm{M}\mathrm{B}^n\mathrm{e}_j \\ &= \sum_l \left(\sum_k \mathrm{M}_{lk}\big(\mathrm{B}^n\mathrm{e}_j\big)_k\right)\big(\mathrm{B}^n\mathrm{e}_i\big)_l = \sum_l \alpha_l \big(\mathrm{B}^n\mathrm{e}_j\big)_l \big(\mathrm{B}^n\mathrm{e}_i\big)_l = 0.\end{aligned}$$

The last equality follows from the fact that, since the supports of the fluid nodes i and j do not intersect (see Figure 6.1), the vectors $\mathrm{B}^n\mathrm{e}_j$ and $\mathrm{B}^n\mathrm{e}_i$ do not have any common non-zero entry. This completes the proof. □

Owing to the results of Lemmas 6.2 and 6.3, we introduce the following new solution procedure:

For $n \geq 1$,

1. Interface update: $\boldsymbol{\phi}_h^n = \boldsymbol{I}_{\boldsymbol{\Sigma}} + \boldsymbol{d}_h^{n-1}$.
2. Find $(\boldsymbol{u}_h^n, p_h^n) \in \boldsymbol{V}_h \times Q_h$, such that

$$\begin{aligned} &\rho^{\mathrm{f}}\big(\partial_\tau \boldsymbol{u}_h^n, \boldsymbol{v}_h\big)_\Omega + a_h^{\mathrm{f}}\big(\boldsymbol{u}_h^{n-1}; (\boldsymbol{u}_h^n, p_h^n), (\boldsymbol{v}_h, q_h)\big) \\ &+ \frac{\rho^{\mathrm{s}}\epsilon}{\tau}\big(\boldsymbol{B}_h(\boldsymbol{u}_h^n \circ \boldsymbol{\phi}_h^n), \boldsymbol{B}_h(\boldsymbol{v}_h \circ \boldsymbol{\phi}_h^n)\big)_{\Sigma,h} \\ &= \frac{\rho^{\mathrm{s}}\epsilon}{\tau}\big(\dot{\boldsymbol{d}}_h^{n-1}, \boldsymbol{B}_h\big(\boldsymbol{v}_h \circ \boldsymbol{\phi}_h^n\big)\big)_{\Sigma,h} - a^{\mathrm{s}}\big(\boldsymbol{d}_h^{n-1}, \boldsymbol{B}_h\big(\boldsymbol{v}_h \circ \boldsymbol{\phi}_h^n\big)\big), \end{aligned} \tag{6.23}$$

   for all $(\boldsymbol{v}_h, q_h) \in \boldsymbol{V}_h \times Q_h$.
3. Find $\boldsymbol{\lambda}_h^n \in \boldsymbol{\Lambda}_h$, such that

$$b_h\big(\boldsymbol{\lambda}_h^n, \boldsymbol{y}_h\big) = \frac{\rho^{\mathrm{s}}\epsilon}{\tau}\big(\boldsymbol{B}_h\big(\boldsymbol{u}_h^n \circ \boldsymbol{\phi}_h^n\big) - \dot{\boldsymbol{d}}_h^{n-1}, \boldsymbol{y}_h\big)_\Sigma + a^{\mathrm{s}}\big(\boldsymbol{d}_h^{n-1}, \boldsymbol{y}_h\big), \tag{6.24}$$

   for all $\boldsymbol{y}_h \in \boldsymbol{Y}_h$.
4. Find $\boldsymbol{d}_h^n \in \boldsymbol{Y}_h$, with $\dot{\boldsymbol{d}}_h^n = \partial_\tau \boldsymbol{d}_h^n$, such that

$$\rho^{\mathrm{s}}\epsilon\big(\partial_\tau \dot{\boldsymbol{d}}_h^n, \boldsymbol{y}_h\big)_{\Sigma,h} + a^{\mathrm{s}}(\boldsymbol{d}_h^n, \boldsymbol{y}_h) = b_h(\boldsymbol{\lambda}_h^n, \boldsymbol{y}_h), \tag{6.25}$$

   for all $\boldsymbol{y}_h \in \boldsymbol{Y}_h$.

From a practical point of view, it is worth noting that, using (6.25), the relations (6.23)–(6.24) can also be rewritten equivalently, by replacing the terms containing $\boldsymbol{d}_h^{n-1}$, as

$$\begin{aligned} &\rho^{\mathrm{f}}\big(\partial_\tau \boldsymbol{u}_h^n, \boldsymbol{v}_h\big) + a_h^{\mathrm{f}}\big(\boldsymbol{u}_h^{n-1}; (\boldsymbol{u}_h^n, p_h^n), (\boldsymbol{v}_h, q_h)\big) \\ &+ \frac{\rho^{\mathrm{s}}\epsilon}{\tau}\big(\boldsymbol{B}_h(\boldsymbol{u}_h^n \circ \boldsymbol{\phi}_h^n), \boldsymbol{B}_h(\boldsymbol{v}_h \circ \boldsymbol{\phi}_h^n)\big)_{\Sigma,h} \\ &= \frac{\rho^{\mathrm{s}}\epsilon}{\tau}\big(\dot{\boldsymbol{d}}_h^{n-1} + \tau\partial_\tau \dot{\boldsymbol{d}}_h^{n-1}, \boldsymbol{B}_h(\boldsymbol{v}_h \circ \boldsymbol{\phi}_h^n)\big)_{\Sigma,h} - b_h(\boldsymbol{\lambda}_h^{n-1}, \boldsymbol{B}_h(\boldsymbol{v}_h \circ \boldsymbol{\phi}_h^n)) \end{aligned}$$

and

$$b_h\big(\boldsymbol{\lambda}_h^n, \boldsymbol{y}_h\big) = \frac{\rho^{\mathrm{s}}\epsilon}{\tau}\big(\boldsymbol{B}_h\big(\boldsymbol{u}_h^n \circ \boldsymbol{\phi}_h^n\big) - \dot{\boldsymbol{d}}_h^{n-1} - \tau\partial_\tau \dot{\boldsymbol{d}}_h^{n-1}, \boldsymbol{y}_h\big)_{\Sigma,h} + b_h(\boldsymbol{\lambda}_h^{n-1}, \boldsymbol{y}_h),$$

for $n \geq 2$. The advantage of these expressions is that, since the solid elastic term has been eliminated, only solid velocities need to be transferred from the solid to the fluid (as in a standard Dirichlet-Neumann loosely coupled scheme). The resulting solution procedure is detailed in Algorithm 6.3.

REMARK 6.5

It should be noted that Algorithm 6.3 requires $\boldsymbol{\lambda}_h^1$, $\dot{\boldsymbol{d}}_h^1$ as initial conditions, which can be obtained by performing the first step of (6.23)–(6.25). In the particular case in which $\boldsymbol{d}_h^0 = \dot{\boldsymbol{d}}_h^0 = \boldsymbol{0}$, we can start the time-stepping directly with Algorithm 6.3 for $n \geq 1$.

Algorithm 6.3 Loosely coupled scheme.

For $n \geq 2$,

1. Interface update: $\boldsymbol{\phi}_h^n = \boldsymbol{I}_{\boldsymbol{\Sigma}} + \boldsymbol{d}_h^{n-1}$.
2. Fluid step: find $(\boldsymbol{u}_h^n, p_h^n) \in \boldsymbol{V}_h \times Q_h$, such that

$$\begin{aligned} &\rho^{\mathrm{f}}\big(\partial_\tau \boldsymbol{u}_h^n, \boldsymbol{v}_h\big)_\Omega + a_h^{\mathrm{f}}\big(\boldsymbol{u}_h^{n-1}; (\boldsymbol{u}_h^n, p_h^n), (\boldsymbol{v}_h, q_h)\big) \\ &\quad + \frac{\rho^{\mathrm{s}}\epsilon}{\tau}\big(\boldsymbol{B}_h(\boldsymbol{u}_h^n \circ \boldsymbol{\phi}_h^n), \boldsymbol{B}_h(\boldsymbol{v}_h \circ \boldsymbol{\phi}_h^n)\big)_{\Sigma,h} \\ &= \frac{\rho^{\mathrm{s}}\epsilon}{\tau}\big(2\dot{\boldsymbol{d}}_h^{n-1} - \dot{\boldsymbol{d}}_h^{n-2}, \boldsymbol{B}_h(\boldsymbol{v}_h \circ \boldsymbol{\phi}_h^n)\big)_{\Sigma,h} - b_h(\boldsymbol{\lambda}_h^{n-1}, \boldsymbol{B}_h(\boldsymbol{v}_h \circ \boldsymbol{\phi}_h^n)), \end{aligned} \tag{6.26}$$

   for all $(\boldsymbol{v}_h, q_h) \in \boldsymbol{V}_h \times Q_h$.

3. Evaluate fluid load: find $\boldsymbol{\lambda}_h^n \in \boldsymbol{\Lambda}_h$, such that

$$b_h\big(\boldsymbol{\lambda}_h^n, \boldsymbol{y}_h\big) = \frac{\rho^{\mathrm{s}}\epsilon}{\tau}\big(\boldsymbol{B}_h\big(\boldsymbol{u}_h^n \circ \boldsymbol{\phi}_h^n\big) - 2\dot{\boldsymbol{d}}_h^{n-1} + \dot{\boldsymbol{d}}_h^{n-2}, \boldsymbol{y}_h\big)_{\Sigma,h} + b_h(\boldsymbol{\lambda}_h^{n-1}, \boldsymbol{y}_h), \tag{6.27}$$

   for all $\boldsymbol{y}_h \in \boldsymbol{Y}_h$.

4. Solid step: find $\boldsymbol{d}_h^n \in \boldsymbol{Y}_h$, with $\dot{\boldsymbol{d}}_h^n = \partial_\tau \boldsymbol{d}_h^n$, such that

$$\rho^{\mathrm{s}}\epsilon\big(\partial_\tau \dot{\boldsymbol{d}}_h^n, \boldsymbol{y}_h\big)_{\Sigma,h} + a^{\mathrm{s}}(\boldsymbol{d}_h^n, \boldsymbol{y}_h) = b_h(\boldsymbol{\lambda}_h^n, \boldsymbol{y}_h), \tag{6.28}$$

   for all $\boldsymbol{y}_h \in \boldsymbol{Y}_h$.

6.4.2 Computer implementation

Let u^n, p^n, d^n, $\dot{\mathrm{d}}^n$, λ^n and ϕ^n denote the arrays of degrees of freedom associated with $\boldsymbol{u}_h^n$, p_h^n, $\boldsymbol{d}_h^n$, $\dot{\boldsymbol{d}}_h^n$, $\boldsymbol{\lambda}_h^n$ and $\boldsymbol{\phi}^n$, respectively. We also denote by x the array of coordinates of the points of the triangulation $\mathcal{T}_h^{\mathrm{s}}$. For the sake of clarity, we first consider the separated solution of the fluid without the coupling with the immersed solid. This yields the following type of linear system at each time-step:

$$\begin{bmatrix} \mathrm{A}^{\mathrm{f}} & \mathrm{C} \\ -\mathrm{C} & \mathrm{S} \end{bmatrix} \begin{bmatrix} \mathrm{u}^n \\ \mathrm{p}^n \end{bmatrix} = \begin{bmatrix} \mathrm{b}^{n-1} \\ 0 \end{bmatrix}, \tag{6.29}$$

with the notation

$$\mathrm{A}^{\mathrm{f}} \stackrel{\text{def}}{=} \frac{\rho^{\mathrm{f}}}{\tau}\mathrm{M}^{\mathrm{f}} + \mathrm{K}^{\mathrm{f}} \quad \text{and} \quad \mathrm{b}^{n-1} \stackrel{\text{def}}{=} \frac{\rho^{\mathrm{f}}}{\tau}\mathrm{M}^{\mathrm{f}}\mathrm{u}^{n-1}.$$

Here, the matrices M^{f} and $\begin{bmatrix} \mathrm{K}^{\mathrm{f}} & \mathrm{C} \\ -\mathrm{C} & \mathrm{S} \end{bmatrix}$ denote the algebraic counterpart of the bilinear forms $(\boldsymbol{u}_h, \boldsymbol{v}_h^{\mathrm{f}})$ and $a_h^{\mathrm{f}}\big(\boldsymbol{u}_h^{n-1}; (\boldsymbol{u}_h, \boldsymbol{v}_h), (\boldsymbol{v}_h^{\mathrm{f}}, q_h)\big)$, respectively. Similarly, without interaction with the fluid, we get, for the solid, the following linear system:

$$\mathrm{A}^{\mathrm{s}}\mathrm{d}^n = \mathrm{r}^{n-1}, \tag{6.30}$$

with

$$\mathrm{A}^{\mathrm{s}} \overset{\text{def}}{=} \frac{\rho^{\mathrm{s}}\epsilon}{\tau^2}\mathrm{M}^{\mathrm{s}} + \mathrm{K}^{\mathrm{e}}, \quad \mathrm{r}^{n-1} \overset{\text{def}}{=} \frac{\rho^{\mathrm{s}}\epsilon}{\tau^2}\mathrm{M}^{\mathrm{s}}\big(\mathrm{d}^{n-1} + \tau\dot{\mathrm{d}}^{n-1}\big) \quad \text{and} \quad \dot{\mathrm{d}}^{n} = \partial_\tau \mathrm{d}^{n}.$$

Here, the matrices M^{s} and K^{s} stand for the algebraic counterpart of the bilinear forms $(\dot{\boldsymbol{d}}_h, \boldsymbol{y}_h)_{\Sigma,h}$ and $a^{\mathrm{s}}(\boldsymbol{d}_h,\boldsymbol{y}_h)$ respectively. Note that, due to the lumped mass approximation, the matrix M^{s} is diagonal. Finally, we consider the matrices B^n and R^n introduced in the proof of Lemma 6.3 and define L^n as the fluid-to-solid vector interpolation matrix, e.g., for $d = 2$ we have

$$\mathrm{L}^n \overset{\text{def}}{=} \begin{bmatrix} \mathrm{B}^n & 0 \\ 0 & \mathrm{B}^n \end{bmatrix}.$$

Based on all these considerations, the steps of Algorithm 6.3 can be reformulated, in an algebraic fashion, as:

1. Set ϕ^n to
$$\phi^n = \mathrm{x} + \mathrm{d}^{n-1}$$
and evaluate the interpolation matrix B^n.
2. Solve the fluid system (with the solid inertial contributions) given by
$$\begin{bmatrix} \mathrm{A}^{\mathrm{f}} + \dfrac{\rho^{\mathrm{s}}\epsilon}{\tau}\mathrm{R}^n & \mathrm{C} \\ -\mathrm{C} & \mathrm{S} \end{bmatrix} \begin{bmatrix} \mathrm{u}^n \\ \mathrm{p}^n \end{bmatrix} = \begin{bmatrix} \mathrm{b}^{n-1} \\ 0 \end{bmatrix}. \tag{6.31}$$
3. Set λ^n to
$$\lambda^n = \frac{\rho^{\mathrm{s}}\epsilon}{\tau}\mathrm{M}^{\mathrm{s}}\big(\mathrm{L}^n\mathrm{u}^n - 2\dot{\mathrm{d}}^{n-1} + \dot{\mathrm{d}}^{n-2}\big) + \lambda^{n-1}.$$
4. Solve the solid system given by
$$\mathrm{A}^{\mathrm{s}}\mathrm{d}^n = \mathrm{r}^{n-1} + \lambda^n.$$

It is worth recalling that, owing to Lemma 6.3, the matrix of the system (6.31) preserves the sparse pattern of the original fluid matrix A^{f}.

6.4.3 Energy stability

In this section, we assume that $a^{\mathrm{s}}(\cdot,\cdot)$ is an inner product into $\boldsymbol{Y}$. The associated solid energy norm is denoted by $\|\cdot\|_{\mathrm{s}} \overset{\text{def}}{=} \sqrt{a^{\mathrm{s}}(\cdot,\cdot)}$. We also introduce the discrete norm $\|\cdot\|_{\Sigma,h} \overset{\text{def}}{=} \sqrt{(\cdot,\cdot)_{\Sigma,h}}$. We shall consider the following discrete reconstruction of the elastic bilinear form a^{s}: for all $\boldsymbol{d}_h \in \boldsymbol{Y}_h$, we define $\boldsymbol{L}^{\mathrm{s}}_h\boldsymbol{d}_h \in \boldsymbol{Y}_h$ such that

$$(\boldsymbol{L}^{\mathrm{s}}_h\boldsymbol{d}_h,\boldsymbol{y}_h)_{\Sigma,h} = a^{\mathrm{s}}(\boldsymbol{d}_h,\boldsymbol{y}_h), \tag{6.32}$$

for all $\boldsymbol{y}_h \in \boldsymbol{Y}_h$. Furthermore, as introduced in Section 2.5.2.3, we define the discrete system mechanical energy at the time-step $n \geq 0$ as

$$E^n = \frac{\rho^{\mathrm{f}}}{2}\|\boldsymbol{u}_h^n\|^2_{0,\Omega} + \frac{\rho^{\mathrm{s}}\epsilon}{2}\|\dot{\boldsymbol{d}}_h^n\|^2_{0,\Sigma} + \frac{1}{2}\|\boldsymbol{d}_h^n\|^2_{\mathrm{s}}.$$

We will use the symbol $\lesssim$ to indicate an inequality written up to a multiplicative constant (independent of the physical and discretization parameters).

The next result establishes the unconditional stability in the energy norm of Algorithm 6.3.

Theorem 6.1
Let $\{(\boldsymbol{u}_h^n, p_h^n, \dot{\boldsymbol{d}}_h^n, \boldsymbol{d}_h^n)\}_{n\geq 1}$ be given by Algorithm 6.3, initialized as in Remark 6.5. The following energy estimate holds, for $n \geq 1$:

$$E^n \lesssim E^0 + \tau^2 \|\dot{\boldsymbol{d}}_h^0\|_s^2 + \frac{\tau^2}{\rho^{\mathrm{s}}\epsilon} \|\boldsymbol{L}_h^s \boldsymbol{d}_h^0\|_{0,\Sigma}^2. \tag{6.33}$$

Proof. From (6.24)–(6.25), we have

$$\frac{\rho^{\mathrm{s}}\epsilon}{\tau}\big(\dot{\boldsymbol{d}}_h^n - \boldsymbol{B}_h\big(\boldsymbol{u}_h^n \circ \boldsymbol{\phi}_h^n\big), \boldsymbol{y}_h\big)_{\Sigma,h} + a^{\mathrm{s}}(\boldsymbol{d}_h^n - \boldsymbol{d}_h^{n-1}, \boldsymbol{y}_h) = 0, \tag{6.34}$$

for all $\boldsymbol{y}_h \in \boldsymbol{Y}_h$. In particular, owing to (6.32), we have

$$\boldsymbol{B}_h\big(\boldsymbol{u}_h^n \circ \boldsymbol{\phi}_h^n\big) = \dot{\boldsymbol{d}}_h^n + \frac{\tau}{\rho^{\mathrm{s}}\epsilon} \boldsymbol{L}_h^{\mathrm{s}}(\boldsymbol{d}_h^n - \boldsymbol{d}_h^{n-1}). \tag{6.35}$$

On the other hand, by taking $\boldsymbol{y}_h = \boldsymbol{B}_h\big(\boldsymbol{v}_h \circ \boldsymbol{\phi}_h^n\big)$ in (6.34) and by adding the resulting expression to (6.23), we get

$$\begin{aligned}\rho^{\mathrm{f}}\big(\partial_\tau \boldsymbol{u}_h^n, \boldsymbol{v}_h\big)_\Omega + a_h^{\mathrm{f}}\big(\boldsymbol{u}_h^{n-1}; (\boldsymbol{u}_h^n, p_h^n), (\boldsymbol{v}_h, q_h)\big) \\ + \rho^{\mathrm{s}}\epsilon\big(\partial_\tau \dot{\boldsymbol{d}}_h^n, \boldsymbol{B}_h\big(\boldsymbol{v}_h \circ \boldsymbol{\phi}_h^n\big)\big)_{\Sigma,h} + a^{\mathrm{s}}\big(\boldsymbol{d}_h^n, \boldsymbol{B}_h\big(\boldsymbol{v}_h \circ \boldsymbol{\phi}_h^n\big)\big) = 0,\end{aligned} \tag{6.36}$$

for all $(\boldsymbol{v}_h, q_h) \in \boldsymbol{V}_h \times Q_h$. By taking $(\boldsymbol{v}_h, q_h) = (\boldsymbol{u}_h^n, p_h^n)$ in this expression and using the fact that

$$a_h^{\mathrm{f}}\big(\boldsymbol{u}_h^{n-1}; (\boldsymbol{u}_h^n, p_h^n), (\boldsymbol{u}_h^n, p_h^n)\big) \geq 2\mu \|\boldsymbol{\epsilon}(\boldsymbol{u}_h^n)\|_{0,\Omega}^2,$$

we get

$$\begin{aligned}\frac{\rho^{\mathrm{f}}}{2}\partial_\tau \|\boldsymbol{u}_h^n\|_{0,\Omega}^2 + 2\mu \|\boldsymbol{\epsilon}(\boldsymbol{u}_h^n)\|_{0,\Omega}^2 \\ + \rho^{\mathrm{s}}\epsilon\big(\partial_\tau \dot{\boldsymbol{d}}_h^n, \boldsymbol{B}_h\big(\boldsymbol{u}_h^n \circ \boldsymbol{\phi}_h^n\big)\big)_{\Sigma,h} + a^{\mathrm{s}}\big(\boldsymbol{d}_h^n, \boldsymbol{B}_h\big(\boldsymbol{u}_h^n \circ \boldsymbol{\phi}_h^n\big)\big) \leq 0.\end{aligned} \tag{6.37}$$

We then proceed similarly to [Fer13], by inserting (6.35) into (6.37). This yields

$$\begin{aligned}\frac{\rho^{\mathrm{f}}}{2}\partial_\tau \|\boldsymbol{u}_h^n\|_{0,\Omega}^2 + 2\mu \|\boldsymbol{\epsilon}(\boldsymbol{u}_h^n)\|_{0,\Omega}^2 + \frac{\rho^{\mathrm{s}}}{2}\partial_\tau \|\dot{\boldsymbol{d}}_h^n\|_{\Sigma,h}^2 + \frac{1}{2}\partial_\tau \|\boldsymbol{d}_h^n\|_{\mathrm{s}}^2 \\ + \underbrace{\tau\big(\partial_\tau \dot{\boldsymbol{d}}_h^n, \boldsymbol{L}_h^{\mathrm{s}}(\boldsymbol{d}_h^n - \boldsymbol{d}_h^{n-1})\big)_{\Sigma,h}}_{T_1} + \underbrace{\frac{\tau}{\rho^{\mathrm{s}}\epsilon} a^{\mathrm{s}}\big(\boldsymbol{d}_h^n, \boldsymbol{L}_h^{\mathrm{s}}(\boldsymbol{d}_h^n - \boldsymbol{d}_h^{n-1})\big)}_{T_2} \leq 0.\end{aligned} \tag{6.38}$$

It only remains to estimate the terms T_1 and T_2. For the first term, using (6.32), we have

$$T_1 = \tau\big(\dot{\boldsymbol{d}}_h^n - \dot{\boldsymbol{d}}_h^{n-1}, \boldsymbol{L}_h^{\mathrm{s}}\dot{\boldsymbol{d}}_h^n\big)_{\Sigma,h} = \tau a^{\mathrm{s}}\big(\dot{\boldsymbol{d}}_h^n - \dot{\boldsymbol{d}}_h^{n-1}, \dot{\boldsymbol{d}}_h^n\big) \geq \frac{\tau}{2}\big(\|\dot{\boldsymbol{d}}_h^n\|_{\mathrm{s}}^2 - \|\dot{\boldsymbol{d}}_h^{n-1}\|_{\mathrm{s}}^2\big).$$

Finally, for the last term, we have

$$T_2 = \frac{\tau}{\rho^{\mathrm{s}}\epsilon}\big(\boldsymbol{L}_h^{\mathrm{s}}\boldsymbol{d}_h^n, \boldsymbol{L}_h^{\mathrm{s}}(\boldsymbol{d}_h^n - \boldsymbol{d}_h^{n-1})\big)_{\Sigma,h} \geq \frac{\tau}{2\rho^{\mathrm{s}}\epsilon}\big(\|\boldsymbol{L}_h^{\mathrm{s}}\boldsymbol{d}_h^n\|_{\Sigma,h}^2 - \|\boldsymbol{L}_h^{\mathrm{s}}\boldsymbol{d}_h^{n-1}\|_{\Sigma,h}^2\big).$$

We conclude by inserting the above two bounds into (6.38), by multiplying the resulting expression by τ, by summing over n and by applying the norms equivalence between $\|\cdot\|_{0,\Sigma}$ and $\|\cdot\|_{\Sigma,h}$ in $\boldsymbol{Y}_h$, uniformly in h (see, e.g., [Tho06]). This completes the proof. □

6.5 Numerical experiments

The purpose of this section is to illustrate the performance of Algorithm 6.3 via comparisons with the results provided by Algorithm 6.1 (with the regularized kinematic condition (6.11)) and by an alternative method recently reported in the literature (see [AFFL16]). As the core motivation of the present work is the efficient simulation of heart valves, two representative two-dimensional examples which mimic the behavior of such systems in the open and closed configurations, have been considered. All the units are expressed in the CGS system, unless specified otherwise.

6.5.1 Idealized valve without contact

Most of the information presented here about this numerical example have already been provided in previous Section 5.4.1 but are recalled here for the purpose of completeness. Note that the spatial and temporal discretization differ from what has been presented in Section 5.4.1.

The first example is the heart-valve-inspired benchmark problem considered in [GABH13, HGAB12, Wic14, KHS+15]. It consists of one idealized valve modeled by a cantilevered elastic beam immersed in a 2D channel filled with an incompressible Newtonian fluid, as shown in Figure 6.2. The geometry of the fluid domain is given by $\Omega = [0, 8] \times [0, 0.805]$. The reference configuration of the solid, Σ, is given by the segment whose endpoints are $\mathrm{A}_0 = (2, 0)$ and $\mathrm{A}_1 = (2, 0.7)$ (see Figure 6.2). The physical parameters are, for the fluid, $\rho^{\mathrm{f}} = 100$, $\mu = 10$, and, for the solid, $\rho^{\mathrm{s}} = 100$, $\epsilon = 0.0212$, with Young's modulus $E = 5.6 \cdot 10^7$ and Poisson's ratio $\nu = 0.4$.

A no-slip boundary condition is enforced on Γ_{bot} and a symmetry boundary condition is imposed on Γ_{top}. Zero traction is enforced on the lateral boundary Γ_{out} and the velocity is prescribed on Γ_{in}, as a half parabolic profile whose maximum amplitude is defined by a positive time-dependent function $u_{\max}(t)$, given by the following expression:

$$u_{\max}(t) = \ 5 \cdot (0.805)^2 \cdot \big(\sin(2\pi t) + 1.1\big), \quad \forall t \in \mathbb{R}^+.$$

The solid is fully clamped at its bottom endpoint A_0. Both the fluid and the solid are

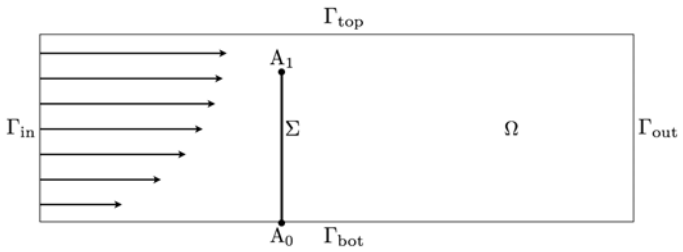

Figure 6.2 – Geometric configuration of the first numerical example.

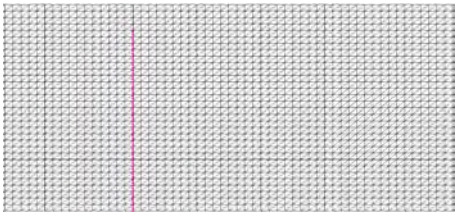

Figure 6.3 – Zoom on the fluid and solid meshes.

initially at rest. Considering the channel width of 0.805 as the characteristic length scale and the peak in flow speed of 6.8 as the characteristic flow speed, the associated Reynolds number is about 55.

In this first numerical example, in which no enclosed fluid is involved, we have observed that the grad-div stabilization has pratically no impact on the quality of the numerical results. Hence, the free stabilization parameters in (6.5) have been set to $\lambda_{\text{M}} = 1$ and $\lambda_{\text{C}} = 0$ in both methods. The penalty parameter ε for Algorithm 6.1 in (6.11) is set to $\varepsilon = 10^{-5}$. More information about the convergence study of the penalty parameter ε for this case are provided in Appendix D. We recall that Algorithm 6.3 does not involve any penalty parameter.

From the perturbed kinematic relation (6.35), Algorithms 6.1 and 6.3 are expected to deliver similar accuracy (up to the penalty error induced by ε in (6.11)) when the time-step length τ is sufficiently small. Hence, we propose to compare the results provided by these two methods, using three levels of time-step refinement given by $\tau \in \{(10^{-3}/2^i)\}_{i=0}^{2}$, and a fixed discretization in space based on a fluid mesh of 16 384 triangles and a solid mesh of 64 segments (see Figure 6.3). Figures 6.4a, 6.4c and 6.4e present, respectively for $i = \{0, 1, 2\}$, the comparison of the time history of the x-displacement of the solid at the upper tip A_1, obtained with Algorithms 6.1 and 6.3. Very close results are already obtained with the largest time-step $\tau = 10^{-3}$ (see Figure 6.4a). The agreement still improves when the time-step is refined. Note that the two curves become practically indistinguishable for the finest time grid $\tau = 2.5 \cdot 10^{-4}$ (see Figure 6.4e). Similar observations can be made from Figures 6.4b, 6.4d and 6.4f which present the results for the y-displacement, respectively for $i = \{0, 1, 2\}$. A slight difference is observed between the two curves for the largest time-step $\tau = 10^{-3}$ (see Figure 6.4b). Nevertheless, this discrepancy practically disappears in the next level of refinement (see Figure 6.4d).

For illustration purposes we have reported in Figure 6.5 some snapshots of the interface

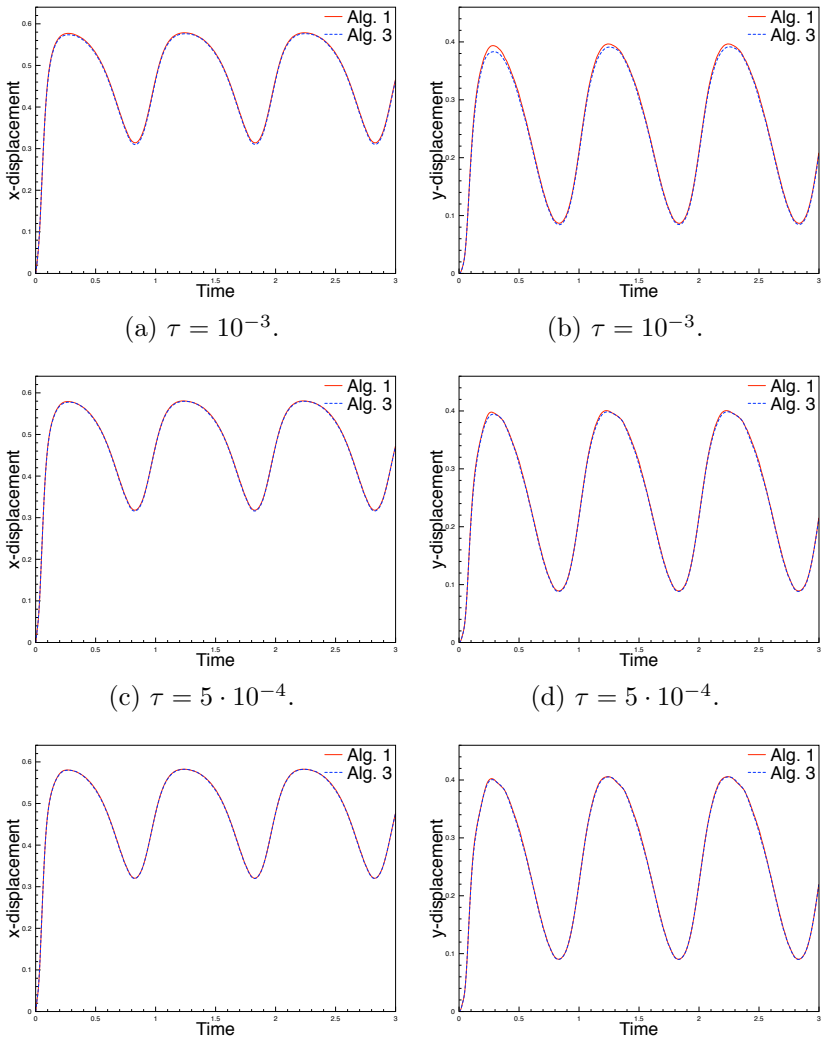

(a) $\tau = 10^{-3}$. (b) $\tau = 10^{-3}$.

(c) $\tau = 5 \cdot 10^{-4}$. (d) $\tau = 5 \cdot 10^{-4}$.

(e) $\tau = 2.5 \cdot 10^{-4}$. (f) $\tau = 2.5 \cdot 10^{-4}$.

Figure 6.4 – Time history of the displacement of solid at the upper tip A_1 obtained with Algorithms 6.1 and 6.3. Left column: x-displacement. Right column: y-displacement.

location and of the fluid velocity magnitude near the solid obtained at different time instants with Algorithms 6.1 and 6.3 for $\tau = 10^{-3}$. The very good agreement between both numerical approximations is noticeable. Similar observation can be inferred from the elevated pressure reported in Figure 6.6, obtained with $\tau = 10^{-3}$. As before, Algorithm 6.3 delivers practically the same results as Algorithm 6.1, predicting the similar shape of the pressure jump across the leaflet.

Computational considerations We finally comment of the relative efficiency of the two methods. By construction, Algorithm 6.3 requires only 1 single fluid and solid evaluations per time-step. The efficiency of Algorithm 6.1 depends on the type of solution procedure for the coupled system (6.12). In the present study, this system has been solved via a

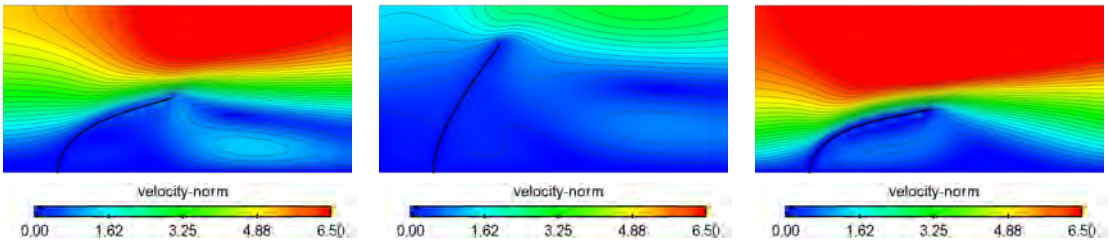

(a) Algorithm 6.1: $t = 0.45$. (b) Algorithm 6.1: $t = 0.85$. (c) Algorithm 6.1: $t = 1.25$.

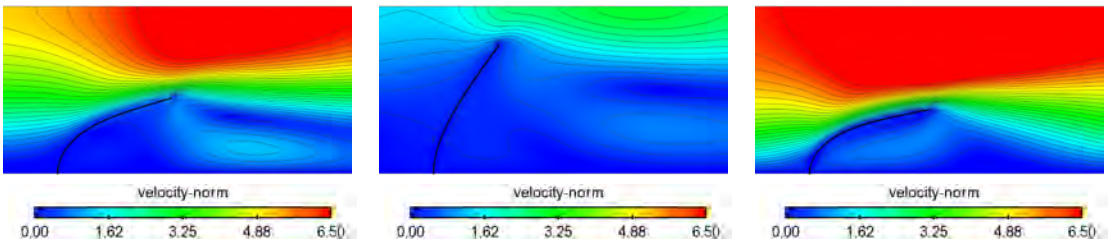

(d) Algorithm 6.3: $t = 0.45$. (e) Algorithm 6.3: $t = 0.85$. (f) Algorithm 6.3: $t = 1.25$.

Figure 6.5 – Snapshots of the fluid velocity magnitude obtained with Algorithms 6.1 and 6.3.

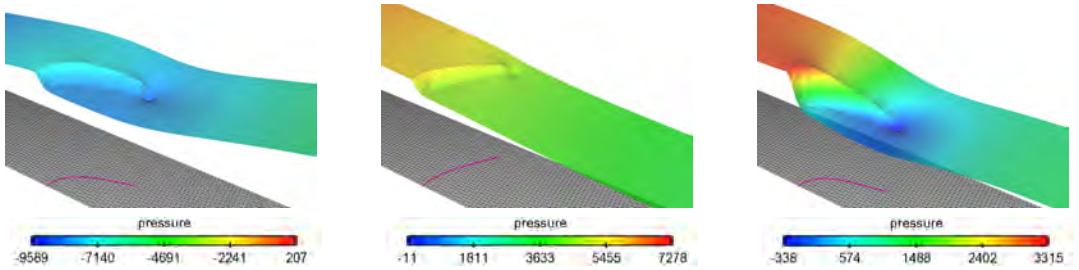

(a) Algorithm 6.1: $t = 0.45$. (b) Algorithm 6.1: $t = 0.85$. (c) Algorithm 6.1: $t = 1.25$.

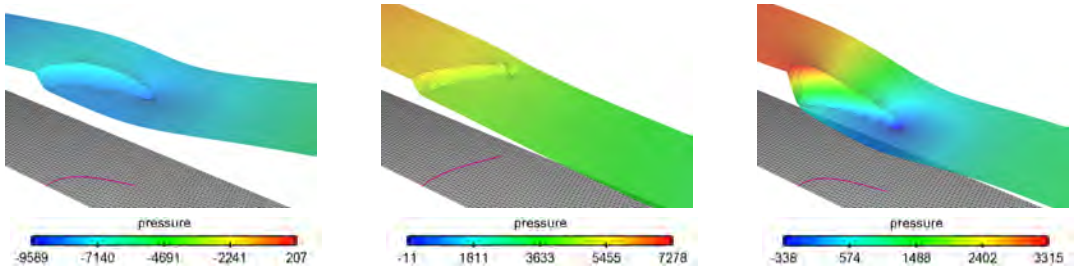

(d) Algorithm 6.3: $t = 0.45$. (e) Algorithm 6.3: $t = 0.85$. (f) Algorithm 6.3: $t = 1.25$.

Figure 6.6 – Snapshots of the fluid elevated pressure obtained with Algorithms 6.1 and 6.3.

Dirichlet-Neumann interface Newton-Generalized Minimal RESidual (GMRES) partitioned iterative method which requires an average of 3 fluid and solid evaluations and 21 tangent fluid and solid evaluations per time-step. Note also that the conditioning of these fluid systems is worse than in Algorithm 6.3 due to the penalized treatment of the interface coupling. This clearly points out the advantages of Algorithm 6.3 in terms of computational

cost.

6.5.2 Idealized valve with contact

As a second example, we consider an extension of the previous one in which the idealized valve is now long enough to get into contact with the upper wall, as shown in Figure 6.7. The geometry of the fluid domain is given by $\Omega = [0, 8] \times [0, 0.805]$ as in the previous

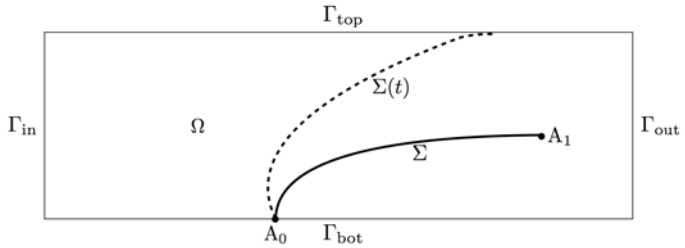

Figure 6.7 – Geometric configuration of the second numerical example.

example. The reference configuration of the solid, Σ, is defined by the following analytical expression:

$$y(x) = \frac{1}{2}\sqrt{1 - \frac{(x - 11/2)^2}{(3/2)^2}}, \quad \forall x \in [4, 5.112].$$

The coordinates of its endpoints, A_0 and A_1, are then (4,0) and $(5.112, 0.483)$, respectively. The physical parameters for the fluid are $\rho^f = 1$ and $\mu = 0.03$. For the solid, we have $\rho^s = 1.2$, $\epsilon = 0.065$, with Young's modulus $E = 10^7$ and Poisson's ratio $\nu = 0.4$.

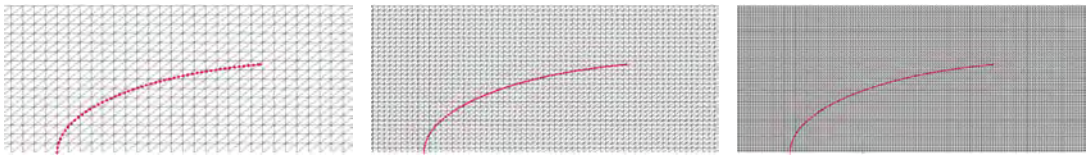

(a) M_1. (b) M_2. (c) M_3.

Figure 6.8 – Zoom on the fluid and solid meshes for the different levels of refinement.

A no-slip boundary condition is enforced on Γ_{bot} while a symmetry boundary condition is imposed on Γ_{top}. Zero traction is enforced on the lateral boundary Γ_{out}, while on Γ_{in}, traction is imposed in terms of the following time-dependent pressure data $p_{in}(t)$:

$$p_{in}(t) = \begin{cases} -200 \cdot \text{atanh}(100 \cdot t) & \text{if} \quad 0 < t < 0.7, \\ 200 & \text{if} \quad t \geq 0.7. \end{cases} \tag{6.39}$$

Finally, a backflow stabilization based on a local regularization of the fluid velocity along the tangential directions on the Neumann boundaries [MBH+11] is applied on Γ_{in} and on Γ_{out}.

The way the contact is managed between the solid and the upper wall Γ_{top} differs from the one presented in Section 2.5.4 but is in the same vein. The associated contact condition

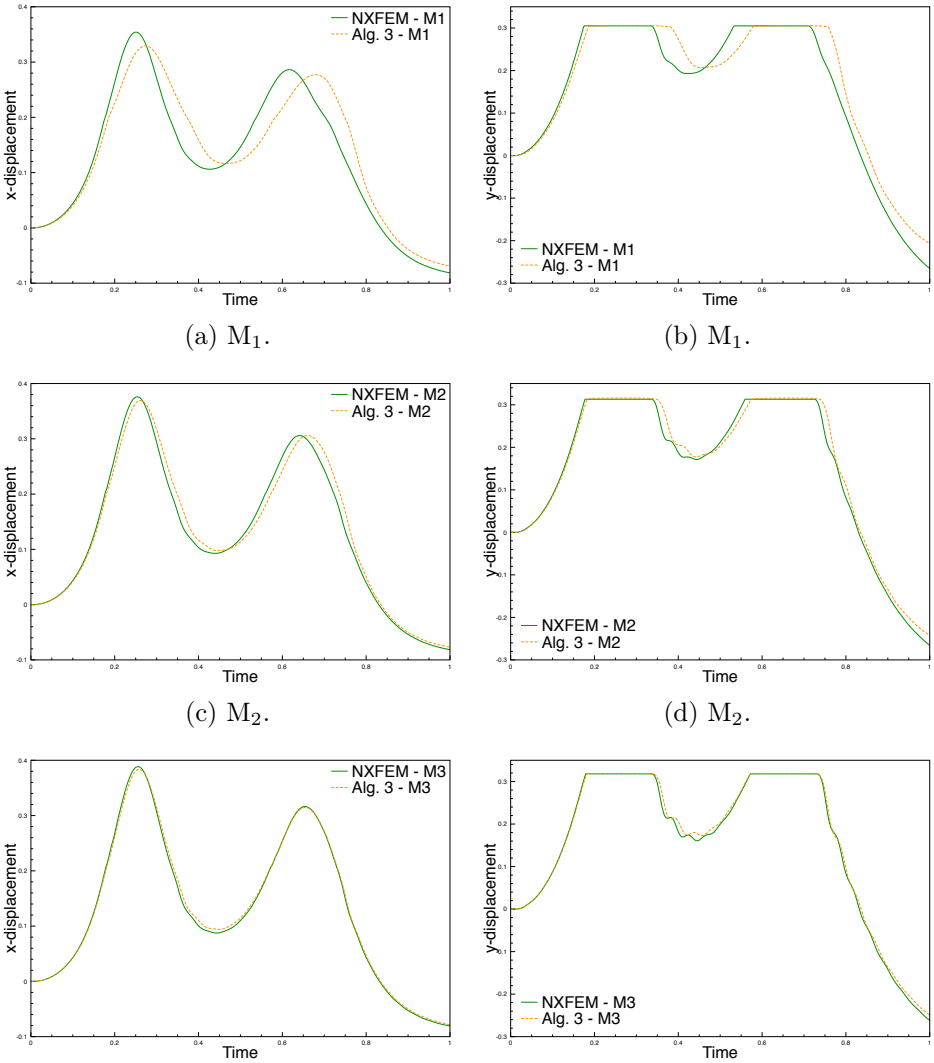

(a) M_1. (b) M_1.

(c) M_2. (d) M_2.

(e) M_3. (f) M_3.

Figure 6.9 – Time history of the displacement of the solid at the upper tip A_1 obtained with Nitsche-XFEM and Algorithm 6.3. Left column: x-displacement. Right column: y-displacement.

is the following:

$$\boldsymbol{d} \cdot \boldsymbol{n}_{\Gamma_{\text{top}}} - g \leq 0 \quad \text{on} \quad \Sigma, \tag{6.40}$$

where $\boldsymbol{n}_{\Gamma_{\text{top}}}$ denotes the (constant) exterior unit normal to Γ_{top} and $g : \Sigma \to \mathbb{R}^+$ stands for the gap function between Σ and Γ_{top}. At the discrete level, the inequality constraint (6.40) is approximated via a penalty method (see, e.g., [Sch84]). This amounts to include, in $a^s(\boldsymbol{d}_h^n, \boldsymbol{y}_h)$, the following additional non-linear term:

$$\frac{\gamma_c E \epsilon}{h^2} \big(\big[\boldsymbol{d}_h^n \cdot \boldsymbol{n}_{\Gamma_{\text{top}}} - g + \varepsilon_h \big]_+ , \boldsymbol{y}_h \big)_\Sigma, \tag{6.41}$$

where $[x]_+ \overset{\text{def}}{=} \max\{0,x\}$, $\gamma_c > 0$ is a (dimensionless) user-defined parameter and $\varepsilon_h > 0$ is a contact tolerance aimed at preventing penetration. In the results presented below, we have taken $\varepsilon_h = \mathcal{O}(h)$ and $\gamma_c = 5 \cdot 10^{-3}$.

The fluid and the solid are initially at rest. The beam is pinched at A_0 (i.e., the rotation degree of freedom is free). We consider the channel width of 0.805 as the characteristic length scale. For the characteristic flow speed, we consider the typical values of 4 and 10, for the closing and opening phases, respectively. The associated Reynolds number is then approximately 107 and 268.

Numerical evidence (reported in Appendix D) indicates that the quality of the approximations provided by Algorithm 6.1 with the regularized kinematic condition (6.11), for this specific example with contact, is extremely sensitive to the penalty parameter ε. In order to circumvent these difficulties, we propose to consider as the reference solution the strongly coupled Nitsche-XFEM unfitted mesh approach reported in previous Section 5.3.2.2. This method has multiple interesting features (e.g., Lagrange multipliers free, consistent treatment of the interface coupling, optimal error estimates, ...) and is known to deliver superior spatial accuracy with respect to Algorithm 6.1 (see last Chapter 5). Nevertheless, the price to pay is an increased computational complexity and a much more involved computer implementation (careful track of the interface intersections, dynamic matrix pattern, etc.) with respect to Algorithms 6.1 and 6.3.

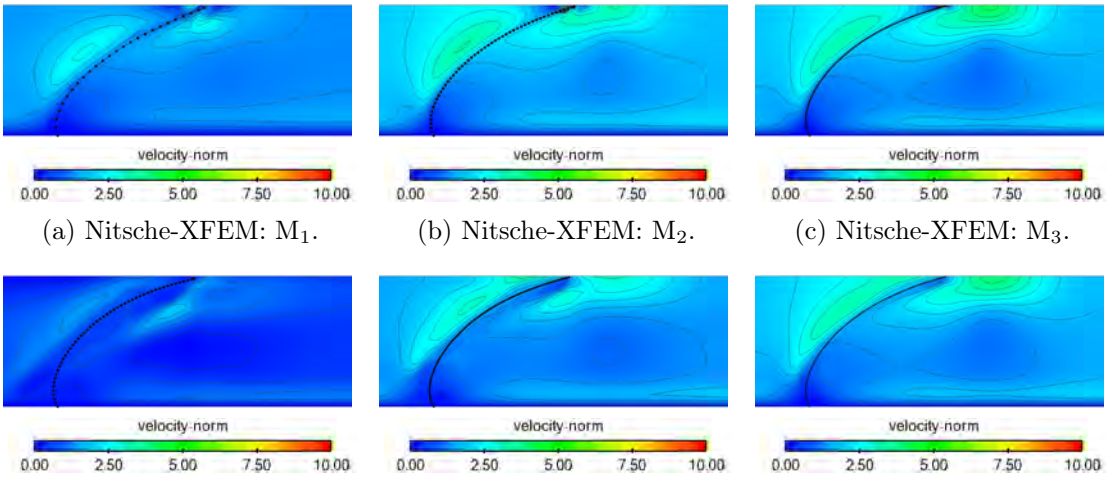

(a) Nitsche-XFEM: M_1. (b) Nitsche-XFEM: M_2. (c) Nitsche-XFEM: M_3.

(d) Algorithm 6.3: M_1. (e) Algorithm 6.3: M_2. (f) Algorithm 6.3: M_3.

Figure 6.10 – Snapshots of the fluid velocity magnitude at $t = 0.7$ obtained with Nitsche-XFEM and Algorithm 6.3.

The accuracy of Algorithm 6.3 will be then evaluated with respect to the Nitsche-XFEM method, by considering three successive levels of grid refinement in space and time. The coarsest level, which will be referred to as M_1, corresponds to a fluid mesh of 4 096 triangles. The solid mesh is made of 25 and 50 segments, respectively for Nitsche-XFEM and Algorithm 6.3. The corresponding time-step is set to $\tau = 2 \cdot 10^{-3}$ and the contact tolerance in (6.41) to $\varepsilon_h = 0.02$. The two subsequent space-time grids, denoted by M_2 and M_3, are uniform refinements of M_1 with, respectively, a factor of 2 and 4 along

both spatial and temporal directions. The three sets of fluid and solid meshes are shown in Figure 6.8. For Algorithm 6.3, the value of the user-defined parameter ε_{M}, in the SUPG/PSPG stabilization with enhanced interfacial mass conservation (6.6), is set to 10^{-4} in all levels of refinement. More information about the definition of ω_h^n for this case are provided in Appendix E for the different levels of refinement. For the Nitsche-XFEM method, the user-defined parameters are set to $\gamma = 10^2$, $\gamma_{\mathrm{g}} = 1$ and $\gamma_{\mathrm{v}} = \gamma_{\mathrm{p}} = 10^{-2}$, as detailed in [AFFL16] and in last Section 5.4.

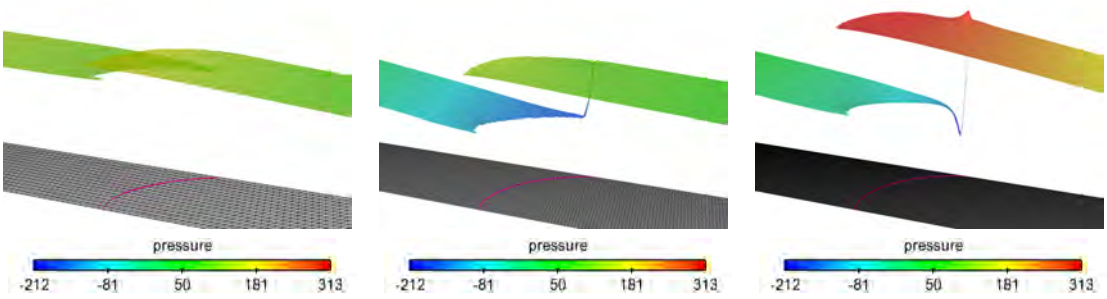

(a) Nitsche-XFEM: M_1. (b) Nitsche-XFEM: M_2. (c) Nitsche-XFEM: M_3.

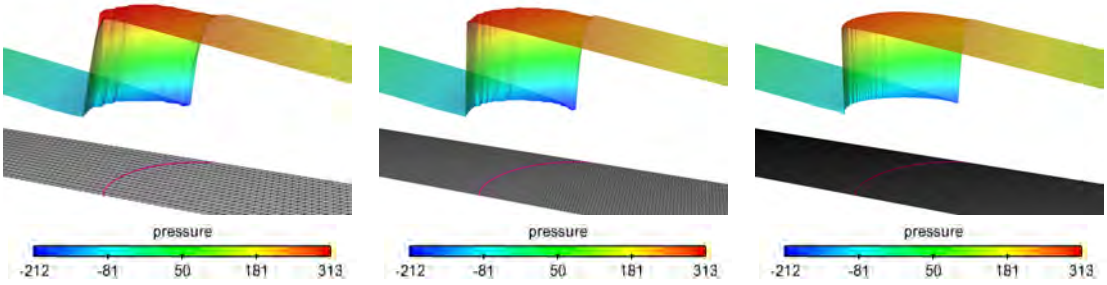

(d) Algorithm 6.3: M_1. (e) Algorithm 6.3: M_2. (f) Algorithm 6.3: M_3.

Figure 6.11 – Snapshots of the fluid elevated pressure at $t = 0.7$ obtained with Nitsche-XFEM and Algorithm 6.3.

As the negative prescribed pressure (6.39) builds up, the solid starts to bend and collides with Γ_{top} after some time instants. Due to the flexible nature of the structure, it is free to slide or even to bounce on the wall. When contact is occurring, the fluid velocity vanishes and a pressure jump across the interface is observed. Finally, after $t = 0.7$, a positive pressure builds up and the valve opens again. Figure 6.9 reports a comparison of the time history of the displacement of the solid at the upper tip A_1 obtained with Nitsche-XFEM and Algorithm 6.3 for the three levels of refinement. The left and right columns show, respectively, the horizontal and vertical components of the displacement. Note that the flat part of the curves in the vertical displacement correspond to instants where contact occurs. The part of the curve between the two successive flat parts corresponds to the bouncing of the leaflet, illustrating the complex dynamics of the problem. A significant phase shift is observed between the two approximations for the coarsest level M_1, but this discrepancy decreases with refinement. A better agreement is finally observed for the space-time grids M_2 and M_3.

For illustration purposes, Figure 6.10 presents the interface location and the fluid velocity magnitude near the leaflet obtained at $t = 0.7$, for the three levels of refinement, with Nitsche-XFEM and Algorithm 6.3. Overall, a good agreement of the fluid velocity field is already observed for the intermediate level M_2 (see Figures 6.10b and 6.10e). Once more, this agreement improves with space-time grid refinement as Figures 6.10c and 6.10f depict practically the same fluid velocity field. The snapshots of the elevated pressure are given in Figures 6.11. The mismatch observed in Figure 6.9 with the coarsest approximation is clearly pointed out here in terms of the pressure jump (see Figures 6.11a and 6.11d). Note that these pressure jumps are not evaluated at the same interface location, even if evaluated at the same instant, which explains the mismatch. The situation improves via space-time grid refinement as we can infer from Figures 6.11c and 6.11f, where the interface locations are now practically the same.

Finally, in order to provide a quantitative comparison of the two approaches, we evaluate the magnitude of the error between the two methods by measuring the L^2-difference of the interface displacement for the three levels of refinement, as shown in Table 6.1. The results clearly show convergence after grid refinement.

Space-time grid	L^2-difference
M_1	$3.18 \cdot 10^{-3}$
M_2	$7.48 \cdot 10^{-4}$
M_3	$1.61 \cdot 10^{-5}$

Table 6.1 – L^2-difference of the displacements approximations provided by Nitsche-XFEM and Algorithm 6.3.

Computational considerations: The benefits of Algorithm 6.3, with respect to the Nitsche-XFEM method considered in this example, are striking in terms of computational complexity and computer implementation. Among them, it is worth mentioning the following: there is no mesh intersection (i.e., only localization of the solid nodes within the fluid mesh are needed) and no cut-FEM (i.e., the fluid equations are integrated in the whole computational domain), the fluid system matrix has both a fixed size and a fixed standard pattern and, last, the coupling scheme is loosely coupled. These advantages should however be pondered carefully, since the spatial accuracy of Algorithm 6.3 relies on the use of the penalty grad-div term (6.5)–(6.6) which can compromise the efficiency of the fluid solver, particularly in three-dimensional simulations (see [KHS+15, CBCG17, KHY+17]). Some details about an alternative grad-div free method, enhancing the interfacial mass conservation without inducing ill-conditioning problems, and based on lower-order finite elements have been provided in Section 5.5 as well as some preliminary results obtained with it. We now apply this alternative method on the current numerical example and we refer to Section 5.5.2 for the definition of the acronyms used in the sequel. We also recall that the $\mathrm{FD}_{\mathrm{stab}}$ methods mentioned below are all strongly coupled.

Figures 6.12a–6.12c represent the macro-patch of pressure stabilization considered in

the context of the FD_{stab} methods for, respectively, the three different levels of refinement M_1, M_2 and M_3, defined in associated Section 6.5.2.

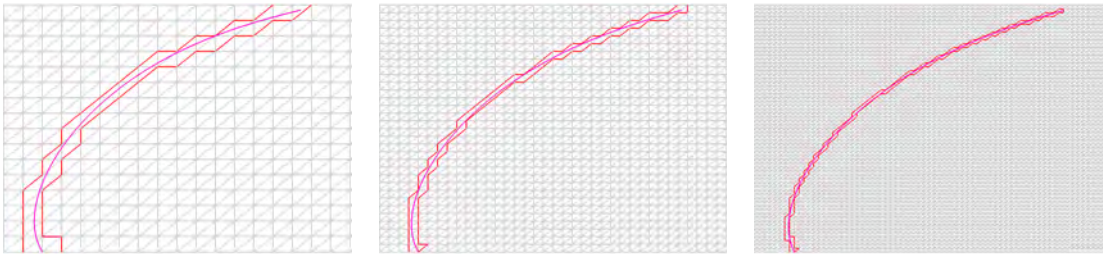

(a) M_1. (b) M_2. (c) M_3.

Figure 6.12 – Representation of the new macro-patch of pressure stabilization at time $t = 0.7$. The inner edges colored in red are the ones where the pressure stabilization has been removed.

The physical value of interest here is the y-displacement magnitude of the upper leaflet tip. The time-history of this value obtained with different methods is depicted in Figure 6.13 for the second level of refinement M_2.

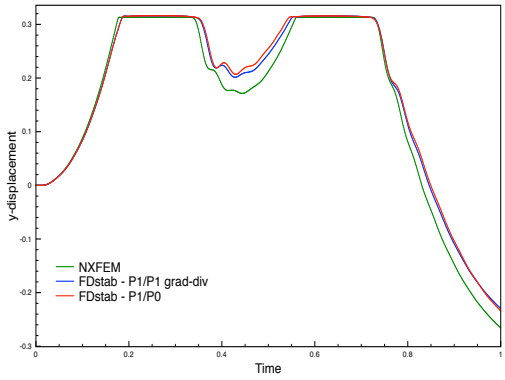

Figure 6.13 – Time-history of the y-displacement of the upper leaflet tip for the case of the idealized valve with contact for the second level of refinement M_2.

Note that for this case, the FD_{stab} grad-div free method gives results very close to the classical FD_{stab} method, but that both of them still show major differences with the reference solution, contrary to what has been obtained for the other numerical examples investigated in Section 5.5.2. This anomaly may be caused by the involved topological change and needs to be investigated in the future.

6.6 Conclusions

In this chapter, we have introduced a new loosely coupled scheme for the numerical approximations of incompressible fluid-structure interaction problems involving immersed thin-walled structures. The key ingredients of the proposed method are the following:

- Unfitted meshes and fictitious domain approximations in space (equivalent to a collocation method).
- Implicit treatment of the solid inertial effects within the fluid and explicit treatment of the elastic contribution.
- Lumped mass approximation in the solid.

A salient feature of the resulting method is that it preserves both the size and the sparsity pattern of the original fluid matrix, while enabling a full splitting between the fluid and the solid time-marchings without compromising stability (Theorem 6.1). The splitting is parameter free and circumvents the usual ill-conditioning issues of fictitious domain methods involving penalized approximations of the kinematic coupling. The numerical evidence of Section 6.5 confirmed these findings and highlighted a very good performance, in terms of accuracy and robustness, with respect to strongly coupled unfitted mesh approaches which are known to be much more computationally onerous.

Chapter 7

Simulation of implantable cardiovascular devices in a complete fluid-structure interaction framework

In this chapter, we illustrate the capabilities of the explicit coupling scheme developed in last chapter. For this purpose, we consider several 2D and 3D numerical experiments where implantable cardiovascular devices are simulated in a complete FSI framework. The goal here is to highlight the computational benefits brought by this new explicit coupling scheme when considering realistic problems.

Contents

7.1 Introduction

In Chapters 3 and 4, we have illustrated how the simulation of realistic problems, where different implantable cardiovascular devices were modeled, can be achieved with the RIS and ARIS models. Nevertheless, these simplified approaches are no longer satisfactory whenever the mechanical behavior of the valve has to be modeled (e.g., the study of the mitral prolapse or the study of the influence of the valves geometry on MR), as detailed in Section 2.3.2.2. In this case, more sophisticated models taking into account the full dynamics of the cardiac valves must be considered: this corresponds to the FSI modeling for which several numerical techniques have been provided and compared in Chapter 5. Still, the simulation of such implantable cardiovascular devices in a full FSI framework is a challenging task. From the numerical point of view, the development of efficient and accurate methods is mandatory to be able to handle complex and physiological 3D cases. The fundamental principle of this idea is that, for efficiency, the numerical methods must avoid strong coupling between the fluid and solid solvers. In Chapter 6, such an example

of loosely coupled scheme has been developed in the context of the FD method and has been applied to academic cases. The main motivation of this chapter is to now illustrate the capabilities and benefits of this new explicit coupling scheme when applied to realistic problems.

Several 2D and 3D numerical examples motivated by the simulation of implantable cardiovascular devices are considered in a complete FSI framework. First, the concept of the adjustable mitral ring developed by Kephalios to treat MR (see Section 1.5.4) is numerically illustrated on a 2D case where the contact between two elastic structures, representing the leaflets of the mitral valve, is taken into account. Then, the fluid-structure-contact interaction phenomenon in the aortic valve is considered. In this numerical example, the explicit coupling scheme is applied on a 3D case for the first time and its benefits in term of computational efficiency are evaluated. Finally, the Epygon valve, previously investigated with the ARIS model (see Section 4.3.2), is now considered in a full FSI framework within a realistic 3D geometry of the left heart. Its dynamics as well as its impact on intraventricular hemodynamics are numerically simulated.

This chapter is organized as follows. Section 7.2 recalls the different coupled problems considered through this chapter. In Section 7.3, the numerical study, whose content is described above, is computed before commenting on the obtained results. Finally, a summary of the main conclusions is given in Section 7.4.

7.2 Problem setting

In what follows, the fluid is modeled by the incompressible Navier-Stokes equations in the Eulerian or in the mixed ALE-Eulerian formalisms. The thin-walled solid is still described by a non-linear Reissner-Mindlin beam model in Lagrangian form. We refer to Sections 2.2.2.2 and 2.5.1.2 for more information about these models.

The geometric configurations and notations are those of Section 2.5.2.1. Then, for the coupled problem with Eulerian formalism in the fluid, used in Sections 7.3.1 and 7.3.2, we refer to (2.14)–(2.16) in previous Section 2.5.2.2. For the coupled problem with mixed ALE-Eulerian formalism in the fluid, used in Section 7.3.3, we refer to (2.23)–(2.25) in previous Section 2.5.2.2.

7.3 Numerical experiments

In what follows, the physical parameters used for the fluid and for the solids are based on physiological values (see, e.g., [PS14, CYMN04] and also Sections 1.2.2.2 and 1.2.2.4). All the units are expressed in the CGS system, unless specified otherwise.

7.3.1 Kephalios ring

The purpose of the first numerical example is to numerically highlight, on a simplified case, the benefits induced by the Kephalios device (introduced in Section 1.5.4) for the treatment of MR. Its working principle, which consists in reducing the mitral annulus in order to restore the lost coaptation of the leaflets (induced, e.g., by a dilatation of the

ventricle (see Section 1.4.2)), is recalled in Figure 7.1. In the following, we will refer to the configuration depicted in Figure 7.1a by "ill configuration" and to one depicted in Figure 7.1b by "corrected configuration".

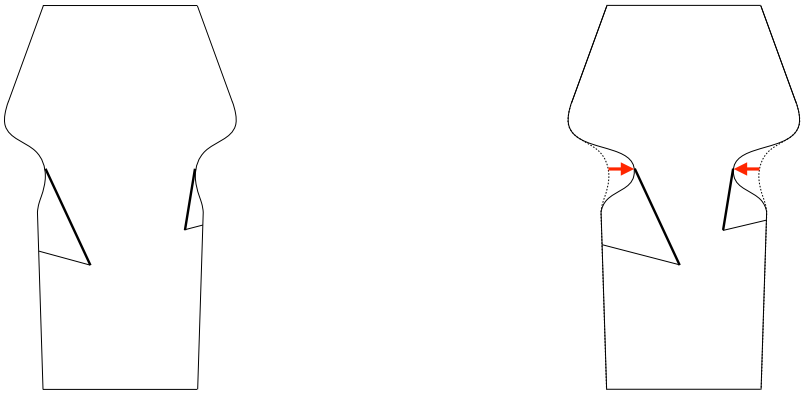

(a) Initial mitral annulus. (b) Reduced mitral annulus.

Figure 7.1 – Schematic representation of the working principle of the Kephalios device in 2D. Red arrows represent the evolution of the mitral annulus between the two configurations.

For the sake of simplicity, the fluid domain, in which the leaflets are immersed, is supposed to be fixed and to be included in $\mathbb{R}^2$. Thus, for this first numerical example, the FSI coupled problem is considered in its Eulerian-Lagrangian formalism (see Section 7.2) and for $d = 2$.

The geometry of the fixed fluid domain is given by Ω which mimics the mains characteristics of a plane section of the left heart, as depicted in Figure 7.2. Its corresponding bounding box is given by $[0.120, -8.310] \times [3.830,0]$. This domain can be split in two subparts representing the atrium (for the above part) and the ventricle (for the bottom part) separated by two immersed solids Σ_1 and Σ_2, which represent the leaflets of the mitral valve.

The reference configuration of these two solids are defined by simple segments whose endpoints are A_0 and A_1 (see Figure 7.2). Σ_2 is shorter than Σ_1 and is not oriented in the same direction in order to reproduce the typical geometrical characteristics of the posterior and anterior leaflets (as detailed in Section 1.2.2.4). In addition, each leaflet Σ_1 and Σ_2 is linked to the wall Γ_{wall} with another solid, respectively Σ_1^* and Σ_2^*, which represents a mitral chordae tendineae whose endpoints are A_1 and A_2 (see Figure 7.2). We recall that the role of such tendinous cords is to prevent the mitral valve from prolapsing into the LA (as detailed in Section 1.3.2).

The physical parameters for the fluid are $\rho^{\text{f}} = 1$ and $\mu = 0.03$. For the solids, we have $\rho^{\text{s}} = 1$ and $\epsilon = 0.065$, with Poisson's ratio $\nu = 0.4$. The Young's modulus E is equal to $2.4 \cdot 10^6$ and to $1.6 \cdot 10^6$ for, respectively, Σ_1 and Σ_2. As the chordae tendineae are less stiff than the leaflets, their Young's modulus E is equal to $2 \cdot 10^3$ and to $8 \cdot 10^2$ for, respectively, Σ_1^* and Σ_2^*.

A no-slip boundary condition is enforced on Γ_{wall}. Zero traction is enforced on the

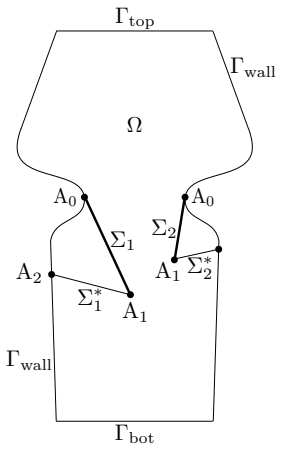

Figure 7.2 – Geometric configuration of the first numerical example.

bottom boundary Γ_{bot}, while on Γ_{top}, traction is imposed in terms of the following time-dependent pressure data $p_{\text{top}}(t)$:

$$p_{\text{top}}(t) = \begin{cases} -\dfrac{A}{5} & \text{if} \quad 0 < t < 1, \\ A & \text{if} \quad t \geq 1, \end{cases} \tag{7.1}$$

with the amplitude $A = 1804$. Finally, a backflow stabilization based on a local regularization of the fluid velocity along the tangential directions on the Neumann boundaries [MBH+11] is applied on Γ_{bot} and on Γ_{top}.

The contact between the leaflets Σ_1 and Σ_2 is taken into account and its modeling has been described in Section 2.5.4. The values of the parameters in the corresponding algorithm are $\varepsilon_{\text{g}} = 10^{-2}$, $\varepsilon_{\mathbf{cvx}} = 10^{-3}$ and $\varepsilon_{\boldsymbol{\mathcal{C}}} = 10^{-3}$. The value of the user-defined parameter ε_{M}, in the SUPG/PSPG stabilization with enhanced interfacial mass conservation (6.6), is set to 10^{-4} for both ill and corrected configurations. More information about the definition of ω_h^n for this numerical example are provided in Appendix E.

The simulation is carried out for a total time of $t = 2$, corresponding to the time required for the full development of the closing and opening phases. The corresponding time-step is set to $\tau = 10^{-3}$. The fluid and the different solids are initially at rest. The leaflets Σ_1 and Σ_2 are fully clamped at A_0 and the tendinous cords Σ_1^* and Σ_2^* are pinched at A_2 (i.e., the rotation degree of freedom is free). As regards the spatial discretization, the whole computational domain Ω is made of 26 430 triangles. The solid meshes Σ_1 and Σ_2 are made of, respectively, 241 and 147 edges of same size h. Finally, Σ_1^* and Σ_2^* are simply made of one single edge.

The two sets of fluid and solid meshes, which are used in the regurgitant and corrected configurations, are shown in Figure 7.3. Starting from the dilated configuration represented in Figure 7.3a, the diameter of the mitral annulus is reduced thanks to the Kephalios device (not represented here) resulting in a rapprochement of two leaflets as depicted in Figure 7.3b.

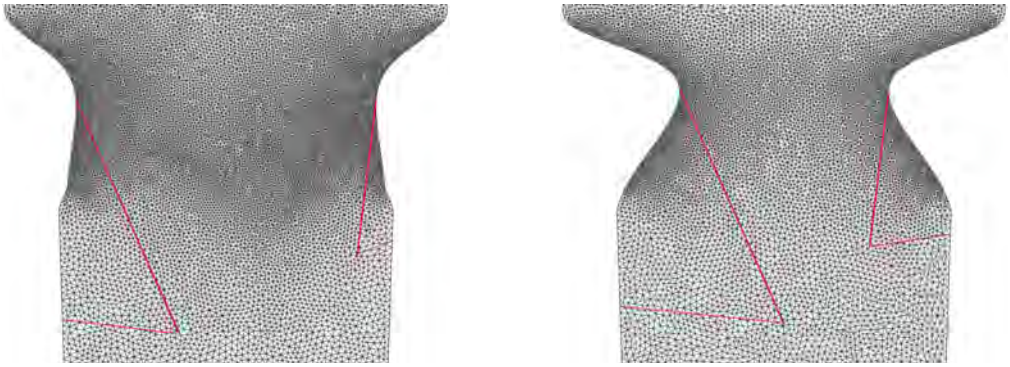

(a) Regurgitant configuration. (b) Corrected configuration.

Figure 7.3 – Zoom on the fluid and solid meshes in the regurgitant and corrected configurations at time $t = 0$.

Figure 7.4 presents some snapshots of the fluid velocity field obtained in the regurgitant and corrected configurations. After an initial transition phase where the leaflets begin to close (see Figures 7.4a and 7.4b), they are prevented from collapsing back into the atrium thanks to the tendinous cords and reach a steady state. For the regurgitant configuration, a backflow towards the atrium is observed due to the absence of coaptation of the leaflets as depicted in Figure 7.4c. On the contrary for the corrected configuration, due to the reduction of diameter of the mitral annulus induced by the Kephalios device, the leaflets enter into contact during the closing phase as shown in Figure 7.4d. After the end of the closing phase at $t = 1$, the mitral valve opens and blood flows towards the ventricle for both configurations (see Figures 7.4e and 7.4f). The corresponding results for the elevated pressure are given in Figure 7.5.

Finally, Figure 7.6 reports a comparison of the time history of the computed flow rate at the inlet during the closing phase in the regurgitant and corrected configurations. For the regurgitant configuration, a non-zero flow rate is still observed after the end of the transition phase, consequence of the absence of coaptation of the leaflets (as illustrated in Figure 7.4c). On the contrary, the correction of blood flow is clearly observed for the corrected configuration where the flow rate is equal to 0 after the leaflets have come into contact at $t = 0.25$, highlighting the fact that the previously lost coaptation has effectively been restored (as illustrated in Figure 7.4d).

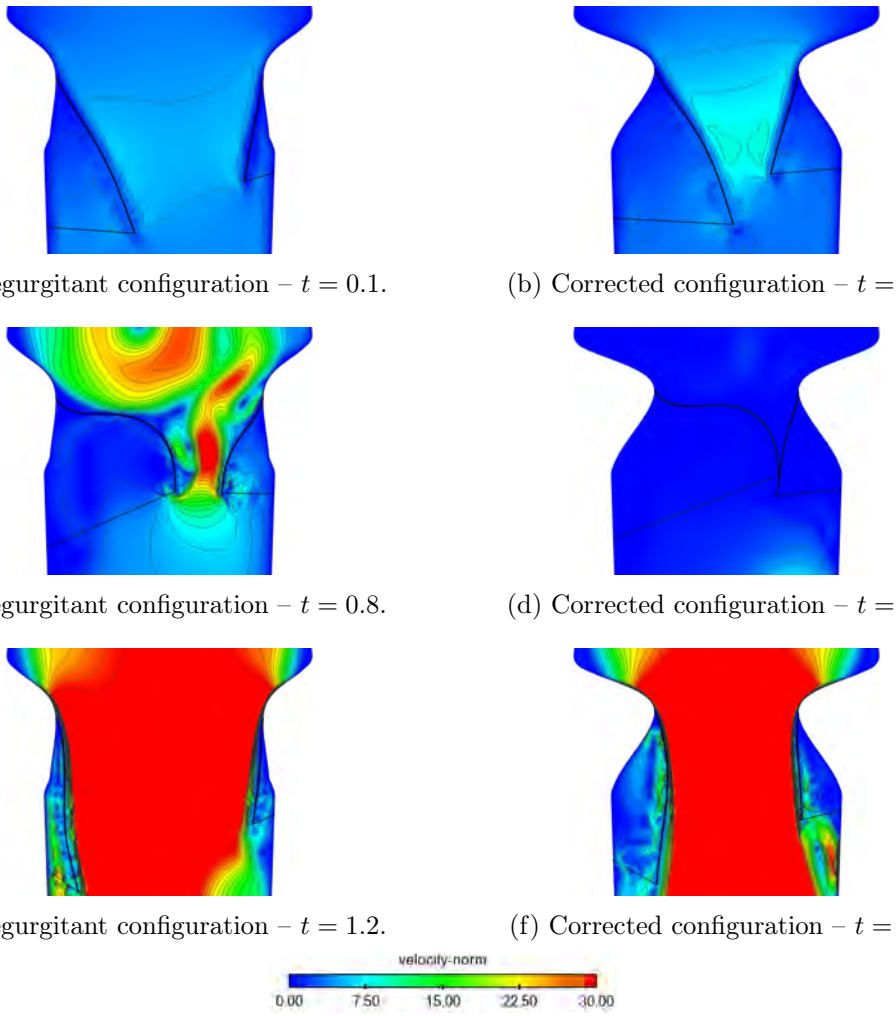

(a) Regurgitant configuration – $t = 0.1$.

(b) Corrected configuration – $t = 0.1$.

(c) Regurgitant configuration – $t = 0.8$.

(d) Corrected configuration – $t = 0.8$.

(e) Regurgitant configuration – $t = 1.2$.

(f) Corrected configuration – $t = 1.2$.

Figure 7.4 – Snapshots of the fluid velocity field obtained in the regurgitant and corrected configurations obtained at different instants.

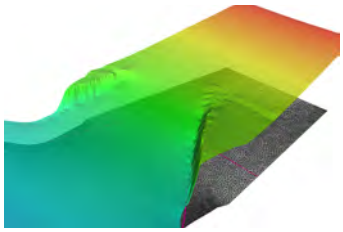

(a) Regurgitant configuration – $t = 0.1$.

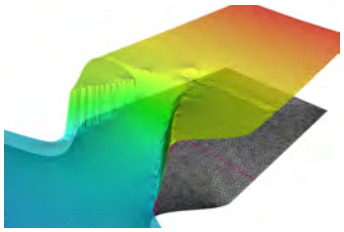

(b) Corrected configuration – $t = 0.1$.

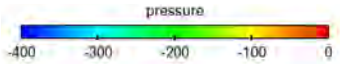

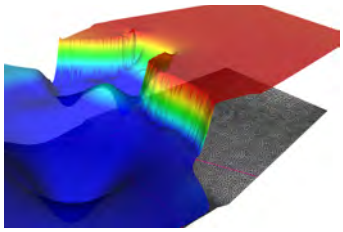

(c) Regurgitant configuration – $t = 0.8$.

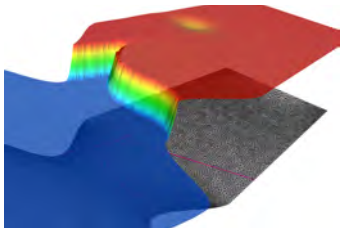

(d) Corrected configuration – $t = 0.8$.

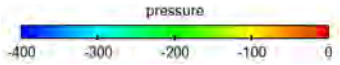

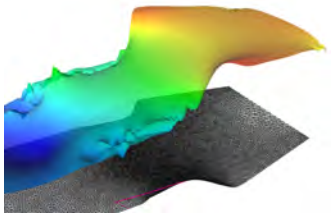

(e) Regurgitant configuration – $t = 1.2$.

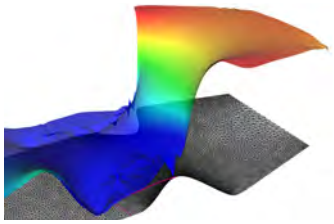

(f) Corrected configuration – $t = 1.2$.

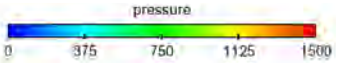

Figure 7.5 – Snapshots of the fluid elevated pressure obtained in the regurgitant and corrected configurations at different instants.

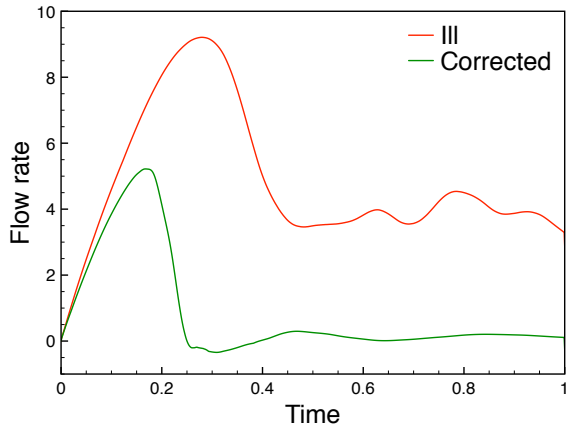

Figure 7.6 – Time history of the flow rate at the inlet during the closing phase in the regurgitant and corrected configurations.

7.3.2 Aortic valve

The second numerical example is based on an aortic-valve-inspired geometry and is based on the one computed in [AGPT09]. The purpose of this section is to apply, for the first time, the new explicit coupling scheme to a 3D case and to assess its benefits in terms of computational efficiency compared to what has been previously obtained with an implicit coupling scheme in [AGPT09]. The different computational domains used in this numerical experiment are depicted in Figure 7.7.

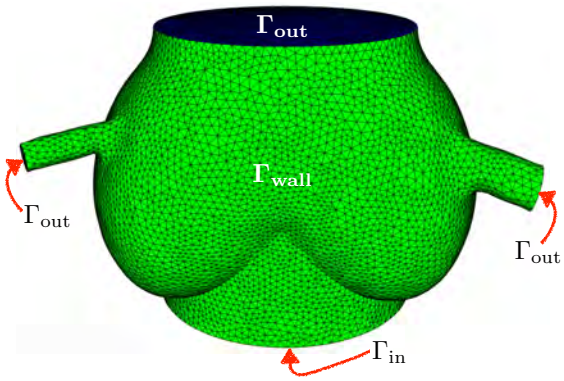

(a) Exterior of the fluid domain.

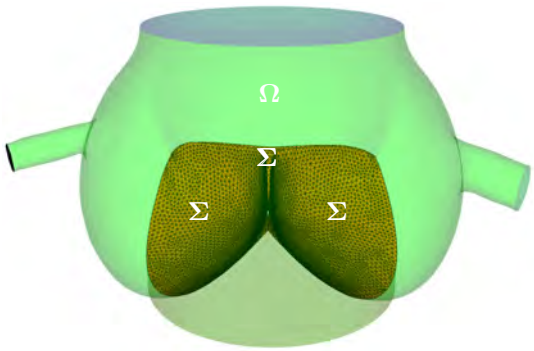

(b) Interior of the fluid domain.

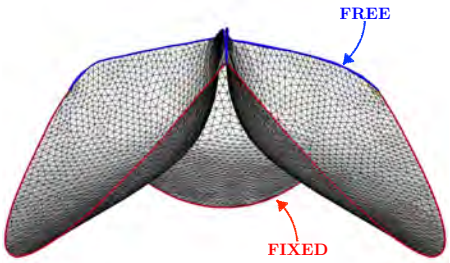

(c) Profile view of the structures meshes.

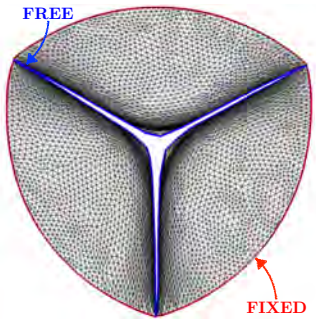

(d) Top view of the structures meshes.

Figure 7.7 – Geometric configuration of the computational domains used for the aortic valve model.

For the sake of simplicity, the fluid domain, in which the leaflets are immersed, is supposed to be fixed. Thus, for this second numerical example, the FSI coupled problem is considered in its Eulerian-Lagrangian formalism (see Section 7.2) and for $d = 3$.

The geometry of the fixed fluid domain Ω is given by a realistic portion of the aortic root (presented in Section 1.2.2.4 and coming from [AGPT09]) and is pictured in Figure 7.7b. Its corresponding bounding box is given by $[-1.681, -0.634, -1.392] \times [1.670, 1.436, 1.255]$. The three associated SL leaflets attached to this aortic root are all represented by Σ and their reference configuration is depicted in Figure 7.7b. Anatomical characteristics and mechanical properties of the valve can be found in [DPSB03, Thi08b]. Finally, more information about the geometry of the aortic valve and its leaflets are provided in Appendix A. The physical parameters for the fluid are $\rho^f = 1$ and $\mu = 0.03$. For the solids,

we have $\rho^s = 1.2$, $\epsilon = 0.065$, with Young's modulus $E = 10^4$ and Poisson's ratio $\nu = 0.5$.

As regards the boundary conditions for the fluid, we refer to Figure 7.7a for the definition of its different boundaries. A no-slip boundary condition is enforced on Γ_{wall}. Zero traction is enforced on the outlets Γ_{out}, while on Γ_{in}, traction is imposed in terms of the following time-dependent pressure data $p_{\text{in}}(t_{\text{T}})$:

$$p_{\text{in}}(t_{\text{T}}) = \begin{cases} A & \text{if} \quad 0 \leq t_{\text{T}} < 0.18, \\ -A & \text{if} \quad 0.18 \leq t_{\text{T}} < 0.6, \end{cases} \tag{7.2}$$

with the amplitude $A = 97.5$ and t_{T} is defined by $t \equiv t_{\text{T}} \pmod{0.6}$. Despite not being physiological, we chose a pressure profile close to the one used in [AGPT09] in order to be able to quantitatively compare the different results. In addition, a backflow stabilization based on a local regularization of the fluid velocity along the tangential directions on the Neumann boundaries [MBH+11] is applied on Γ_{in} and on Γ_{out}.

The contact between the three leaflets of the aortic valve is taken into account and represents an illustration of the multi-body contact mentioned in Section 2.5.4.1. The values of the parameters in the corresponding algorithm are $\varepsilon_{\text{g}} = 5 \cdot 10^{-3}$, $\varepsilon_{\mathbf{cvx}} = 10^{-4}$ and $\varepsilon_{\boldsymbol{\mathcal{C}}} = 5 \cdot 10^{-4}$.

The simulation is carried out for a total time of $t = 1$, corresponding to the duration of one full cycle followed by the beginning of a new opening phase. The corresponding time-step is set to $\tau = 10^{-3}$. The fluid and the different solids are initially at rest. As depicted in Figures 7.7c and 7.7d, the structures are fully clamped where they are attached to the aortic root and are free elsewhere.

As regards the spatial discretization, the whole computational domain Ω is made of 341 062 tetrahedra. Each leaflet is approximatively made of 3 000 triangles of same size h. We recall that these meshes have been shown in Figure 7.7.

Figure 7.8 presents some snapshots of the fluid velocity field obtained at different instants. Similarly to what is observed in [AGPT09], blood recirculation is obtained behind the aortic valve during the closing phase (see Figures 7.8c, 7.8d and 7.8e). A maximum velocity of approximatively 10 is computed at $t = 0.45$ during the closing phase when the section of the fluid domain is the most narrowed, as depicted in Figure 7.8e. When the valve is fully closed (see Figure 7.9f), a small residual flow rate is still observed through it, consequence of the poor interfacial mass conservation due to the use of the FD method instead of the FD_{stab} one for this numerical experiment. Then, the corresponding results for the pressure field are given in Figure 7.9. A significant pressure drop is observed through the valve when it is closing and fully closed as depicted, respectively, in Figures 7.9e and 7.9f.

Figure 7.10 reports the time history of the computed flow rate at the outlet. It is observed that the flow rate increases during the opening phase (i.e., for $0 < t < 0.18$). Then, when the pressure at the inlet becomes negative, the closing of the valve begins and the flow rate starts to decrease. When the valve is fully closed (i.e., for $0.5 < t < 0.6$), the flow rate is almost null and only a small residual value is still computed, as previously illustrated in Figure 7.8f by the velocity field at $t = 0.59$. The same pattern is observed for the next cycle starting at $t = 0.6$.

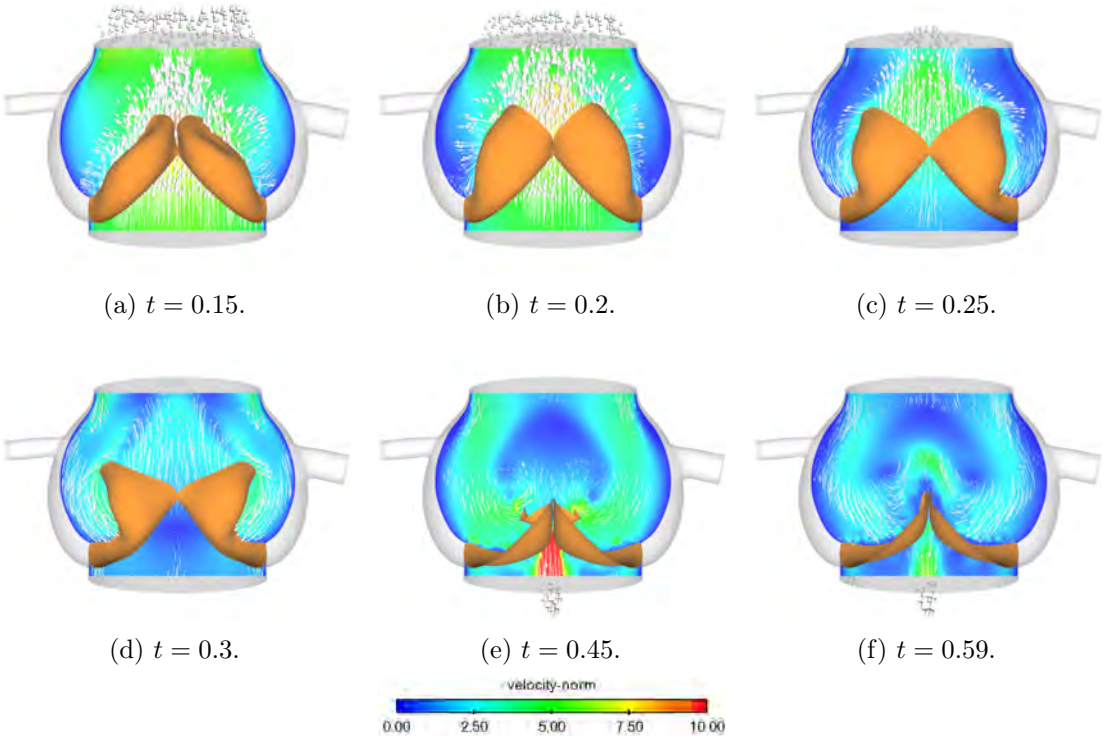

(a) $t = 0.15$. (b) $t = 0.2$. (c) $t = 0.25$.

(d) $t = 0.3$. (e) $t = 0.45$. (f) $t = 0.59$.

Figure 7.8 – Snapshots of the fluid velocity field obtained at different instants for the case of the aortic valve model.

Finally, some snapshots of the deformations of the valve obtained from two points of view and at different instants are depicted in Figure 7.11. The general shape of the valve obtained during its distortion is similar to what is shown in [AGPT09], in particular for Figures 7.11a and 7.11c. Some situations where multi-body contact between the different leaflets occurs are obtained when the valve is almost fully closed (i.e., for $t > 0.4$) and are depicted in Figures 7.11e and 7.11f at, respectively, $t = 0.45$ and $t = 0.59$.

Computational considerations: We finally evaluate the benefits in terms of relative efficiency brought by this new explicit coupling scheme when 3D numerical experiments are computed. As mentioned in last Chapter, this loosely coupled scheme, described by Algorithm 6.3, requires only 1 single fluid and 1 solid evaluations per time-step, by construction. On the contrary, the previous strongly coupled scheme, described by Algorithm 6.1 and solved via a Dirichlet-Neumann interface Newton-GMRES partitioned iterative method, requires several fluid and solid evaluations per time-step.

In order to quantitatively illustrate the computational cost of the two coupling schemes, the current numerical example has been computed with both of them. For the implicit one, around 220 hours have been required to compute the full simulation. For the explicit one, only approximatively 14 hours were required.

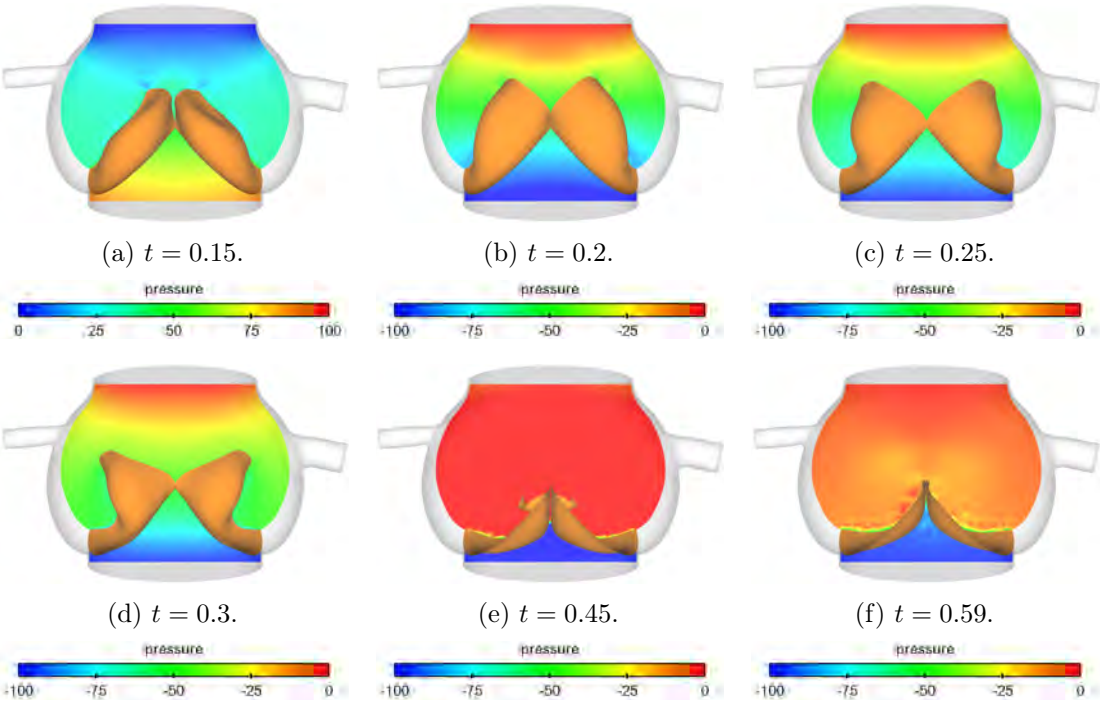

(a) $t = 0.15$. (b) $t = 0.2$. (c) $t = 0.25$.

(d) $t = 0.3$. (e) $t = 0.45$. (f) $t = 0.59$.

Figure 7.9 – Snapshots of the pressure field obtained at different instants for the case of the aortic valve model.

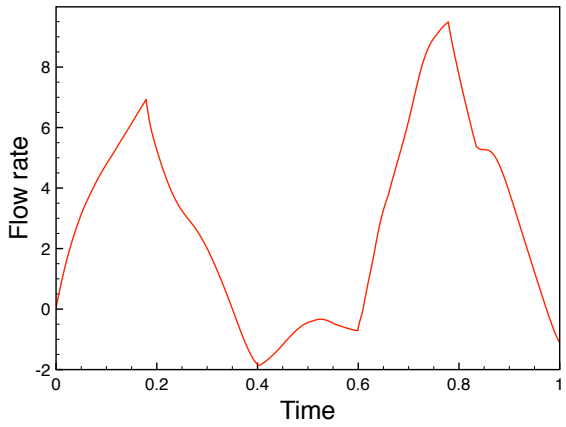

Figure 7.10 – Time history of the flow rate at the outlet for the case of the aortic valve model.

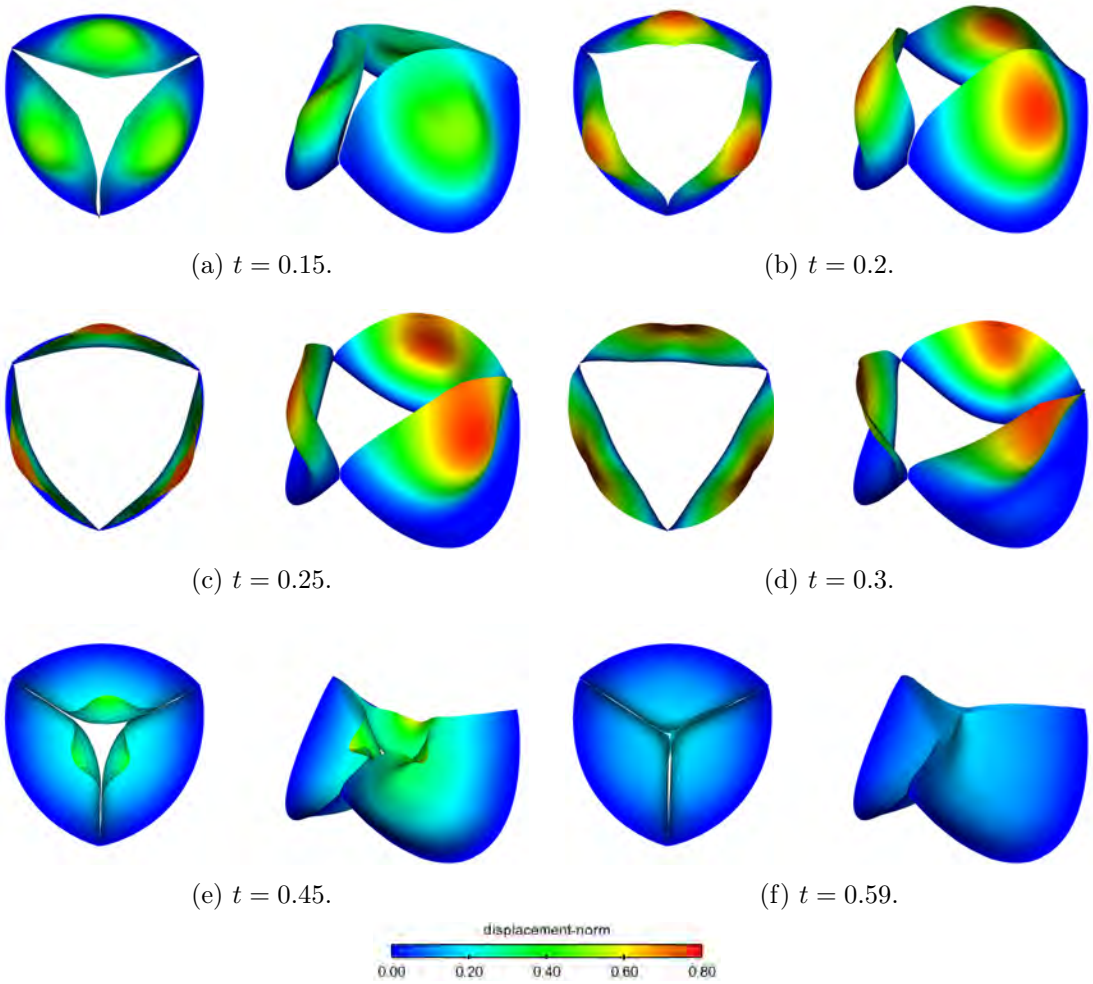

(a) $t = 0.15$. (b) $t = 0.2$.

(c) $t = 0.25$. (d) $t = 0.3$.

(e) $t = 0.45$. (f) $t = 0.59$.

Figure 7.11 – Snapshots of the deformations of the valve from two points of view and at different instants, colored by displacement magnitude, for the case of the aortic valve model.

7.3.3 Epygon valve

The third and last numerical experiment of this chapter consists in the simulation of the Epygon valve in a full FSI framework and in a realistic 3D geometry of the left heart. The fluid domain $\Omega = \Omega_1 \cup \Omega_2 \cup \Omega_3$, in which the Epygon valve is immersed, is the one coming from Zygote and has been previously described in Section 3.3.2 (see Figure 3.12a in particular). The upper part of the LV surface has been slightly modified in order to fit the annulus of the artificial valve (see Figure 4.2c). The different computational domains used in this numerical experiment are depicted in Figure 7.12. More information about the geometry of the Epygon valve is provided in Appendix A.

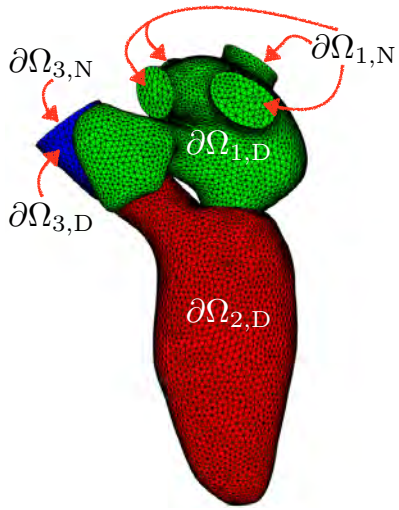

(a) Exterior of the fluid domain.

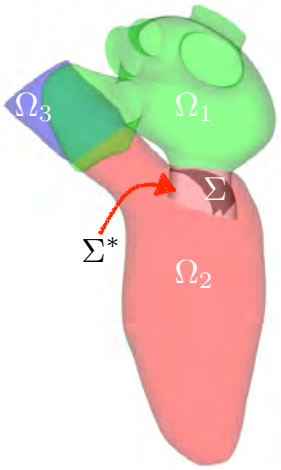

(b) Interior of the fluid domain.

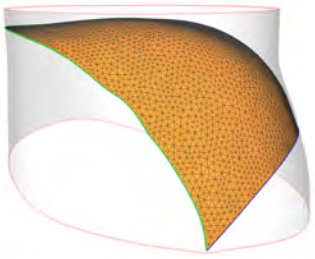

(c) Zoom on the Epygon valve.

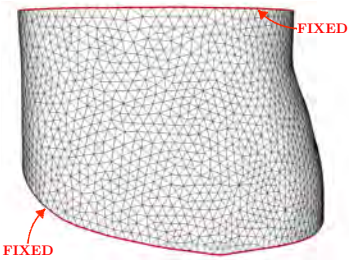

(d) The stent - Σ^*.

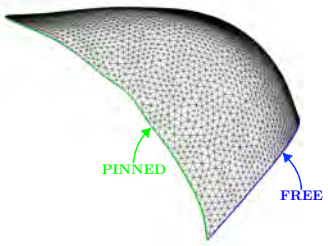

(e) The single leaflet - Σ.

Figure 7.12 – Geometric configuration of the computational domains used for the Epygon valve model.

Same as before, the whole computational domain Ω is assumed to distort over time due to a displacement field applied on the LV (i.e., on $\partial\Omega_{2,\mathrm{D}}$) and coming from an external electromechanical simulation. In addition, the Epygon valve, made of the elastic leaflet Σ wrapped into the rigid stent Σ^* (see Figures 7.12c–7.12e), is immersed into Ω_2. It is assumed that its distortion is dictated by the pressure evolution in the LV due to its change of volume. Thus, for this third numerical example, the FSI coupled problem is considered in its mixed ALE-Eulerian-Lagrangian formulation (see Section 7.2) and for $d = 3$.

The physical parameters for the fluid are $\rho^{\mathrm{f}} = 1$ and $\mu = 0.03$. For the solids, we have $\rho^{\mathrm{s}} = 1$, $\epsilon = 0.0496$, with Poisson's ratio $\nu = 0.45$. The Young's modulus E is equal to $5 \cdot 10^6$ and to 10^{11} for, respectively, Σ and Σ^*. The great value of E for Σ^* ensures that the stent will not deform during the simulation.

As regards the boundary conditions for the fluid we refer to Figure 7.12a for the definition of its different boundaries. A no-slip boundary condition is enforced on $\partial\Omega_{1,\mathrm{D}} \cup \partial\Omega_{2,\mathrm{D}} \cup \partial\Omega_{3,\mathrm{D}}$. Zero traction is enforced on the pulmonary veins $\partial\Omega_{1,\mathrm{N}}$. A null velocity is applied on $\partial\Omega_{3,\mathrm{N}}$ in order to mimic the presence of a closed aortic valve. The surface displacement prescribed on $\partial\Omega_{2,\mathrm{D}}$ is extended to Ω using an appropriate non-linear lifting operator [LVCF17] (denoted $\boldsymbol{\mathcal{L}}_{\mathrm{wall}}$ in (2.23)–(2.25)). The displacement is set to 0 on all other surfaces defining the fluid domain. Finally, a backflow stabilization based on a local regularization of the fluid velocity along the tangential directions on the Neumann boundaries [MBH+11] is applied on $\partial\Omega_{1,\mathrm{N}}$.

Based on the reference pressures depicted for the realistic model in Figure 3.13, the initial state of the simulation is set to the configuration of the cardiac cycle at $t = 0.5$. This corresponds to the beginning of the second isovolumetric phase, when the aortic valve just closed and when the mitral valve is about to open. The simulation is carried out for a total time of $t = 0.35$, corresponding to the time remaining until the end of the cardiac cycle. The corresponding time-step is $\tau = 10^{-3}$. The fluid and the different solids are initially at rest. As depicted in Figure 7.12d, the stent Σ^* is totally clamped at its extremities. On Figure 7.12d, it is highlighted that the leaflet Σ is initially in its closed configuration. Its extremities are pinched (i.e., the two rotation degrees of freedom are free) where the artificial valve is attached to the stent and free elsewhere. The contact between Σ and Σ^* is not taken into account.

REMARK 7.1
Since the top extremities of the stent Σ^* are assumed to be fixed, the displacement field provided by the electromechanical simulation and applied on the surface $\partial\Omega_{2,D}$ of the LV must also meet this condition.

As regards the spatial discretization, the whole computational domain Ω is made of 236 401 tetrahedra. The stent Σ^* is made of 5 408 triangles and the leaflet Σ is made of 8 440 triangles.

Figures 7.13 and 7.14 present some snapshots of the fluid velocity and pressure fields obtained at different instants. After a short opening phase due to the strong pressure differential between the atrium and the ventricle in the early moments of the simulation (see Figures 7.14a and 7.14b), the filling of the ventricle starts around $t = 0.35$, as depicted in Figure 7.13b. As regards the structure of the intraventricular blood flow, the same typical features as the ones obtained with the ARIS model (see Section 4.3.2) are observed here: after having been ejected in the ventricle (see Figure 7.13c), blood hits the ventricle wall (see Figure 7.13d) and a diastolic asymmetric flow oriented towards the posterior wall is obtained (see Figure 7.13e). Blood keeps flowing towards the apex before turning clockwise and going back towards the top of the ventricle (see Figure 7.13f). Then, when the pressure differential decreases (see Figures 7.14g and 7.14h), the Epygon valve closes

and a residual velocity pattern remains in the ventricle (see Figures 7.13g and 7.13h).

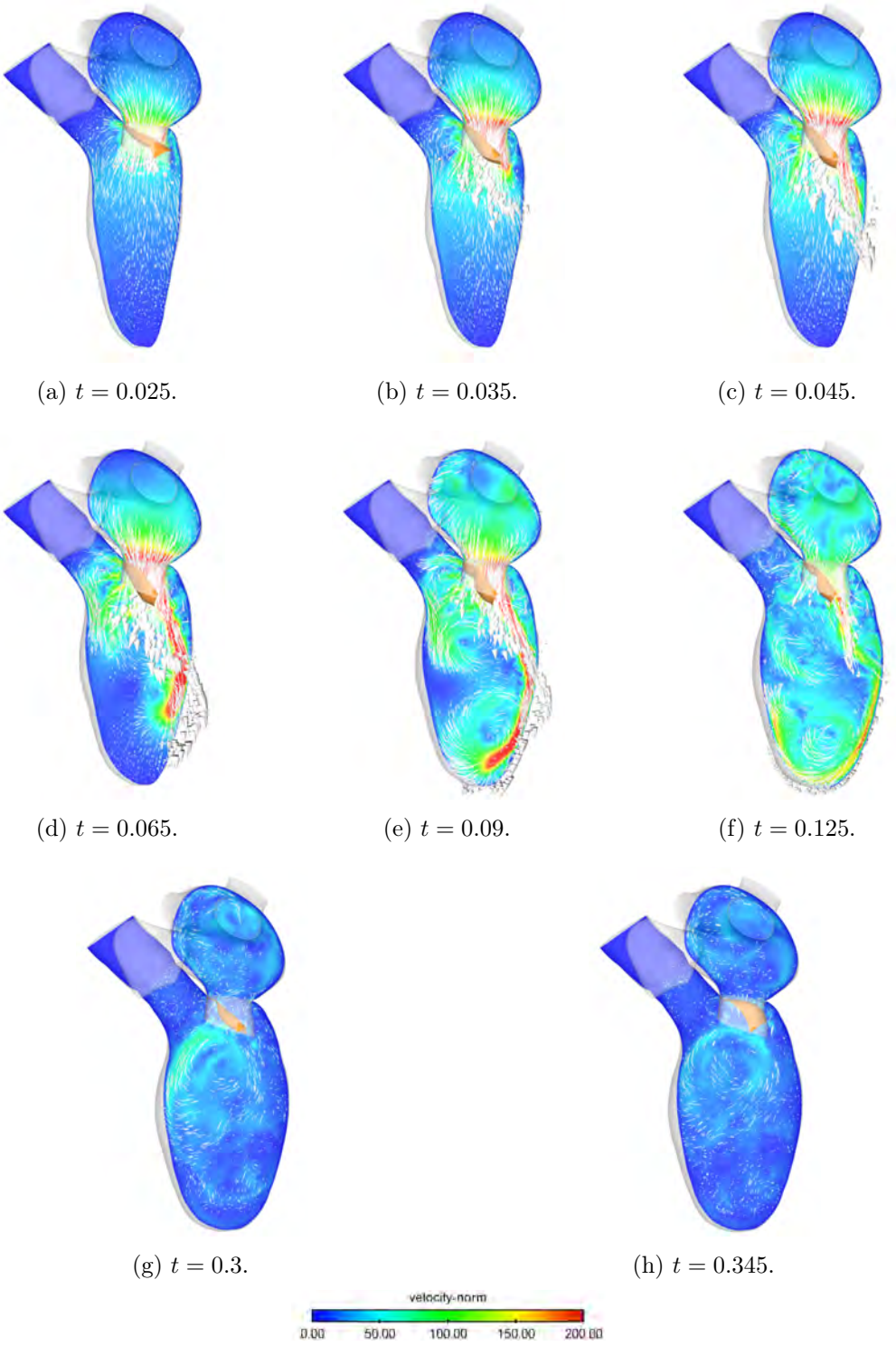

(a) $t = 0.025$. (b) $t = 0.035$. (c) $t = 0.045$.

(d) $t = 0.065$. (e) $t = 0.09$. (f) $t = 0.125$.

(g) $t = 0.3$. (h) $t = 0.345$.

Figure 7.13 – Snapshots of the fluid velocity field obtained at different instants for the case of the Epygon valve model.

Some snapshots of the deformations of the valve obtained from two points of view and at different instants are depicted in Figure 7.15. A change of convexity is gradually observed in the early moments of the numerical simulation (see Figure 7.15a). Its opening phase presents a fast dynamics as illustrated by the evolution of the displacement magnitude between $t = 0.025$ and $t = 0.035$ (see Figures 7.15a and 7.15b). Some of its widest opening configurations are illustrated in Figures 7.15d–7.15f. Various folds are observed at different instants (see Figures 7.15e–7.15g), which can be interpreted as illustrations of the elastic and thin nature of the leaflet. Then, the valve starts closing around $t = 0.3$ (see Figure 7.15g) and goes back to its initial concave state (see Figure 7.15h).

Finally, preliminary comparisons of several deformed configurations of the Epygon valve coming from numerical simulation and from experimentation are provided in Figure 7.16. In order to obtain these experimental results, the artificial valve has been placed in an *in silico* experimentation able to reproduce the left heart circulation flow dynamics thanks to a pulsed mock circulatory system (see [TBK+10]). Similar patterns can be observed between the two types of results at different instants (see Figures 7.16a–7.16c).

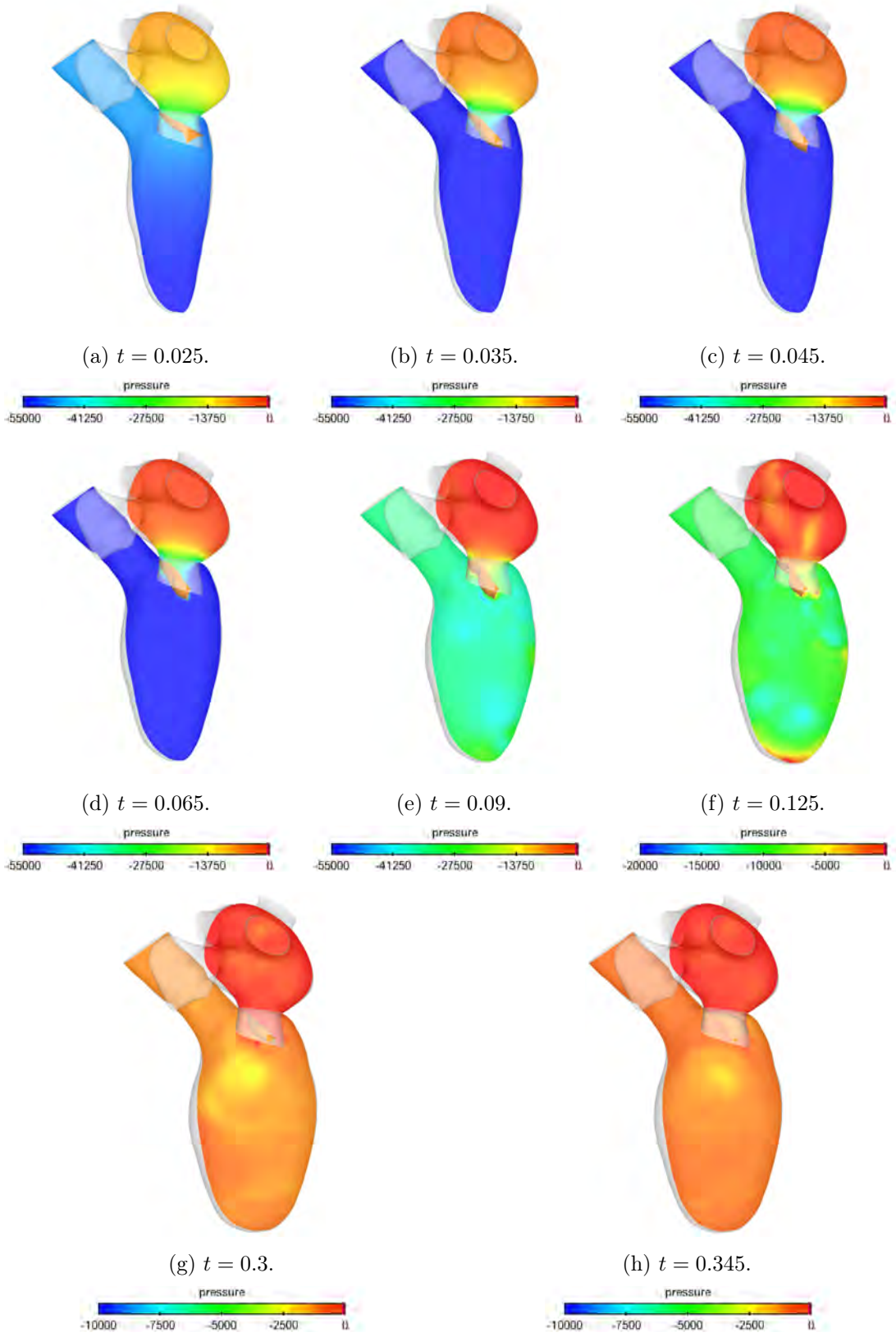

(a) $t = 0.025$. (b) $t = 0.035$. (c) $t = 0.045$.

(d) $t = 0.065$. (e) $t = 0.09$. (f) $t = 0.125$.

(g) $t = 0.3$. (h) $t = 0.345$.

Figure 7.14 – Snapshots of the pressure field obtained at different instants for the case of the Epygon valve model.

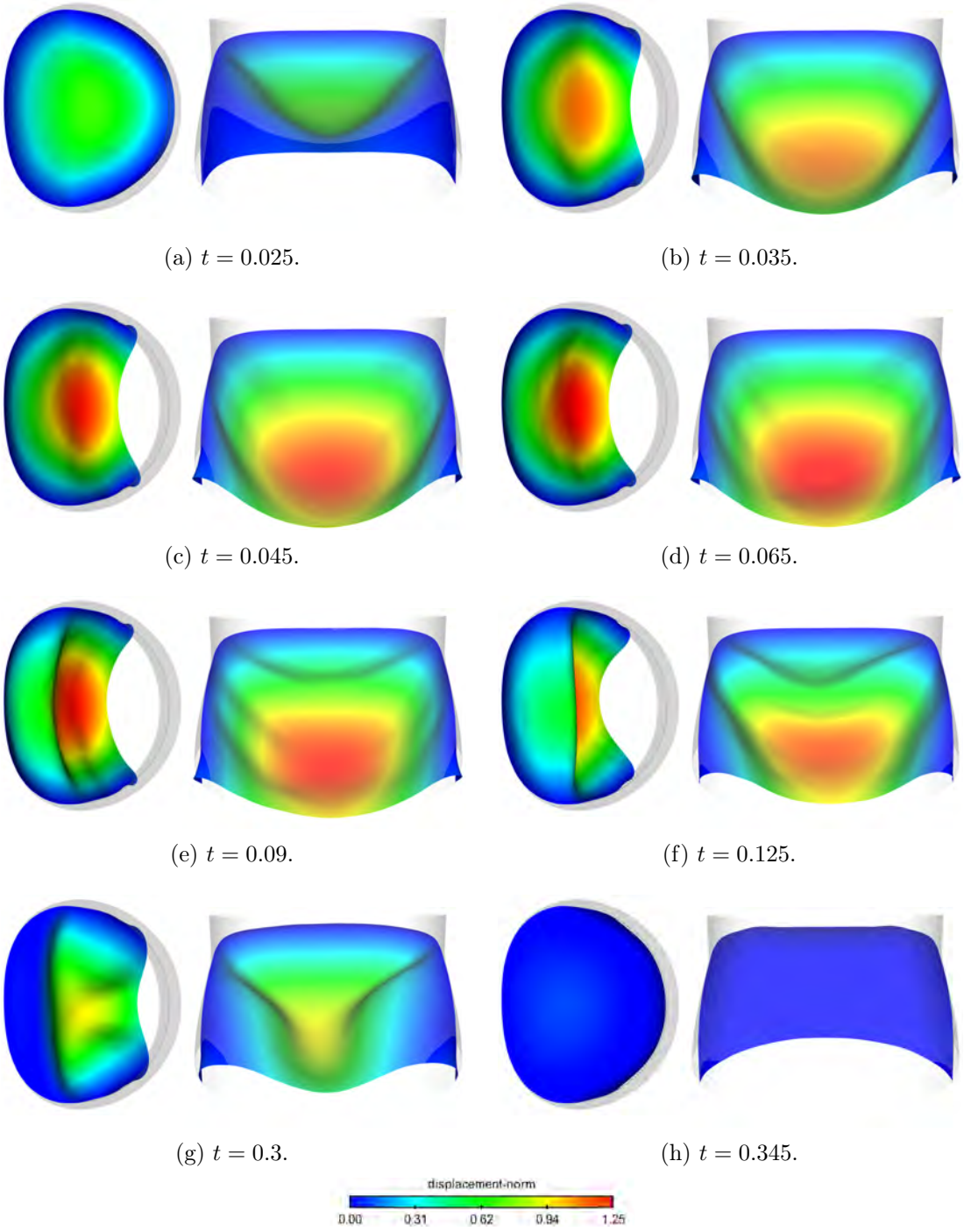

(a) $t = 0.025$. (b) $t = 0.035$.

(c) $t = 0.045$. (d) $t = 0.065$.

(e) $t = 0.09$. (f) $t = 0.125$.

(g) $t = 0.3$. (h) $t = 0.345$.

Figure 7.15 – Snapshots of the deformations of the valve from two points of view and at different instants, colored by displacement magnitude, for the case of the Epygon valve model.

(a) Open configuration.

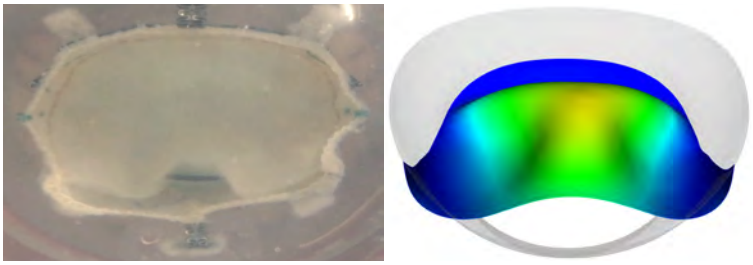

(b) Intermediate configuration.

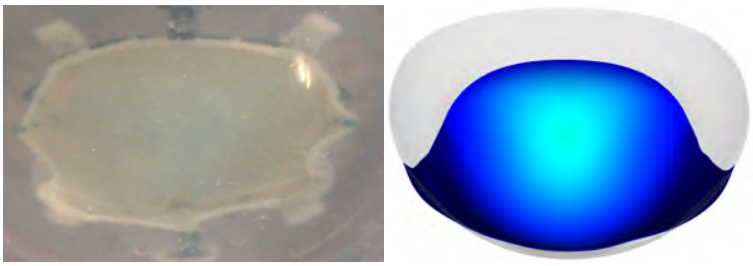

(c) Closed configuration.

Figure 7.16 – Comparisons of several deformed configurations of the Epygon valve obtained with, respectively, experimentation and numerical simulation.

7.4 Conclusions

In this chapter, we have applied the new explicit coupling scheme, developed in the context of the FD method in Chapter 6, on several 2D and 3D numerical simulations that included implantable cardiovascular devices modeled in a full FSI framework. Several fundamental results have been highlighted and we list some of them below:

- The working principle of the adjustable mitral ring from Kephalios for the treatment of MR has been numerically validated on a simplified 2D case of left heart.
- The implicit and explicit coupling schemes, respectively described by Algorithms 6.1 and 6.3, have been applied on a 3D case of aortic valve with contact. The computational time required to run the full simulation with the strongly coupled scheme was 15 times greater than the one obtained with the loosely coupled scheme.
- The Epygon valve has been modeled in a realistic 3D geometry of the left heart and the influence of its distortion on the computed intraventricular flow has been studied. Similarities with previous results obtained with the ARIS model have been highlighted. Moreover, the dynamics of its opening and closing phases has also been compared to preliminary experimental results where common patterns have been identified.

Nevertheless, two main limitations can however be mentioned. First, despite the clear superiority of the FD_{stab} method over the classical FD one for ensuring mass conservation across interfaces (as illustrated in detail in Chapter 5 for 2D cases), locking phenomena have been observed for the structures of the 3D examples. In order to avoid them, the classical FD method was used instead and further investigations are still required to understand their origins. Second, a non-physiological pressure profile has been used for the fluid-structure-contact simulation in the aortic valve. In spite of the improvements of the numerical implementation of the contact algorithm presented in Section 2.5.4.3, no convergence has been obtained for it when a physiological pressure profile has been used. This convergence issue has also been obtained in the case of the Epygon valve and therefore no contact has been considered in this case. Thus, due to these limitations, the 3D numerical experiments of this chapter are for the moment simply illustrative and should be only considered as a preliminary step towards realistic simulations of implantable cardiovascular devices.

General conclusion and perspectives

With recent major advances in mathematical modeling and computer technology, simulations in biomechanics, and notably in cardiac hemodynamics, can provide useful insights. A consequence of this is that the design of new experimental devices can now be assisted by such numerical tools resulting into a strong industrial and clinical interest.

This work was devoted to the modeling of implantable cardiovascular devices for the treatment of mitral regurgitation, common pathology of the mitral valve. The two main goals were to better understand (i) the influence of the valves (including the native mitral one and the common artificial ones implanted at the mitral position) on cardiac hemodynamics inside the left ventricle and (ii) the impacts of the annulus ring on mitral regurgitation. This thesis can be considered as a first step to reach these goals.

Each chapter of this thesis was ended with a dedicated conclusion. Therefore, in what follows, we establish a global conclusion before providing a general overview about possible axes of future work.

Simulation of intracardiac blood flow with a simplified model of valves

In Chapter 3, we have investigated the RIS model and we have illustrated its encountered difficulties when considering the numerical simulation of cardiac hemodynamics that include simplified cardiac valves and isovolumetric phases. An analysis of the intraventricular pressure during these phases has been provided, leading us to derive additional resistive corrective terms in the momentum equation of the fluid. These terms, whose definitions are based on pressure data coming from external electromechanical simulations, allow to circumvent the previously mentioned difficulties. Finally, the benefits of this pressure correction have been numerically illustrated on a simplified heart model.

In Chapter 4, several numerical simulations including implantable cardiovascular devices have been investigated with the RIS and ARIS models in order to illustrate their capabilities. In particular, the structure of intraventricular blood flow has been computed for different configurations of artificial valves implanted at the mitral position and has been compared to the physiological one. This study has highlighted the superiority of the D-shape monoleaflet valve on the commonly used bioprosthetic tricuspid valve when it comes to restoring a physiological blood flow in a context of mitral valve replacement.

Several limitations to the developed ARIS model can however be mentioned. First, a reference pressure data is required to use the resistive corrective terms. While obtainable in an uncoupled electromechanical/fluid framework, *in vivo* recovery of the intraventricular pressure by catheterization is an invasive procedure and might not always be feasible. Secondly, the ARIS model is based on a reduced valve model and therefore inherits from

all its limitations. In particular, we can mention the fact that the dynamics of the valve is not computed meaning that it instantaneously switches between its open and closed configurations, drastically simplifying reality. Last but not least, consequence of the previous remark, these simplified models cannot address more complex problems, such as mitral valve prolapse or the closing of a mechanical valve.

Simulation of intracardiac blood flow with a complete fluid-structure interaction model

In Chapter 5, we have compared three different unfitted and fitted mesh methods for immersed FSI (namely, the FD and the Nitsche-XFEM methods, belonging to the first group, and the ALE method, belonging to the second one) in a series of 2D benchmarks involving fully non-linear models and large interface deflections. The results of this study have emphasized that, for a given level of refinement, the best accuracy is obtained with the Nitsche-XFEM method. Also, in spite of the accuracy issues exhibited by the FD method and driven by its artificial interfacial mass losses, its alternative method FD_{stab}, obtained with the modification of the SUPG/PSPG and grad-div stabilizations near the interface, has provided very good results. Therefore, based on this study, the FD_{stab} method has been determined as the most appropriate method for the simulation of intracardiac blood flow with a complete fluid-structure interaction model.

In Chapter 6, we have introduced a new loosely coupled scheme for the FD method. Many benefits resulting from this explicit coupling scheme have been highlighted: (i) it preserves both the size and the sparsity pattern of the original fluid matrix and (ii) it circumvents the usual ill-conditioning issues of the FD methods (because no penalized approximation of the kinematic coupling is considered). Then, we have proved its unconditional stability in the energy norm, fundamental result not obtained by similar explicit approaches in other FSI settings. Finally, we have applied this new scheme to various 2D numerical examples and we have illustrated its very good performance, in terms of accuracy and robustness, by comparing it to strongly coupled unfitted approaches which are known to be much more computationally onerous. Therefore, based on these results, this loosely coupled scheme has been determined as the most appropriate scheme for the simulation of intracardiac blood flow with a complete fluid-structure interaction model.

In Chapter 7, we have applied the new explicit coupling scheme, developed in the context of the FD method in Chapter 6, on several numerical simulations that included implantable cardiovascular devices modeled in a full FSI framework. In particular, for the first time in this work, FSI simulations of cardiac hemodynamics in 3D cases, which were unachievable with the previous strongly coupled scheme because of computational efficiency, have been investigated with the explicit coupling scheme. Interesting results have been obtained from them. First, the working principle of the adjustable mitral ring from Kephalios has been numerically validated on a simplified 2D case of mitral valve. Then, a 3D case of fluid-structure-contact interaction phenomenon in the aortic valve has been computed. Finally, the Epygon valve has been modeled in a realistic 3D geometry of the left heart and the influence of its distortion on the computed intraventricular flow

has been studied. Similarities with previous results obtained with the ARIS model have been highlighted. Moreover, the dynamics of its opening and closing phases has also been compared to preliminary experimental results where common patterns have been identified.

While the FD_{stab} method and the explicit coupling scheme have been widely tested and validated in Chapters 5 and 6 on several academic and realistic 2D cases, the numerical experiments of Chapter 7 have highlighted several limitations when it comes to their extension to 3D. First, in addition of the previously studied ill-conditioning issues of the FD_{stab} method, locking effects, not existing in 2D, have been observed for the structures, preventing the proper use of this alternative method in 3D instead of the classic FD one. Secondly, the benefits of the explicit coupling scheme in terms of computational efficiency (by also taking into account its accuracy compared to strongly coupled reference solutions) have not been rigorously demonstrated in 3D and a detailed study, in the same vein as what has been done in Chapter 6 on 2D cases, must be carried on. Finally, for the sake of convergence of the contact algorithm, the pressure profiles used in 3D cases have been restricted to non-physiological values, much lower than the native ones.

Some ideas are provided in what follows in order to tackle all the above-mentioned issues and their associated limitations.

Perspectives

Based on the contributions and limitations mentioned above, several directions can be followed in future work. They are listed below in no particular order:

- An interesting extension of the results obtained with the ARIS model in Chapters 3 and 4 would be to compare them with the simulations coming from a complete FSI framework (in the spirit of what is done in [AHSG12] for the velocity field and for the evaluation of the effective orifice area index). This would allow to quantitatively evaluate the effects of the *one-way* uncoupling assumption on complex and physiological cases in order to assess if using this approximation does not distort the results too much compared to FSI.
- In Section 4.2.4, we have considered a simple modeling of mitral regurgitation (coming from [Ale19]) in the context of the RIS framework. Nevertheless, modeling the different types of mitral regurgitation (given by the Carpentier's functional classification in Section 1.4.2) is actually not straightforward as various differences are observed between healthy and regurgitant configurations (not only geometrical ones, but also ones related to the properties of the chordae tendineae). Therefore, a natural extension of this work consists in the modeling of mitral regurgitation in a full FSI framework. This would require to add the chordae tendineae (and possibly the papillary muscles) of the mitral valve (described in Section 1.2.2.4) in the Lagrangian description of the structures, as we did for the tendinous cords with the simplified 2D illustration of the Kephalios ring (see Section 7.3.1) but now extended to 3D. We refer the interested reader to various references in the literature for 3D modelings of this problem (see, e.g., [KEC07, KXL+18] and [TJE+16] in a context of, respectively, cables and fibers models assumptions).

- As already mentioned at the end of Chapter 5, another interesting approach in the context of the FD_{stab} method would be to circumvent its ill-conditioning problems, induced by the grad-div penalty near the interface, by considering an alternative approach for the control of its artificial interfacial mass losses. A possible solution would consist in removing the inconsistency of the pressure jumps across the structure. This could be done by considering lower-order mixed and stabilized $\mathbb{P}_1/\mathbb{P}_0$ finite elements whose pressure stabilization coefficient would vanish within a h-dependent vicinity of the interface. A preliminary discussion about this perspective is provided in Section 5.5.
- As mentioned in Section 7.4, the 3D numerical experiments of Chapter 7, where implantable cardiovascular devices are simulated in a complete FSI framework, are for the moment simply illustrative because of two main limitations. The first one, which is about the locking phenomenon (which has been observed for the structures when using the FD_{stab} method), could be solved with the previous item of this list. The other one, which is the non-convergence of the contact algorithm when considering physiological pressure profiles, needs further investigations. In particular, **Loop 2** of the contact algorithm, detailed in Section 2.5.4.2, could also benefit from a better numerical implementation as the one provided for **Loop 3** in Section 2.5.4.3.
- An interesting extension of the explicit coupling scheme developed in Chapter 6, in the context of the FD method for FSI coupling with immersed thin-walled solids, would be to extend it to the case of immersed thick-walled solids. A first attempt in this direction could be to combine the arguments of Chapter 6 with the ideas from [FMV15, BG17]. This is a particularly difficult problem, because the thick-walled nature of the solid is expected to harm the optimality of the time-splitting error, as it is the case for fitted meshes (see [FMV15, FM16]).
- In the spirit of what has been done in Chapters 5 and 6 for a benchmark of various 2D numerical examples, the comparison of the $\text{FD}/\text{FD}_{\text{stab}}$ methods with other references for unfitted meshes (in particular with the NXFEM method) could be extended to 3D. This would allow us to assess if the conclusions of Chapter 5 about the strengths and weaknesses of each method are still true in higher dimension. However, the extension of the considered NXFEM method to 3D presents several technical challenges which need to be addressed in future work (see, e.g., [ZVF18] and [Lan16]).
- An interesting further step of validation of our numerical methods would consist in confronting them with real experiments, in the spirit of the end of Section 7.3.3 or [LVCF17] in the context of the FSI forward prediction challenge. A preliminary work has been addressed towards this direction, in collaboration with the *Laboratoire de Biomécanique Appliquée* of the Aix-Marseille University[1], using an *in silico* experimentation able to reproduce the left heart circulation flow dynamics thanks to a pulsed mock circulatory system (see [TBK+10]). This experiment includes silicon molds of the different chambers of the left heart and of the cardiac valves while the

[1] Laboratoire de Biomécanique Appliqueée, Aix-Marseille Universiteé, IFSTTAR, LBA UMR T24, Marseille, France

pulmonary and systemic circulatory systems are represented with resistances and compliances. Very preliminary comparative studies between numerical results and experimental ones have been carried out (not presented in this work) and need to be further investigated.

- In Chapters 3, 4 and 7, we have considered data coming from external electromechanical simulations to enhance our fluid simulations (either as a boundary condition for the displacement field of the left ventricle surface or as an additional resistive term for the pressure correction in the ARIS model). The implicit assumption behind this approach is the *one-way* uncoupling between electromechanics and cardiac hemodynamics (meaning there is no feedback from the second solver on the first one). Therefore, a natural extension would be the full coupling between these two solvers in order to get a more in-depth physiological approach of the whole coupled physics of the left heart. This type of *two-way* coupling remains a very challenging topic in the current scientific literature, notably in terms of computational efficiency.

Appendix A

Geometry of the designed valve meshes

We present the different geometries of the valve meshes that we have used through this thesis: the native mitral valve, the native aortic valve, the bioprosthetic tricuspid valve and the D-shape monoleaflet valve from Epygon. When they are available, we also provide associated references and typical values about their geometrical characteristics.

A.1 Modeling the different geometries configurations

Depending on the framework adopted for the description of the cardiac valves (RIS or FSI models), two distinct situations appear for the modeling of the different configurations of the geometries of the valve:

- For the RIS framework: the closed and open configurations of the valve are both considered in the fluid mesh at the same time as immersed surfaces. Usually, starting from a given configuration (closed or open), the valve, immersed into a surrounding fluid, is arbitrary displaced in a FSI framework to distort it and to obtain the other corresponding configuration (open or closed).
- For the FSI framework: the valve is handled by a structure solver fully dedicated to it and is geometrically modeled in a given single configuration. Its starting configuration is chosen to be coherent with the initial conditions of the rest of the simulation and may be different from the open or closed configuration.

Illustrating all the different configurations considered for our designed valves would needlessly complicate this appendix. Therefore, in what follows, geometries of the different valve meshes are introduced and depicted in a single given configuration.

Moreover, as detailed in Section 2.2.1, the typical dimensions of the LV are slightly smaller than the ones coming from physiological data. Therefore, after that the further cardiac valves have been designed based on the following descriptions and references, they have been finally slightly reduced (with the use of a scale factor of 0.9 with the 3-matic[1] software) in order to fit the undersized LV.

A.2 Native mitral valve

Figure A.1 represents the geometry of the native mitral valve we have considered through this work.

[1] See https://www.materialise.com/.

(a) Top view. (b) Profile view. (c) Frontal view.

Figure A.1 – Representation of the geometry of the native mitral valve mesh.

This geometry has been designed using physiological data coming from the literature. Values of physical quantities we have used for the modeling of the native mitral valve are given in Table A.1.

Physical quantity	Value	References
Anterior leaflet height	2.22 cm	[RLWS70, RSE52, TL+16]
Anterior leaflet width	3.38 cm	[RLWS70, CLT56]
Posterior leaflet P1 height	0.98 cm	[RLWS70, RSE52, TL+16]
Posterior leaflet P1 width	1.28 cm	[RLWS70, CLT56]
Posterior leaflet P2 height	1.28 cm	[RLWS70, RSE52, TL+16]
Posterior leaflet P2 width	2.90 cm	[RLWS70, CLT56]
Posterior leaflet P3 height	0.98 cm	[RLWS70, RSE52, TL+16]
Posterior leaflet P3 width	1.28 cm	[RLWS70, CLT56]
Commisural height	0.75 cm	[RLWS70, CLT56, RSE52]
Commisural width	1.00 cm	[RLWS70, CLT56]
Closed anterior leaflet - mitral plane angle	0.12 rad	[OGJ+98]
Open anterior leaflet - mitral plane angle	1.01 rad	[WAN+14, OGJ+98]
Mitral annulus perimeter	10.82 cm	[BDC+15, VCV+08, N+16]
Mitral annulus area	8.44 cm^2	[BDC+15, TL+16, N+16]
Aortic plane - mitral plane angle	2.27 rad	[TL+16]
Inter-commisural distance	3.5 cm	[TL+16, N+16]

Table A.1 – Values of the physical quantities relative to the native mitral valve.

A.3 Aortic valve

Figure A.2 represents the geometry of the native aortic valve we have considered through this work.

(a) Top view. (b) Profile view. (c) Frontal view.

Figure A.2 – Representation of the geometry of the native aortic valve mesh.

This geometry comes from previous works whose some anatomical characteristics can be found in [AGPT09, Ast10].

A.4 Bioprosthetic tricuspid valve

Figure A.3 represents the geometry of the bioprosthetic tricuspid valve we have considered through this work.

(a) Top view. (b) Profile view. (c) Frontal view.

Figure A.3 – Representation of the geometry of the bioprosthetic tricuspid valve mesh.

This geometry has been designed based on those presented in [KLSC08, KHS+15] in the context of bioprosthetic heart valves. It has been then sightly rescaled to have a similar size compared to the other native valves.

A.5 Epygon valve – D-shape monoleaflet valve

Figure A.4 represents the geometry of the D-shape monoleaflet valve from Epygon we have considered through this work.

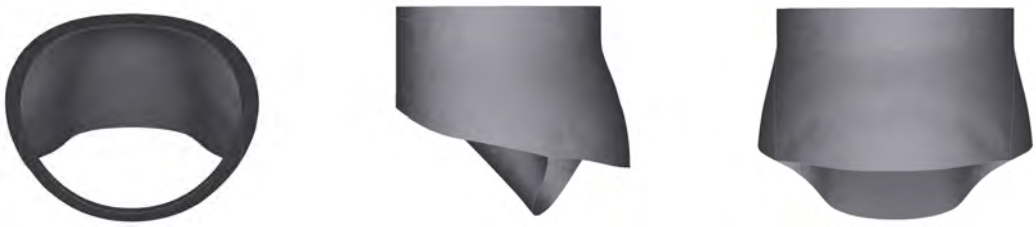

(a) Top view. (b) Profile view. (c) Frontal view.

Figure A.4 – Representation of the geometry of the D-shape monoleaflet valve mesh from Epygon. The single leaflet is enclosed in a surrounding stent.

This geometry has been directly provided by Epygon and then no references or values of geometrical characteristics will be provided here. The only remark which can be made is that its spatial characteristics (meaning, e.g., height and width) are very similar to those of the native mitral valve in order to be able to reproduce physiological blood flow as detailed in Section 1.5.3.

Appendix B

An overview of electromechanical simulations

We present additional information about the electromechanical simulations used in the context of the numerical examples of Chapters 3, 4 and 7. The electrical and mechanical models are quickly introduced before presenting others results, in addition of the pressure and displacements values used as boundary conditions in the above-mentioned chapters.

As detailed in Chapter 1, the heart wall is made of three layers: the pericardium, the myocardium and the endocardium. We refer to Section 1.2.2.3 for a description of their substructures and properties. Here, the different characteristics and roles played by these layers are recalled: protection, lubrication, resistance to fatigue and stress, and, in particular, muscular activity coordinated by electrical activity. Any mathematical description whose purpose is to model the heart wall must then take into account all these phenomena.

B.1 A simplified FSI model of the heart

A simplified FSI model of the heart can be split into three different main components [SMCCS06, CFG+09, CLMS12]: the electrical activity of the heart-torso, the mechanical model of the muscles and the cardiovascular blood compartments. All the related equations are given in [CFG+09] and only the general ideas are discussed here. For the sake of completeness, we also refer to [HPS03] for a general overview of the main cardiac modeling issues. In what follows, the three above components are detailed:

- The electrical activity of the heart-torso. It is modeled by bidomain equations for the heart [SLC+07] and by a Laplace equation for the torso. This model aims to simulate the genesis of the myocardial activation sequence and to study the process of generation of the body surface potentials which are responsible for the generation of the ElectroCardioGraphy (ECG) [Zem09].
- The mechanical model of the muscles. It is based on excitation-contraction laws of myofibres (controlled by chemical reactions) integrated in the 3D continuum mechanics description [SMCCS06] and based on Huxley's model [Hux57]. The model combines an active law, based on a chemically-controlled constitutive law of cardiac myofibre mechanics [BCS01], and a passive component which relies on the hyperelastic and viscoelastic laws [CFG+09].
- The cardiovascular blood compartments. They are represented by adequate Windkessel models [SMCCS06].

As regards the coupling between the different models, the standard approach of electromechanical modeling is considered here. It consists in an *one-way* uncoupling where the results coming from the electrical activity are used as inputs in the mechanical simulations but without considering any feedback from the mechanics on the electrophysiology [SMCCS06, CFG+09]. Blood also needs to be considered to get a whole coherent simulation between electromechanics and cardiac hemodynamics. Then, in these simulations, blood compartments are modeled as simplified lumped models, separated by resistive valves. Each of these valves is characterized by an operating curve $(Q, \Delta P)$ where Q is the flow rate through it and ΔP the pressure difference between the two compartments separated by the considered valve. This operating curve is very similar to the one of a realistic diode [Moi08] and is the main responsible of the regulation of the simplified 0D model of blood between the chambers of the LH.

The combination of these three interlinked models allow to obtain accurate numerical descriptions of the main electromechanical phenomena. In addition, these simulations provide meaningful medical indicators (pressures, volumes, ...) which, for some of them, are not easily accessible by the measurement (e.g., local values of the stresses in cardiac tissue), highlighting their benefits.

B.2 Electromechanical simulations

In the sequel, standard geometries and meshes, on which these electromechanical simulations are based on, are depicted before providing snapshots of typical associated results (displacement, velocity, electrical activation, ...).

B.2.1 Geometries and meshes

Figure B.1 represents the computational domains considered for the electromechanical simulations. Note that the RH is also present in these simulations even if it is not considered into the further simulations of cardiac hemodynamics.

(a) Side view. (b) Top view.

Figure B.1 – Representation of the computational domain considered for the electromechanical simulations.

As mentioned in Section 4.2.1, the upper part of the ventricle surface slightly varies when considering different types of mitral valve in order to fit the corresponding annulus,

inducing slight differences in the final electromechanical 3D meshes.

B.2.2 Typical results

Figure B.2 depicts various typical results coming from a standard electromechanical simulation. This case has been carried out for a total time of $t = 2.55$, based on averaged physiological values for three full heartbeats, with adaptive time-stepping where the maximum allowed time-step is $\tau = 10^{-3}$.

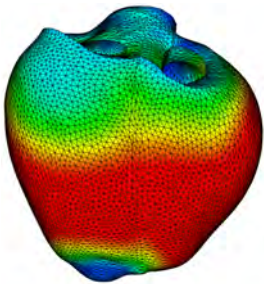

(a) Displacement magnitude – Side view.

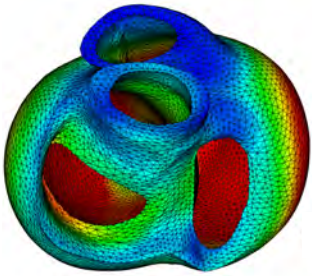

(b) Displacement magnitude – Top view.

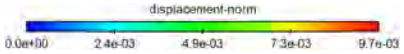

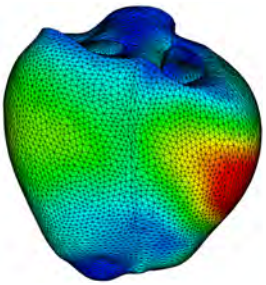

(c) Velocity field – Side view.

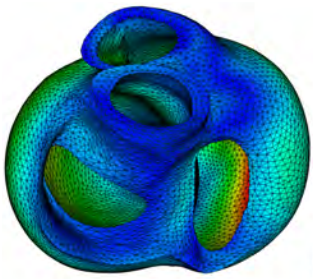

(d) Velocity field – Top view.

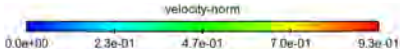

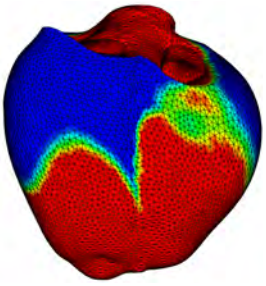

(e) Electrical potential – Side view.

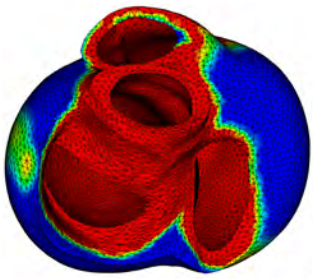

(f) Electrical potential – Top view.

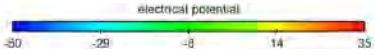

Figure B.2 – Various typical results coming from the electromechanical simulation of several heartbeats at $t = 1.07$. All the units are expressed in the SI system.

Moreover, based on our needs, we might choose to let the mitral annulus unfixed (as it is done in Chapters 3 and 4 for the RIS simulations) or to fix it (as it is done in Chapter 7 for the FSI simulations). The electromechanical results slightly differ when the annulus is fixed: globally, it is observed that the LH is a little more stressed during its distortion, inducing small increases for the computed pressures in the chambers (but nevertheless $< 1\%$ compared to the unfixed case) and a global displacement field where the upper part of the ventricle is less contracted during the systole.

B.2.3 Extraction of results to improve the simulations of cardiac hemodynamics

Based on our needs, the displacement field on the LV surface is of crucial interest and represents the information that needs to be extracted and to be used as a boundary condition in the simulations of cardiac hemodynamics. Figure B.3 represents the matching of the displacement field of the LV surface between the electromechanical and the cardiac hemodynamics simulations.

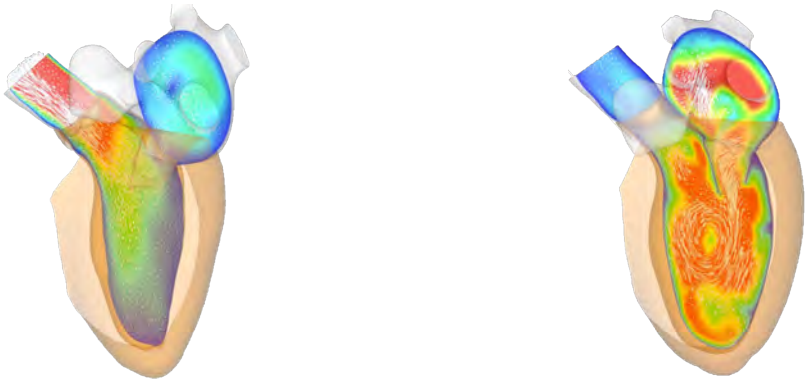

(a) Late systole. (b) Late diastole.

Figure B.3 – Representation of the matching of the displacement field of the LV between the electromechanical and the cardiac hemodynamics simulations at the end of each characteristic phase of a heartbeat. The electromechanical domain is colored in light orange (only the left heart has been represented here) and the fluid domain is colored with the velocity field associated to the flow.

In addition, 0D pressures coming from the simplified lumped models of the different blood compartments of the LH (atrium, ventricle and aorta) are also extracted and used as boundary conditions in the corresponding chambers of the fluid mesh, as detailed in the numerical examples of Chapters 3, 4 and 7.

B.2.4 Model parameters

The values of various model parameters used in the electromechanical simulations are given in Table B.1. All the values are expressed in SI units, unless specified otherwise. For

the purpose of illustration, the cross section of the computational domain considered for the electromechanical simulations is depicted in Figure B.4.

Table B.1 – Model parameters used in the electromechanical simulations.

Quantity	Value
Transient	
Maximum time-step	10^{-3}
Minimum time-step	10^{-6}
Scale factor applied when divergence	0.5
Duration of a heartbeat	0.85
Total time of the simulation	2.55
Mesh	
X-coordinates – bounding box	$[-19.49\,\text{mm}, 58.46\,\text{mm}]$
Y-coordinates – bounding box	$[77.80\,\text{mm}, 174.31\,\text{mm}]$
Z-coordinates – bounding box	$[-9.11\,\text{mm}, 80.29\,\text{mm}]$
Number of triangles	34 457
Number of tetrahedra	247 041
Electrical activation	
Maximum amplitude	35
Minimum amplitude	-50
Depolarization duration	0.005
Repolarization duration	0.5
Cardiac law (active law)	
Damping parallel (μ)	70
Series stiffness (Es)	$3 \cdot 10^7$
Destruction rate (α)	1.5
Crossbridge stiffness (k_0)	$1 \cdot 10^5$
Contractility – left ventricle (σ_0)	$3.1 \cdot 10^5$
Contractility – right ventricle (σ_0)	$3.72 \cdot 10^5$
Cardiac law (passive law)	
Hyperelastic potential (W_e)	$W_{e,1} + W_{e,2} + W_{e,3} + W_{e,4}$
$W_{e,1}$	$\mu_1(J_1 - 3)$
$W_{e,2}$	$\mu_2(J_2 - 3)$
$W_{e,3}$	$C_0 e^{(C_1(J_1-3)^2)} + C_2 e^{(C_3(J_4-1)^2)}$

Continued from previous page

Quantity	Value
$W_{e,4}$	$K(J_3 - 1 - \ln(J_3))$
μ_1, μ_2	0
C_0, C_2 – mitral valve region	$1 \cdot 10^7$
C_0, C_2 – aortic valve region	$1 \cdot 10^6$
C_0, C_2 – Base of the LV	$28.5 \cdot 10^3$
C_0, C_2 – Right & Left cavity	$5.7 \cdot 10^3$
C_1, C_3	$1.1 \cdot 10^{-1}$
Hyperelastic bulk (K)	$2 \cdot 10^5$
Lamé (μ)	$2\ (C_0 + C_1)$
Lamé (λ)	K - $[4(C_0 + C_1)]/3$
Young's modulus (E)	$[\mu(3\lambda + 2\mu)]\ /(\lambda + \mu)$
Poisson's ratio (ν)	$\lambda/\ [2(\lambda + \mu)]$
Viscosity (η)	70
Solid	
Volumic mass	10^3
Pressures of the left cavity	
Venous pressure	1000
Initial cavity pressure	500
Initial arterial pressure	11000
Initial distal pressure	11000
Windkessel models of the left cavity	
Capacitance – left proximal Windkessel (C)	$1.6 \cdot 10^{-9}$
Resistance – left proximal Windkessel (R_p)	$1.3 \cdot 10^7$
Capacitance – left distal Windkessel (C_d)	$6.06 \cdot 10^{-9}$
Resistance – left distal Windkessel (R_d)	$1.725 \cdot 10^8$
Valve law in the left cavity	
Atrial conductance (K_1 – K_{at})	$9 \cdot 10^{-6}$
Closed conductance (K_2 – K_{iso})	$5 \cdot 10^{-10}$
Arterial conductance (K_3 – K_{ar})	$1.3 \cdot 10^{-5}$
Atrial capacitance (C_{fm})	$5 \cdot 10^{-12}$
Closed capacitance (C_{fi})	$5 \cdot 10^{-12}$
Arterial capacitance (C_{fa})	$5 \cdot 10^{-12}$
Valve resistance (R_c)	$7.69 \cdot 10^4$

Continued from previous page

Quantity	Value
Pressures of the right cavity	
Venous pressure	1000
Initial cavity pressure	25
Initial arterial pressure	1000
Initial distal pressure	1000
Windkessel models of the right cavity	
Capacitance – right proximal Windkessel (C)	$2 \cdot 10^{-10}$
Resistance – right proximal Windkessel (R_p)	$1 \cdot 10^{7}$
Capacitance – right distal Windkessel (C_d)	$1 \cdot 10^{-8}$
Resistance – right distal Windkessel (R_d)	$3 \cdot 10^{7}$
Valve law in the right cavity	
Atrial conductance (K_1 – K_{at})	$9 \cdot 10^{-6}$
Closed conductance (K_2 – K_{iso})	$5 \cdot 10^{-12}$
Arterial conductance (K_3 – K_{ar})	$1.0 \cdot 10^{-5}$
Atrial capacitance (C_{fm})	$5 \cdot 10^{-12}$
Closed capacitance (C_{fi})	$5 \cdot 10^{-12}$
Arterial capacitance (C_{fa})	$5 \cdot 10^{-12}$
Valve resistance (R_c)	$1 \cdot 10^{5}$
Visco-elastic boundary conditions	
Damping – upper left cavity	$3 \cdot 10^{4}$
Damping – other contracting surfaces	$1 \cdot 10^{4}$
Stiffness – upper left cavity	$9.5 \cdot 10^{6}$
Stiffness – other contracting surfaces	$1 \cdot 10^{6}$

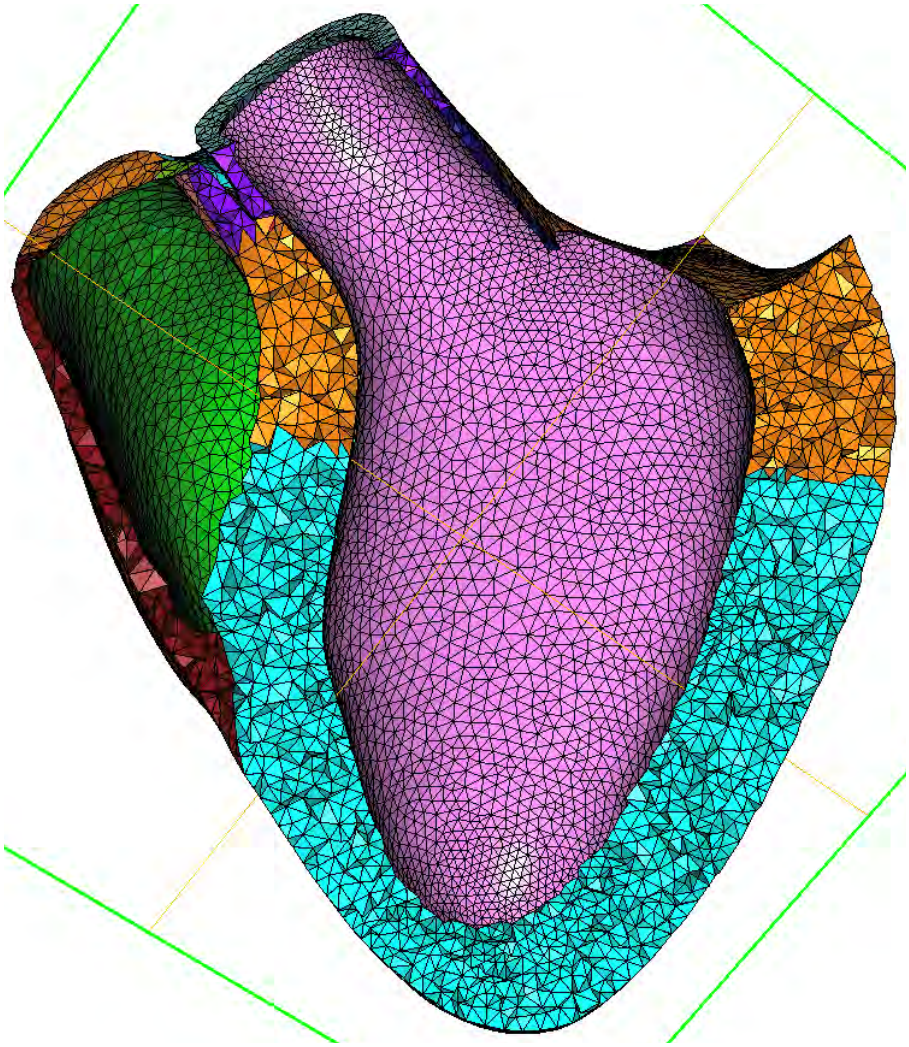

Figure B.4 – Cross section of the computational domain used in the electromechanical simulations. The tetrahedra have been colored according to the sub-region they have been assigned to. The surface colored in pink is the LV endorcardial surface that is in common with the fluid simulations.

Acknowledgements: These electromechanical models have been provided by D. Chapelle, P. Moireau, R. Chabiniok, G. Bureau and others, from the M3DISIM Inria project-team[1]. In addition, our colleagues have supported us with the electromechanical simulations and are thanked here.

[1]M3DISIM aims at proposing novel mathematical and numerical methods and tools in the realm of the biomechanical modeling of tissues and organs, with a non-exclusive focus on the cardiovascular system.

Appendix C

Mathematical modeling of cardiac valves

We present the derivation of the thin-walled solid models introduced in Section 2.5.1.2. For this purpose, we follow the presentation proposed in [Lan16]: starting from the general elastodynamics equations, the different models of interest for the mathematical modeling of cardiac valves are described and their inherent assumptions are also highlighted and discussed.

The content of this appendix is inspired from [FFGQ09, Ast10, CB11, Lan16].

In what follows, an overview of the models dedicated to the description of the cardiac valves, cornerstones of this thesis, are given. For this purpose, a general three-dimensional elastic model, commonly referred to as elastodynamics equations, is introduced. Then, the thin-walled solid models, valid under some assumptions and commonly encountered in cardiac hemodynamics, are presented. All these models are in general characterized by complex highly non-linear mechanical behaviors, as described in the sequel.

C.1 The elastodynamics equations

In what follows, $\Omega^s(t)$ represents a solid bounded time-dependent domain of $\mathbb{R}^d$, where $d = 2$ or 3, occupied by an elastic material governed by the general d-dimensional non-linear elastodynamics equations. This domain possesses a Lipschitz continuous boundary, denoted $\partial\Omega^{\mathrm{s}}(t)$, and an oriented exterior normal, denoted $\boldsymbol{n}^{\mathrm{s}}$. The symbol t represents the physical time.

Moreover, we assume that $\Omega^s(t)$ is parametrized by a smooth, injective and orientation preserving mapping $\boldsymbol{\phi}$ defined as

$$\boldsymbol{\phi} : \widehat{\Omega^{\mathrm{s}}} \times \mathbb{R}^+ \to \mathbb{R}^d, \quad (\widehat{\boldsymbol{x}}, t) \to \boldsymbol{x} = \boldsymbol{\phi}(\widehat{\boldsymbol{x}}, t),$$

where $\widehat{\Omega^{\mathrm{s}}}$ is the reference fixed configuration such that $\widehat{\Omega^{\mathrm{s}}} = \boldsymbol{\phi}(\widehat{\Omega^{\mathrm{s}}}, 0) = \Omega^{\mathrm{s}}(0)$ and $\Omega^{\mathrm{s}}(t) = \boldsymbol{\phi}(\widehat{\Omega^{\mathrm{s}}}, t)$, for all $t \in \mathbb{R}^+$.

In terms of notation, we will use $\boldsymbol{d}$ for the solid displacement defined as $\boldsymbol{d}(\widehat{\boldsymbol{x}}, t) \overset{\text{def}}{=} \boldsymbol{\phi}(\widehat{\boldsymbol{x}}) - \widehat{\boldsymbol{x}}$, for $(\widehat{\boldsymbol{x}}, t) \in \widehat{\Omega^{\mathrm{s}}} \times \mathbb{R}^+$. We also use $\boldsymbol{\phi}_t \overset{\text{def}}{=} \boldsymbol{\phi}(\cdot, t)$ for the solid deformation, $\boldsymbol{F}^{\mathrm{s}} \overset{\text{def}}{=} \boldsymbol{\nabla}\boldsymbol{\phi}_t$ for the associated solid deformation gradient and $J^{\mathrm{s}} \overset{\text{def}}{=} \det \boldsymbol{F}^{\mathrm{s}}$ for the associated Jacobian.

The non-linear elastodynamics equations in the Lagrangian frame read: find the solid displacement $\boldsymbol{d} : \widehat{\Omega^{\mathrm{s}}} \times \mathbb{R}^+ \to \mathbb{R}^d$ and the velocity $\dot{\boldsymbol{d}} : \widehat{\Omega^{\mathrm{s}}} \times \mathbb{R}^+ \to \mathbb{R}^d$, such that

$$\begin{cases} \rho^{\mathrm{s}} \partial_t \dot{\boldsymbol{d}} - \boldsymbol{\nabla} \cdot \boldsymbol{\Pi}(\boldsymbol{d}, \dot{\boldsymbol{d}}) = \boldsymbol{f}^{\mathrm{s}} & \text{in } \widehat{\Omega^{\mathrm{s}}}, \\ \dot{\boldsymbol{d}} = \partial_t \boldsymbol{d} & \text{in } \widehat{\Omega^{\mathrm{s}}}, \end{cases} \tag{C.1}$$

where ρ^{s} represents the solid density and $\boldsymbol{\Pi} \overset{\text{def}}{=} J^{\mathrm{s}}\boldsymbol{\sigma}^{\mathrm{s}}(\boldsymbol{F}^{\mathrm{s}})^{-\mathrm{T}}$ the first Piola-Kirchhoff stress tensor of the structure, where $\boldsymbol{\sigma}^{\mathrm{s}}$ is the solid Cauchy stress tensor. $\boldsymbol{f}^{\mathrm{s}}$ is a body force, function of space and time, and is assumed to be equal to $\mathbf{0}$ when not specified.

Remark C.1
Unlike the solid Cauchy stress tensor $\boldsymbol{\sigma}^{\mathrm{s}}$, the first Piola-Kirchhoff stress tensor of the structure $\boldsymbol{\Pi}$ is non-symmetric. Since, it is better and easier to express the constitutive laws in terms of symmetric stress tensors, we naturally introduce the second Piola-Kirchhoff stress tensor of the structure $\boldsymbol{\Sigma}$ defined as

$$\boldsymbol{\Sigma} \overset{\text{def}}{=} (\boldsymbol{F}^{s})^{-1}\boldsymbol{\Pi} = J^{s}(\boldsymbol{F}^{s})^{-1}\boldsymbol{\sigma}^{s}(\boldsymbol{F}^{s})^{-T}, \tag{C.2}$$

which is symmetric.

By using (C.2), problem (C.1) can be reformulated as: find the solid displacement $\boldsymbol{d} : \widehat{\Omega^{\mathrm{s}}} \times \mathbb{R}^{+} \to \mathbb{R}^{d}$ and the velocity $\dot{\boldsymbol{d}} : \widehat{\Omega^{\mathrm{s}}} \times \mathbb{R}^{+} \to \mathbb{R}^{d}$, such that

$$\begin{cases} \rho^{\mathrm{s}}\partial_t\dot{\boldsymbol{d}} - \boldsymbol{\nabla}\cdot(\boldsymbol{F}^{\mathrm{s}}\boldsymbol{\Sigma}(\boldsymbol{d},\dot{\boldsymbol{d}})) = \boldsymbol{f}^{\mathrm{s}} & \text{in} \quad \widehat{\Omega^{\mathrm{s}}}, \\ \dot{\boldsymbol{d}} = \partial_t\boldsymbol{d} & \text{in} \quad \widehat{\Omega^{\mathrm{s}}}. \end{cases} \tag{C.3}$$

The problems (C.1) and (C.3) have to be completed with initial conditions:

$$\begin{cases} \boldsymbol{d}(0) = \boldsymbol{d}_0 & \text{in} \quad \Omega^{\mathrm{s}}(0), \\ \dot{\boldsymbol{d}}(0) = \dot{\boldsymbol{d}}_0 & \text{in} \quad \Omega^{\mathrm{s}}(0) \end{cases} \tag{C.4}$$

and with boundary conditions on $\partial\Omega^{\mathrm{s}}(t)$. For instance, the following homogeneous Dirichlet condition may be prescribed:

$$\boldsymbol{d} = \mathbf{0} \quad \text{on} \quad \widehat{\partial\Omega^{\mathrm{s}}}. \tag{C.5}$$

Note that other boundary conditions for $\boldsymbol{d}$ (named Dirichlet) exist and that boundary conditions for $\boldsymbol{\Sigma}$ (named Neumann) can also be considered (see, e.g., [Ast10, Lan16]).

Many constitutive laws (i.e., relations between $\boldsymbol{\Sigma}(\boldsymbol{d},\dot{\boldsymbol{d}})$ and both variables $\boldsymbol{d}$ and $\dot{\boldsymbol{d}}$) can be devised for a solid. For a hyperelastic framework, which is the most common approach (see, e.g., [Gur81, Cia88, LT94]), we have the following relation:

$$\boldsymbol{\Sigma}(\boldsymbol{E}) = \frac{\partial W}{\partial \boldsymbol{E}}(\boldsymbol{E}),$$

where $\boldsymbol{E}$, defined by

$$\boldsymbol{E} \overset{\text{def}}{=} \frac{1}{2}((\boldsymbol{F}^{\mathrm{s}})^{\mathrm{T}}\boldsymbol{F}^{\mathrm{s}} - \boldsymbol{I}), \tag{C.6}$$

stands for the Green-Lagrange strain tensor and $W : \mathbb{R}^{d\times d} \to \mathbb{R}^{+}$ is the density of elastic energy of the solid.

A simple example of such W is given by the Saint Venant-Kirchhoff three-dimensional

elastic model (common assumption made for a homogeneous isotropic material), where

$$W(\boldsymbol{E}) = \frac{L_1}{2}(\mathrm{tr}(\boldsymbol{E}))^2 + L_2(\mathrm{tr}(\boldsymbol{E}^2)). \tag{C.7}$$

Consequently, we obtain the generalized Hooke's law, given by

$$\boldsymbol{\Sigma}(\boldsymbol{E}) = L_1(\mathrm{tr}(\boldsymbol{E}))\boldsymbol{I} + 2L_2\boldsymbol{E} \tag{C.8}$$

and simply obtained by deriving (C.7) with respect to $\boldsymbol{E}$.

In (C.7) and (C.8), L_1 and L_2 denote the Lamé coefficients of the material. Due to their easier physical interpretation, the Young's modulus E and the Poisson ratio ν are generally preferred, as these quantities are directly measured from experiments, which is not the case for L_1 and L_2. All these quantities are related via the following relations:

$$L_1 = \frac{E\nu}{(1-2\nu)(1+\nu)}, \quad L_2 = \frac{E}{2(1+\nu)}$$

and, conversely,

$$E = L_2\frac{3L_1+2L_2}{L_1+L_2}, \quad \nu = \frac{1}{2}\frac{L_1}{L_1+L_2}.$$

Finally, another common assumption consists in linearizing this Saint Venant-Kirchhoff elastic model (valid in the context of infinitesimal deformations). Within this assumption, the previous solid Cauchy stress tensor $\boldsymbol{\sigma}^{\mathrm{s}}$ is approximated by

$$\boldsymbol{\sigma}^{\mathrm{s}}(\boldsymbol{d},\dot{\boldsymbol{d}}) = 2L_1(\mathrm{tr}(\boldsymbol{\varepsilon}(\boldsymbol{d})))\boldsymbol{I} + 2L_2\boldsymbol{\varepsilon}(\boldsymbol{d}),$$

where the linearized strain tensor $\boldsymbol{\varepsilon}(\boldsymbol{d})$ is the approximation of the previous Green-Lagrange strain tensor $\boldsymbol{E}$ and is given by

$$\boldsymbol{\varepsilon}(\boldsymbol{d}) \overset{\mathrm{def}}{=} \frac{1}{2}(\boldsymbol{\nabla d} + \boldsymbol{\nabla d}^{\mathrm{T}}). \tag{C.9}$$

C.2 Thin-walled solid models

Only the main ideas of shell theory are detailed here and we refer to [Bat96, BBWR04, CB11] for more general introductions about this topic. Moreover, for the sake of simplicity, the following derivation is only presented here in the frame of the linear theory of shells (meaning that only infinitesimal deformations are described by this approach). These small displacements are clearly not satisfactory for the study of cardiac valves (where large displacements may occur) and non-linear shell models are actually used in Chapters 5, 6 and 7 and in the FSI models described in Section 2.5. Nevertheless, this assumption of linearity ensures a clear introduction of thin-walled solid models. We refer to [LS05, CB11] for texts introducing the mathematical theory of non-linear shells.

In the context of co-dimensional one structures, we consider that the solid reference configuration $\widehat{\Omega^{\mathrm{s}}}$ (previously introduced in the section dedicated to the elastodynamics equations) is now defined by its mid-surface Σ and by a constant thickness $\epsilon > 0$. Its

boundary is denoted $\partial\Sigma$. Moreover, we assume we are working in 3D hence $d = 3$. In the sequel, Greek indexes take values in $\{1,2\}$ and Latin indexes in $\{1,2,3\}$. The Einstein summation convention for repeating indices is adopted.

We start by defining the chart $\boldsymbol{\psi}$ as

$$\boldsymbol{\psi} : \omega \subset \mathbb{R}^2 \to \mathbb{R}^3, \quad (\xi_1,\xi_2) \to \boldsymbol{\psi} = \boldsymbol{\psi}(\xi_1,\xi_2),$$

that parametrizes the solid reference mid-surface $\Sigma = \boldsymbol{\psi}(\omega)$, as pictured in Figure C.1. The local covariant basis is given by $(\boldsymbol{a}_1,\boldsymbol{a}_2)$, with $\boldsymbol{a}_\alpha = \partial_\alpha \boldsymbol{\psi} = \dfrac{\partial \boldsymbol{\psi}}{\partial \xi_\alpha}$, where $\alpha = \{1,2\}$. The corresponding contravariant basis is denoted by $(\boldsymbol{a}^1,\boldsymbol{a}^2)$ and the normal unit vector is defined as

$$\boldsymbol{a}_3 \overset{\text{def}}{=} \frac{\boldsymbol{a}_1 \times \boldsymbol{a}_2}{|\boldsymbol{a}_1 \times \boldsymbol{a}_2|},$$

as depicted in Figure C.1.

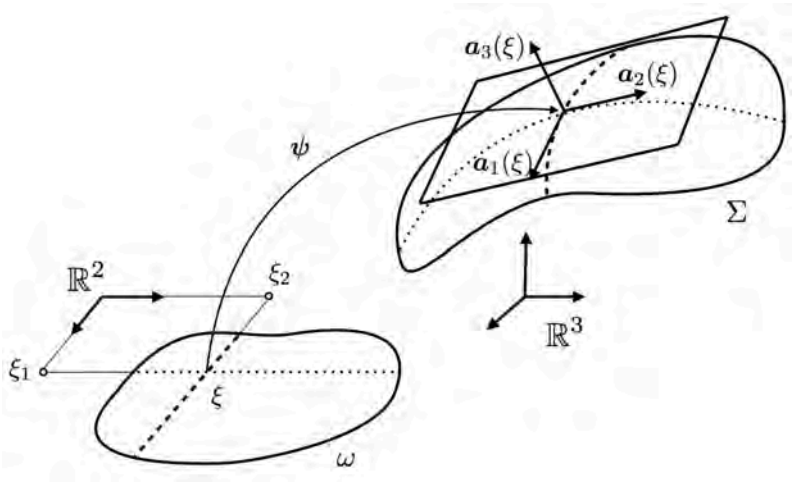

Figure C.1 – Geometric description of the chart $\boldsymbol{\psi}$ and its local covariant basis $\{\boldsymbol{a}_1,\boldsymbol{a}_2,\boldsymbol{a}_3\}$. Image from [Lan16].

Based on the theory of differential geometry, the first fundamental form $a_{\alpha\beta}$ is defined by $a_{\alpha\beta} \overset{\text{def}}{=} \boldsymbol{a}_\alpha \cdot \boldsymbol{a}_\beta$ and its corresponding inverse $a^{\alpha\beta}$ by $a^{\alpha\beta} \overset{\text{def}}{=} \boldsymbol{a}^\alpha \cdot \boldsymbol{a}^\beta$. Acting on the same principle, the second and third fundamental forms, $b_{\alpha\beta}$ and $c_{\alpha\beta}$, are defined, respectively, by $b_{\alpha\beta} \overset{\text{def}}{=} \boldsymbol{a}_3 \cdot \partial_\alpha \boldsymbol{a}_\beta$ and $c_{\alpha\beta} \overset{\text{def}}{=} b_{\alpha\gamma} b^\gamma_\beta$, where $b^\gamma_\beta = a^{\gamma\lambda} b_{\lambda\beta}$. Given a vector field $\boldsymbol{q} = \boldsymbol{q}(\xi_1,\xi_2)$ on the mid-surface Σ, we denote by $q_{\alpha|\beta}$ the surface covariant derivative of its covariant component q_α, defined as $q_{\alpha|\beta} \overset{\text{def}}{=} \partial_\beta q_\alpha - \Gamma^\lambda_{\alpha\beta} q_\lambda$, where $\Gamma^\lambda_{\alpha\beta} = \boldsymbol{a}_\alpha \cdot \partial_\beta \boldsymbol{a}_\beta$ denote Christoffel symbols (see, e.g., [CB11]). Finally, based on the chart $\boldsymbol{\psi}$ represented in Figure C.1, we define the 3D medium corresponding to the shell with the following mapping:

$$\boldsymbol{\Psi} : \Theta \subset \mathbb{R}^3 \to \mathbb{R}^3, \quad (\xi_1,\xi_2,\xi_3) \to \boldsymbol{\Psi}(\xi_1,\xi_2,\xi_3) = \boldsymbol{\psi}(\xi_1,\xi_2) + \xi_3 \boldsymbol{a}_3(\xi_1,\xi_2),$$

where $\Theta \overset{\text{def}}{=} \left\{ (\xi_1,\xi_2,\xi_3) \in \mathbb{R}^3 \middle/ (\xi_1,\xi_2) \in \omega, \quad \xi_3 \in \left[-\frac{\epsilon}{2}, \frac{\epsilon}{2}\right] \right\}$. The reference configuration

$\widehat{\Omega^{\mathrm{s}}}$ (also known as the undeformed configuration) is assumed to be parametrized by $\boldsymbol{\Psi}$, i.e., $\widehat{\Omega^{\mathrm{s}}} = \boldsymbol{\Psi}(\Theta)$.

In general, mathematical shell models assume that any material line orthogonal to the reference mid-surface remains straight and unstretched during deformation. This hypothesis is known as the Reissner-Mindlin kinematical assumption [Rei45, Min51]. Therefore, the displacement $\boldsymbol{D}$ of a point of coordinates (ξ_1,ξ_2,ξ_3) belonging to the shell can be expressed by

$$\boldsymbol{D}(\xi_1,\xi_2,\xi_3) \overset{\text{def}}{=} \boldsymbol{d}(\xi_1,\xi_2) + \xi_3\theta_\lambda(\xi_1,\xi_2)\boldsymbol{a}^\lambda(\xi_1,\xi_2). \tag{C.10}$$

REMARK C.2

In terms of physical interpretation, based on Figure C.1, the Reissner-Mindlin kinematical assumption describes a material line in the direction of $\boldsymbol{a}_3$ at the coordinates (ξ_1,ξ_2). $\boldsymbol{d}(\xi_1,\xi_2)$ and $\theta_\lambda(\xi_1,\xi_2)$ represent, respectively, the displacement of the mid-surface Σ and the rotation of a line normal to this mid-surface Σ [FFGQ09].

Based on the above remark, we define the rotation vector around the normal to the mid-surface Σ, denoted $\boldsymbol{\theta}$, as $\boldsymbol{\theta}(\xi_1,\xi_2) \overset{\text{def}}{=} \theta_\lambda(\xi_1,\xi_2)\boldsymbol{a}^\lambda(\xi_1,\xi_2)$. Hence, (C.10) can be reformulated as

$$\boldsymbol{D}(\xi_1,\xi_2,\xi_3) = \boldsymbol{d}(\xi_1,\xi_2) + \xi_3\boldsymbol{\theta}(\xi_1,\xi_2), \tag{C.11}$$

meaning that the unknowns we must determine to fully describe the displacement field of the shell are the displacement of the mid-surface $\boldsymbol{d}$ and the rotation vector $\boldsymbol{\theta}$ in the deformed configuration. Note that $\boldsymbol{\theta}$ correspond to the material line in the reference configuration.

Assuming (C.11), a general elastic thin-walled solid is described by: find the solid displacement $\boldsymbol{d} : \Sigma \times \mathbb{R}^+ \to \mathbb{R}^3$ and the rotation vector $\boldsymbol{\theta} : \Sigma \times \mathbb{R}^+ \to \mathbb{R}^3$, such that

$$\begin{cases} \rho^{\mathrm{s}}\epsilon\partial_t\dot{\boldsymbol{d}} + \boldsymbol{L}_{\boldsymbol{d}}(\boldsymbol{d},\boldsymbol{\theta}) = \boldsymbol{T} & \text{on} \quad \Sigma, \\ \boldsymbol{L}_{\boldsymbol{\theta}}(\boldsymbol{d},\boldsymbol{\theta}) = \boldsymbol{0} & \text{on} \quad \Sigma, \\ \dot{\boldsymbol{d}} = \partial_t\boldsymbol{d} & \text{on} \quad \Sigma, \end{cases} \tag{C.12}$$

where $\boldsymbol{T}$ denotes a given source term (e.g., a force per unit area) and the surface operators $(\boldsymbol{L}_{\boldsymbol{d}},\boldsymbol{L}_{\boldsymbol{\theta}})$ represent the strong formulation of the thin-solid elastic contributions. $(\text{C.12})_1$ and $(\text{C.12})_2$ represent, respectively, the equation for the displacement $\boldsymbol{d}$ and for the rotation $\boldsymbol{\theta}$. The velocity $\dot{\boldsymbol{d}}$ is obtained with $(\text{C.12})_3$. The problem (C.12) has to be completed with initial conditions:

$$\begin{cases} \boldsymbol{d}(0) = \boldsymbol{d}_0 & \text{on} \quad \Sigma, \\ \dot{\boldsymbol{d}}(0) = \dot{\boldsymbol{d}}_0 & \text{on} \quad \Sigma, \\ \boldsymbol{\theta}(0) = \boldsymbol{\theta}_0 & \text{on} \quad \Sigma \end{cases} \tag{C.13}$$

and with boundary conditions (e.g., on $\boldsymbol{d}$ and/or on $\boldsymbol{\theta}$) on $\partial\Sigma$.

Remark C.3
As usually assumed in the theory of shell dynamics, the rotational inertial term (represented by the unknown $\dot{\boldsymbol{\theta}}$) has been neglected in problem (C.12). We refer to [CB11] for more complex models including such considerations. Also, other models taking into account viscosity and known as viscoelastic thin-walled models exist but do not belong to the scope of this work (see, e.g., [Lan16]).

The above (assumed linear) strong formulation of the thin-solid elastic contributions admit the following decomposition:

$$\begin{aligned} \boldsymbol{L_d}(\boldsymbol{d},\boldsymbol{\theta}) &\overset{\text{def}}{=} \boldsymbol{A_d}\boldsymbol{d} + \boldsymbol{B_d}\boldsymbol{\theta}, \\ \boldsymbol{L_\theta}(\boldsymbol{d},\boldsymbol{\theta}) &\overset{\text{def}}{=} \boldsymbol{B_\theta}\boldsymbol{d} + \boldsymbol{A_\theta}\boldsymbol{\theta}. \end{aligned} \tag{C.14}$$

As mentioned above, $\boldsymbol{L_d}$ and $\boldsymbol{L_\theta}$ describe the elastic behaviour of the beam, with $\boldsymbol{L_\theta}(\boldsymbol{d},\boldsymbol{\theta}) = \boldsymbol{0}$ representing, in particular, the bending moments and shear stresses equilibrium.

In order to explicit the operators $\boldsymbol{A_d}, \boldsymbol{A_\theta}, \boldsymbol{B_d}$ and $\boldsymbol{B_\theta}$ involved in (C.14), we must refer to the constitutive laws specifying the relationship between stresses and strains. As we are currently handling a general linearized shell model, the strain measures are given by the linearized strain tensor (C.9). The components ε of this tensor corresponding to the displacement $\boldsymbol{D}$, defined in (C.11), are given, in curvilinear coordinates, by

$$\begin{aligned} \varepsilon_{\alpha\beta} &= \gamma_{\alpha\beta}(\boldsymbol{d}) + \xi_3\chi_{\alpha\beta}(\boldsymbol{d},\boldsymbol{\theta}) - \xi_3^2\kappa_{\alpha\beta}(\boldsymbol{\theta}), \\ \varepsilon_{\alpha 3} &= \zeta_\alpha(\boldsymbol{d},\boldsymbol{\theta}), \\ \varepsilon_{33} &= 0, \end{aligned} \tag{C.15}$$

where

$$\begin{aligned} \gamma_{\alpha\beta}(\boldsymbol{d}) &= \frac{1}{2}(d_{\alpha|\beta} + d_{\beta|\alpha}) - b_{\alpha\beta}d_3, \\ \chi_{\alpha\beta}(\boldsymbol{d},\boldsymbol{\theta}) &= \frac{1}{2}(\theta_{\alpha|\beta} + \theta_{\beta|\alpha} - b_\beta^\lambda d_{\lambda|\alpha} - b_\alpha^\lambda d_{\lambda|\beta}) + b_{\alpha\beta}d_3, \\ \kappa_{\alpha\beta}(\boldsymbol{\theta}) &= \frac{1}{2}(b_\beta^\lambda\theta_{\lambda|\alpha} + b_\alpha^\lambda\theta_{\lambda|\beta}), \\ \zeta_\alpha(\boldsymbol{d},\boldsymbol{\theta}) &= \frac{1}{2}(\theta_\alpha + \partial_\alpha d_3 + b_\alpha^\lambda d_\lambda). \end{aligned} \tag{C.16}$$

The quantities $\gamma_{\alpha\beta}(\boldsymbol{d})$, $\chi_{\alpha\beta}(\boldsymbol{d},\boldsymbol{\theta})$ and $\zeta_\alpha(\boldsymbol{d},\boldsymbol{\theta})$ represent, respectively, the covariant components of the membrane, the bending and the shear strain tensors of the shell (see, e.g., [CB11] for further details).

As usual in shell modeling, because of the small thickness ϵ (which is the case for cardiac valves), we make the further assumption of plane stresses (i.e., zero stresses along the normal direction). The stress-strain relationship is given by Hooke's law and the associated equations governing the dynamics of a shell are easier to write directly using the weak formulation. For the sake of simplicity, in the sequel, we only provide the equations

of the model resulting from this assumption. We refer to [FFGQ09] for the details of its derivation.

In what follows, the scalar product in $L^2(\omega)$ is denoted by $(\cdot,\cdot)_\omega$ and its norm by $\|\cdot\|_{0,\omega}$ with ω being a given domain or surface in $\mathbb{R}^3$. The new formulation, resulting from the above assumption of plane stresses, is directly and naturally obtained from the basic shell model discussed above by truncating the higher order terms in the transverse coordinate ξ_3 and by integrating with respect to ξ_3 (see [CB11] for the details). We obtain the following model, known as the shear-membrane-bending model:

$$\begin{aligned}\rho^s\epsilon\big(\partial_t\dot{\boldsymbol{d}},\boldsymbol{w}\big)_\Sigma+\epsilon\big(C^{\alpha\beta\lambda\xi}\gamma_{\alpha\beta}(\boldsymbol{d}),\gamma_{\lambda\xi}(\boldsymbol{w})\big)_\Sigma+\frac{\epsilon^3}{12}\big(C^{\alpha\beta\lambda\xi}\chi_{\alpha\beta}(\boldsymbol{d},\boldsymbol{\theta}),\chi_{\lambda\xi}(\boldsymbol{w},\boldsymbol{\vartheta})\big)_\Sigma\\ +\epsilon\big(D^{\alpha\lambda}\zeta_\alpha(\boldsymbol{d},\boldsymbol{\theta}),\zeta_\lambda(\boldsymbol{w},\boldsymbol{\vartheta})\big)_\Sigma=\big(\boldsymbol{T},\boldsymbol{w}\big)_\Sigma,\end{aligned}\tag{C.17}$$

with the arbitrary test functions $(\boldsymbol{w},\boldsymbol{\vartheta})$ being equal to 0 on $\partial\Sigma$ and the coefficients $C^{\alpha\beta\lambda\xi}$ and $D^{\alpha\lambda}$ defined by

$$C^{\alpha\beta\lambda\xi}\overset{\text{def}}{=}\frac{E}{2(1+\nu)}\left(a^{\alpha\lambda}a^{\beta\xi}+a^{\alpha\xi}a^{\beta\lambda}+\frac{2\nu}{1-\nu}a^{\alpha\beta}a^{\lambda\xi}\right)\quad\text{and}\quad D^{\alpha\lambda}\overset{\text{def}}{=}\frac{2E}{1+\nu}a^{\alpha\lambda}.$$

Finally, in this framework of shear-membrane-bending model, the abstract operators introduced in (C.14) are given by

$$\begin{aligned}\big(\boldsymbol{A_d}\boldsymbol{d},\boldsymbol{w}\big)_\Sigma&=\epsilon\big(C^{\alpha\beta\lambda\xi}\gamma_{\alpha\beta}(\boldsymbol{d}),\gamma_{\lambda\xi}(\boldsymbol{w})\big)_\Sigma+\frac{\epsilon^3}{12}\big(C^{\alpha\beta\lambda\xi}\chi_{\alpha\beta}(\boldsymbol{d},\boldsymbol{0}),\chi_{\lambda\xi}(\boldsymbol{w},\boldsymbol{0})\big)_\Sigma\\ &\quad+\epsilon\big(D^{\alpha\lambda}\zeta_\alpha(\boldsymbol{d},\boldsymbol{0}),\zeta_\lambda(\boldsymbol{w},\boldsymbol{0})\big)_\Sigma,\\ \big(\boldsymbol{B_d}\boldsymbol{\theta},\boldsymbol{w}\big)_\Sigma&=\frac{\epsilon^3}{12}\big(C^{\alpha\beta\lambda\xi}\chi_{\alpha\beta}(\boldsymbol{0},\boldsymbol{\theta}),\chi_{\lambda\xi}(\boldsymbol{w},\boldsymbol{0})\big)_\Sigma+\epsilon\big(D^{\alpha\lambda}\zeta_\alpha(\boldsymbol{0},\boldsymbol{\theta}),\zeta_\lambda(\boldsymbol{w},\boldsymbol{0})\big)_\Sigma,\\ \big(\boldsymbol{B_\theta}\boldsymbol{d},\boldsymbol{\vartheta}\big)_\Sigma&=\frac{\epsilon^3}{12}\big(C^{\alpha\beta\lambda\xi}\chi_{\alpha\beta}(\boldsymbol{d},\boldsymbol{0}),\chi_{\lambda\xi}(\boldsymbol{0},\boldsymbol{\vartheta})\big)_\Sigma+\epsilon\big(D^{\alpha\lambda}\zeta_\alpha(\boldsymbol{d},\boldsymbol{0}),\zeta_\lambda(\boldsymbol{0},\boldsymbol{\vartheta})\big)_\Sigma,\\ \big(\boldsymbol{A_\theta}\boldsymbol{\theta},\boldsymbol{\vartheta}\big)_\Sigma&=\frac{\epsilon^3}{12}\big(C^{\alpha\beta\lambda\xi}\chi_{\alpha\beta}(\boldsymbol{0},\boldsymbol{\theta}),\chi_{\lambda\xi}(\boldsymbol{0},\boldsymbol{\vartheta})\big)_\Sigma+\epsilon\big(D^{\alpha\lambda}\zeta_\alpha(\boldsymbol{0},\boldsymbol{\theta}),\zeta_\lambda(\boldsymbol{0},\boldsymbol{\vartheta})\big)_\Sigma.\end{aligned}\tag{C.18}$$

Proposition C.1
As regards the operators $\boldsymbol{A_d}$, $\boldsymbol{A_\theta}$, $\boldsymbol{B_d}$ and $\boldsymbol{B_\theta}$, the following equalities hold:

$$(\boldsymbol{A_d})^T=\boldsymbol{A_\theta}\quad\text{and}\quad(\boldsymbol{B_d})^\dagger=\boldsymbol{B_\theta},$$

where $\dagger$ is the adjoint operator.

Proof. The proof is left to the reader. □

Remark C.4
The derivation of problem (C.12), introduced above, has been presented in the linear framework, where the different considered unknowns were the displacement $\boldsymbol{d}$, the velocity $\dot{\boldsymbol{d}}$ and the rotation $\boldsymbol{\theta}$. For the sake of completeness, we now introduce it within the non-linear framework, allowing the description of large displacements [Bat96, CB11]. In

order to differentiate the equations between the two frameworks, the previous rotation vector $\boldsymbol{\theta}$ is now replaced by the director vector $\boldsymbol{a}$ with unit length (i.e., $|\boldsymbol{a}| = 1$). In addition, the equations are now given for the general dimension d.

Finally, based on the previous remark, the shear-membrane-bending model (C.12), resulting from the initial problem (C.3) simplified with the thin-walled solid assumption and with the Reissner-Mindlin kinematical assumption (C.11) and extended to the non-linear framework, will be the model of reference for the description of the cardiac valves in this work. This model is described by (2.12): find the solid mid-surface displacement $\boldsymbol{d} : \Sigma \times \mathbb{R}^+ \to \mathbb{R}^d$, the solid mid-surface velocity $\dot{\boldsymbol{d}} : \Sigma \times \mathbb{R}^+ \to \mathbb{R}^d$ and the director vector $\boldsymbol{a} : \Sigma \times \mathbb{R}^+ \to \mathbb{R}^d$ with unit length (i.e., $|\boldsymbol{a}| = 1$), such that

$$\begin{cases} \rho^{\mathrm{s}} \epsilon \partial_t \dot{\boldsymbol{d}} + \boldsymbol{L}_{\boldsymbol{d}}(\boldsymbol{d},\boldsymbol{a}) = \boldsymbol{T} & \text{on} \quad \Sigma, \\ \boldsymbol{L}_{\boldsymbol{a}}(\boldsymbol{d},\boldsymbol{a}) = \boldsymbol{0} & \text{on} \quad \Sigma, \\ \dot{\boldsymbol{d}} = \partial_t \boldsymbol{d} & \text{on} \quad \Sigma, \end{cases} \tag{C.19}$$

The problem (C.19) has to be completed with initial conditions:

$$\begin{cases} \boldsymbol{d}(0) = \boldsymbol{d}_0 & \text{on} \quad \Sigma, \\ \dot{\boldsymbol{d}}(0) = \dot{\boldsymbol{d}}_0 & \text{on} \quad \Sigma, \\ \boldsymbol{a}(0) = \boldsymbol{a}_0 & \text{on} \quad \Sigma \end{cases} \tag{C.20}$$

and with boundary conditions (e.g., on $\boldsymbol{d}$ and/or on $\boldsymbol{a}$) on $\partial\Sigma$.

Appendix D

Convergence study of the penalty parameter ε

We present additional numerical results about the convergence study made in the context of the strongly coupled FD method (and of the FD_{stab} alternative method when considered) with respect to the penalty parameter ε, for the different numerical examples investigated through Chapters 5 and 6.

D.1 Open valve from Section 5.4.1 – Idealized valve without contact from Section 6.5.1

Figures D.1a–D.1c represent the convergence study of the penalty parameter ε for the case of the open valve for, respectively, the three different levels of refinement M_1, M_2 and M_3, defined in associated Section 5.4.1. The physical value of interest here is the total displacement magnitude of the immersed upper leaflet tip. All the units are expressed in the CGS system.

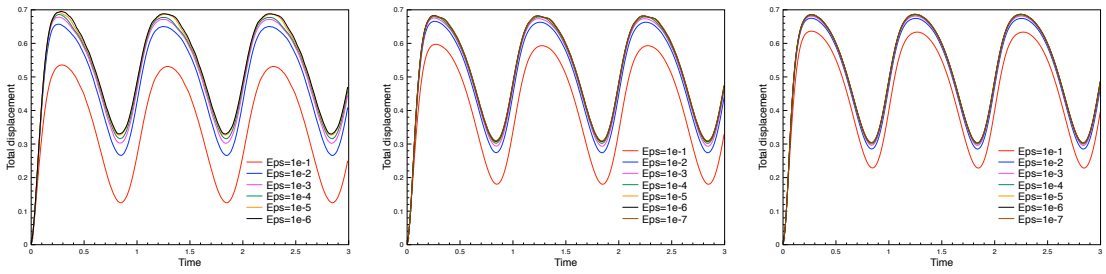

(a) M_1. (b) M_2. (c) M_3.

Figure D.1 – Convergence study of the penalty parameter ε for the case of the open valve.

For this case, the convergence with respect to ε is clear and justifies our choices of considering $\varepsilon = 10^{-5}$, $\varepsilon = 10^{-6}$ and $\varepsilon = 10^{-6}$, respectively, for the three levels of refinement M_1, M_2 and M_3.

Note that the above study has been realized for the case of the open valve considered in Section 5.4.1 where three different levels of temporal and spatial refinements have been considered. In the case of the idealized valve without contact considered in Section 6.5.1, the refinement is only temporal and the discretization in space is fixed and corresponds to the one used in the above refinement M_2. However, the same typical behavior of the convergence study of the penalty parameter ε, depicted in Figures D.1a–D.1c for the open

valve, is also obtained for the idealized valve without contact. In the latter case, we consider $\varepsilon = 10^{-5}$ for the three levels of time-step refinement.

D.2 Closed valve from Section 5.4.2

Figures D.2a–D.2c represent the convergence study of the penalty parameter ε for the case of the closed valve for, respectively, the three different levels of refinement M_1, M_2 and M_3, defined in associated Section 5.4.2. The physical value of interest here is the x-displacement magnitude of the valve mid-point. All the units are expressed in the CGS system.

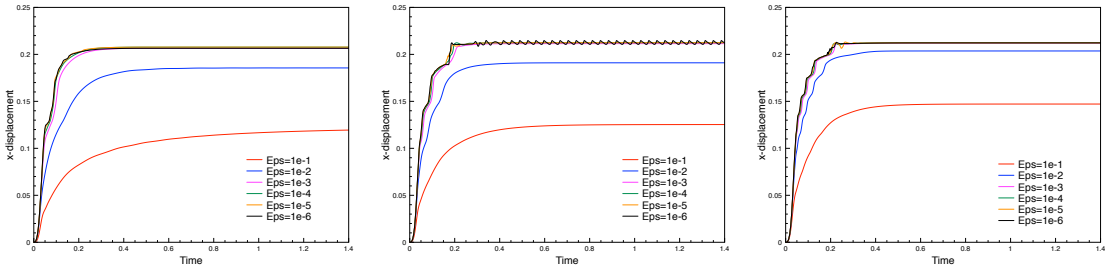

(a) M_1. (b) M_2. (c) M_3.

Figure D.2 – Convergence study of the penalty parameter ε for the case of the closed valve.

For this case, the convergence with respect to ε is clear and justifies our choices of considering $\varepsilon = 10^{-5}$ for the three levels of refinement M_1, M_2 and M_3.

D.3 Vesicle in lid-driven cavity flow from Section 5.4.3

Figures D.3a–D.3c represent the convergence study of the penalty parameter ε for the case of the vesicle in lid-driven cavity flow for, respectively, the three different levels of refinement M_1, M_2 and M_3, defined in associated Section 5.4.3. The physical value of interest here is the total displacement magnitude of the bottom of the vesicle. All the units are expressed in the CGS system.

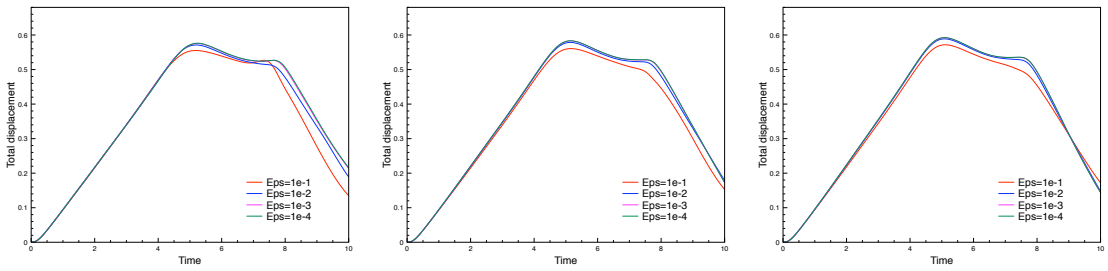

(a) M_1. (b) M_2. (c) M_3.

Figure D.3 – Convergence study of the penalty parameter ε for the case of the vesicle in lid-driven cavity flow.

For this case, the convergence with respect to ε is clear and justifies our choices of considering $\varepsilon = 10^{-4}$ for the three levels of refinement M_1, M_2 and M_3.

D.4 Idealized valve with contact from Section 6.5.2

Figures D.4a–D.4a represent the convergence study of the penalty parameter ε for the case of the idealized valve with contact for, respectively, the three different levels of refinement M_1, M_2 and M_3, defined in associated Section 6.5.2. The physical value of interest here is the y-displacement magnitude of the immersed upper leaflet tip. All the units are expressed in the CGS system.

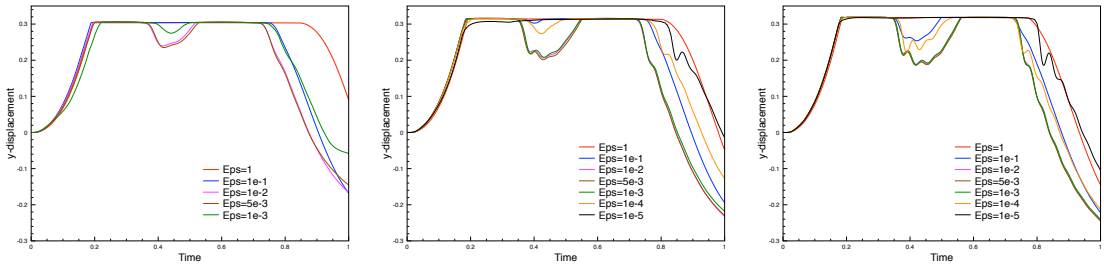

(a) M_1. (b) M_2. (c) M_3.

Figure D.4 – Convergence study of the penalty parameter ε for the case of the idealized valve with contact.

For this specific case with contact, the convergence with respect to ε is not clear and results are extremely sensitive to the choice of its value, no matter which level of refinement is considered. A clear convergence behavior seems to be obtained until $\varepsilon = 5 \cdot 10^{-3}$ but then degrades when ε keeps increasing. This observation justifies to rather consider the strongly coupled Nitsche-XFEM method as the reference solution for the comparisons of results reported in Section 6.5.2.

Appendix E

Neighborhood of the interface for the modification of the stabilizations with the $\mathrm{FD}_{\mathrm{stab}}$ method

We present additional figures illustrating the neighborhood ω_h^n of the interface Σ_h^n considered in the context of the strongly coupled and loosely coupled FD_{stab} method, for the different numerical examples investigated through Chapters 5, 6 and 7.

E.1 Closed valve from Section 5.4.2

Figures E.1a–E.1c represent the neighborhood ω_h^n of the interface Σ_h^n, considered in the context of the $\mathrm{FD}_{\mathrm{stab}}$ method and for the case of the closed valve, for, respectively, the three different levels of refinement M_1, M_2 and M_3, defined in associated Section 5.4.2.

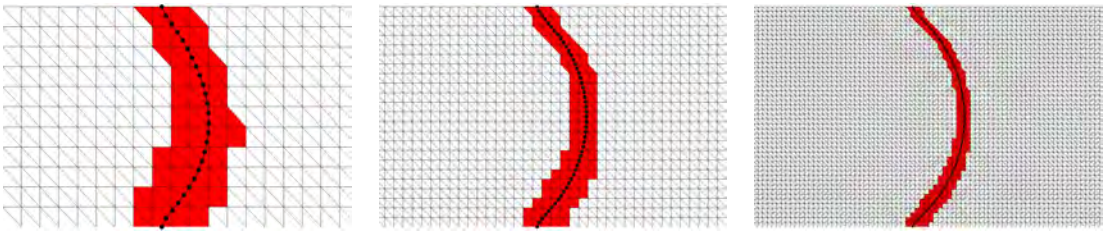

(a) M_1. (b) M_2. (c) M_3.

Figure E.1 – Neighborhood ω_h^n of the interface Σ_h^n at time $t = 0.125$ for the case of the closed valve.

E.2 Vesicle in lid-driven cavity flow from Section 5.4.3

Figures E.2a–E.2c represent the neighborhood ω_h^n of the interface Σ_h^n, considered in the context of the $\mathrm{FD}_{\mathrm{stab}}$ method and for the case of the vesicle in lid-driven cavity flow, for, respectively, the three different levels of refinement M_1, M_2 and M_3, defined in associated Section 5.4.3.

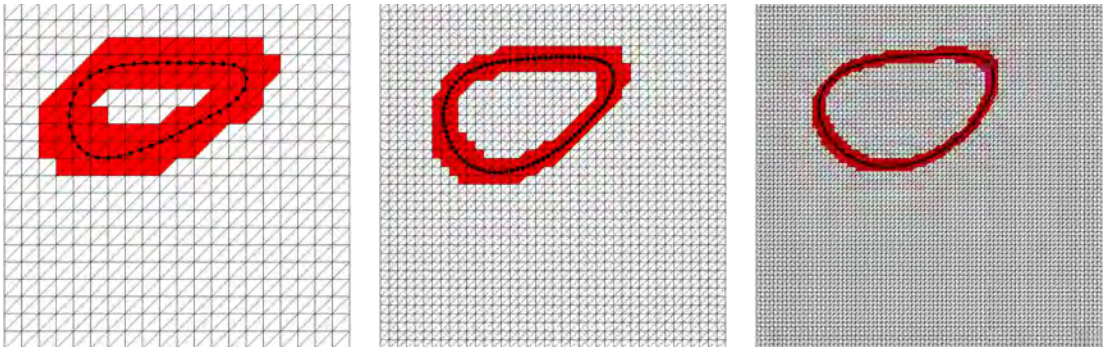

(a) M_1. (b) M_2. (c) M_3.

Figure E.2 – Neighborhood ω_h^n of the interface Σ_h^n at time $t = 6$ for the case of the vesicle in lid-driven cavity flow.

Note how ω_h^n covers almost the entirety of the elements within the vesicle for Figure E.2a, justifying the fact that no major difference in observed between the results obtained with the FD_{stab} method and the ones obtained with the classical FD one.

E.3 Idealized valve with contact from Section 6.5.2

Figures E.3a–E.3c represent the neighborhood ω_h^n of the interface Σ_h^n, considered in the context of the FD_{stab} method and for the case of the idealized valve with contact, for, respectively, the three different levels of refinement M_1, M_2 and M_3, defined in associated Section 6.5.2.

(a) M_1. (b) M_2. (c) M_3.

Figure E.3 – Neighborhood ω_h^n of the interface Σ_h^n at time $t = 0.7$ for the case of the idealized valve with contact.

E.4 Working principle of the Kephalios device from Section 7.3.1

Figures E.4a and E.4b represent the neighborhood ω_h^n of the interface Σ_h^n, considered in the context of the FD_{stab} method and for the case of the idealized valve with contact, for, respectively, the three different levels of refinement M_1, M_2 and M_3, defined in associated Section 6.5.2.

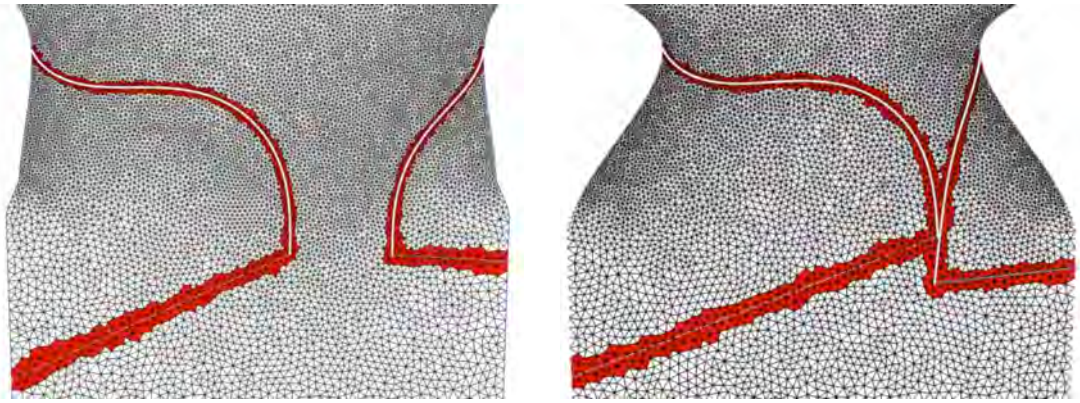

(a) Ill configuration. (b) Corrected configuration.

Figure E.4 – Neighborhood ω_h^n of the interface Σ_h^n at time $t = 0.82$ for the case of the principle of Kephalios device.

Note that the definition of ω_h^n also considers the tendinous cords, which is not relevant for the needs of the simulation. However, as each of these chordae tendineae is modeled as a single segment (i.e., the fluid only sees them as two immersed structures nodes separated by multiple layers of elements), the over-extension of ω_h^n does not perturb the fluid in this region.

E.5 Closed valve from Section 5.4.2 extended to 3D

For the purpose of the physiological simulations considered in Chapter 7 (with valves described in a FSI framework), the FD_{stab} method, previously investigated in 2D, must be extended to 3D. In this section, we validate the FD_{stab} method on the previous closed valve case now extended to 3D. The associated 3D computational domains are obtained with a simple extrusion of the 2D ones over a distance of 1 along the Z-axis. The description of the physics and of the boundary conditions of the 2D case provided in Section 5.4.2 are still relevant here. We will not depict the neighborhood ω_h^n of the interface Σ_h^n because it is not really meaningful in 3D. Nevertheless, for illustrative purposes, the initial and distorted configurations of the unfitted meshes are depicted in Figure E.5.

(a) $t = 0$. (b) $t = 0.125$.

Figure E.5 – Zoom on the fluid and solid meshes at different time instants for the case of the closed valve extended to 3D.

Figure E.6 reports a comparison of various physical values for the case of the closed valve extended to 3D obtained with the FD and FD_{stab} methods. As regards the x-displacement of the valve mid-point depicted in Figure E.6a, a clear difference of dynamics is observed between the two methods, which is similar to the one previously observed in Figure 5.21 for the same case in 2D. Moreover, Figure E.6b highlights an important leak obtained through the valve with the FD method and which disappears with the FD_{stab} method. The same behavior has been previously depicted in Figures 5.16 and 5.17 for the same case in 2D. All the units are expressed in the CGS system.

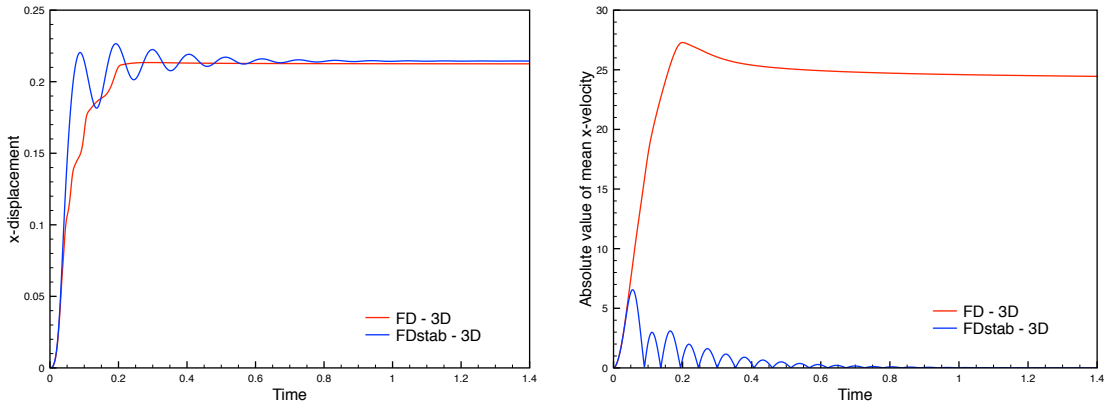

(a) x-displacement of the valve mid-point. (b) Absolute value of mean x-velocity at the inlet.

Figure E.6 – Time history of various physical values obtained with the FD and FD_{stab} methods for the case of the closed valve extended to 3D.

Similarly to what has been mentioned in Section 5.6 in 2D, the above depicted results clearly illustrate the benefits brought by the FD_{stab} method compared to the classical FD method for the mass conservation issues across the interface. This validates the implementation and the extension of this method to 3D.

References

[A+14] M.A. Acker et al. Mitral-valve repair versus replacement for severe ischemic mitral regurgitation. *N. Engl. J. Med.*, 370(1):23–32, 2014.

[ACK+13] H. Abe, G. Caracciolo, A. Kheradvar, G. Pedrizzetti, B.K. Khandheria, J. Narula, and P.P. Sengupta. Contrast echocardiography for assessing left ventricular vortex strength in heart failure: a prospective cohort study. *Eur. Heart. J. Cardiovasc. Imaging*, 14(11):1049–1060, 2013.

[AFFL16] F. Alauzet, B. Fabrèges, M.A. Fernández, and M. Landajuela. Nitsche-XFEM for the coupling of an incompressible fluid with immersed thin-walled structures. *Comput. Methods Appl. Mech. Eng.*, 301:300–335, 2016.

[AGPT09] M. Astorino, J.F. Gerbeau, O. Pantz, and K.F. Traoré. Fluid-structure interaction and multi-body contact: application to aortic valves. *Comput. Methods Appl. Mech. Eng.*, 198(45-46):3603–3612, 2009.

[AHSG12] M. Astorino, J. Hamers, S.C. Shadden, and J.F. Gerbeau. A robust and efficient valve model based on resistive immersed surfaces. *Int. J. Numer. Methods Biomed. Eng.*, 28(9):937–959, 2012.

[Ala14] F. Alauzet. A changing-topology moving mesh technique for large displacements. *Eng. Comput.*, 30(2):175–200, 2014.

[Ale19] T. Alexandre. *Image/model fusion for the quantification of mitral regurgitation severity*. PhD Thesis, Université Paris VI, 2019.

[AN04] E.A. Ashley and J. Niebauer. *Cardiology explained*. Remedica, 2004.

[Ann] Annuloplasty. https://www.mayoclinic.org/tests-procedures/annuloplasty/pyc-20384965/.

[Ann17] M. Annese. *Time integration schemes for fluid-structure interaction problems: non-fitted FEMs for immersed thin structures*. PhD Thesis, Università degli studi di Brescia, 2017.

[Ant12] E.M. Antman. *Cardiovascular Therapeutics: A Companion to Braunwald's Heart Disease*. Elsevier, Fourth edition, 2012.

[Ari89] R. Aris. *Vectors, Tensors and the Basic Equations of Fluid Mechanics*. Dover Publications, 1989.

[Ast10] M. Astorino. *Fluid-structure interaction in the cardiovascular system. Numerical analysis and simulation*. PhD Thesis, Université Paris VI, France, 2010.

[ASV+18] C. Ager, B. Schott, A.T. Vuong, A. Popp, and W.A. Wall. A consistent approach for fluid-structure-contact interaction based on a porous flow model for rough surface contact. *arXiv preprint arXiv:1809.04004*, 2018.

[ATN04] S.S. Antman, C.A. Truesdell, and W. Noll. *The Non-Linear Field Theories of Mechanics*. Springer-Verlag Berlin, Third edition, 2004.

[Baa01] F. Baaijens. A fictitious domain/mortar element method for fluid-structure interaction. *Int. Jour. Numer. Methods Fluids*, 35:743–761, 2001.

[Bac97] D.S. Bach. Stress echocardiography for evaluation of hemodynamics: valvular heart disease, prosthetic valve function, and pulmonary hypertension. *Prog. Cardiovasc. Dis.*, 39(6):543–554, 1997.

[Bat96] K.J. Bathe. *Finite Element Procedures*. Prentice Hall, 1996.

[BBBB10] K.E. Barrett, H.L. Brooks, S. Boitano, and S.M. Barman. *Ganong's Review of Medical Physiology*. McGraw-Hill Education, 2010.

[BBS+16] V. Bonnet, C. Boisselier, V. Saplacan, A. Belin, J.L. Gérard, J.L. Fellahi, J.L. Hanouz, and M.O. Fischer. The role of age and comorbidities in postoperative outcome of mitral valve repair. *Medicine (Baltimore)*, 95(25), 2016.

[BBWR04] M. Bischoff, K.U. Bletzinger, W.A. Wall, and E. Ramm. Models and finite elements for thin-walled structures. In *Encyclopedia of Computational Mechanics*, chapter 2. John Wiley & Sons, 2004.

[BCG11] D. Boffi, N. Cavallini, and L. Gastaldi. Finite element approach to immersed boundary method with different fluid and solid densities. *Math. Models Methods Appl. Sci.*, 21(12):2523–2550, 2011.

[BCG+13] M. Bukac, C. Canic, R. Glowinski, T. Tambaca, and A. Quaini. Fluid-structure interaction in blood flow capturing non-zero longitudinal structure displacement. *J. Comput. Phys.*, 235:515–541, 2013.

[BCG15] D. Boffi, N. Cavallini, and L. Gastaldi. The finite element immersed boundary method with distributed Lagrange multiplier. *SIAM J. Numer. Anal.*, 53(6):2584–2604, 2015.

[BCGG12a] D. Boffi, N. Cavallini, F. Gardini, and L. Gastaldi. Local mass conservation of Stokes finite elements. *SIAM J. Sci. Comput.*, 52(2):383–400, 2012.

[BCGG12b] D. Boffi, N. Cavallini, F. Gardini, and L. Gastaldi. Stabilized Stokes elements and local mass conservation. *Boll. Un. Mat. Ital.*, 5(3):543–573, 2012.

[BCM60] N.S. Braunwald, T. Cooper, and A.G. Morrow. Complete replacement of the mitral valve. successful clinical application of a flexible polyurethane prosthesis. *J. Thorac. Cardiovasc. Surg.*, 40:1–11, 1960.

[BCS01] J. Bestel, F. Clément, and M. Sorine. A biomechanical model of muscle contraction. In *Lecture Notes in Computer Science*, pages 1159–1161, 2001.

[BDC+15] P. Blanke, D. Dvir, A. Cheung, R.A. Levine, C. Thompson, J.G. Webb, and J. Leipsic. Mitral annular evaluation with CT in the context of transcatheter mitral valve replacement. *JACC: Cardiovasc. Imaging*, 8(5):612–615, 2015.

[BDG+17] Y. Bao, A. Donev, B.E. Griffith, D.M. McQueen, and C.S. Peskin. An immersed boundary method with divergence-free velocity interpolation and force spreading. *J. Comput. Phys.*, 347:183–206, 2017.

[BF09] E. Burman and M.A. Fernández. Stabilization of explicit coupling in fluid-structure interaction involving fluid incompressibility. *Comput. Methods Appl. Mech. Eng.*, 198(5-8):766–784, 2009.

[BF14] E. Burman and M.A. Fernández. An unfitted Nitsche method for incompressible fluid-structure interaction using overlapping meshes. *Comput. Methods Appl. Mech. Eng.*, 279:497–514, 2014.

[BFH06] E. Burman, M.A. Fernández, and P. Hansbo. Continuous interior penalty finite element method for Oseen's equations. *SIAM J. Numer. Anal.*, 44(3):1248–1274, 2006.

[BG17] D. Boffi and L. Gastaldi. A fictitious domain approach with Lagrange multiplier for fluid-structure interactions. *Numer. Math.*, 135(3):711–732, 2017.

[BH07] D.J. Brenner and E.J. Hall. Computed tomography–an increasing source of radiation exposure. *N. Engl. J. Med.*, 357(22):2277–2284, 2007.

[BHS14] J.W. Banks, W.D. Henshaw, and D.W. Schwendeman. An analysis of a new stable partitioned algorithm for FSI problems. Part II: Incompressible flow and structural shells. *J. Comput. Phys.*, 268:399–416, 2014.

[BK12] H. Baek and G.E. Karniadakis. A convergence study of a new partitioned fluid-structure interaction algorithm based on fictitious mass and damping. *J. Comput. Phys.*, 231(2):629–652, 2012.

[BLS03] G.L. Botto, M. Luzi, and A. Sagone. Atrial fibrillation: the remodelling phenomenon. *Eur. Heart J. Suppl.*, 5:H1–H7, 2003.

[BNAC13] B. Bush, L.W. Nifong, H. Alwair, and W.R. Chitwood. Robotic mitral valve surgery-current status and future directions. *Ann. Cardiothorac. Surg.*, 2(6):814, 2013.

[BNV08] S. Badia, F. Nobile, and C. Vergara. Fluid-structure partitioned procedures based on Robin transmission conditions. *J. Comput. Phys.*, 227(14):7027–7051, 2008.

[BQQ08a] S. Badia, A. Quaini, and A. Quarteroni. Modular vs. non-modular preconditioners for fluid-structure systems with large added-mass effect. *Comput. Methods Appl. Mech. Eng.*, 197(49-50):4216–4232, 2008.

[BQQ08b] S. Badia, A. Quaini, and A. Quarteroni. Splitting methods based on algebraic factorization for fluid-structure interaction. *SIAM J. Sci. Comput.*, 30(4):1778–1805, 2008.

[BTT97] F. Bertrand, P.A. Tanguy, and F. Thibault. A three-dimensional fictitious domain method for incompressible fluid flow problems. *Internat. J. Numer. Methods Fluids*, 25(6):719–736, 1997.

[Bur10] E. Burman. Ghost penalty. *C. R. Math. Acad. Sci. Paris*, 348(21-22):1217–1220, 2010.

[CAF11] A. Carpentier, D.H. Adams, and F. Filsoufi. *Carpentier's Reconstructive Valve Surgery*. Elsevier Health Sciences, 2011.

[Car] Carpentier's functional classification. https://thoracickey.com/principles-of-carpentiers-reconstructive-mitral-valve-surgery/.

[Car83] A. Carpentier. Cardiac valve surgery–the "French correction". *J. Thorac. Cardiovasc. Surg.*, 86:323–337, 1983.

[CB11] D. Chapelle and K.J. Bathe. *The Finite Element Analysis of Shells - Fundamentals*. Springer, Second edition, 2011.

[CBCG17] H. Casquero, C. Bona-Casas, and H. Gomez. NURBS-based numerical proxies for red blood cells and circulating tumor cells in microscale blood flow. *Comput. Methods Appl. Mech. Eng.*, 316:646–667, 2017.

[CBCGZ17] H. Casquero, C. Bona-Casas, H. Gomez, and Y. Zhang. Divergence-conforming and fully-implicit simulation of microscale blood flow. In *International Conference on Isogeometric Analysis (IGA 2017)*, 2017.

[CCV+15] Y.J. Choi, J. Constantino, V. Vedula, N. Trayanova, and R. Mittal. A new MRI-based model of heart function with coupled hemodynamics and application to normal and diseased canine left ventricles. *Front. Bioeng. Biotechnol.*, 3:140–154, 2015.

[CDFQ11] P. Crosetto, S. Deparis, G. Fourestey, and A. Quarteroni. Parallel algorithms for fluid-structure interaction problems in haemodynamics. *SIAM J. Sci. Comput.*, 33(4):1598–1622, 2011.

[CF03] D. Chapelle and A. Ferent. Modeling of the inclusion of a reinforcing sheet within a 3D medium. *Math. Models Methods Appl. Sci.*, 13(4):573–595, 2003.

[CFG+09] D. Chapelle, M.A. Fernández, J.F. Gerbeau, P. Moireau, J. Sainte-Marie, and N. Zemzemi. Numerical simulation of the electromechanical activity of the heart. In *Lecture Notes in Computer Science*, pages 357–365, 2009.

[CFGM11] A. Caiazzo, M.A. Fernández, J.F. Gerbeau, and V. Martin. Projection schemes for fluid flows through a porous interface. *SIAM J. Sci. Comput.*, 33(2):541–564, 2011.

[CGN05] P. Causin, J.F. Gerbeau, and F. Nobile. Added-mass effect in the design of partitioned algorithms for fluid-structure problems. *Comput. Methods Appl. Mech. Eng.*, 194(42–44):4506–4527, 2005.

[Cia88] P.G. Ciarlet. *Three-Dimensional Elasticity*. Elsevier Science Publishers, 1988.

[Cia00] P.G. Ciarlet. *Theory of shells*. North-Holland, 2000.

[CLM+18] J.L. Chan, M. Li, D. Mazilu, J.G. Miller, A.C. Diaconescu, and K.A. Horvath. Novel direct annuloplasty fastener system for minimally invasive mitral valve repair. *Cardiovasc. Eng. Technol.*, 9(1):53–59, 2018.

[CLMS12] D. Chapelle, P. Le Tallec, P. Moireau, and M. Sorine. Energy-preserving muscle tissue model: formulation and compatible discretizations. *Int. J. for Multi. Comput. Eng.*, 10(2):189–211, 2012.

[CLR+95] A.F. Carpentier, A. Lessana, J.Y.M. Relland, E. Belli, S. Mihaileanu, A.J. Berrebi, E. Palsky, and D.F. Loulmet. The "Physio-Ring": an advanced concept in mitral valve annuloplasty. *Ann. Thorac. Surg.*, 60(5):1177–1186, 1995.

[CLT56] M.A. Chiechi, W.M. Lees, and R. Thompson. Functional anatomy of the normal mitral valve. *J. Thorac. Surg.*, 32(3):378–398, 1956.

[CLW06] J. Chen, X.Y. Lu, and W. Wang. Non-Newtonian effects of blood flow on hemodynamics in distal vascular graft anastomoses. *J. Biomech.*, 39(11):1983–1995, 2006.

[CMM08] G.H. Cottet, E. Maitre, and T. Milcent. Eulerian formulation and level set models for incompressible fluid-structure interaction. *M2AN Math. Model. Numer. Anal.*, 42(3):471–492, 2008.

[CMN16] C. Chnafa, S. Mendez, and F. Nicoud. Image-based simulations show important flow fluctuations in a normal left ventricle: what could be the implications? *Ann. Biomed. Eng.*, 44(11):3346–3358, 2016.

[Cro] Cross section of the heart. http://studentradiographer.com/?p=2975/.

[CTR15] L.H. Cohn, V. Tchantchaleishvili, and T.K. Rajab. Evolution of the concept and practice of mitral valve repair. *Ann. Cardiothorac. Surg.*, 4(4):315, 2015.

[CWL+15] C. Cao, H. Wolfenden, K. Liou, F. Pathan, S. Gupta, T.A. Nienaber, D. Chandrakumar, P. Indraratna, and T.D. Yan. A meta-analysis of robotic versus conventional mitral valve surgery. *Ann. Cardiothorac. Surg.*, 4(4):305–314, 2015.

[CYMN04] L. Chen, F.C. Yin, and K. May-Newman. The structure and mechanical properties of the mitral valve leaflet-strut chordae transition zone. *J. Biomech. Eng.*, 126(2):244–251, 2004.

[DBHV08] J. Degroote, P. Bruggeman, R. Haelterman, and J. Vierendeels. Stability of a coupling technique for partitioned solvers in FSI applications. *Comput. & Struct.*, 86(23-24):2224–2234, 2008.

[DGH82] J. Donea, S. Giuliani, and J.P. Halleux. An arbitrary Lagrangian-Eulerian finite element method for transient dynamic fluid-structure interactions. *Comput. Methods Appl. Mech. Eng.*, 33(1-3):689–723, 1982.

[DHPRF04] J. Donea, A. Huerta, J.P. Ponthot, and A. Rodríguez-Ferran. *Arbitrary Lagrangian–Eulerian Methods*, volume 1. John Wiley & Sons, Ltd, 2004.

[Dif] Differences between primary and secondary mitral regurgitation. http://www.tinyscarvalvesurgery.com/2017/04/07/difference-primary-secondary-mitral-valve-regurgitation-florida/.

[DJR+90] A. Deloche, V.A. Jebara, J.Y. Relland, S. Chauvaud, J.N. Fabiani, P. Perier, G. Dreyfus, S. Mihaileanu, and A. Carpentier. Valve repair with Carpentier techniques. The second decade. *J. Thorac. Cardiovasc. Surg.*, 99(6):990–1001, 1990.

[DPM64] L.A. Du Plessis and P. Marchand. The anatomy of the mitral valve and its associated structures. *Thorax*, 19:221–227, 1964.

[DPSB03] J. De Hart, G.W.M. Peters, P.J.G. Schreurs, and F.P.T. Baaijens. A three-dimensional computational analysis of fluid-structure interaction in the aortic valve. *J. Biomech.*, 36(1):103–112, 2003.

[DQCP07] F. Domenichini, G. Querzoli, A. Cenedese, and G. Pedrizzetti. Combined experimental and numerical analysis of the flow structure into the left ventricle. *J. Biomech.*, 40(9):1988–1994, 2007.

[dS07] N.D. dos Santos. *Numerical methods for fluid-structure interaction problems with valves*. PhD Thesis, Université Paris VI, France, 2007.

[dSGB08] N.D. dos Santos, J.F. Gerbeau, and J.F. Bourgat. A partitioned fluid-structure algorithm for elastic thin valves with contact. *Comput. Methods Appl. Mech. Eng.*, 197(19-20):1750–1761, 2008.

[EH87] W.A. Eaton and J. Hofrichter. Hemoglobin S gelation and sickle cell disease. *Blood*, 70(5):1245–1266, 1987.

[EKR+04] D.R. Einstein, K.S. Kunzelman, P.G. Reinhall, M.A. Nicosia, and R.P. Cochran. Haemodynamic determinants of the mitral valve closure sound: a finite element study. *Med. Biol. Eng. Comput.*, 42(6):832–846, 2004.

[Epy] Epygon website. http://www.epygon.com/.

[F+09] T. Feldman et al. Percutaneous mitral repair with the MitraClip system: safety and midterm durability in the initial EVEREST (Endovascular Valve Edge-to-Edge REpair Study) cohort. *J. Am. Coll. Cardiol.*, 54(8):686–694, 2009.

[F+10] R. Faludi et al. Left ventricular flow patterns in healthy subjects and patients with prosthetic mitral valves: an in vivo study using echocardiographic particle image velocimetry. *J. Thorac. Cardiovasc. Surg.*, 139(6):1501–1510, 2010.

[F+13] J.A. Finegold et al. Mortality from ischaemic heart disease by country, region, and age: statistics from World Health Organisation and United Nations. *Int. J. Cardiol.*, 168(2):934–945, 2013.

[Fay94] J.A. Fay. *Introduction to Fluid Mechanics*. Massachusetts Institute of Technology Press, 1994.

[FAYA13] Z.M. Fairuz, M.Z. Abdullah, H. Yusoff, and M.K. Abdullah. Fluid structure interaction of unsteady aerodynamics of flapping wing at low Reynolds number. *Eng. Appl. Comput. Fluid Mech.*, 7(1):144–158, 2013.

[FCNH01] J.E. Felger, W.R. Chitwood, L.W. Nifong, and D. Holbert. Evolution of mitral valve surgery: toward a totally endoscopic approach. *Ann. Thorac. Surg.*, 72(4):1203–1209, 2001.

[FDOA06] J.M. Ferrão De Oliveira and M.J. Antunes. Mitral valve repair: better than replacement. *Heart*, 92(2):275–281, 2006.

[Fer11a] M.A. Fernández. Coupling schemes for incompressible fluid-structure interaction: implicit, semi-implicit and explicit. *SeMA J.*, 55(1):59–108, 2011.

[Fer11b] M.A. Fernández. Incremental displacement-correction schemes for the explicit coupling of a thin structure with an incompressible fluid. *C. R. Math. Acad. Sci. Paris*, 349(7-8):473–477, 2011.

[Fer13] M.A. Fernández. Incremental displacement-correction schemes for incompressible fluid-structure interaction: stability and convergence analysis. *Numer. Math.*, 123(1):21–65, 2013.

[FFDQ17] M. Fedele, E. Faggiano, L. Dedè, and A. Quarteroni. A patient-specific aortic valve model based on moving resistive immersed implicit surfaces. *Biomech. Model. Mechanobiol.*, 16(5):1779–1803, 2017.

[FFGQ09] M.A. Fernández, L. Formaggia, J.F. Gerbeau, and A. Quarteroni. The derivation of the equations for fluids and structures. In *Cardiovascular mathematics*, volume 1 of *MS&A. Model. Simul. Appl.*, pages 77–121. Springer, 2009.

[FG09] M.A. Fernández and J.F. Gerbeau. Algorithms for fluid-structure interaction problems. In *Cardiovascular mathematics*, volume 1 of *MS&A. Model. Simul. Appl.*, pages 307–346. Springer, 2009.

[FGG07] M.A. Fernández, J.F. Gerbeau, and C. Grandmont. A projection semi-implicit scheme for the coupling of an elastic structure with an incompressible fluid. *Int. J. Numer. Methods Eng.*, 69(4):794–821, 2007.

[FGM08] M.A. Fernández, J.F. Gerbeau, and V. Martin. Numerical simulation of blood flows through a porous interface. *M2AN Math. Model. Numer. Anal.*, 42(6):961–990, 2008.

[FHB03] W. Flameng, P. Herijgers, and K. Bogaerts. Recurrence of mitral valve regurgitation after mitral valve repair in degenerative valve disease. *Circulation*, 107(12):1609–1613, 2003.

[FK07] J. Feldschuh and S. Katz. The importance of correct norms in blood volume measurement. *Am. J. Med. Sci.*, 334(1):41–46, 2007.

[FL08] H. Fukuta and W.C. Little. The cardiac cycle and the physiological basis of left ventricular contraction, ejection, relaxation, and filling. *Heart Failure Clin.*, 4(1):1–11, 2008.

[FL15] M.A. Fernández and M. Landajuela. Splitting schemes for incompressible fluid/thin-walled structure interaction with unfitted meshes. *C. R. Math. Acad. Sci. Paris.*, 353(7):647–652, 2015.

[FLV15] M.A. Fernández, M. Landajuela, and M. Vidrascu. Fully decoupled time-marching schemes for incompressible fluid/thin-walled structure interaction. *J. Comput. Phys.*, 297:156–181, 2015.

[FM05] M.A. Fernández and M. Moubachir. A Newton method using exact Jacobians for solving fluid-structure coupling. *Comput. & Struct.*, 83(2-3):127–142, 2005.

[FM14] B. Fabrèges and B. Maury. Approximation of single layer distributions by Dirac masses in finite element computations. *SIAM J. Sci. Comput.*, 58(1):25–40, 2014.

[FM16] M.A. Fernández and J. Mullaert. Convergence and error analysis for a class of splitting schemes in incompressible fluid-structure interaction. *IMA J. Numer. Anal.*, 36(4):1748–1782, 2016.

[FMV13] M.A. Fernández, J. Mullaert, and M. Vidrascu. Explicit Robin-Neumann schemes for the coupling of incompressible fluids with thin-walled structures. *Comput. Methods Appl. Mech. Eng.*, 267:566–593, 2013.

[FMV15] M.A. Fernández, J. Mullaert, and M. Vidrascu. Generalized Robin-Neumann explicit coupling schemes for incompressible fluid-structure interaction: stability analysis and numerics. *Internat. J. Numer. Methods Eng.*, 101(3):199–229, 2015.

[FPK15] A. Falahatpisheh, N.M. Pahlevan, and A. Kheradvar. Effect of the mitral valve's anterior leaflet on axisymmetry of transmitral vortex ring. *Ann. Biomed. Eng.*, 43(10):2349–2360, 2015.

[FQV09] L. Formaggia, A. Quarteroni, and A. Veneziani. *Modeling and simulation of the circulatory system.* Springer-Verlag Mailand, 2009.

[Fre01] P. Frey. YAMS: a fully automatic adaptive isotropic surface remeshing procedure. Technical Report 0252, Inria, 2001.

[FWR07] C. Förster, W.A. Wall, and E. Ramm. Artificial added mass instabilities in sequential staggered coupling of nonlinear structures and incompressible viscous flows. *Comput. Methods Appl. Mech. Eng.*, 196(7):1278–1293, 2007.

[G+08] J. Gorcsan et al. Echocardiography for cardiac resynchronization therapy: recommendations for performance and reporting. *J. Am. Soc. Echocardiogr.*, 21(3):191–213, 2008.

[G+13] A.S. Go et al. Heart disease and stroke statistics–2013 update. *Circulation*, 127:e6–e245, 2013.

[GABH13] A.J. Gil, A. Arranz Carreño, J. Bonet, and O. Hassan. An enhanced immersed structural potential method for fluid-structure interaction. *J. Comput. Phys.*, 250:178–205, 2013.

[GBN+08] A.M. Gillinov, E.H. Blackstone, E.R. Nowicki, W. Slisatkorn, G. Al-Dossari, D.R. Johnston, K.M. George, P.L. Houghtaling, B. Griffin, J.F. Sabik, and L.G. Svensson. Valve repair versus valve replacement for degenerative mitral valve disease. *J. Thorac. Cardiovasc. Surg.*, 135(4):885–893, 2008.

[GCHR17] E. Girdauskas, L. Conradi, E.K. Harmel, and H. Reichenspurner. Minimally invasive mitral valve annuloplasty with realignment of both papillary muscles for correction of type IIIb functional mitral regurgitation. *Innovations: Technology and Techniques in Cardiothoracic and Vascular Surgery*, 12(5):329–332, 2017.

[GFQ+17] H. Gao, L. Feng, N. Qi, C. Berry, B.E. Griffith, and X. Luo. A coupled mitral valve–left ventricle model with fluid-structure interaction. *Med. Eng. & Phys.*, 47:128–136, 2017.

[GGCC09] G. Guidoboni, R. Glowinski, N. Cavallini, and S. Canic. Stable loosely-coupled-type algorithm for fluid-structure interaction in blood flow. *J. Comput. Phys.*, 228(18):6916–6937, 2009.

[GHS90] P.L. George, F. Hecht, and É. Saltel. Fully automatic mesh generator for 3d domains of any shape. *IMPACT Comput. Sci. Eng.*, 2(3):187–218, 1990.

[GKW11] M.W. Gee, U. Küttler, and W.A. Wall. Truly monolithic algebraic multigrid for fluid-structure interaction. *Int. J. Numer. Methods Eng.*, 85(8):987–1016, 2011.

[GL17] B.E. Griffith and X. Luo. Hybrid finite difference/finite element immersed boundary method. *Int. J. Numer. Methods Biomed. Eng.*, 33(12):e2888, 2017.

[GLKP99] I. Goldsmith, G.Y. Lip, H. Kaukuntla, and R.L. Patel. Hospital morbidity and mortality and changes in quality of life following mitral valve surgery in the elderly. *J. Heart Valve Dis.*, 8(6):702–707, 1999.

[GLMP09] B.E. Griffith, X. Luo, D.M. McQueen, and C.S. Peskin. Simulating the fluid dynamics of natural and prosthetic heart valves using the immersed boundary method. *Int. J. Appl. Mech.*, 1(01):137–177, 2009.

[Glo12] D.D. Glower. Surgical approaches to mitral regurgitation. *J. Am. Coll. Cardiol.*, 60(15):1315–1322, 2012.

[GLRW12] K.J. Galvin, A. Linke, L.G. Rebholz, and N.E. Wilson. Stabilizing poor mass conservation in incompressible flow problems with large irrotational forcing and application to thermal convection. *Comput. Methods Appl. Mech. Eng.*, 237/240:166–176, 2012.

[GPHJ99] R. Glowinski, T.W. Pan, T.I. Hesla, and D.D. Joseph. A distributed Lagrange mutiplier/fictitious domain method for particulate flows. *Int. J. Multiph. Flow*, 25:755–794, 1999.

[Gri12] B.E. Griffith. On the volume conservation of the immersed boundary method. *Comm. Comput. Phys.*, 12(2):401–432, 2012.

[GRK+06] M. Gharib, E. Rambod, A. Kheradvar, D.J. Sahn, and J.O. Dabiri. Optimal vortex formation as an index of cardiac health. *Proc. Natl. Acad. Sci.*, 103(16):6305–6308, 2006.

[GSFA06] B. Grüner Sveälv, G. Fritzon, and B. Andersson. Gender and age related differences in left ventricular function and geometry with focus on the long axis. *Eur. J. Echocardiogr.*, 7(4):298–307, 2006.

[Gur81] M. Gurtin. *An Introduction to Continuum Mechanics*. Elsevier, 1981.

[GW08] A. Gerstenberger and W.A. Wall. An extended finite element method/Lagrange multiplier based approach for fluid-structure interaction. *Comput. Methods Appl. Mech. Eng.*, 197(19-20):1699–1714, 2008.

[Har15] J. Hart. Normal resting pulse rate ranges. *J. Nurs. Educ. Pract.*, 5(8):95, 2015.

[HCC15] C. Harris, B. Croce, and C. Cao. Tissue and mechanical heart valves. *Ann. Cardiothorac. Surg.*, 4(4):399, 2015.

[Her07] I.P. Herman. *Physics of the Human Body.* Springer, 2007.

[HF87] T.J.R. Hughes and L.P. Franca. A new finite element formulation for computational fluid dynamics: VII. The Stokes problem with various well-posed boundary conditions: Symmetric formulations that converge for all velocity/pressure spaces. *Comput. Methods Appl. Mech. Eng.*, 65(1):85–96, 1987.

[HFCC13] E. Hachem, S. Feghali, R. Codina, and T. Coupez. Immersed stress method for fluid-structure interaction using anisotropic mesh adaptation. *Internat. J. Numer. Methods Eng.*, 94(9):805–825, 2013.

[HGAB12] C. Hesch, A.J. Gil, A. Arranz Carreño, and J. Bonet. On continuum immersed strategies for fluid-structure interaction. *Comput. Methods Appl. Mech. Eng.*, 247-248:51–64, 2012.

[HKB+14] M.C. Hsu, D. Kamensky, Y. Bazilevs, M.S. Sacks, and T.J.R. Hughes. Fluid–structure interaction analysis of bioprosthetic heart valves: significance of arterial wall deformation. *Comput. Mech.*, 54(4):1055–1071, 2014.

[Ho09] S.Y. Ho. Structure and anatomy of the aortic root. *Eur. J. Echocardiogr.*, 10(1):i3–i10, 2009.

[HP18] J. Han and C.S. Peskin. Spontaneous oscillation and fluid-structure interaction of cilia. *Proc. Natl. Acad. Sci. U.S.A.*, 115(17):4417–4422, 2018.

[HPS03] P.J. Hunter, A.J. Pullan, and B.H. Smaill. Modeling total heart function. *Ann. Biomed. Eng.*, 5(1):147–177, 2003.

[HSR67] J.C. Harlan, E.E. Smith, and T.Q. Richardson. Pressure-volume curves of systemic and pulmonary circuit. *Am. J. Physiol.*, 213(6):1499–1503, 1967.

[Hux57] A.F Huxley. Muscle structure and theories of contraction. *Prog. Biophys. Biophys. Chem*, 7:255–318, 1957.

[HWL12] G. Hou, J. Wang, and A. Layton. Numerical methods for fluid-structure interaction – a review. *Comm. Comput. Phys.*, 12(2):337–377, 2012.

[HY11] R.B. Hinton and K.E. Yutzey. Heart valve structure and function in development and disease. *Annu. Rev. Physiol.*, 73:29–46, 2011.

[Iai15] Paul A. Iaizzo. *Handbook of Cardiac Anatomy, Physiology, and Devices.* Springer, Third edition, 2015.

[Ill] Illustration of mitral regurgitation. https://myheart.net/articles/mitral-regurgitation/.

[JDA+92] V.A. Jebara, P. Dervanian, C. Acar, P. Grare, S. Mihaileanu, S. Chauvaud, J.N. Fabiani, and A. Deloche. Mitral valve repair using Carpentier techniques in patients more than 70 years old. *Circulation*, 5:6–3, 1992.

[JMS10] J. Janela, A. Moura, and A. Sequeira. A 3D non-Newtonian fluid-structure interaction model for blood flow in arteries. *J. Comput. Appl. Math.*, 234(9):2783–2791, 2010.

[KBL+06] A. Kulik, P. Bédard, B.K. Lam, F.D. Rubens, P.J. Hendry, R.G. Masters, T.G. Mesana, and M. Ruel. Mechanical versus bioprosthetic valve replacement in middle-aged patients. *Eur. J. Cardiothorac. Surg.*, 30(3):485–491, 2006.

[KBT+16] J. Kabil, L. Belguerras, S. Trattnig, C. Pasquier, J. Felblinger, and A. Missoffe. A review of numerical simulation and analytical modeling for medical devices safety in MRI. *Yearb. Med. Inform.*, pages 152–158, 2016.

[KDP18] C. Kadapa, W.G. Dettmer, and D. Perić. A stabilised immersed framework on hierarchical B-spline grids for fluid-flexible structure interaction with solid-solid contact. *Comput. Methods Appl. Mech. Eng.*, 335:472–489, 2018.

[KEC07] K.S. Kunzelman, D.R. Einstein, and R.P. Cochran. Fluid–structure interaction models of the mitral valve: function in normal and pathological states. *Philos. Trans. R. Soc. Lond. B Biol. Sci.*, 362(1484):1393–1406, 2007.

[Kep] Kephalios the two typical configurations of the kephalios device. http://www.kephalios.eu/.

[KF+10] B.B. Kelly, V. Fuster, et al. *Promoting cardiovascular health in the developing world: a critical challenge to achieve global health.* National Academies Press (US), 2010.

[KHS+15] D. Kamensky, M.C. Hsu, D. Schillinger, J.A. Evans, A. Aggarwal, Y. Bazilevs, M.S. Sacks, and T.J.R. Hughes. An immersogeometric variational framework for fluid-structure interaction: Application to bioprosthetic heart valves. *Comput. Methods Appl. Mech. Eng.*, 284:1005–1053, 2015.

[Khu08] I. Khurana. *Essentials of Medical Physiology.* Elsevier India, 2008.

[KHY+17] D. Kamensky, M.C. Hsu, Y. Yu, J.A. Evans., M.S. Sacks, and T.J.R. Hughes. Immersogeometric cardiovascular fluid-structure interaction analysis with divergence-conforming B-splines. *Comput. Methods Appl. Mech. Eng.*, 314:408–472, 2017.

[KLC18] W. Kim, I. Lee, and H. Choi. A weak-coupling immersed boundary method for fluid-structure interaction with low density ratio of solid to fluid. *J. Comput. Phys.*, 359:296–311, 2018.

[KLSC08] H. Kim, J. Lu, M.S. Sacks, and K.B. Chandran. Dynamic simulation of bioprosthetic heart valves using a stress resultant shell model. *Ann. Biomed. Eng.*, 36(2):262–275, 2008.

[KS92] N. Kechkar and D. Silvester. Analysis of locally stabilized mixed finite element methods for the Stokes problem. *Math. Comput.*, 58(197):1–10, 1992.

[KXL+18] D. Kamensky, F. Xu, C.H. Lee, J. Yan, Y. Bazilevs, and M.C. Hsu. A contact formulation based on a volumetric potential: application to isogeometric simulations of atrioventricular valves. *Comput. Methods Appl. Mech. Eng.*, 330:522–546, 2018.

[KYW+00] P.J. Kilner, G.Z. Yang, A.J. Wilkes, R.H. Mohiaddin, D.N. Firmin, and M.H. Yacoub. Asymmetric redirection of flow through the heart. *Nature*, 404(6779):759–761, 2000.

[L+17] S. Lazam et al. Twenty-year outcome after mitral repair versus replacement for severe degenerative mitral regurgitation: analysis of a large, prospective, multicenter, international registry. *Circulation*, 135(5):410–422, 2017.

[LA16] N.B. Langer and M. Argenziano. Minimally invasive cardiovascular surgery: Incisions and approaches. *Methodist Debakey Cardiovasc. J.*, 12(1):4–9, 2016.

[Lan16] M. Landajuela. *Coupling schemes and unfitted mesh methods for fluid-structure interaction.* PhD Thesis, Université Paris VI, France, 2016.

[LCB06] A. Legay, J. Chessa, and T. Belytschko. An Eulerian-Lagrangian method for fluid-structure interaction based on level sets. *Comput. Methods Appl. Mech. Eng.*, 195(17-18):2070–2087, 2006.

[LDSB10] K.D. Lau, V. Diaz, P. Scambler, and G. Burriesci. Mitral valve dynamics in structural and fluid-structure interaction models. *Med. Eng. & Phys.*, 32(9):1057–1064, 2010.

[LL06] Y. Liu and W.K. Liu. Rheology of red blood cell aggregation by computer simulation. *J. Comput. Phys.*, 220(1):139–154, 2006.

[LLX08] J.M. Liu, J.C. Lu, and L.P. Xue. Investigation of airship aeroelasticity using fluid-structure interaction. *J. Hydrodynamics*, 20(2):164–171, 2008.

[LMRHZ13] M. Lukáčová-Medvid'ová, G. Rusnáková, and A. Hundertmark-Zaušková. Kinematic splitting algorithm for fluid-structure interaction in hemodynamics. *Comput. Methods Appl. Mech. Eng.*, 265:83–106, 2013.

[LP00] M.C. Lai and C.S. Peskin. An immersed boundary method with formal second-order accuracy and reduced numerical viscosity. *J. Comput. Phys.*, 160(2):705–719, 2000.

[LS05] A. Libai and J.G. Simmonds. *The nonlinear theory of elastic shells.* Cambridge University Press, 2005.

[LT94] P. Le Tallec. Numerical methods for nonlinear three-dimensional elasticity. *Handbook of numerical analysis*, 3:465–622, 1994.

[LTHW87] R.A. Levine, M.O. Triulzi, P. Harrigan, and A.E. Weyman. The relationship of mitral annular shape to the diagnosis of mitral valve prolapse. *Circulation*, 75(4):756–767, 1987.

[LVCF17] M. Landajuela, M. Vidrascu, D. Chapelle, and M.A. Fernández. Coupling schemes for the FSI forward prediction challenge: comparative study and validation. *Int. J. Numer. Methods Biomed. Eng.*, 33(4):e2813, 2017.

[M+15] F. Maisano et al. The future of transcatheter mitral valve interventions: competitive or complementary role of repair vs. replacement? *Eur. Heart J.*, 36(26):1651–1659, 2015.

[Mal69] L.E. Malvern. *Introduction to the Mechanics of a Continuous Medium.* Prentice-Hall, 1969.

[MBH+11] M.E. Moghadam, Y. Bazilevs, T.Y. Hsia, I.E. Vignon-Clementel, A.L. Marsden, et al. A comparison of outlet boundary treatments for prevention of backflow divergence with relevance to blood flow simulations. *Comput. Mech.*, 48(3):277–291, 2011.

[MEC+02] R.H. Mehta, K.A. Eagle, L.P. Coombs, E.D. Peterson, F.H. Edwards, F.D. Pagani, G.M. Deeb, S.F. Bolling, and R.L. Prager. Influence of age on outcomes in patients undergoing mitral valve replacement. *Ann. Thorac. Surg.*, 74(5):1459–1467, 2002.

[MFF+10] A.E. Moran, M.H. Forouzanfar, A.D. Flaxman, G. Roth, G. Mensah, M. Ezzati, M. Naghavi, and C.J.L. Murray. Temporal trends in ischemic heart disease mortality in 21 world regions, 1980-2010: the global burden of disease 2010 study. *J. Am. Coll. Cardiol.*, 61(10):e1407, 2010.

[MGG+13] X. Ma, H. Gao, B.E. Griffith, C. Berry, and X. Luo. Image-based fluid-structure interaction model of the human mitral valve. *Comput. & Fluids*, 71:417–425, 2013.

[MH18] D.E. Mohrman and L.J. Heller. *Cardiovascular Physiology.* McGraw-Hill Education, 2018.

[MHC83] J.E. Marsden, T.J.R. Hughes, and D.E. Carlson. *Mathematical Foundations of Elasticity.* Dover Publications, 1983.

[Min51] R.D. Mindlin. Influence of rotary inertia and shear on flexural motions of isotropic elastic plates. *J. Appl. Mech.*, 18:31–38, 1951.

[Mita] Mitral valve incompetence: epidemiology and causes. https://www.escardio.org/Journals/E-Journal-of-Cardiology-Practice/Volume-16/Mitral-valve-incompetence-epidemiology-and-causes/.

[Mitb] Mitral valve repair. http://www.chirurgiecardiaquejacquescartier.com/chirurgie-de-linsuffisance-mitrale/.

[MLL13] A. Massing, M.G. Larson, and A. Logg. Efficient implementation of finite element methods on nonmatching and overlapping meshes in three dimensions. *SIAM J. Sci. Comput.*, 35(1):C23–C47, 2013.

[MMG08] H.C. McGill, C.A. McMahan, and S.S. Gidding. Preventing heart disease in the 21st century: implications of the pathobiological determinants of atherosclerosis in youth (PDAY) study. *Circulation*, 117(9):1216–1227, 2008.

[MMH12] R.L. Muddle, M. Mihajlović, and M. Heil. An efficient preconditioner for monolithically-coupled large-displacement fluid-structure interaction problems with pseudo-solid mesh updates. *J. Comput. Phys.*, 231(21):7315–7334, 2012.

[Moi08] P. Moireau. *Filtering based data assimilation for second order hyperbolic PDEs - Applications in cardiac mechanics.* PhD Thesis, École Polytechnique, 2008.

[MPF92] S. Mantero, R. Pietrabissa, and R. Fumero. The coronary bed and its role in the cardiovascular system: a review and an introductory single-branch model. *J. Biomed. Eng.*, 14(2):109–116, 1992.

[MPGW10] U.M. Mayer, A. Popp, A. Gerstenberger, and W.A. Wall. 3D fluid-structure-contact interaction based on a combined XFEM FSI and dual mortar contact approach. *Comput. Mech.*, 46(1):53–67, 2010.

[MROH12] B.R. Munson, A.P. Rothmayer, T.H. Okiishi, and W.W. Huebsch. *Fundamentals of Fluid Mechanics.* Wiley, 2012.

[MRSB10] K. Maganti, V.H. Rigolin, M.E. Sarano, and R.O. Bonow. Valvular heart disease: diagnosis and management. In *Mayo Clinic Proceedings*, volume 85, pages 483–500, 2010.

[MSV+16] R. Mittal, J.H. Seo, V. Vedula, Y.J. Choi, H. Liu, H.H. Huang, S. Jain, L. Younes, T. Abraham, and R.T. George. Computational modeling of cardiac hemodynamics: current status and future outlook. *J. Comput. Phys.*, 305:1065–1082, 2016.

[MW14] J.R. Mitchell and J.J. Wang. Expanding application of the Wiggers diagram to teach cardiovascular physiology. *Adv. Physiol. Educ.*, 38(2):170–175, 2014.

[N+16] C. Naoum et al. Mitral annular dimensions and geometry in patients with functional mitral regurgitation and mitral valve prolapse. *JACC Cardiovasc. Imaging*, 9(3):269–280, 2016.

[NCS+00] S. Nazari, F. Carli, S. Salvi, C. Banfi, A. Aluffi, Z. Mourad, P. Buniva, and G. Rescigno. Patterns of systolic stress distribution on mitral valve anterior leaflet chordal apparatus. A structural mechanical theoretical analysis. *J. Cardiovasc. Surg.*, 41:193–202, 2000.

[New18] T. Newman. The heart: all you need to know. https://www.medicalnewstoday.com/articles/320565.php, 2018.

[NGS+06] V.T. Nkomo, J.M. Gardin, T.N. Skelton, J.S. Gottdiener, C.G. Scott, and M. Enriquez-Sarano. Burden of valvular heart diseases: a population-based study. *The Lancet*, 368(9540):1005–1011, 2006.

[NL12] T. Nakata and H. Liu. A fluid-structure interaction model of insect flight with flexible wings. *J. Comput. Phys.*, 231(4):1822–1847, 2012.

[Nob01] F. Nobile. *Numerical approximation of fluid-structure interaction problems with application to haemodynamics*. PhD Thesis, École Polytechnique Fédérale de Lausanne, 2001.

[NPV13] F. Nobile, M. Pozzoli, and C. Vergara. Time accurate partitioned algorithms for the solution of fluid-structure interaction problems in haemodynamics. *Comput. & Fluids*, 86:470–482, 2013.

[NV08] F. Nobile and C. Vergara. An effective fluid-structure interaction formulation for vascular dynamics by generalized Robin conditions. *SIAM J. Sci. Comput.*, 30(2):731–763, 2008.

[OGJ+98] Y. Otsuji, D. Gilon, L. Jiang, S. He, M. Leavitt, M.J. Roy, M.J. Birmingham, and R.A. Levine. Restricted diastolic opening of the mitral leaflets in patients with left ventricular dysfunction: evidence for increased valve tethering. *J. Am. Coll. Cardiol.*, 32(2):398–404, 1998.

[Ove] Overview of the four valves in the heart. https://www.ottawaheart.ca/heart-condition/heart-valve-disease/.

[Pan11] O. Pantz. A frictionless contact algorithm for deformable bodies. *ESAIM: Math. Model. Numer. Anal.*, 45(2):235–254, 2011.

[Pat11] A. Patel. Lagrange multiplier method with penalty for elliptic and parabolic interface problems. *J. Appl. Math. Comput.*, 37(1-2):37–56, 2011.

[PD15] G. Pedrizzetti and F. Domenichini. Left ventricular fluid mechanics: the long way from theoretical models to clinical applications. *Ann. Biomed. Eng.*, 43(1):26–40, 2015.

[PDT10] G. Pedrizzetti, F. Domenichini, and G. Tonti. On the left ventricular vortex reversal after mitral valve replacement. *Ann. Biomed. Eng.*, 38(3):769–773, 2010.

[Pes02] C.S. Peskin. The immersed boundary method. *Acta Numer.*, 11:479–517, 2002.

[Pit11] R.N. Pittman. *Chapter 4: Oxygen transport.* Morgan & Claypool Life Sciences, 2011.

[PKO+17] M. Penicka, M. Kotrc, T. Ondrus, Y. Mo, F. Casselman, M. Vanderheyden, G. Van Camp, F. Van Praet, and J. Bartunek. Minimally invasive mitral valve annuloplasty confers a long-term survival benefit compared with state-of-the-art treatment in heart failure with functional mitral regurgitation. *Int. J. Cardiol.*, 244:235–241, 2017.

[PLCAT14] G. Pedrizzetti, G. La Canna, O. Alfieri, and G. Tonti. The vortex–an early predictor of cardiovascular outcome? *Nat. Rev. Cardiol.*, 11(9):545, 2014.

[PP93] C.S. Peskin and B.F. Printz. Improved volume conservation in the computation of flows with immersed elastic boundaries. *J. Comput. Phys.*, 105(1):33–46, 1993.

[Proa] Profile view of the anatomy of the mitral valve. https://thoracickey.com/aortic-valve-disease-4/.

[Prob] Profile view of the anatomy of the mitral valve. https://www.heart-valve-surgery.com/heart-surgery-blog/2008/09/02/mitral-valve-annulus-definition-diagrams-prolapse-calcification-treatment/.

[PS14] T. Pham and W. Sun. Material properties of aged human mitral valve leaflets. *J. Biomed. Mater. Res. A.*, 102(8):2692–2703, 2014.

[QQ07] A. Quaini and A. Quarteroni. A semi-implicit approach for fluid-structure interaction based on an algebraic fractional step method. *Math. Models Methods Appl. Sci.*, 17(6):957–983, 2007.

[RAB07] I. Ramière, P. Angot, and M. Belliard. A fictitious domain approach with spread interface for elliptic problems with general boundary conditions. *Comput. Methods Appl. Mech. Eng.*, 196(4-6):766–781, 2007.

[RDKFO89] M.J. Roman, R.B. Devereux, R. Kramer-Fox, and J. O'Loughlin. Two-dimensional echocardiographic aortic root dimensions in normal children and adults. *Am. J. Cardiol.*, 64(8):507–512, 1989.

[Rei45] E. Reissner. The effect of transverse shear deformation on the bending of elastic plates. *J. Appl. Mech.*, pages A69–A77, 1945.

[RGDRC17] A. Regueiro, J.F. Granada, F. Dagenais, and J. Rodés-Cabau. Transcatheter mitral valve replacement: insights from early clinical experience and future challenges. *J. Am. Coll. Cardiol.*, 69(17):2175–2192, 2017.

[RHC15] S. Roy, L. Heltai, and F. Costanzo. Benchmarking the immersed finite element method for fluid-structure interaction problems. *Comput. Math. Appl.*, 69(10):1167–1188, 2015.

[Ric13] T. Richter. A fully Eulerian formulation for fluid-structure-interaction problems. *J. Comput. Phys.*, 233:227–240, 2013.

[RKL+05] M. Ruel, A. Kulik, B.K. Lam, F.D. Rubens, P.J. Hendry, R.G. Masters, P. Bédard, and T.G. Mesana. Long-term outcomes of valve replacement with modern prostheses in young adults. *Eur. J. Cardiothorac. Surg.*, 27(3):425–433, 2005.

[RLWS70] N. Ranganathan, J.H.C. Lam, E.D. Wigle, and M.D. Silver. Morphology of the human mitral valve: II. The valve leaflets. *Circulation*, 41(3):459–467, 1970.

[RSE52] I.E. Rusted, C.H. Scheifley, and J.E. Edwards. Studies of the mitral valve. I. Anatomic features of the normal mitral valve and associated structures. *Circulation*, 6(6):825–831, 1952.

[RW10] T. Richter and T. Wick. Finite elements for fluid-structure interaction in Arbitrary Lagrangian-Eulerian and fully Eulerian coordinates. *Comput. Methods Appl. Mech. Eng.*, 199(41-44):2633–2642, 2010.

[RZB+17] A. Rossi, G. Zoppini, G. Benfari, G. Geremia, S. Bonapace, C. Bonora, E. Vassanelli, M. Enriquez-Sarano, and G. Targher. Mitral regurgitation and increased risk of all-cause and cardiovascular mortality in patients with type 2 diabetes. *Am. J. Med.*, 130(1):70–76, 2017.

[S+16] K. Sud et al. Degenerative mitral stenosis: unmet need for percutaneous interventions. *Circulation*, 133(16):1594–1604, 2016.

[SASZA+18] A. Santiago, J. Aguado-Sierra, M. Zavala-Aké, R. Doste-Beltran, S. Gómez, R. Arís, J.C. Cajas, E. Casoni, and M. Vázquez. Fully coupled fluid-electro-mechanical model of the human heart for supercomputers. *Int. J. Numer. Methods Biomed. Eng.*, 34(12):e3140, 2018.

[SB09] F. Sotiropoulos and I. Borazjani. A review of state-of-the-art numerical methods for simulating flow through mechanical heart valves. *Med. & Biol. Eng. & Comput.*, 47(3):245–256, 2009.

[Sch] Schematic representation of the human cardiovascular system. https://www.thinglink.com/scene/792075535718023169/.

[Sch78] P. Scheid. Analysis of gas exchange between air capillaries and blood capillaries in avian lungs. *Respir. Physiol.*, 32(1):27–49, 1978.

[Sch84] R. Scholz. Numerical solution of the obstacle problem by the penalty method. *Comput.*, 32(4):297–306, 1984.

[Sch08] F.J. Schoen. Evolving concepts of cardiac valve dynamics. *Circulation*, 118(18):1864–1880, 2008.

[SDL13] R.A. Sauer and L. De Lorenzis. A computational contact formulation based on surface potentials. *Comput. Methods Appl. Mech. Eng.*, 253:369–395, 2013.

[SENT88] Y. Sahasakul, W.D. Edwards, J.M. Naessens, and A.J. Tajik. Age-related changes in aortic and mitral valve thickness: implications for two-dimensional echocardiography based on an autopsy study of 200 normal human hearts. *Am. J. Cardiol.*, 62(7):424–430, 1988.

[SFGL06] J.V. Soulis, T.M. Farmakis, G.D. Giannoglou, and G.E. Louridas. Wall shear stress in normal left coronary artery tree. *J. Biomech.*, 39(4):742–749, 2006.

[SGN+11] G. Schaefers, W. Goertz, Y. Noureddine, C. Koch, and M.J. Pawlenka. Magnetic resonance (MR) safety testing of implants using numerical simulation for worst-case determination. In *General Assembly and Scientific Symposium, 2011 30th URSI*, pages 1–4, 2011.

[SH68] M.E. Silverman and J.W. Hurst. The mitral complex: interaction of the anatomy, physiology, and pathology of the mitral annulus, mitral valve leaflets, chordae tendineae, and papillary muscles. *Am. Heart J.*, 76(3):399–418, 1968.

[SHN13] T. Suzuki, T. Hikage, and T. Nojima. Numerical assessment method for implantable cardiac pacemaker EMI triggered by 10MHz-band wireless power transfer coils. In *Microwave Workshop Series on RF and Wireless Technologies for Biomedical and Healthcare Applications (IMWS-BIO), 2013 IEEE MTT-S International*, pages 1–3, 2013.

[SKP+11] J. Seeburger, H.A. Katus, S.T. Pleger, U. Krumsdorf, F.W. Mohr, and R. Bekeredjian. Percutaneous and surgical treatment of mitral valve regurgitation. *Dtsch. Arztebl. Int.*, 108(48):816, 2011.

[SLC+07] J. Sundnes, G.T. Lines, X. Cai, B.F. Nielsen, K.A. Mardal, and A. Tveito. *Computing the electrical activity in the heart*, volume 1. Springer Science & Business Media, 2007.

[SLG16] F. Sotiropoulos, T.B. Le, and A. Gilmanov. Fluid mechanics of heart valves and their replacements. *Annu. Rev. Fluid Mechanics*, 48:259–283, 2016.

[SMBM11] K.E. Sherlock, G. Muthuswamy, R. Basu, and I.M. Mitchell. The Alfieri stitch: the advantages for mitral valve repair in difficult circumstances. *J. Card. Surg.*, 26(5):475–477, 2011.

[SMCCS06] J. Sainte-Marie, D. Chapelle, R. Cimrman, and M. Sorine. Modeling and estimation of the cardiac electromechanical activity. *Comput. & Struct.*, 84(28):1743–1759, 2006.

[Smi04] N.P. Smith. A computational study of the interaction between coronary blood flow and myocardial mechanics. *Physiol. Meas.*, 25(4):863–877, 2004.

[SMS09] M.S. Sacks, D.W. Merryman, and D.E. Schmidt. On the biomechanics of heart valve function. *J. Biomech.*, 42(12):1804–1824, 2009.

[SR85] M.A. Silver and W.C. Roberts. Detailed anatomy of the normally functioning aortic valve in hearts of normal and increased weight. *Am. J. Cardiol.*, 55(4):454–461, 1985.

[SS99] G.K. Snyder and B. Sheafor. Red blood cells: centerpiece in the evolution of the vertebrate circulatory system. *Am. Zool.*, 39(2):189–198, 1999.

[SSBW16] E.J. Stöhr, R.E. Shave, A.L. Baggish, and R.B. Weiner. Left ventricular twist mechanics in the context of normal physiology and cardiovascular disease: a review of studies using speckle tracking echocardiography. *Am. J. Physiol. Heart. Circ. Physiol.*, 311(3):H633–H644, 2016.

[ST11] T. Sawada and A. Tezuka. LLM and X-FEM based interface modeling of fluid-thin structure interactions on a non-interface-fitted mesh. *Comput. Mech.*, 48(3):319–332, 2011.

[STB03] K. Stein, T. Tezduyar, and R. Benney. Mesh moving techniques for fluid-structure interactions with large displacements. *J. Appl. Math.*, 70(1):58–63, 2003.

[STB04] K. Stein, T.E. Tezduyar, and R. Benney. Automatic mesh update with the solid-extension mesh moving technique. *Comput. Methods Appl. Mech. Eng.*, 193(21-22):2019–2032, 2004.

[Ste99] A. Stefanovska. Physics of the human cardiovascular system. *Contemp. Phys.*, 40(1):31–55, 1999.

[Sva02] K. Svanberg. A class of globally convergent optimization methods based on conservative convex separable approximations. *SIAM J. Optim.*, 12(2):555–573, 2002.

[TBK+10] D. Tanné, E. Bertrand, L. Kadem, P. Pibarot, and R. Rieu. Assessment of left heart and pulmonary circulation flow dynamics by a new pulsed mock circulatory system. *Exp. in Fluids*, 48(5):837–850, 2010.

[TDK+99] C.A. Taylor, M.T. Draney, J.P. Ku, D. Parker, B.N. Steele, K. Wang, and C.K. Zarins. Predictive medicine: computational techniques in therapeutic decision-making. *Comput. Aided Surg.*, 4(5):231–247, 1999.

[TDQ17] A. Tagliabue, L. Dedè, and A. Quarteroni. Fluid dynamics of an idealized left ventricle: the extended Nitsche's method for the treatment of heart valves as mixed time varying boundary conditions. *Int. J. Numer. Methods Fluids*, 85(3):135–164, 2017.

[Tez91] T.E. Tezduyar. *Stabilized finite element formulations for incompressible flow computations*, volume 28 of *Adv. Appl. Mech.* Academic Press, Boston, MA, 1991.

[The] The main phases of a heartbeat. https://www.thoughtco.com/phases-of-the-cardiac-cycle-anatomy-373240/.

[Thi08a] M. Thiriet. *Biology and Mechanics of Blood Flows - Part I: Biology*, volume 1 of *CRM Series in Mathematical Physics*. Springer, 2008.

[Thi08b] M. Thiriet. *Biology and Mechanics of Blood Flows - Part II: Mechanics and Medical Aspects of Blood Flows*, volume 2 of *CRM Series in Mathematical Physics*. Springer, 2008.

[Tho06] V. Thomée. *Galerkin finite element methods for parabolic problems*, volume 25 of *Springer Series in Computational Mathematics*. Springer, Berlin, Second edition, 2006.

[TJE+16] M. Toma, M.O. Jensen, D.R. Einstein, A.P. Yoganathan, R.P. Cochran, and K.S. Kunzelman. Fluid–structure interaction analysis of papillary muscle forces using a comprehensive mitral valve model with 3D chordal structure. *Ann. Biomed. Eng.*, 44(4):942–953, 2016.

[TKHL16] S.G. Tan, S. Kim, J.K. Hon, and H.L. Leo. A D-shaped bileaflet bioprosthesis which replicates physiological left ventricular flow patterns. *PLoS One*, 11(6):e0156580, 2016.

[TL+16] Thériault-Lauzier et al. Quantitative multi-slice computed tomography assessment of the mitral valvular complex for transcatheter mitral valve interventions part 2: geometrical measurements in patients with functional mitral regurgitation. *EuroIntervention*, 12(8):e1021–e1030, 2016.

[TM] W.D. Tucker and K. Mahajan. Anatomy, blood vessels. https://www.ncbi.nlm.nih.gov/books/NBK470401/.

[TM11] M.N. Tillquist and T.M. Maddox. Cardiac crossroads: deciding between mechanical or bioprosthetic heart valve replacement. *Patient Prefer. Adherence*, 5:91, 2011.

[Topa] Top view of the anatomy of the aortic valve. https://www.intechopen.com/books/medical-and-surgical-education-past-present-and-future/proposed-synthetic-tissues-that-replace-human-cadavers-for-training/.

[Topb] Top view of the anatomy of the mitral valve. https://www.mitralvalverepair.org/leaflets/.

[TT12] K. Takizawa and T.E. Tezduyar. Computational methods for parachute fluid-structure interactions. *Arch. Comput. Methods Eng.*, 19(1):125–169, 2012.

[Tur12] M.L. Turgeon. *Clinical Hematology Theory & Procedures*. Lippincott Williams & Wilkins, 2012.

[TV96] L. Tobiska and R. Verfürth. Analysis of a streamline diffusion finite element method for the Stokes and Navier-Stokes equations. *SIAM J. Numer. Anal.*, 33(1):107–127, 1996.

[V+10] C. Valfrè et al. The fate of hancock II porcine valve recipients 25 years after implant. *Eur. J. Cardiothorac. Surg.*, 38(2):141–146, 2010.

[VABV05] R. Van Loon, P.D. Anderson, F.P.T. Baaijens, and F.N. Van De Vosse. A three-dimensional fluid-structure interaction method for heart valve modelling. *Comptes-Rendus Mécanique*, 333(12):856–866, 2005.

[Van11] E.H. Van Brummelen. Partitioned iterative solution methods for fluid-structure interaction. *Int. J. Numer. Methods Fluids*, 65(1-3):3–27, 2011.

[vB09] E.H. van Brummelen. Added mass effects of compressible and incompressible flows in fluid-structure interaction. *J. Appl. Mech.*, 76(2):021206–7, 2009.

[VCV+08] E. Votta, E. Caiani, F. Veronesi, M. Soncini, F.M. Montevecchi, and A. Redaelli. Mitral valve finite-element modelling from ultrasound data: a pilot study for a new approach to understand mitral function and clinical scenarios. *Phil. Trans. A Math. Phys. Eng. Sci.*, 366(1879):3411–3434, 2008.

[Vida] Video of a mitral valve repair. https://www.youtube.com/watch?v=ae8T9rGtrkU/.

[Vidb] Video of a mitral valve replacement. https://www.youtube.com/watch?v=If-k1LdrUjo/.

[Vin08] J.L. Vincent. Understanding cardiac output. *Crit. Care*, 12(4):174, 2008.

[vLAdHB04] R. van Loon, P.D. Anderson, J. de Hart, and F.P.T. Baaijens. A combined fictitious domain/adaptive meshing method for fluid-structure interaction in heart valves. *Int. J. Numer. Methods Fluids*, 46(5):533–544, 2004.

[vLAvdV06] R. van Loon, P.D. Anderson, and F.N. van de Vosse. A fluid-structure interaction method with solid-rigid contact for heart valve dynamics. *J. Comput. Phys.*, 217(2):806–823, 2006.

[vLAvdVS07] R. van Loon, P.D. Anderson, F.N. van de Vosse, and S.J. Sherwin. Comparison of various fluid-structure interaction methods for deformable bodies. *Comput. & Struct.*, 85(11-14):833–843, 2007.

[VRDV00] J.A. Vierendeels, K. Riemslagh, E. Dick, and P.R. Verdonck. Computer simulation of intraventricular flow and pressure gradients during diastole. *J. Biomech. Eng.*, 122(6):667–674, 2000.

[VS06] A. Valencia and F. Solis. Blood flow dynamics and arterial wall interaction in a saccular aneurysm model of the basilar artery. *Comput. & Struct.*, 84(21):1326–1337, 2006.

[W+16] H. Wang et al. Global, regional, and national life expectancy, all-cause mortality, and cause-specific mortality for 249 causes of death, 1980–2015: a systematic analysis for the Global Burden of Disease Study 2015. *The Lancet*, 388(10053):1459–1544, 2016.

[WAN+14] T. Watanabe, H. Arai, E. Nagaoka, K. Oi, T. Hachimaru, H. Kuroki, T. Fujiwara, and T. Mizuno. Influence of procedural differences on mitral valve configuration after surgical repair for functional mitral regurgitation: in which direction should the papillary muscle be relocated? *J. Cardiothorac. Surg.*, 9(1):185, 2014.

[WBWW78] J. Wikstrand, G. Berglund, L. Wilhelmsen, and I. Wallentin. Value of systolic and diastolic time intervals. Studies in normotensive and hypertensive 50-year-old men and in patients after myocardial infarction. *Br. Heart J.*, 40(3):256–267, 1978.

[WDHY06] G.D. Weymouth, D.G. Dommermuth, K. Hendrickson, and D.K.P. Yue. Advancements in cartesian-grid methods for computational ship hydrodynamics. In *26th Symposium on Naval Hydrodynamics*, pages 1–18, Rome, Italy, September 2006.

[Wic11] T. Wick. Fluid-structure interactions using different mesh motion techniques. *Comput. & Struct.*, 89(13–14):1456–1467, 2011.

[Wic14] T. Wick. Flapping and contact FSI computations with the fluid-solid interface-tracking/interface-capturing technique and mesh adaptivity. *Comput. Mech.*, 53(1):29–43, 2014.

[Wie63] M.P. Wiedeman. Dimensions of blood vessels from distributing artery to collecting vein. *Circ. Res.*, 12(4):375–378, 1963.

[Wig] Wiggers diagram. https://commons.wikimedia.org/wiki/File:Wiggers_Diagram.svg.

[WKM05] E.J. Weinberg and M.R. Kaazempur-Mofrad. On the constitutive models for heart valve leaflet mechanics. *Cardiovasc. Eng.*, 5(1):37–43, 2005.

[WWW11] World Health Organization WHO, World Heart Federation WHF, and World Stroke Organization WSO. Global atlas on cardiovascular disease prevention and control. *World Health Organization*, 2011.

[WZ10] X. Wang and L.T. Zhang. Interpolation functions in the immersed boundary and finite element methods. *Comput. Mech.*, 45(4):321–334, 2010.

[YCS05] A.P. Yoganathan, K.B. Chandran, and F. Sotiropoulos. Flow in prosthetic heart valves: state-of-the-art and future directions. *Ann. Biomed. Eng.*, 33(12):1689–1694, 2005.

[YG08] F. Yilmaz and M.Y. Gundogdu. A critical review on blood flow in large arteries; relevance to blood rheology, viscosity models, and physiologic conditions. *Korea-Aust. Rheol. J.*, 20(4):197–211, 2008.

[ZD11] J. Zhuo and R. Dillon. Using the immersed boundary method to model complex fluids-structure interaction in sperm motility. *Dis. Cont. Dyn. Sys. Ser. B*, 15(2):343–355, 2011.

[Zem09] N. Zemzemi. *Étude théorique et numérique de l'activité électrique du coeur: applications aux électrocardiogrammes.* PhD Thesis, Université Paris VI, 2009.

[ZL08] A. Zilian and A. Legay. The enriched space-time finite element method (EST) for simultaneous solution of fluid-structure interaction. *Internat. J. Numer. Methods Eng.*, 75(3):305–334, 2008.

[ZS14] G. Zhou and N. Saito. Analysis of the fictitious domain method with penalty for elliptic problems. *Jpn. J. Ind. Appl. Math.*, 31(1):57–85, 2014.

[ZVF18] S. Zonca, S. Vergara, and L. Formaggia. An unfitted formulation for the interaction of an incompressible fluid with a thick structure via an XFEM/DG approach. *SIAM J. Sci. Comput.*, 40(1):B59–B84, 2018.